Interfacial Tension of Reservoir Fluids: an Integrated Experimental and Modelling Investigation

by

Luís M. C. Pereira

Thesis submitted for the degree of Doctor of Philosophy in

Petroleum Engineering

School of Energy, Geoscience, Infrastructure and Society

Heriot-Watt University

July 2016

PREFACE

The work presented in this manuscript has been developed as part of my PhD studies at Heriot-Watt University (HWU) under the supervision of Prof. Bahman Tohidi and Dr. Antonin Chapoy, between January 2013 and June 2016. The research described here was performed in the context of a Joint Industrial Project conducted in the Gas Hydrates, Flow Assurance and Phase Equilibria research group at HWU. Phase behaviour models implemented in the in-house PVT software of this research group (HWPVT) were used throughout this work. Part of the material in this manuscript has been presented or published elsewhere before; the list of publications concerning the studies described in this manuscript is given in **LIST OF PUBLICATIONS BY THE CANDIDATE**.

Luís Pereira
July 2016

ABSTRACT

Interfacial tension (*IFT*) is a property of paramount importance in many technical areas as it deals with the forces acting at the interface whenever two immiscible or partially miscible phases are in contact. With respect to petroleum engineering operations, it influences most, if not all, multiphase processes associated with the extraction and refining of Oil and Gas, from the optimisation of reservoir engineering strategies to the design of petrochemical facilities. This property is also of key importance for the development of successful and economical CO_2 geological storage projects as it controls, to a large extent, the amount of CO_2 that can be safely stored in a target reservoir. Therefore, an accurate knowledge of the *IFT* of reservoir fluids is needed.

Aiming at filling the experimental gap found in literature and extending the measurement of this property to reservoir conditions, the present work contributes with fundamental *IFT* data of binary and multicomponent synthetic reservoir fluids. Two new setups have been developed, validated and used to study the impact of high pressures (up to 69 MPa) and high temperatures (up to 469 K) on the *IFT* of hydrocarbon systems including *n*-alkanes and main gas components such as CH_4, CO_2, and N_2, as well as of the effect sparingly soluble gaseous impurities and NaCl on the *IFT* of water and CO_2 systems. Saturated density data of the phases, required to determine pertinent *IFT* values, have also been measured with a vibrating U-tube densitometer. Results indicated a strong dependence of the *IFT* values with temperature, pressure, phase density and salt concentration, whereas changes on the *IFT* due to the presence of up to 10 mole% gaseous impurities (sparingly soluble in water) laid very close to experimental uncertainties.

Additionally, the predictive capabilities of classical methods for computing *IFT* values have been compared to a more robust theoretical approach, the Density Gradient Theory (DGT), as well as to experimental data measured in this work and collected from literature. Results demonstrated the superior capabilities of the DGT for accurately predicting the *IFT* of synthetic hydrocarbon mixtures and of a real petroleum fluid with no further adjustable parameters for mixtures. In the case of aqueous systems, one binary interaction coefficient, estimated with the help of a single experimental data point, allowed the correct description of the *IFT* of binary and multicomponent systems in both two- and three-phase equilibria conditions, as well as the impact of salts with the DGT.

Aos meus pais, pelo amor incondicional e educação.

ACKNOWLEDGMENTS

This work would have been impossible without the help, support and contributions of all the people that were around me during these three and a half years and for which I will forever be grateful.

First, I would like to thank Prof. Bahman Tohidi for having given me the opportunity to conduct my PhD studies in his group, for what I have learnt with him and for his guidance throughout these years. Special and countless thanks are owed to Dr. Antonin Chapoy for his much valued inputs towards my research, for his support and for his seemingly limitless patience; this work is much indebted to him. I cannot forget also the help and assistance given by Dr. Rod Burgass in the laboratory and by Mr. Jim Allinson and Mr. Jack Irvine during the design and construction of the experimental setups used in this work. Moreover, I specially appreciate the financial support received from GALP Energia through my scholarship. Last but foremost, I am extremely grateful to Prof. João Coutinho, my MSc supervisor, for believing that I was up to the challenge, for sharing with me his knowledge of thermodynamics, and most importantly, life lessons that made a better “me”, and for all the invaluable discussions we had.

I had the privilege of sharing the office with fantastic people, each one with unique ways of companionship, and to have met friends who were the source of revitalization outside the working hours. For their friendship, dinners and adventures we shared together, I am truly grateful to Alfonso (Fon), Foroogh, Anthony, Duarte, Wissem, Mohamed, Bouja, Morteza, Mohammadreza, Edris, Diana and Martha. An extra special thank must go to Fon, who, with his *fonsenglish* and excellent mathematical knowledge, among many others talents, was always there not only to cheer me up, but also to help me overcome the obstacles and tackle the problems that arose during an important period of my PhD.

Words cannot express my gratitude to my long-term companion, Ana, for her love and her patience (most of the time), to her goes my biggest Thank You.

HERIOT
WATT
UNIVERSITY

ACADEMIC REGISTRY
Research Thesis Submission

Name:	Luís Manuel Cravo Pereira		
School/PGI:	School of Energy, Geoscience, Infrastructure and Society		
Version: *(i.e. First, Resubmission, Final)*	Final	Degree Sought (Award **and** Subject area)	PhD Petroleum Engineering

Declaration

In accordance with the appropriate regulations I hereby submit my thesis and I declare that:

1) the thesis embodies the results of my own work and has been composed by myself
2) where appropriate, I have made acknowledgement of the work of others and have made reference to work carried out in collaboration with other persons
3) the thesis is the correct version of the thesis for submission and is the same version as any electronic versions submitted*.
4) my thesis for the award referred to, deposited in the Heriot-Watt University Library, should be made available for loan or photocopying and be available via the Institutional Repository, subject to such conditions as the Librarian may require
5) I understand that as a student of the University I am required to abide by the Regulations of the University and to conform to its discipline.

* *Please note that it is the responsibility of the candidate to ensure that the correct version of the thesis is submitted.*

Signature of Candidate*:*	Luís Pereira	Date:	25/07/2016

Submission

Submitted By *(name in capitals):*	
Signature of Individual Submitting:	
Date Submitted:	

For Completion in the Student Service Centre (SSC)

Received in the SSC by *(name in capitals):*			
Method of Submission *(Handed in to SSC; posted through internal/external mail):*			
E-thesis Submitted (**mandatory for final theses)**			
Signature:		Date:	

Please note this form should bound into the submitted thesis.

Updated February 2008, November 2008, February 2009, January 2011

TABLE OF CONTENTS

LIST OF PUBLICATIONS BY THE CANDITATE

L.M.C. Pereira, A. Chapoy, R. Burgass, B. Tohidi, *Interfacial tension of* CO_2 *+ brine systems under geological sequestration conditions: experiments, modelling and implications*, (in preparation).

L.M.C. Pereira, A. Chapoy, R. Burgass, B. Tohidi, *Measurement and modelling of high pressure density and interfacial tension of (gas + n-alkane) binary mixtures*, J. Chem. Thermodyn. **97**, 55–69 (2016).

K. Kashefi, **L.M.C. Pereira**, A. Chapoy, R. Burgass, B. Tohidi, *Measurement and modelling of interfacial tension in methane/water and methane/brine systems at reservoir conditions*, Fluid Phase Equilib. **409**, 301–311 (2016).

L.M.C. Pereira, A. Chapoy, R. Burgass, M.B. Oliveira, J.A.P. Coutinho, B. Tohidi, *Study of the impact of high temperatures and pressures on the equilibrium densities and interfacial tension of the carbon dioxide/water system*, J. Chem. Thermodyn. **93**, 404–415 (2016). Part of the special issue of JCT on Thermophysical Properties for Carbon Dioxide Transportation and Storage.

L.M.C. Pereira, A. Chapoy, B. Tohidi, *Modelling of* CO_2*/brine interfacial tensions under* CO_2 *geological storage conditions*, presented (poster) in Scottish Carbon Capture & Storage Conference, Edinburgh, UK (2015).

A. Gonzalez, **L. Pereira**, P. Paricaud, C. Coquelet, A. Chapoy, *Modeling of transport properties using the SAFT-VR Mie equation of state*, published and presented (oral) in SPE Annual Technical Conference and Exhibition (Paper # SPE-175051-MS), Houston, Texas, USA (2015).

L.M.C. Pereira, A. Chapoy, B. Tohidi, *Vapor-liquid and liquid-liquid interfacial tension of water and hydrocarbon systems at representative reservoir conditions: experimental and modeling results*, published and presented (oral) in SPE Annual Technical Conference and Exhibition (Paper # SPE-170670-MS), Amsterdam, The Netherlands (2014).

L.M.C. Pereira, A. Chapoy, B. Tohidi, *Interfacial tension studies in* CO_2*-rich mixtures at representative reservoir conditions*, published and presented (oral) in Rio Oil & Gas Expo and Conference (Paper # IBP 1902_14), Rio de Janeiro, Brazil (2014).

L. Pereira, A. Chapoy, B. Tohidi, *A comprehensive study of the impact of elevated temperatures and pressures on the interfacial tension of the carbon dioxide/water system*, presented (oral) in the 20th European Conference on Thermophysical Properties, Porto, Portugal (2014).

L. Pereira, M. Kapateh, A. Chapoy, *Impact of impurities on thermophysical properties and dehydration requirements of* CO_2*-rich systems*, presented (oral) in UKCCSRC Biannual Meeting, Cambridge, UK (2014).

LIST OF TABLES

LIST OF FIGURES

NOMENCLATURE

List of Main Symbols

%AAD	Percentage average absolute deviation
$[c]$	Matrix of influence parameters
A	Interface area / Constant
a	Capillary constant / Energy parameter in the EoS / Constant
a_0	Pure compound parameter in the energy part of the CPA EoS
ADSA	Axisymmetric drop shape analysis
Ar	Argon
a_w	Activity of mixed salt solution
a_w^0	Activity of single salt solution
B	Constant
b	Co-volume parameter in the EoS
BMC	Backward-multiple-contact
Bo	Bond number
c	Influence parameter
c_1	Pure compound parameter in the energy part of the CPA EoS
$CaCl_2$	Calcium chloride
CCS	Carbon capture and storage
CH_4	Methane
CO_2	Carbon dioxide
CPA	Cubic-plus-association
CR	Capillary rise
DGT	Density gradient theory
E	Scaling exponent
EOR	Enhanced oil recovery
EoS	Equation of state
F	Helmholtz free energy
f	Helmholtz free energy density / Function
FMC	Forward-multiple-contact
G	Gibbs free energy
g	Gravitational acceleration / Radial distribution function in the CPA EoS

H	Maximum column of CO_2 / Constant
h	Height of the liquid rise or depression in the capillary tube
H_2	Molecular hydrogen
H_2O	Water
H_2S	Hydrogen sulphide
h_{is}	Adjustable interaction coefficient between salt and non-electrolyte components
HPHT	High pressure and high temperature
I	Ionic strength
ID	Inner diameter
IFT	Interfacial tension
k	Binary interaction coefficient in the EoS
KCl	Potassium chloride
L	Length of the interface / Liquid state / Liquid phase
L_1	Water-rich liquid phase
L_2	Hydrocarbon-rich liquid phase / CO_2-rich liquid phase
LGT	Linear gradient theory
m	Salt molality
MC	Monte Carlo computer simulation
M_{CO_2}	Mass of CO_2 per unit area of the reservoir (CO_2 storage capacity)
*m*CR-1	Modified CR-1 mixing rule
MD	Molecular Dynamics computer simulation
$MgCl_2$	Magnesium chloride
MIX-0, -1, -2, -3, -4 and -5	Multicomponent mixture 0, 1, 2, 3, 4 and 5
M_m	Salt-free mixture molecular weight
MW	Molecular weight
N	Number of grid points
N_2	Molecular nitrogen
NaCl	Sodium chloride
n-C_{10}	Normal decane
n-C_{16}	Normal hexadecane
n-C_6	Normal hexane
N_{comp}	Number of components
O_2	Molecular oxygen

P	Pressure
PC	*Pseudo*-component / Perturbed Chain
P_{ce}	Capillary entry pressure
P_{ch}	Parachor value
PD	Pendant drop
PPR78	Predictive Peng-Robinson 1978
PR78	Peng-Robinson 1978
r	Radius
R	Radii of curvature / Maximum radius of cylindrical pores / Universal gas constant
RFS-1	Real black oil
SAFT	Statistical associating fluid theory
SC	Supercritical
SG	Specific gravity
SRK72	Soave-Redlich-Kwong 1972
ST	Surface tension
S_w	Residual water saturation
T	Temperature
u	Standard uncertainty
U	Expanded uncertainty
UCEP	Upper critical end point
V	Volume / Vapour state / Vapour phase / Fluid phase rich in light components (*e.g.*, CO_2 and CH_4)
v	Molar volume
VLE	Vapour−liquid equilibrium
VT	Volume-translated
W	Reversible work
WAG	Water-alternating-gas
x	Liquid mole fraction
X_A	Mole fraction of molecules not bounded at site A
y	Vapour mole fraction / Ionic strength fraction
z	Normal distance across the interfacial region / Ion charge

Greek Letters

α	Symmetrical concentration / Tilting angle / Stationary point

β	Binary interaction coefficient in the DGT and the LGT / Bond number / Stationary point
β_{CPA}	Association volume in the CPA EoS
γ	Interfacial tension / Surface tension
Γ	Adsorption / Surface excess / Interfacial excess
γ^{EL}	Debye-Hückel activity coefficient
Δ	Difference / Variation
Δ^{AB}	Association strength
ΔC	Symmetrical interface segregation
Δh	Difference between the levels of two menisci in capillary tubes with different inner diameter
ε	Association energy parameter in the CPA EoS
θ	Contact angle
μ	Chemical potential
ρ	Density
ϕ	Porosity / Fugacity coefficient
ω	Acentric factor
Ω	Grand thermodynamic potential

List of Main Subscripts and Superscripts

0	Property evaluated at local density $\rho(z)$ / Origin / Reference dimension
c	Critical / Capillary tube / Correction / Combined
Eq.	Property evaluated at bulk phase compositions
Est.	Estimated value
Exp.	Experimental value
h	Hydrocarbon phase
I	Phase I
i, j and k	Components i,j and k
II	Phase II
L	Liquid phase
r	Reduced
ref	Reference component
Sat.	Saturation
V	Vapour phase
w	Water phase

INTRODUCTION

Background

Mitigating the atmospheric carbon dioxide (CO_2) concentration is known to be one of the most challenging and compelling endeavours humanity will face in the years to come [1]. One defining stage in the process involves the safe storage of captured CO_2. Among current options, geological storage of CO_2 is considered to be one of the most promising approaches [1,2]. Furthermore, since nearly two-thirds of the original oil in place is left unrecovered in reservoirs at the end of primary recovery and secondary waterfloods, carbon dioxide enhanced oil recovery and water-alternating-gas injection methods have attracted interest in the Oil and Gas industry not only as technical and profitable techniques to increase oil recovery efficiency, but also as economical and ecological methods to reduce CO_2 emissions [3–5]. In these multiphase subsurface processes, the flow and accumulation of fluids through the reservoir rock are controlled to a large extent by fluid−fluid and fluid−solid (rock) interactions [3,6].

A quantitative index of the interactions between fluid phases is given by the *interfacial tension* [6]. This property provides an idea of the dissimilarities between the contacting fluid phases; that is, near miscible fluids will have a low interfacial tension whereas immiscible fluids will show a greater value of interfacial tension. When dealing with reservoir engineering processes, such as those mentioned in the previous paragraph, reservoir fluids coexist in the interstices of the rock typically as a mixture of immiscible or partially miscible fluid phases. These fluids can be grouped into three broad phases: an *oil* phase, a *water* (brine) phase and a *gas* phase. Depending on the reservoir conditions, these three fluid phases may coexist simultaneously in the pore space of the rock and thus, three fluid−fluid interfaces arise: oil−water, gas−water and oil−gas. The volume occupied by each one of these phases in the pore space and their chemical properties depend on the nature of the reservoir (petroleum/aquifer) and may vary as a result of injection/production operations. For instance, when pressure in a petroleum reservoir drops below that of the saturation pressure, both oil and gas phases may be formed from what was initially only an oil phase (as in an oil reservoir) or a gas phase (as in a gas reservoir) in contact with a water phase. Likewise, when injected into a reservoir, CO_2 will partially dissolve in the resident fluid (water/oil) and some may remain as a separated phase. It is precisely the existence of this multiphase behaviour over a broad range of pressure and temperatures, coupled with different fluid compositions, that makes the study of the interfacial tension of reservoir fluids of practical importance. Although entirely related to the fluid phases in contact, this property greatly influences several rock properties such as capillary pressure, wettability and relative permeabilities [3,6]. Consequently, the accurate knowledge of the interfacial tension of reservoir fluids is crucial not only for maximising the storage of CO_2 in subsurface formations [7], but also for designing more efficient oil recovery processes [3].

Thesis Objectives

Despite its key role in reservoir engineering processes, experimental interfacial tension data of reservoir fluids at subsurface conditions are still scarce. Moreover, the simulation of multiphase processes requires the development of a general and robust thermodynamic model which when validated with experimental data can be used for estimating the interfacial tension of reservoir fluids. Thus, the main objective of the work developed in this thesis has been to contribute with reliable experimental interfacial tension data of model reservoir mixtures relevant for CO_2 storage and enhanced oil recovery projects, and to showcase the capabilities of selected theoretical approaches for replicating them. The studied systems comprised binary and multicomponent synthetic mixtures composed of water, salts, *n*-alkanes and gases, as well as one real petroleum fluid. The examined theoretical approaches included standard methods used in the Oil and Gas industry and an approach with a sound theoretical background, based on the energy of the interface, called the Density Gradient Theory. The investigations covered a broad range of pressures and temperatures (up to 300 MPa and 473 K), including two- and three-phase equilibria conditions.

Thesis Outline

This thesis commences with relevant background knowledge on the concept of *interfacial tension*, together with a brief description of its impact on industrial processes and a review of previous studies available in literature (**CHAPTER 1**). Following this, a complete description of the experimental apparatus used to measure this property is given in **CHAPTER 2**, while the selected theoretical models are briefly described in **CHAPTER 3**. The experimental and modelling results are presented, analysed and discussed in **CHAPTER 4** for hydrocarbon systems and in **CHAPTER 5** for aqueous systems. The main achievements and conclusions of this thesis as well as recommendations for future work are summarised in **CHAPTER 6**.

CHAPTER 1 – INTERFACIAL TENSION

1.1 Fundamentals

Interfacial forces are present in many practical situations of life as well as in numerous industrial processes dealing with multiphase conditions. Whenever two homogenous phases of different nature (*e.g.*, oil and water) or physical state (*i.e.*, gas, liquid and solid) coexist in equilibrium, forces acting at the boundary of the contiguous phases are often described using the concept of *interfacial tension* or *surface tension*. The term *surface tension* is often reserved to describe vapour−liquid interfaces and the term *interfacial tension* to describe liquid−liquid and solid−liquid interfaces. Generally speaking, all surfaces also act as interfaces and hence, the term interfacial tension (*IFT*) encompasses surface tension (*ST*). For the sake of clarity, the term *ST* is used henceforth for describing the interfacial forces in single component systems (*e.g.*, a liquid/solid in equilibrium with its own vapour) and the term *IFT* is used for multicomponent phase contacts, namely fluid−liquid and fluid−solid interfaces. For simplicity, the Greek letter γ is also used throughout to denote both *ST* and *IFT*.

As the name suggests, interfaces are under tension and this can be readily visualised through **Figure 1.1**, which shows schematically the direction of intermolecular forces acting near the boundary between two fluid phases (*I* and *II*) in contact. Molecules in phases *I* and *II* are attracted equally from all directions by intermolecular forces (*e.g.*, hydrogen bonding) resulting in a zero sum of force vectors. On the other hand, molecules at the interface experience a net imbalance of forces; they are attracted inward and to the side by neighbouring molecules but not outward, creating an inward pull of molecules back to the bulk of phases *I* and *II*. As a result, the interface tends to diminish its area as molecules move from a state of high energy (interface) to a state of lower energy (bulk phase). This contraction continues until both bulk phases reach the maximum number of molecules that can allocate in its interior for a given volume and set of conditions or external forces [8,9]. In this sense, the interface remains in a state of *tension*, with the system being characterised by a value of interfacial tension or surface tension. Based on this, *IFT* (or *ST*) is often interpreted as a mechanical quantity corresponding to the reversible work (*W*) required to increase the interface area (*A*) by an infinitesimal amount [9–11]:

$$\gamma = \left(\frac{\partial W}{\partial A} \right)_{T,V=constant} \qquad \textbf{1.1}$$

where γ is given in units of force per unit length (mN.m^{-1} or dyn.cm^{-1}) and it represents the tensile force acting at the interface which tends to decrease the area of the interface.

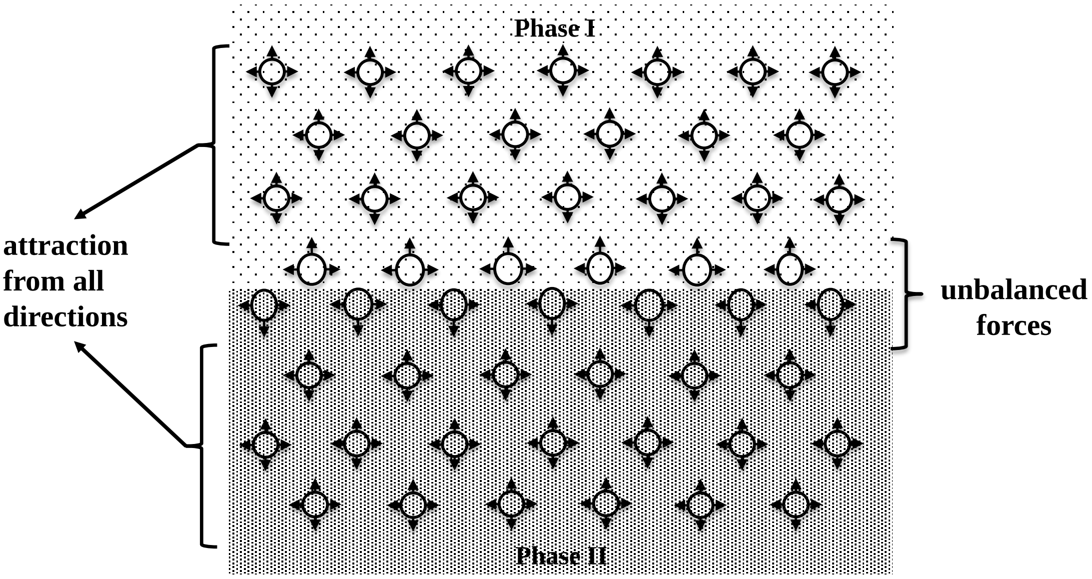

Figure 1.1. *Schematic illustration of the concept of interfacial tension between two fluid phases. Adapted from Dandekar´s book* [6].

The interface however, should not be regarded simply as plane which separates the two phases but rather as a small region of thickness Δz where properties, like density ρ, vary continuously from one bulk phase to another adjoining bulk phase, as depicted in **Figure 1.2**. Hence, the interface possesses an anisotropic characteristic *i.e.*, magnitude of properties changes in the direction normal to the interface, and the contained fluid is said to be an inhomogeneous fluid or phase. From this viewpoint and since the interface is very thin (typically 1 to 2 nm for fluid−liquid interfaces far from the critical point), the interface can be analysed mathematically using Gibbs formalism [9,12] and the *IFT* defined in thermodynamic terms as the change in the Helmholtz free energy, *F*, (or Gibbs free energy, *G*) of the interface when its area is increased reversibly by an infinitesimal amount at constant temperature and composition, and at constant volume (or pressure) [9–12]:

$$\gamma = \left(\frac{\partial F}{\partial A} \right)_{V,T,n=constant} = \left(\frac{\partial G}{\partial A} \right)_{P,T,n=constant} \qquad \textbf{1.2}$$

where γ is given in units of energy per unit area (J.m^{-2}). From this interpretation, which is a more fundamental one, γ can be regarded also as an *interfacial free energy* (or *surface free energy*) and is dimensionally equivalent to that obtained in **Equation 1.1** *i.e.*, 1 mN.m^{-1} = 0.001 J.m^{-2}. Surface/interfacial tensions as defined in **Equations 1.1** and **1.2** are also numerically equivalent for vapour−liquid and liquid−liquid interfaces formed between bulk phases in thermodynamic equilibrium, but it may differ for non-equilibrium liquids and solids [11].

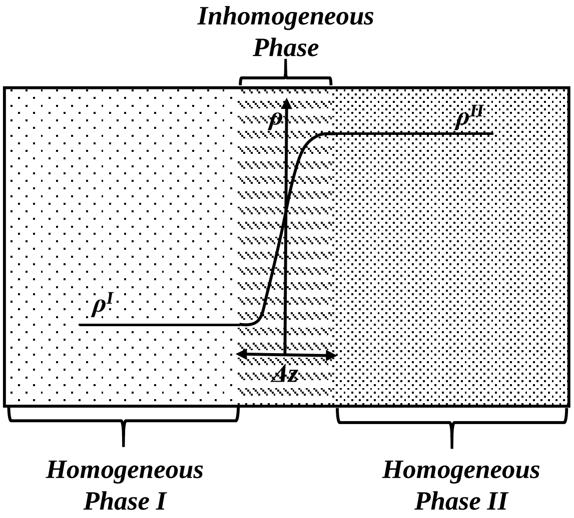

Figure 1.2. *Density variation along the normal distance z in the interfacial region between two fluid phases in contact.*

Interfacial forces between fluid and solid phases are preferably characterised using the concepts of wettability and contact angle [9,12]. As illustrated schematically in **Figure 1.3**, when two fluids are contacted with a solid surface, one of them will show greater affinity to spread or adhere to the solid surface; in other words, one phase will be attracted more strongly to the solid. This phenomenon is intrinsically linked to the interfacial tensions acting at the three-phase contact point, which are interrelated via the Young’s or Young-Dupré’s equation [9,12]:

$$\gamma_{solid-fluid_2} - \gamma_{solid-fluid_1} = \gamma_{fluid_1-fluid_2}\cos\theta \qquad \mathbf{1.3}$$

where θ is the characteristic contact angle formed between the solid surface and the denser fluid and it represents a quantitative measure of the wettability of a solid surface. For example, taking *fluid*$_1$ to be water and *fluid*$_2$ to be oil, the solid is said to be water wet if $\theta < 90^{\circ}$, oil wet if $\theta > 90^{\circ}$ and of intermediate wettability for values of θ approaching 90°.

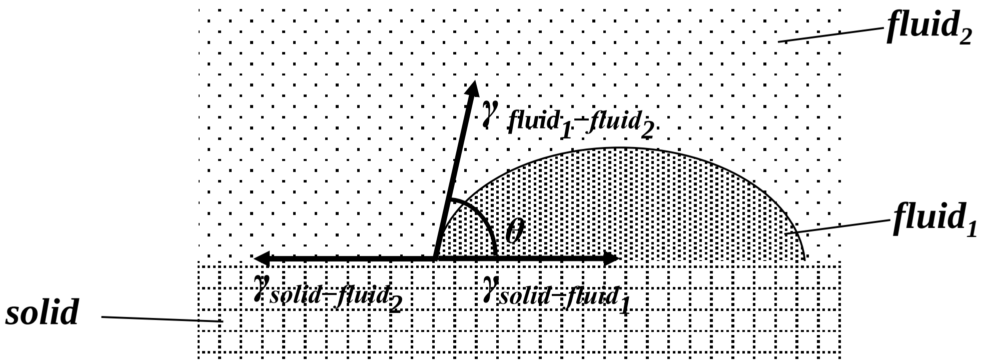

Figure 1.3. *Interfacial forces at the three-contact point between a solid and two fluid phases.*

Since interfaces are in tension and they tend to be curved, a pressure difference exists across the interface. This can be visualised through **Figure 1.4**, where the forces acting on an imaginary section of a spherical liquid (*L*) drop, of radius *r*, immersed in its own vapour (*V*) are shown. The liquid surface tension acts as a force which tends to reduce the volume of the drop whilst the pressure felt in the liquid increases as liquid molecules are brought closer together. Consequently, the pressure is greater in the concave side (P_L) of the interface than in the convex side (P_V) by an amount $\Delta P = P_L - P_V$ and this creates, in turn, an opposing force acting radially outward which tends to increase the volume of the drop. Under equilibrium conditions, these forces are balanced, by considering only one hemisphere of the drop, as follows [10]:

$$2\pi r\gamma = (P_L - P_V)\pi r^2 \tag{1.4}$$

where $2\pi r$ is the length of the circumference (at the equator of the sphere) and πr^2 is the projected area of the hemisphere.

By rearranging the previous equation:

$$\Delta P = \frac{2\gamma}{r} \tag{1.5}$$

where γ is, as previously denoted, the surface tension or surface free energy. **Equation 1.5** is a simple form of the fundamental equation of capillarity, also known as Young-Laplace equation, which in its generalized form is given as:

$$\Delta P = \gamma\left(\frac{1}{R_1} - \frac{1}{R_2}\right) \qquad \textbf{1.6}$$

where R_1 and R_2 are the principal radii of curvature. A comprehensive review on the mathematical principles and fundamentals leading to the derivation of this equation can be found elsewhere [9,12,13].

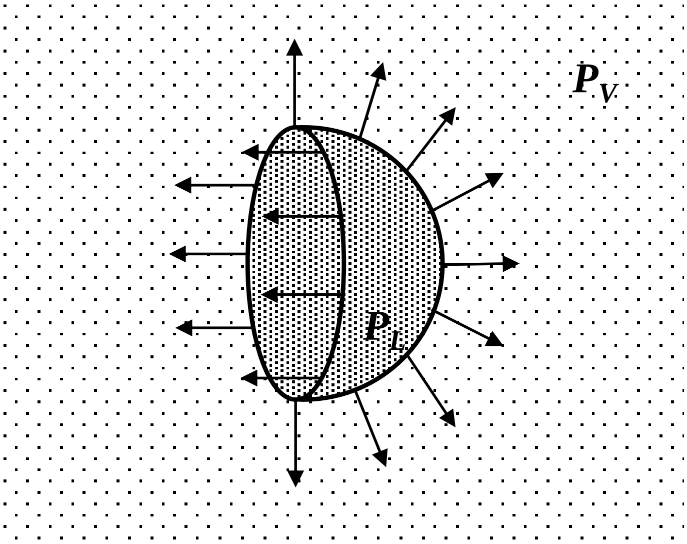

Figure 1.4. *Direction of forces acting on an imaginary section of one hemisphere of a spherical liquid drop immersed in its own vapour. Adapted from Pellicer et al.* [10].

From the aforementioned definitions, interfacial tension is the best known property used to identify and describe the behaviour and characteristics of fluid interfaces. Therefore, it is easy to rationalise that accurate knowledge of this property is paramount in numerous engineering applications throughout the chemical and petroleum industry where multiple phases coexist in equilibrium [3,6,14].

1.2 Significance of Fluid−Liquid Interfacial Tensions

In many chemical engineering processes, such as distillation, adsorption and extraction, to name just a few, the interfacial tension is decisive in the control of mass and heat transfer between fluids and hence, it greatly influences the design of process equipment [15,16]. This property also affects the quality of products such as glues, coatings, paints, agrochemicals, drugs, detergents and food, as well as many other industrial processes associated with the formation of emulsions, foams, micelles, thin films and gels [14].

With respect to the petroleum industry, fluid−liquid interfacial tensions influence most, if not all, processes involved in the extraction and refining of oil and gas, from the optimisation of reservoir engineering schemes to the design of petrochemical facilities. For example, recent results [17] indicated that oil−water *IFT* affects, to a great extent, the flow characteristics in horizontal pipes. Others [18] showed that the liquid hold up and slip velocity of phases in a packed column are also influenced by liquid−liquid interfacial tensions. Furthermore, it is well established that several rock properties such as wettability, capillary pressure and relative permeabilities strongly depend on the *IFT* between fluid phases. Thus, *IFT* is a key parameter that determines the displacement of hydrocarbons in the pore spaces of a reservoir rock and, in turn, the amount of oil produced [3,6].

Several studies have shown that lowering the *IFT* between the displacing and in-place fluids in oil recovery processes reduces the capillary forces over viscous forces (which are related by the capillary number[1]). This reduction improves the mobility of hydrocarbon reservoir fluids resulting in higher recovery efficiencies [19–25]. Surfactant flooding schemes and miscible gas injection processes are among the most commonly used enhanced oil recovery (EOR) techniques. The latter is of particular interest for this work. In a miscible (or near miscible) gas injection process, the reduction of oil−gas *IFT* is achieved as a result of enhanced mutual miscibility between the phases at high pressures. In general, the injected gas is rich in carbon dioxide (CO_2-EOR) and may contain other common gases such as methane and nitrogen. Wagner and Leach's [26] measurements confirmed that the residual oil saturation is significantly influenced by the variation of the *IFT* in methane + *n*-pentane systems. Firoozabadi *et al.* [27] stressed the importance of proper estimation of oil−gas *IFT*, particularly for fractured reservoirs, where gravity drainage is the main mechanism responsible for oil recovery. Other studies [28–30] revealed that liquid loss to the formation in gas condensate reservoirs can be considerably reduced by maintaining flow rates at low *IFT* values (<0.1 mN.m^{-1}). The understanding of the *IFT* between fluids phases is also fundamental for the application of water-alternating-gas (WAG) injection schemes. For example, the presence of CO_2

---

[1] The capillary number is a dimensionless number which relates the ratio of viscous to capillary forces in porous media and it is generally defined as: $N_c = \mu v/(\gamma\phi)$, where μ is the fluid viscosity, v is the flow velocity, γ is the interfacial tension and ϕ is the porosity [6].

favourably reduces oil–water *IFT* [31] which, in turn, reduces the capillary forces resisting the displacement of the fluids towards producing wells.

In the context of Carbon Capture and Storage (CCS) projects, one key constraint in the safe geological storage of CO_2 involves the accurate knowledge of the sealing capillary pressure which prevents the migration (*i.e.*, leakage) of CO_2 from the storage site through the caprock (structural trapping). This pressure characterises the capillary-sealing efficiency of a caprock and it corresponds to the pressure at which the non-wetting phase (CO_2) penetrates the largest pore of a caprock previously saturated with a wetting phase (typically H_2O/brine), leading to the escape of CO_2 from the storage site (reservoir). The sealing capillary pressure (or capillary entry pressure − P_{ce}) can be approximated with the Young-Laplace equation for a caprock with pores of cylindrical shape and maximum radius R as follows [7,32–34]:

$$P_{ce} = P_{CO_2} - P_{H_2O/Brine} \approx \frac{2\gamma_{CO_2-H_2O/Brine}\cos\theta}{R} \tag{1.7}$$

where θ is the contact angle of the H_2O/brine phase with the solid surface. In this sense, the effective storage of CO_2 requires P_{ce} to be greater than the buoyancy pressure exerted by fluids in the underlying layer of the caprock. Using this concept, the maximum column of CO_2 (H) that can be trapped just beneath the caprock can be estimated by equating the buoyancy pressure to the capillary entry pressure as follows [7,33,34]:

$$(\rho_{H_2O/\mathrm{Brine}} - \rho_{CO_2})gH = \frac{2\gamma_{CO_2-H_2O/Brine}\cos\theta}{R}$$

$$\Leftrightarrow H = \frac{2\gamma_{CO_2-H_2O/Brine}\cos\theta}{(\rho_{H_2O/\mathrm{Brine}} - \rho_{CO_2})gR} \tag{1.8}$$

where $\rho_{H_2O/\mathrm{Brine}}$ and ρ_{CO_2} correspond to the density of H_2O/brine and CO_2, respectively, and g is the gravitational acceleration. The maximum column of CO_2 can be transformed to mass of CO_2 per unit area of the reservoir and the CO_2 storage capacity expressed as follows [7,33]:

$$M_{CO_2} = \rho_{CO_2} H\phi(1-S_w) \tag{1.9}$$

where M_{CO_2} is the mass of CO_2 per unit of surface area of the reservoir, ϕ is the porosity and S_w is the residual water saturation in the reservoir. From previous definitions it becomes clear that CO_2−H_2O/brine *IFT* is a key parameter in the capillary-sealing efficiency of a caprock and, consequently, in the CO_2 storage capacity by structural trapping. In the same way, oil−water and oil−gas interfacial tensions are crucial for a proper estimation of oil and gas reserves [35,36].

Capillary forces are also responsible for the trapping of injected CO_2 in the pore spaces of reservoir rocks such as aquifers. When injected, CO_2 will displace the formation fluids through connected paths in the pore network of a reservoir rock. However, the existence of a finite CO_2−fluid (water/brine) interfacial tension means that CO_2 bubbles will remain immobilized when the formation is reimbibed with the water/brine. This mechanism is known as capillary or residual trapping and it can account for trapping saturations ranging from 10 to 30 % of the pore volume of the rock at the end of reimbibition, depending on the initial CO_2 saturation and the reservoir rock properties [37]. It is also important to note that other mechanisms responsible for the sequestration of CO_2 in underground formations are solubility and mineral trapping [2]. However, these mechanisms operate in the long-term (from hundreds to millions of years) and their contribution in the short-term (decades), namely during the injection period, is expected to be small [38].

Among possible geological sites, deep saline aquifers offer the largest CO_2 capacity [39]; however, the need for considerable investment in infrastructures have turned depleted hydrocarbon reservoirs in more attractive alternatives. These reservoirs have an established geological database and the experience acquired during the oil and gas exploitation as well as infrastructures already in-place (pipelines, well and surface equipment) strengthens their potential use as CO_2 storage sites [39,40]. Depleted hydrocarbon reservoirs are filled with connate fluids, constituted of residual gas, oil, water and ions in solution, and are located in general at depths greater than 800 m, where temperatures and pressures normally exceed the critical conditions of pure CO_2 ($T_c \sim 304$ K and $P_c \sim 7.38$ MPa).

All aspects considered, accurate estimation of the effect of pressure, temperature and composition on the *IFT* of fluid phases is indispensable for the design and/or optimisation of not only production and recovery processes of petroleum technology, but also for the safe and efficient geological storage of CO_2.

1.3 Literature Survey

Due to its key role in the design and optimisation of the processes mentioned in the foregoing section, the study of interfacial tension of both simple and complex mixtures has been subject of extensive research for many years. Several authors have focused on measuring fundamental *IFT* data of binary systems which, in turn, are necessary for the development and validation of thermodynamic models. A case to point out is the study of Weinaug and Katz [41] who investigated the interfacial tension of methane + propane mixtures with the capillary rise technique at temperatures up to 363.2 K and pressures ranging from 10.34 MPa down to ambient, with measured *IFT* values ranging from 12.13 down to 0.50 $mN.m^{-1}$. Through validation with measured data, Weinaug and Katz [41] heuristically extended to mixtures the equation originally proposed by Macleod [42] and Sugden [43] for pure substances. This equation is known as the Parachor method and is still to date widely used in commercial PVT software packages and reservoir simulators for predicting the interfacial tension between oil and gas phases (**CHAPTER 3**). A brief review of *IFT* data available in literature for systems of interest is now presented.

1.3.1 Hydrocarbon systems

High pressure *IFT* binary data between *n*-alkanes and common gases such as carbon dioxide, methane and nitrogen have been collected for this work. Sources as well as temperature and pressure conditions are listed in **Tables 1.1**, **1.2** and **1.3**. From these it can be seen that most studies have been conducted for systems containing *n*-alkanes with a carbon number ≤ 10 and over a limited range of temperatures and pressures. Furthermore, as will be emphasised throughout this work, the measurement of fluid−liquid interfacial tensions through indirect techniques requires an accurate estimation of the density of the equilibrated phases in contact. Nourozieh *et al.* [44] showed that experimental saturated density data of the CO_2 + *n*-decane system are still scarce, with most studies limited to measurements of the saturated liquid phase and a temperature of 344 K. The most wide-ranging study was reported by Reamer and Sage [45] who measured the volumetric properties of this system at temperatures over the range 278 to 511 K and pressures up to 69 MPa. Nagarajan and Robinson [46], Shaver *et al.* [47] and Mejía *et al.* [48] have also reported saturated phase densities of this system at temperatures up to 377 K and pressures up to near the critical point. Saturated density data of *n*-decane with either CH_4 or N_2 are also, to the author's knowledge, still limited to the works of Sage and co-workers [49,50], Amin and Smith [51] and Jianhua *et al.*

[52]. As a result, the experimental investigation of the *IFT* of these systems is also, in most cases, limited to the mentioned studies. Only Georgiadis *et al.* [53] extended the *IFT* measurements between CO_2 and *n*-alkanes, including *n*-decane, to a broader range of temperatures. Using the pendant drop method, the authors measured the *IFT* of CO_2 + *n*-decane at temperatures ranging from 298 to 443 K and pressures up to 12.15 MPa. However, reported *IFT* values were obtained using pure compound densities for the bulk phases, which can lead to an inaccurate estimation of the *IFT* of CO_2 + *n*-alkanes systems [54].

Some authors have also measured the *IFT* of synthetic multicomponent hydrocarbon mixtures. Danesh *et al.* [55] reported high pressure *IFT* data of 5 and 10 component gas condensate mixtures in the temperature range 303 to 394 K. Gasem *et al.* [56] measured near critical *IFT* data of CO_2 + 10 hydrocarbons systems at T = 322 and 339 K. Huygens *et al.* [57] presented *IFT* measurements of N_2 + volatile oils systems for volatile oils containing different compositions of methane, *n*-butane and *n*-tetradecane at T = 373 K and pressures ranging from 30 to 40 MPa. In spite of containing significantly few components compared to real reservoir fluids, experimental *IFT* data of synthetic mixtures can be used as benchmark for testing the predictive capabilities of thermodynamic models.

***Table 1.1**. Literature IFT data of CH_4 (1) + n-alkane (2) binary systems.*

(2)	T / K	P / MPa	Source	Year
ethane	93 to 283	0.002 to 3.9	Baidakov *et al.* [58]	2013
propane	258 to 363	0.3 to 10.3	Weinaug and Katz [41]	1943
n-butane	311 to 344	8.9 to 10.7	Pennington and Hough [59]	1965
n-pentane	311	4.1 to 15.5	Hough and Stegemeier [35]	1961
	311	8.2 to 16.7	Wagner and Leach [26]	1966
	311 to 411	2.8 to 15.9	Amin and Smith [51]	1998
n-hexane	298	0.02 to 7.6	Massoudi and King [60]	1975
	300 and 350	2 to 10	Niño-Amézquita *et al.* [61]	2010
n-heptane	311 to 428	2.8 to 24.8	Warren and Hough [62]	1970
	298	0.1 to 5	Niño-Amézquita *et al.* [61]	2010
	298	0.1 to 15	Jaeger *et al.* [63]	2010
	323	0.1 to 17.0	Jaeger and Eggers [64]	2012
	311 to 394	2.8 to 24.8	Amin and Smith [51]	1998
n-octane	274 to 282	0.1 to 8.5	Peng *et al.* [65]	2011
n-nonane	239 to 298	0.1 to 10.2	Deam and Maddox [66]	1970
n-decane	311	8.6 to 34.5	Hough and Stegemeier [35]	1961
	311 to 361	10.3 to 36.5	Stegemeier *et al.* [67]	1962
	311 to 411	2.8 to 34.5	Amin and Smith [51]	1998

Table 1.2. *Literature IFT data of CO_2 (1) + n-alkane (2) binary systems.*

(2)	***T* / K**	***P* / MPa**	**Source**	**Year**
n-butane	319 to 378	2.2 to 8.0	Hsu *et al.* [68]	1984
n-hexane	298	0.02 to 4.6	Massoudi and King [60]	1975
n-heptane	323 and 353	0.1 to 11.2	Niño-Amézquita *et al.* [69]	2010
	323 and 353	0.1 to 11.2	Jaeger *et al.* [63]	2010
	323	0.1 to 9.3	Jaeger and Eggers [64]	2012
	313 to 393	0.3 to 7.6	Zolghadr *et al.* [70]	2013
n-decane	344 and 378	6.9 to 16.5	Nagarajan and Robinson [46]	1986
	344	0.9 to 12.7	Shaver *et al.* [47]	2001
	298 to 443	0.1 to 12.2	Georgiadis *et al.* [53]	2010
	344	0.1 to 10.4	Mejía *et al.* [48]	2014
n-dodecane	298 to 443	0.1 to 15.2	Georgiadis *et al.* [53]	2010
	344	0.1 to 12	Cumicheo *et al.* [54]	2014
n-tridecane	344	0.1 to 13	Cumicheo *et al.* [54]	2014
n-tetradecane	344	11.1 to 16.3	Gasem *et al.* [71]	1989
	344	0.1 to 14	Cumicheo *et al.* [54]	2014
n-hexadecane	298 to 443	0.1 to 23.0	Georgiadis *et al.* [53]	2010
	313 to 393	0.3 to 11.4	Zolghadr *et al.* [70]	2013
n-eicosane	323	0.1 to 10.3	Mejía *et al.* [48]	2014

Table 1.3. *Literature IFT data of N_2 (1) + n-alkane (2) binary systems.*

(2)	***T* / K**	***P* / MPa**	**Source**	**Year**
ethane	93 to 283	0.002 to 3.9	Baidakov *et al.* [72]	2012
n-butane	298	1.49 to 7.00	Reno and Katz [73]	1943
n-pentane	313	0.1 to 40	Jianhua *et al.* [52]	1993
n-hexane	303	4 to 10.5	Firoozabadi *et al.* [27]	1988
	313	0.1 to 40	Jianhua *et al.* [52]	1993
	303 to 333	0.1 to 15	Garrido *et al.* [74]	2014
n-heptane	298 to 358	1.48 to 7.00	Reno and Katz [73]	1943
	313	0.1 to 40	Jianhua *et al.* [52]	1993
	323 and 373	0.1 to 10.4	Niño-Amézquita *et al.* [69]	2010
	323	0.1 to 10.4	Jaeger *et al.* [63]	2010
	313 to 393	8.6 to 37.6	Zolghadr *et al.* [75]	2013
n-octane	313	0.1 to 40	Jianhua *et al.* [52]	1993
n-decane	313	0.1 to 40	Jianhua *et al.* [52]	1993
n-tetradecane	373	31.5 to 40	Huygens *et al.* [57]	1996
n-hexadecane	313 to 393	0.3 to 41.7	Zolghadr *et al.* [75]	2013

1.3.2 Aqueous systems

The interfacial properties of aqueous systems have attracted a great attention from researchers during the past two decades due to its influence in many different technical areas. Considering its importance on the geological storage of CO_2, many studies have been conducted on the experimental measurement of the *IFT* of the CO_2 + H_2O system [7,76–94]. In most of these studies the pendant drop method has been used to measure CO_2−H_2O *IFT*s over a wide range of experimental conditions. However, at the time of this work and to the author's knowledge, data available in literature above 398 K are still limited to the study of Shariat *et al.* [93].

A brief literature review carried by Georgiadis *et al.* [91] showed that CO_2−H_2O *IFT* data above CO_2 supercritical conditions are scarce and/or inconsistent. Amongst all factors pointed for these discrepancies, the assumption of pure density for the phases involved and the presence of impurities stand out as the most important factors. Yaginuma *et al.* [95], Hebach *et al.* [96], Kvamme *et al.* [87], Chiquet *et al.* [7], Bachu and Bennion [89], Tabasinejad *et al.* [97], Shariat *et al.* [93] and, more recently, Efika *et al.* [98], measured densities of the saturated phases with a vibrating U-tube densitometer. Their results showed that the approximation of the water-saturated CO_2-rich phase density to that of pure CO_2 [99] is in fact valid for temperatures and pressures up to 473 K and 140 MPa, respectively. However, as demonstrated by Chiquet *et al.* [7], the effect of dissolved CO_2 on the density of the liquid aqueous phase can cause severe underestimation of the *IFT*s close to the density inversion conditions, where the deviations of the real (measured) density difference from that of pure substances are greatest. For systems with relatively low mutual solubility such as hydrocarbon + water and nitrogen + water, the density of the saturated phases has been commonly approximated to that of pure substances [100–104] without any significant loss of accuracy. The second factor is the most difficult to control. Impurities are inherently present in trace amounts in any high pressure setup and can behave as surfactants decreasing the interfacial tension values [81,83,84,86]. Thus, a thorough cleaning procedure of the experimental device with different solvents is recommended before measuring this property. All things considered, the experimental studies on CO_2−H_2O *IFT* considered in this work are listed in **Table 1.4**.

Table 1.4. *Selected literature IFT data of* CO_2 *+* H_2O*.*

T / K	*P* / MPa	Source	Year
278 to 335	0.1 to 20	Hebach *et al.*[82]	2002
344	0.1 to 17.7	Park *et al.*[84]	2005
308 to 383	5 to 45	Chiquet *et al.*[7]	2007
323	1.1 to 22.5	Kvamme *et al.* [87]	2007
293 to 398	2 to 27	Bachu and Bennion [89]	2008
298 to 374	1 to 60	Georgiadis *et al.*[91]	2010
298 to 333	1.5 to 20.8	Bikkina *et al.* [92]	2011
323 to 477	7.8 to 124.1	Shariat *et al.*[93] *	2012

* Data available only through graphical form

In general, CO_2 streams associated with EOR and/or CCS operations come from capturing and separation processes. As a result, these streams can contain impurities which are sparingly soluble in water such as methane, nitrogen, hydrogen or oxygen and others more soluble such as hydrogen sulphide, sulphur dioxide or nitrous oxide, to name just a few. However, experimental data on the interfacial tension between CO_2-rich mixtures (CO_2 content > 70 mole%) and water are still limited to a small number of studies and impurities. Guo and co-workers [105,106] conducted *IFT* measurements of CO_2 + CH_4 + H_2O and CO_2 + N_2 + H_2O systems for different gas compositions in the temperature and pressure range of 298 to 373 K and 1 to 30 MPa, respectively. Their measurements demonstrated that the addition of diluent gases such as CH_4 and N_2 resulted in an increase of the *IFT* values when compared to that of the CO_2 + H_2O system under analogous temperature and pressure conditions. More recently, Shah *et al.* [33] measured the *IFT* between water and a gas mixture 70 mole% CO_2 + 30 mole% H_2S at $T = 350$ K and pressures up to 15.5 MPa, and observed a decrease of the *IFT* with the addition of H_2S. Since the sealing capillary pressure of the caprock and, in turn, the maximum column of gas that can be stored in a reservoir are direct functions of the *IFT*, as given in **Equation 1.8**, the selection of a reservoir for storing securely and efficiently a CO_2-rich gas stream must, therefore, take into account these variations in *IFT*. Indeed, Shah *et al.* [33] estimated that gas storage capacity would decrease significantly with increasing content in H_2S for reservoirs at depths greater than 2000 m, where, based on their experiments, the lowest interfacial tensions would be attained.

The presence of dissolved ions in the formation water is also an important aspect that should be taken into account. Cations such as Na^+, K^+ Ca^{2+}, Mg^{2+} and anions such as Cl^-, SO_4^- and HCO_3^-, to name just a few, are among the most abundant ions in the reservoir brine; the total concentration of these ions typically increases with reservoir depth and can reach concentrations of up to or greater than 400 $g.L^{-1}$ [89].

It is well established that the addition of salts such as NaCl, KCl, $CaCl_2$ or $MgCl_2$, affects the physical properties and phase behaviour of aqueous systems, in particular the *IFT*. Several authors [90,107–113] have related the increase of gas−water *IFT* upon the addition of salts to the distribution of ions between the interfacial region and the bulk aqueous phase. Johansson and Eriksson [108] reported surface tension values for different salt solutions that exceeded those of salt-free water under analogous conditions. Using the concept of an electrolyte free layer and Gibbs adsorption equation, the authors [108] showed that the *IFT* increase must be related to the negative adsorption (*i.e.*, depletion) of ions in the interface and, thereby to their tendency to remain in the aqueous bulk phase. Hey *et al.* [114] showed that in 1:1 electrolytes solutions this increase was directly proportional to the enthalpy of hydration of ions (*i.e.*, attraction to water), suggesting that ions were preferably fully hydrated in the bulk aqueous phase than partly hydrated in the interface. In general, the attraction of cations to water molecules is stronger than anions and hence, cations are strongly repelled while anions approach more closely to the interface [108,113]. Such gradient of ions results in an electrostatic potential differential at the interface which enhances the offset of water molecules from the interface towards the aqueous bulk phase and increases the magnitude of the interfacial tension [115]. Cation hydration increases as the ratio of cation charge to cation surface area is increased and thus the impact on the *IFT* is expected to increase as follows [116]:

$$Cs^+ < Rb^+ < NH_4^+ < K^+ < Na^+ < Li^+ < Ca^{2+} < Mg^{2+} \tag{1.10}$$

The findings described above are in agreement with Molecular Dynamics simulations performed by Li *et al.* [117] for CO_2 + brine systems and salts with the chloride (Cl^-) anion over a broad range of pressure and temperature conditions. In their work, computed *IFT* values and density profiles of species across the interface also indicated a negative adsorption (negative surface excess) of ions at the interface.

Another important contribution to the increase of *IFT* values may be attributed to the density increase of the aqueous phase and gas solubility decrease ("salting-out" effect). The addition of salts increases the average molecular weight of the aqueous phase, which under the assumption that the excess volume of mixing is zero results in an overall density increase. Such increase in the density of the aqueous phase amplifies the density difference between phases ($\Delta\rho$). This effect may greatly influence the experimental determination of *IFT* values through indirect measurement techniques which require the use of $\Delta\rho$, such as the pendant drop method. For example, at $T = 373$ K and $P = 50$ MPa, the density differences between phases of $CO_2 + H_2O$ [118] and $CO_2 + CaCl_2(aq)$ [119] systems reach a relative difference of approximately 94 and 179 % for $CaCl_2$ molalities $m = 2.5$ and 5.0 mol.kg^{-1}, respectively. Furthermore, in the case of CO_2 + brine systems, the well-known salting-out effect on the carbon dioxide solubility enhances the differences between the equilibrated phases promoting the increase of *IFT*.

In spite of their relevance, and somewhat surprisingly, examination of literature shows that few studies have investigated the *IFT* between CO_2 and single/binary salt solutions at reservoir conditions. These studies are limited not only in the type of salt and brine composition, as summarized in **Table 1.5**, but also in some cases the results are inconsistent. For example, most of these studies show that $CO_2{-}H_2O$ *IFT* increases with salt concentration for any temperature and pressure state. However, as can be seen in **Figure 1.5**, *IFT* values reported by Chalbaud *et al.* [90] and Li *et al.* [115] for different brines containing NaCl are lower for all salinities than those between CO_2 and pure water measured by Georgiadis *et al.* [91] and in this work at $T = 298$ K. It is worth nothing that Chalbaud *et al.* [90] and Li *et al.* [115] have already accounted for the increase in density of the brine-rich phase due to the dissolution of CO_2 and therefore, it is necessary to perform further measurements to clarify such discrepancies ("low" *IFT*).

IFT data of water/brine + liquid hydrocarbon systems have also been reported by several authors. Wiegand and Franck [100] measured interfacial tensions between water and either propane, *n*-hexane or *n*-decane at temperatures and pressures up to 473 K and 300 MPa. Cai *et al.* [101] reported *IFT* data between water/brine and 10 *n*-alkanes, and their mixtures, for pressures up to 30 MPa and temperatures in the range 298 to 353 K. Badakhshan and Bake [120] performed *IFT* measurements between brine and either *n*-hexane, cyclohexane or toluene. *IFT* data between *n*-hexane and brine systems were also reported by Ikeda *et al.* [121]. However, *IFT* experimental data between sparingly soluble gases and brine at reservoir conditions are scarce in literature and, to the author's knowledge, still limited to the *IFT* of brine + natural gas [122] and brine + methane systems [103].

Of relevance for the scope of this work are also the works of Jennings and Newman [123] and Georgiadis *et al.* [31] as well as studies previously conducted in our laboratories [124]. Jennings and Newman [123] and Georgiadis *et al.* [31] reported two-phase *IFT* data of the CH_4 + *n*-decane + H_2O and CO_2 + *n*-decane + H_2O systems, respectively. Therein, the authors investigated the impact of CH_4/CO_2 composition in the single hydrocarbon phase on the interfacial tension with water. The required density difference data were estimated by Jennings and Newman [123] based on density measurements of the mutually saturated phases whereas Georgiadis *et al.* [31] used pure H_2O density for the water-rich phase and modelled densities for the *n*-decane-rich phase. On the other hand, volumetric and *IFT* data of four water + hydrocarbon mixtures were measured in our laboratories in the context of a reservoir fluid studies project (2002−2005) [124], and the results reported through the works of Bahramian *et al.* [125] and Pereira *et al.* [126]. The systems investigated included three ternary mixtures CH_4 + *n*-decane + H_2O, CH_4 + *n*-hexadecane + H_2O and CH_4 + toluene + H_2O, and a quaternary mixture CH_4 + *n*-decane + cyclohexane + H_2O. Two- and three-phase interfacial tensions were measured at T = 423 K and over a wide range of equilibrium pressures (up to 140 MPa). *IFT* measurements were made between water-rich liquid and equilibrium vapour phase, hydrocarbon-rich liquid and equilibrium vapour phase, and water-rich liquid and hydrocarbon-rich liquid. Together, these studies provide valuable insights on the *IFT* between phases that coexist in the pore spaces of reservoir rocks and simulate, to some extent, *IFT*s variations during EOR and CO_2 storage processes due to changes in composition, temperature and pressure.

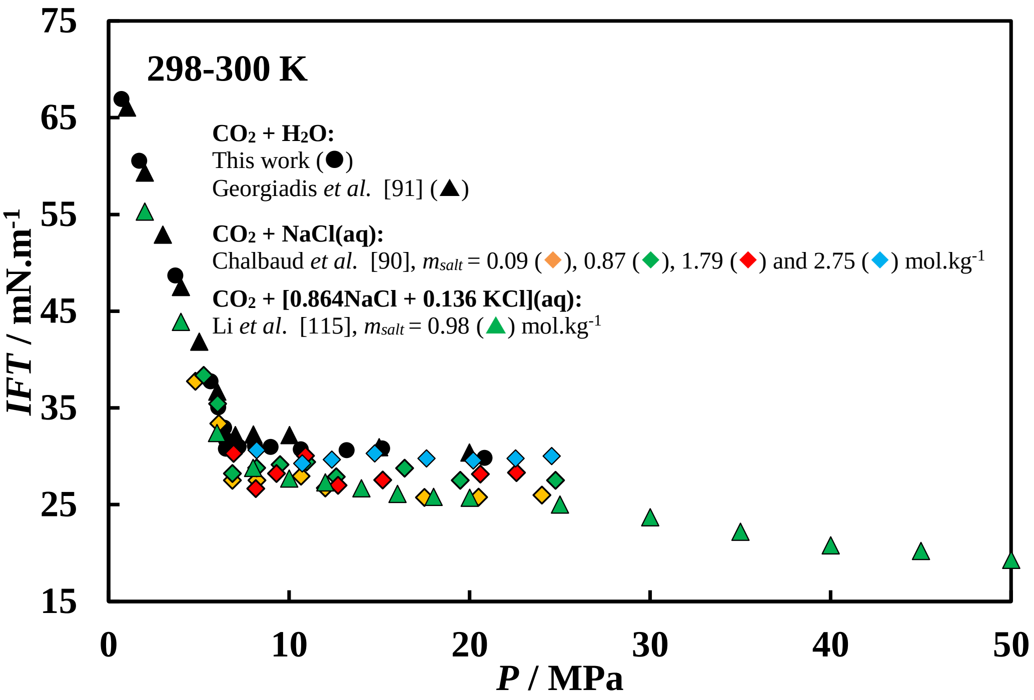

***Figure 1.5**. IFT-pressure diagram of CO_2 + H_2O and CO_2 + H_2O + Salt systems. IFT data reported by Georgiadis* et al. *[91] were recalculated using the correlation developed in this work for estimating the density of the CO_2-saturated water phase.*

***Table 1.5**. Literature IFT data of CO_2 + single/binary salt aqueous solutions. NA = not applicable.*

***T* / K**	***P* / MPa**	**Salt 1**	**Salt 2**	**Source**	**Year**
		molality / mol.kg^{-1}			
NaCl (1)					
298	0.1 to 6.0	0.51 to 5.78	NA	Massoudi and King [127]	1975
308	5 to 45	0.35	NA	Chiquet *et al.* [7]	2007
300 to 373	4.8 to 25.8	0.085 to 2.75	NA	Chalbaud *et al.* [90]	2009
300 to 313	3 to 9	0.1 and 1.03	NA	Liu *et al.* [128]	2015
$CaCl_2$ (1)					
300 to 373	4.9 to 25.2	0.05 to 2.7	NA	Aggelopoulos *et al.* [129]	2010
343 to 423	2 to 50	2.5 and 5.0	NA	Li *et al.* [119]	2012
$MgCl_2$(1)					
343 to 423	2.0 to 50.0	2.5, 5.0	NA	Li *et al.* [119]	2012
Na_2SO_4 (1)					
343 to 373	2 to 16	0.49 and 0.98	NA	Li *et al.* [119]	2012
NaCl (1) + $CaCl_2$ (2)					
300 to 373	5.0 to 25.3	0.05 to 1.5	0.05 to 1.5	Aggelopoulos *et al.* [130]	2011
NaCl (1) + KaCl (2)					
298 to 448	2.0 to 50.0	0.85 to 4.28	0.13 to 0.67	Li *et al.* [115]	2012

1.4 Summary

The interpretation of *interfacial tension* has been explained along with the concepts of wettability, contact angle and capillary pressure. From these it was possible to show that fluid−liquid interfacial tensions play a key role in many practical applications where multiple phases coexist in equilibrium. Particular attention was given to the impact of *IFT*s on the saturation, distribution and displacement of hydrocarbon and aqueous phases in a reservoir as well as on the geological storage of CO_2.

A critical analysis has also been performed on experimental *IFT* data available in literature for binary and multicomponent systems comprising reservoir fluids. The impact of density, diluent gases and salts on the *IFT* were briefly discussed. The systems which require further investigation were identified: gas + *n*-decane (gas = CO_2, CH_4 and N_2) and carbon dioxide + water/brine.

CHAPTER 2 – EXPERIMENTAL TECHNIQUES FOR MEASURING INTERFACIAL TENSION

2.1 Introduction

Due to its major role in many technical areas, a number of *tensiometers* have been developed for the experimental determination of the *IFT* between fluid phases in contact. Among all 17 techniques reviewed by Dorsey [131] in 1926, only a few are still commonly employed for interfacial tension measurements in fluid−liquid interfaces. The most popular techniques are depicted schematically in **Figure 2.1**. They were briefly reviewed in 2002 by Drelich *et al.* [132] and are described in detail in Rusanov and Prokhorov's book [11]. The Pendant Drop (PD) and Capillary Rise (CR) methods, due to their simplicity and ease of implementation at high pressure and high temperature (HPHT) conditions, are arguably the most widely used methods for measuring the *IFT* of reservoir fluids.

In the context of the PD technique, a drop of a denser fluid is formed at the tip of a capillary tube and kept in equilibrium with a surrounding less dense fluid (vapour or liquid) and the shape of the drop is subsequently analysed, as depicted in **Figure 2.1*f***. On the other hand, the CR method relies on the fundamentals of capillarity and on the rise of fluids in capillary tubes as depicted in **Figure 2.1*e***. Once the profile of the drop or the height of the liquid column are determined, they are combined with pertinent phase density data to obtain interfacial tension values. In essence, the estimation of the *IFT* with the foregoing techniques relies on the balance between capillary and gravity forces. In the CR method the *IFT* forces are balanced with a variable volume of liquid, whereas in the PD drop the effect of gravity on the shape of a drop of fixed volume is analysed [132].

The accurate measurement of *IFT* with the PD method requires a sufficiently large density difference between the phases to elongate the drop, reducing the errors that arise from the determination of the profile of the drop. For this reason, the CR technique is in general preferred for systems at/or near critical conditions, where the density difference and the *IFT* values are considerably lower. Overall, these methods have been applied in the study of interfacial phenomena of a variety of fluids and interfaces over a broad range of conditions and with established high precision and repeatability [11].

In this chapter a brief historical and technical discussion of the theoretical background of the PD and CR techniques is presented along with a detailed description of the apparatus used in this work to measure the interfacial tension of reservoir fluids over a broad range of experimental conditions.

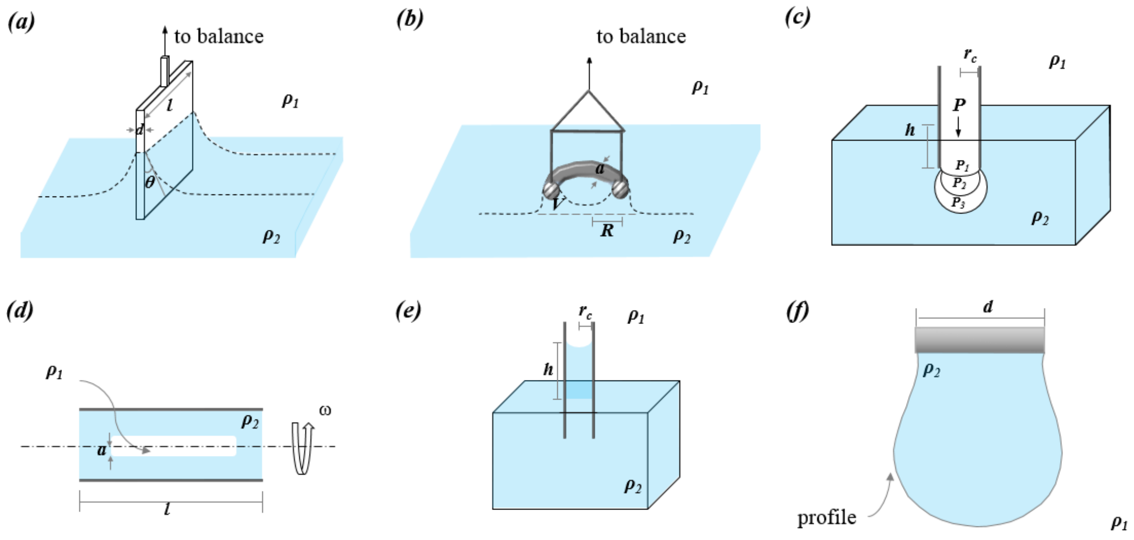

***Figure 2.1**. Schematic illustration of various techniques used for interfacial tension measurements: **(a)** Wilhelmy plate, **(b)** Du Noüy ring, **(c)** Maximum bubble pressure, **(d)** Spinning drop or bubble, **(e)** Capillary rise and **(f)** Pendant drop. Adapted from Drelich et al.* [132] *and Berry et al.* [133].

2.2 Capillary Rise Technique

2.2.1 Generalities

The capillary rise technique is one of the oldest methods (if not the oldest one) used to study the interfacial phenomena between adjacent fluid phases. The earliest records date back to the liquid rise studies of Leonardo da Vinci in small tubes with an apparent inner diameter of the size of a hair, hence the term capillary or *capillus* (Latin for hair) [134].

When an open capillary tube of inner radius r_c is immersed in a liquid (in equilibrium with an ambient fluid *i.e.*, vapour or liquid), a spontaneous rise or descent of the liquid along the cylindrical capillary occurs and a curved meniscus is formed between the wall of the tube and the liquid at an angle θ, as illustrated in **Figure 2.2**.

The translation of liquid in the tube is influenced by the relative strength between *adhesive* forces to the wall of the tube and *cohesive* forces between the molecules of the liquid. If the *adhesive* forces are greater than the *cohesive* forces, the liquid is translated upward to a height h above the flat liquid surface and the fluid−liquid interface forms a concave meniscus (**Figure 2.2*a***). In other words, it can be argued that adhesion of liquid molecules to the solid surface causes the capillary rise whilst the cohesion between molecules maintains the upward translation of liquid by pulling other liquid molecules and this effect is balanced by the gain in gravitational potential energy. A common example of capillary rise is the water + air + glass system. On the other hand, if *cohesive* forces are greater than *adhesive* forces, the liquid molecules at the fluid−liquid interface will have a stronger attraction towards liquid molecules in the bulk liquid phase and a downward force is created. This effect would pull the fluid−liquid interface downwards creating a capillary depression of depth *h* and a convex meniscus (**Figure 2.2*b***). The mercury + air + glass system is a popular example of this phenomenon.

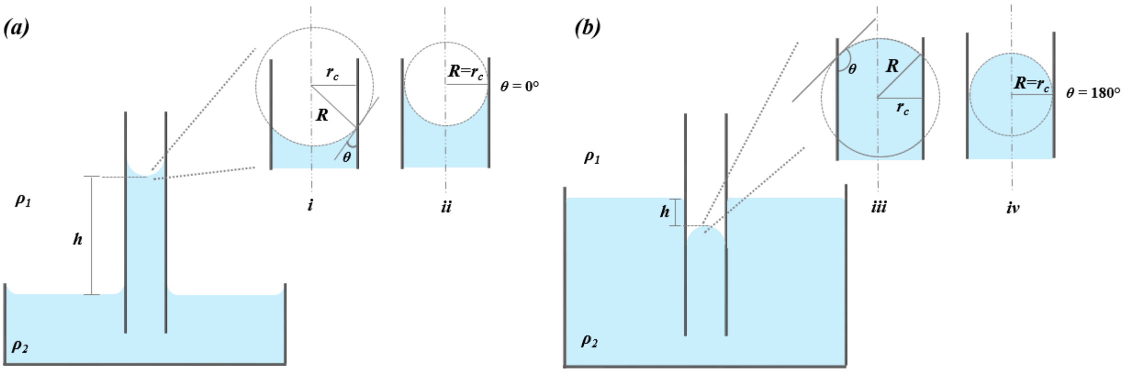

***Figure 2.2**. Schematic illustration of **(a)** capillary rise and **(b)** capillary depression in a vertical capillary tube. The contact angle θ between the liquid and the wall of the tube is less than 90° in cases **i** and **ii** where the adhesive forces are stronger than cohesive forces. In cases **iii** and **iv**, θ is greater than 90° and cohesive forces are predominant. ρ_1 and ρ_2 correspond to the density of the fluid (vapour or liquid) and liquid phases, respectively.*

At equilibrium, the force exerted by the solid tube on the liquid column is approximately counter balanced by the weight of the liquid column as follows [10]:

$$2\pi r_c(\gamma_{solid-fluid} - \gamma_{solid-liquid}) = \pi r_c^2 \rho g h \tag{2.1}$$

which can be rearranged to give:

$$h = \frac{2(\gamma_{solid-fluid} - \gamma_{solid-liquid})}{r_c \rho g} \tag{2.2}$$

From **Equation 2.2** it can be argued that the interfacial free energy difference (*i.e.*, $\gamma_{solid-fluid} - \gamma_{solid-liquid}$) is the main driving mechanism responsible for the rise or depression of the liquid body in the capillary [10,135]. If $\gamma_{solid-fluid} > \gamma_{solid-liquid}$, the liquid rises in the capillary (*h* is positive) and if $\gamma_{solid-fluid} < \gamma_{solid-liquid}$, the liquid moves downward (*h* is negative). Moreover, **Equation 2.2** also implies that the capillary rise or depression is inversely proportional to the capillary radius r_c.

Introducing **Equation 1.3** into **Equation 2.2** and by not neglecting the density of the ambient fluid, the following expression, also known as Jurin's law [136], is obtained:

$$h = \frac{2\gamma_{fluid-liquid}\cos\theta}{r_c \Delta\rho g} \qquad \textbf{2.3}$$

where $\Delta\rho$ is the density difference between the liquid and ambient fluid, g is the gravitational acceleration (9.81589 m.s^{-1}), θ is the contact angle formed between the liquid and the glass wall, and $\gamma_{fluid-liquid}$ is the fluid–liquid interfacial tension. In this equation, $\gamma_{fluid-liquid}$ is always positive and the sign of h is defined by the angle at which the liquid contacts the glass wall (*i.e.*, $\cos\theta > 0$ for $\theta < 90^\circ$ and $\cos\theta < 0$ for $\theta > 90^\circ$).

It is worth mentioning that many authors [8,9,137,138] have stressed that the pressure difference across the fluid–liquid interface is precisely the main driving mechanism responsible for the upward translation of a liquid body inside a capillary tube rather than the interactions between the phases (liquid, fluid and solid). Accordingly, the existence of a low pressure region in one side of the interface creates a pressure gradient along the capillary tube and the result is a vertical force which drives the liquid and pushes (as opposed to pulling) the column of liquid upward subjected to an opposing gravity force. From this viewpoint, at equilibrium, the pressure difference across the interface described by the Young-Laplace equation is equal to the hydrostatic pressure. In the case of small diameter tubes ($r_c << h$), the meniscus will be approximately hemispherical [9,12] and thus, $R_1 = R_2 = r_c (\cos\theta)^{-1}$ in **Equation 1.6,** and the balance between pressures yields:

$$\Delta P = \Delta\rho g h$$

$$\Leftrightarrow \frac{2\gamma_{fluid-liquid}\cos\theta}{r_c} = \Delta\rho g h$$

$$\Leftrightarrow h = \frac{2\gamma_{fluid-liquid}\cos\theta}{r_c \Delta\rho g} \qquad \textbf{2.4}$$

Arguments in favour and against each of these views can be found elsewhere [137,139–142]. Nevertheless, it is evident that **Equation 2.4**, derived from the pressure difference in a curved interface, and **Equation 2.3**, derived from the forces acting at three contact line, are equivalent and can be used to obtain the interfacial tension values between liquid and fluid (vapour or liquid) phases from capillary rise experiments.

Most of organic liquids, including the type investigated in this work with this technique (*n*-alkanes), are generally assumed to fully wet the surface of glass tubes (*i.e.*, $\theta = 0°$ and $\cos 0° = 1$). Introducing this into **Equation 2.4** and after rearrangement, the interfacial tension of fluid–liquid interfaces can be measured from capillary rise experiments as follows:

$$IFT = \frac{a^2 \Delta\rho g}{2} \qquad \textbf{2.5}$$

with $a^2 = hr_c$ and a is the capillary constant in units of length.

The calculation of interfacial tension values from the capillary rise with **Equation 2.5** must account for deviations of the meniscus from sphericity [13]. In the case of nearly spherical meniscus in narrow tubes ($r_c << h$), Rayleigh [143] introduced an approximate solution of the curvature by deriving an expression around a deviation function. The approximate solution is given by:

$$a^2 = r_c\left(h + \frac{r_c}{3} - \frac{0.1288 r_c^{\ 2}}{h} + \frac{0.1312 r_c^{\ 3}}{h^2}\right) \qquad \textbf{2.6}$$

The problem is now reduced to the measurement of h in vertical tubes. Recently, Barozzi and Angeli [144] investigated the effect of varying the angle of inclination of the capillary tube towards the vertical (*i.e.*, tilting angle: α) on the capillary rise. The results indicated that for α values between 0° and 88°, h is reduced gradually with increasing α, with significant relative deviations to the *true h* ($\alpha = 0°$) obtained for $\alpha > 50°$. Even though their results did not allow the deduction of any macroscopic change in the shape of the meniscus from axial symmetry, these results alone highlight the impact of inclination of the capillary tube on the measurement of reliable h values and, in turn, on the estimation of accurate interfacial tension values.

These problems can be removed with the variant of the CR method in which two capillary tubes with different r_c are used [11]. This variant, known as the differential CR method, is based on the measurement of the distance $\Delta h = h_1\text{-}h_2$ between two meniscus formed in capillary tubes with $r_c = r_1$ and $r_c = r_2$, as depicted in **Figure 2.3**. The calculation of the interfacial tension is then obtained by successive approximations of the square of the capillary constant a^2 (also known as Sugden's parameter) calculated by the function:

$$a^2 = \frac{\Delta h}{1/R_1 - 1/R_2} \qquad \textbf{2.7}$$

to values given in tables proposed by Sugden [145]. In **Equation 2.7** R_1 and R_2 correspond to the radii of curvature of the two capillary tubes. Lane [146] suggested two polynomial functions for estimating R_1 and R_2 with an accuracy that exceeded the data of Sugden's table. Therefore, in this work R_1 and R_2 are calculated using Lane's equation.

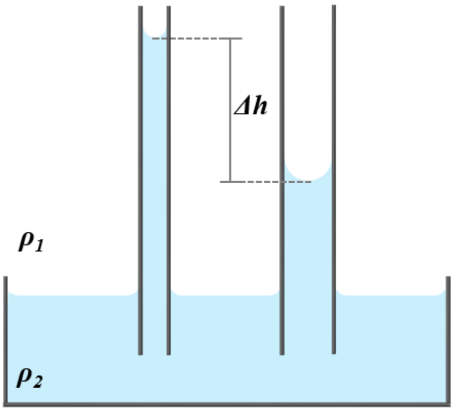

Figure 2.3. *Schematic illustration of the differential capillary rise method.*

The differential CR method has been used for the measurement of the interfacial tension of a variety of systems and in wide range of experimental conditions, including both vapour−liquid and liquid−liquid interfaces [147–153, 154 and references therein].

2.2.2 Experimental setup

In this work, the *IFT* and equilibrium densities of gas + *n*-alkane mixtures are measured with the experimental setup based on the differential CR method illustrated schematically in **Figure 2.4**.

The setup consists of a 500 cm^3 high-pressure see-through windowed equilibrium cell (**CR.A**) with three fluid ports (**CR.A$_1$**, **CR.A$_2$** and **CR.A$_3$**), a vibrating U-tube densitometer (**CR.B**) model DMA HPM and evaluation unit (**CR.C**) model mPDS 5, both manufactured by Anton Paar, a 100 cm^3 small movable piston (**CR.D**), two check valves (**CR.E$_1$** and **CR.E$_2$**) model 720.4631, manufactured by Sitec and with an opening pressure between 0.01 and 0.02 MPa, 300 or 600 cm^3 sample vessels (**CR.F$_1$** and **CR.F$_2$**)

and an automatic high pressure positive displacement DBR pump system (**CR.G**) with a maximum capacity of 500 cm^3.

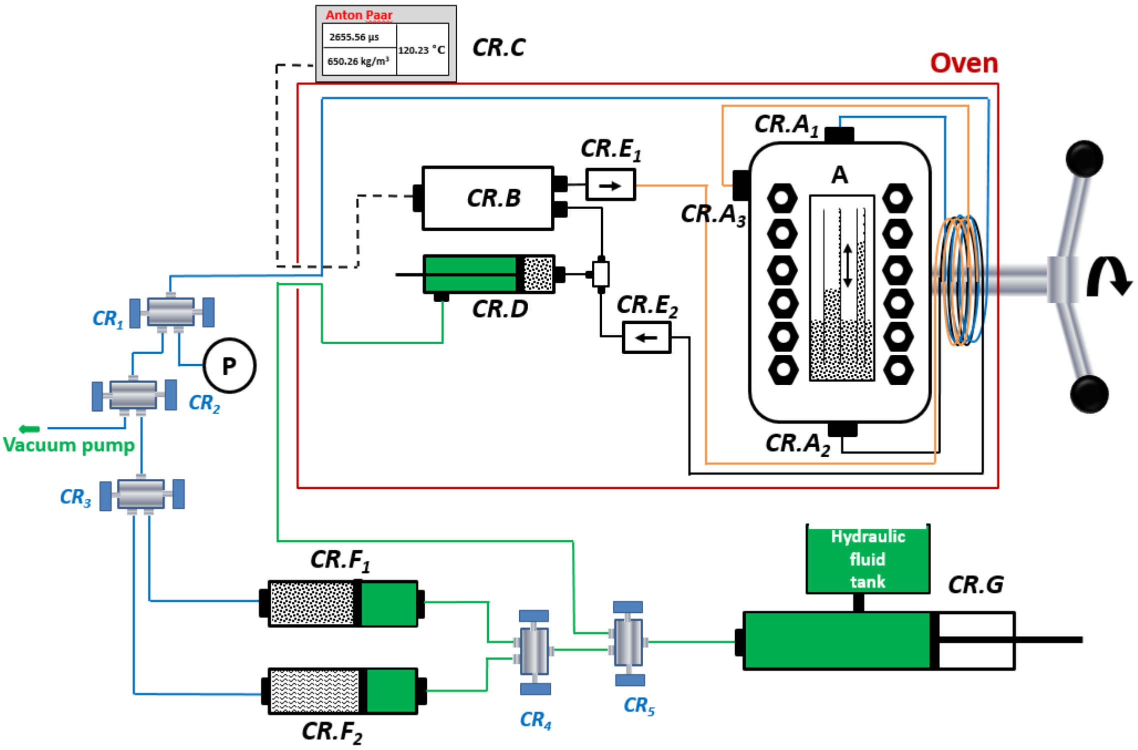

***Figure 2.4**. Schematic illustration of the experimental facility based on the differential CR method. In the scheme the followings are annotated: high-pressure see-through windowed equilibrium cell (**CR.A**); fluid ports (**CR.A$_1$**, **CR.A$_2$ and CR.A$_3$**); vibrating U-tube densitometer (**CR.B**) and evaluation unit (**CR.C**); 100 cm^3 movable piston (**CR.D**); check valves (**CR.E$_1$** and **CR.E$_2$**); 300 or 600 cm^3 sample vessels (**CR.F$_1$** and **CR.F$_2$**); automatic high pressure DBR pump system (**CR.G**) and valves **CR$_1$**, **CR$_2$**, **CR$_3$**, **CR$_4$** and **CR$_5$**.*

The high-pressure equilibrium cell (**CR.A**) is designed to hold pressures up to 103.4 MPa and temperatures up to 473 K. A magnetic stirrer positioned at the bottom of the cell helps to minimize potential temperature gradients within the sample in the cell and provides a good homogenization of the system. Two capillary glass tubes, with inner diameter (ID) of 0.396 and 0.986 mm, are positioned inside the cell by means of a custom-build stainless steel circular holder.

To determine the ID, several pictures of the top of the capillary tubes were taken with a USB camera fitted with magnifying lenses and the images analysed in a computer screen. The magnification ratio and a reference length were used to calculate the ID of the tubes from each picture and the values averaged accordingly. Taking into account all uncertainties and from dispersion of the calculated values, a standard uncertainty of ± 0.003 mm can be estimated for the ID of the tubes.

The fluid ports **CR.A$_2$** and **CR.A$_3$** of the cell are connected to the inlet and outlet of the densitometer (**CR.B**) by means of 0.29 mm ID high-pressure tubing with measured length of 3 m which ensures a minimum volume of approximately 0.2 cm^3. The two check valves (**CR.E$_1$** and **CR.E$_2$**) and the movable piston (**CR.D**) enables a closed loop flow of fluids between the equilibrium cell and the densitometer. Turning the equilibrium cell upside down allows the density measurement of either the saturated liquid or vapour phase. All parts described before are housed inside an oven, manufactured by Cincinnati Sub-Zero model Z-16, with an overall temperature control stability of ± 0.1 K.

The pressure is monitored by means of a pressure transducer (Quartzdyne Series I) connected to valve **CR$_1$** and previously calibrated against a dead weight pressure balance. This calibration procedure ensures a standard uncertainty of $u(P)$ = 0.04 MPa. The temperature is measured by a high precision built-in thermometer in the densitometer with a specified standard uncertainty of $u(T)$ = 0.1 K. The temperature readings from the densitometer were checked against a Prema 3040 high precision thermometer and deviations were observed to be within the densitometer uncertainties.

Tested fluids are stored in sample vessels and loaded into equilibrium cell through valves **CR$_1$**, **CR$_2$** and **CR$_3$** and fluid port **CR.A$_1$**. Each sample vessel contains a piston which can be used to control the internal volume of the vessel and, consequently, the pressure. The back pressure in both the sample vessels (**CR.F$_1$** and **CR.F$_2$**) and the movable piston (**CR.D**) are controlled by means of pressurized hydraulic fluid and the DBR pump system (**CR.G**), and also valves **CR$_4$** and **CR$_5$**.

An image capturing system (not shown in **Figure 2.4**) is used to measure the height of the liquid rise in the capillaries. It consists of a camera (Cohu model DSP 3600) mounted in a structure capable of vertical displacement (cathetometer). High magnification lenses are fitted into the camera and images, with a magnification factor higher than 15x, are displayed in a computer screen. As an example, a picture taken with this setup is depicted in **Figure 2.5**.

***Figure 2.5**. Picture of the liquid rise in the capillary tubes obtained with the setup based on the differential CR method for a mixture composed of CO_2 and n-decane.*

2.3 Pendant Drop Technique

2.3.1 Generalities

The measurement of the interfacial tension from the shape of pendants drops was first proposed by Worthington [155] in 1881, who examined the curved shape of a static drop hanging from a glass tube and its relation with the pressure drop across the interface. Two years later, Bashforth and Adams [156] stablished the foundations of the method used until today to analyse the profile of pendant drops deformed by gravity. These authors have showed that the profile of a pendant drop can be described by a single dimensionless number β, defined as $\beta \equiv \Delta\rho g R_0^2/IFT$, where $\Delta\rho$ corresponds to the density difference between the liquid and the surrounding fluid, g is the gravitational acceleration and R_0 is the radius of curvature at the apex of the drop. The quantity β, also known as the "Bond number" or Bo, corresponds to a measure of the relative strength between gravitational and interfacial forces. Bashforth and Adams [156] also compiled a collection of tables with the approximate numerical solution of the Young-Laplace equation for a series of drops with different values of Bo. As a result, the procedure for estimating the interfacial tension was reduced to an interpolation of measurements from drops to the values in their tables. However, the method for obtaining manually and precisely the Bo of a given system was quite difficult. It is only after the work of Andreas *et al.* [157] in 1937 that the Pendant Drop method found its widespread use in the measurement of this property with acceptable accuracy [11].

Andreas *et al.* [157] suggested an alternative and simple approach based on the selected plane method in pendant drops. Accordingly, the *IFT* from pendant drops can be readily calculated with an easily measurable parameter S, given by $S = d_s/d_e$, and with a shape dependent quantity defined as $H = \beta(d_e/R_0)^2$. In the context of this approach, d_e is the equatorial diameter and d_s is the diameter measured at a distance d_e up from the bottom of the drop, as illustrated in **Figure 2.6**. Subsequently, the *IFT* of a given system can be obtained as follows:

$$IFT = \frac{\Delta\rho g d_e^2}{H} \qquad \textbf{2.8}$$

Andreas *et al.* [157] generated experimentally tables of S versus $1/H$ for values of S ranging from 0.7 to 1. Tables for a wider range of values and also more accurate were obtained later by others [158,159] through numerical integration of the Young-Laplace equation.

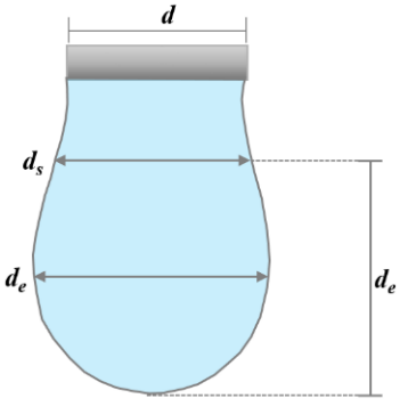

***Figure 2.6**. Schematic illustration of the selected plane method in pendant drops.*

The significant development of computational power over the last decades has led to more robust and accurate methods for the estimation of interfacial tension values from the shape of pendant drops. These modern methods are based on the analysis of the entire pendant drop profile rather than just some characteristic dimensions (d_e and d_s).

The Axisymmetric Drop Shape Analysis (ADSA) method, originally developed by Rotenberg *et al.* [160] in 1983, is one of the most widely used techniques. A detailed description of the theoretical background of this method can be found in the manuscripts of Cheng *et al.* [161], Song and Springer [162,163] and Hoorfar and Neumann [164] as well as in Neumann and co-workers' book [12]. In short, the principle of the ADSA method is based on matching the experimental drop profile from a digitalized image to a series of Laplacian curves with known interfacial tension values. The objective function to minimise is equal to the sum of squares between the coordinates extracted through edge detection of an image of the pendant drop (experimental curve) and theoretical curves. The best calculated curve identifies the interfacial tension value which, in turn, is related to the parameters of the pendant drop by:

$$IFT = \frac{\Delta\rho g}{(Bk_{apex})^2} \tag{2.9}$$

where $\Delta\rho$ is the density difference between the equilibrated phases, g is the gravitational acceleration and B and k_{apex} are parameters adjusted to the profile of the drop.

The development of better video images processing methods, more efficient algorithms and optical distortion correction techniques has significantly improved the precision of this technique [12,161,165–167]. Furthermore, the extraction of the drop profiles and subsequent numerical treatment automatically have also enabled the study of the impact of aging processes on the interfacial tension values [164]. It is important to note that the quality of the images and the elongation of the drop are key factors contributing to the overall consistency and accuracy of the *IFT* measurements [164]. The former can be controlled by the use of a filter in the light source in order to reduce chromatic effects in the captured images of the drops. On the other hand, the elongation of generated drops can be monitored by the parameter B in **Equation 2.9**. Drops with small B values (B <0.5) are nearly spherical whereas with increasing B values the drops become more and more elongated. The errors in the calculated *IFT* are kept at a minimum for values of B between 0.7 and 0.8 [162]. Since this parameter is a function of the diameter of the capillary tube (d in **Figure 2.6**), it can be easily modified to attain lower errors. In general, capillary tubes with larger diameters will provide larger ranges of drop shapes that are adequate for interfacial tension measurements [164].

In essence, the ADSA has proven to be a simple and accurate technique for determining the interfacial tension from pendant drops and it has been widely used to investigate this property in a variety of systems and interfaces. An examination of literature shows that this method has been commonly used to investigate this property in reservoir fluids at HPHT conditions, in particular for water−gas [7,82,91,168,169] and water−hydrocarbon interfaces [31,170].

2.3.2 Experimental setup

The Pendant Drop setup, used in this work to measure the *IFT* of pure CO_2 and CO_2-rich mixtures against water and brines, is similar in design to the setup used by Georgiadis *et al.* [31,53,91] and is depicted in **Figure 2.7**.

The setup consists of a custom-designed high-pressure cylinder made of Hastelloy C-276 (**PD.A**), a 300 cm^3 sample vessel (**PD.B**), a 15 cm^3 hand pump manufactured by Sitec (**PD.C**) model 710.4340 and an automatic high pressure positive displacement DBR pump system (**PD.D**) with a maximum capacity of 500 cm^3.

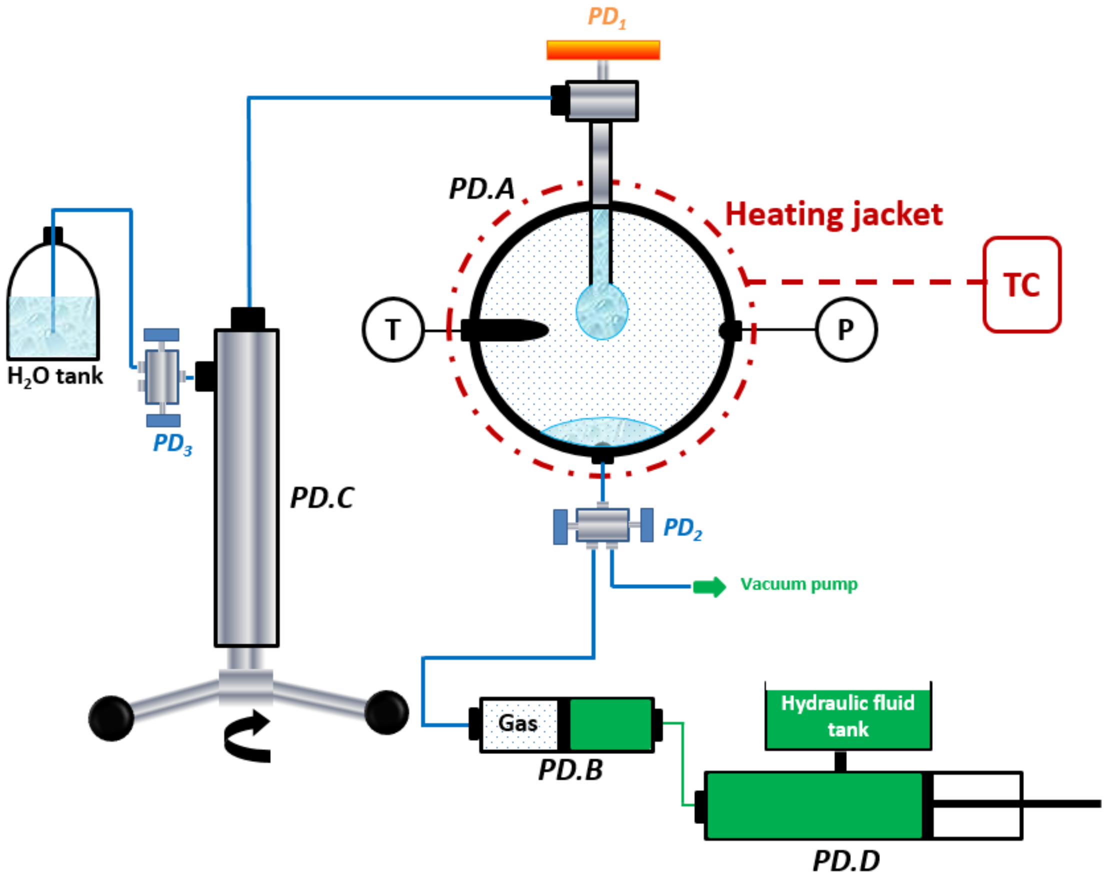

Figure 2.7. *Schematic illustration of the setup based on the PD method. In the scheme the followings are annotated: high-pressure cylindrical equilibrium cell (**PD.A**); 300 cm^3 sample vessel (**PD.B**); hand pump (**PD.C**), automatic high pressure DBR pump system (**PD.D**) and valves **PD$_1$**, **PD$_2$** and **PD$_3$**.*

The cell (**PD.A**) is capable of withstanding pressures and temperatures up to 100 MPa and 473 K, respectively. It has an internal volume of 23 cm^3, 4 fluid ports equally distributed around the cell and is closed at both ends by two sapphire windows. The cell temperature is controlled by means of an electrical heating jacket connected to a controller capable of regulating the temperature of the cell with a stability of ± 0.1 K. The temperature inside the cell is measured by a high precision PRT probe inserted in the cell, which is sufficiently long to ensure direct contact with the fluids. The pressure is measured by a piezo resistive silicon pressure transducer (Druck PDCR 4060) connected directly to the cell. The temperature and pressure probes are regularly calibrated against a Prema 3040 precision thermometer and a dead weight pressure balance, respectively. This calibration procedure ensures standard uncertainties of $u(P)$ = 0.04 MPa and $u(T)$ = 0.1 K.

The less dense phase (pure CO_2 or CO_2-rich mixture) is stored in a 300 cm^3 sample vessel (**PD.B**) connected to the cell by means of high pressure tubing and the backpressure in the vessel is controlled by means of pressurized hydraulic fluid and the automatic high pressure positive displacement DBR pump (**PD.D**). The denser phase (degassed water or brine) is transferred from a glass container (H_2O tank) into the hand pump (**PD.C**) and connected to the valve **PD$_1$**, located at the top of the cell.

Water/brine drops are created inside the cell at the tip of a capillary tube (outer diameter 1.610 ± 0.001 mm) and maintained at equilibrium in contact with the CO_2 phase. Live images of the drops are magnified and displayed on a computer screen by means of a USB camera and magnification lenses. A white LED light source (Euromex, model LE.5211) and a diffusion filter are used to adjust the contrast of the images. Digitalized images have a resolution of 752x480 pixels. As an example, the image of a water drop in a CO_2 atmosphere captured with this setup is depicted in **Figure 2.8**. The ADSA method implemented in the commercial software SCA 20 (Data Physics, Germany) is then used to determine the interfacial tension from the digitalized images.

***Figure 2.8**. Example of a drop of water in a CO_2 atmosphere captured with the setup based on the PD method at P = 3.66 MPa and T = 333 K.*

From **Equation 2.9**, the density difference between the equilibrated phases is required for the determination of pertinent *IFT* values. Hence, the volumetric properties of the aqueous systems of interest are also investigated.

The density of the saturated phases in the $CO_2 + H_2O$ system at pertinent conditions is measured using the experimental setup illustrated in **Figure 2.9.** This setup is the same setup used in the differential CR method depicted in **Figure 2.4** but with slight modifications. The parts annotated as **CR.D**, **CR.E$_1$** and **CR.E$_2$** are removed and the fluid port **CR.A$_3$** is closed. The inlet of the densitometer is connected to the fluid port **CR.A$_2$** while the outlet is connected to atmosphere and the flow of fluids out of the equilibrium cell is controlled through valve **CR$_5$**. Pure CO_2 and H_2O are stored in the two 300 cm^3 sample vessels and loaded into the equilibrium cell through the fluid port **CR.A$_1$**. Thereby, the density of each saturated phase can be measured alternatively by rotating the cell and purging it through the densitometer at constant pressure.

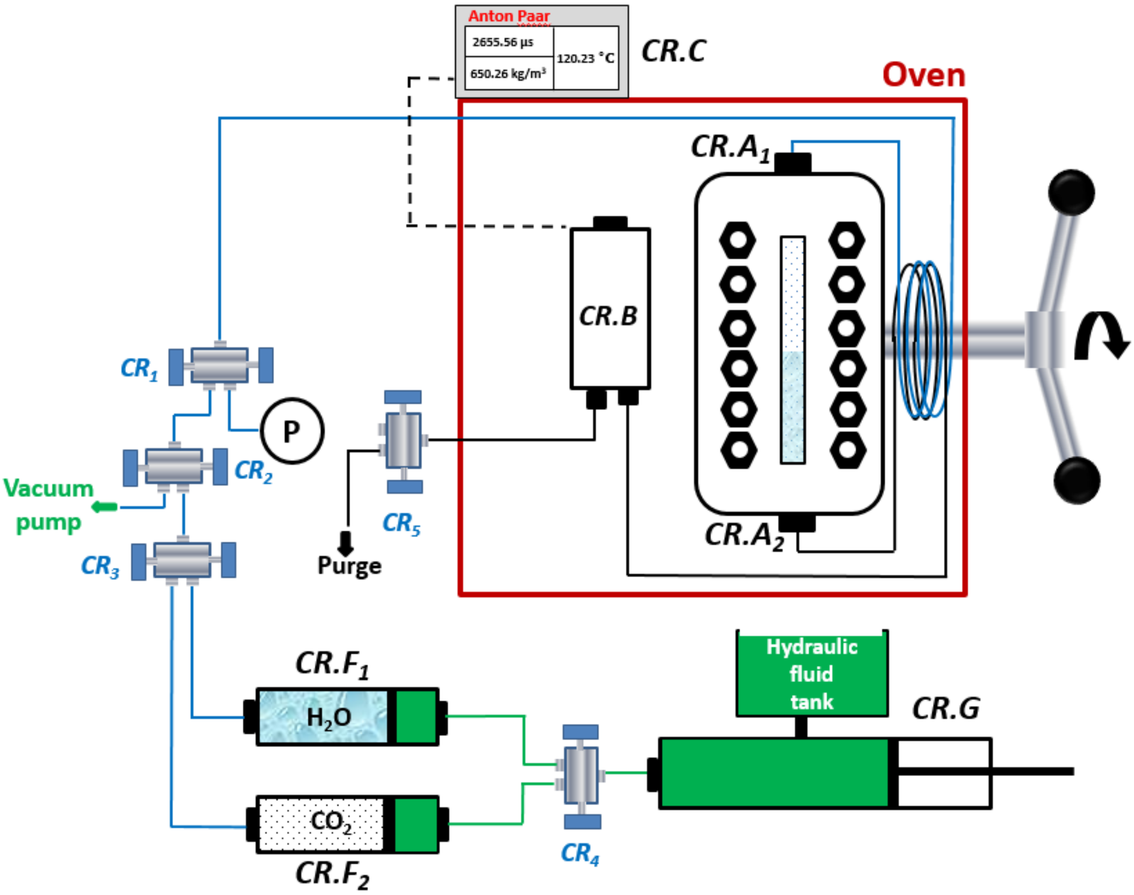

Figure 2.9. Schematic illustration of the density measuring setup based on the differential CR setup. Annotations are the same as in ***Figure 2.4****.*

As will be shown in **CHAPTER 5**, the saturated density of the CO_2-rich phase in the CO_2 + H_2O system is very close to that of pure CO_2 [99] under same pressure and temperature conditions. Therefore, in the case of systems including water and CO_2-rich mixtures (>90 mole% CO_2), only the saturated density of the water-rich phase is measured. This is performed in-situ for each pressure and temperature of interest by connecting the vibrating U-tube Anton Paar densitometer (**CR.B**) and a 16 cm^3 movable piston (**PD.E**) to the bottom of the PD cell (**PD.A**) and rearranging other parts, as illustrated schematically in **Figure 2.10**. In this manner, the equilibrated liquid phase is transferred to the densitometer by reducing the backpressure in the movable piston **PD.E** while keeping the pressure in the PD cell constant. The densitometer **CR.B** is thermostatised using a thermostat bath circulator (Jubalo model MA-4), with a temperature stability of 0.1 K, through two flow lines directly connected to the densitometer.

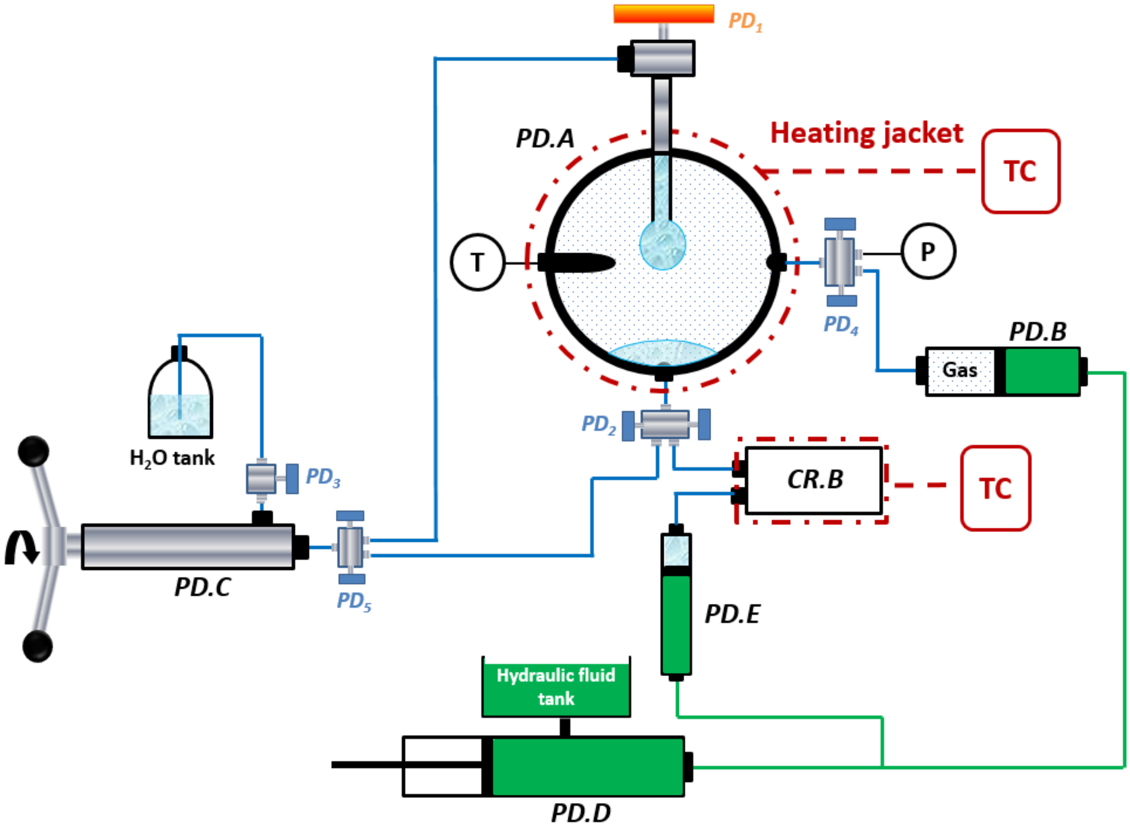

***Figure 2.10**. Schematic illustration of the PD setup with in-situ density measurements of the saturated liquid phase. Annotations are the same as in **Figures 2.4** and **2.7**. In the scheme the new parts are annotated as: 16 cm^3 movable piston (**PD.E**) and valves **PD$_4$** and **PD$_5$**.*

2.4 Summary

Two experimental setups and their theoretical background for measuring the *IFT* of fluid−liquid interfaces have been described. The experimental setups are based on the differential capillary rise (CR) and pendant drop (PD) techniques. The first is suitable for measuring this property in systems at/or near critical conditions where low values are expected (*IFT* < 1.5 $mN.m^{-1}$). Hence, the CR setup is used in **CHAPTER 4** to measure the *IFT* of synthetic hydrocarbon reservoir fluids. The *IFT* between aqueous and CO_2-rich phases is measured with the PD setup and the results presented in **CHAPTER 5**. Aiming at reporting more *realistic IFT* values, a vibrating U-tube densitometer is also used to measure saturated density data of the investigated systems.

CHAPTER 3 – THERMODYNAMIC MODELLING OF INTERFACIAL TENSION

3.1 Introduction

The high costs of experimental facilities and the time needed to perform these measurements necessitate the deployment of theoretical tools, which when validated with experimental data over a broad range of conditions can be used to correlate or even predict interfacial tensions.

Numerous approaches have been proposed and many empirical or semi-empirical methods are being used as standard models in commercial simulators for the Oil and Gas industry. The most popular approaches include the Parachor method [42,43], scaling law [171], the corresponding-states theory [172–174], thermodynamic [175,176] and empirical correlations [116,177,178]. Among these, the Parachor method [41,42] and the scaling law [171] gained the most attention due to their simplicity and accuracy for describing the *IFT* of vapour−liquid interfaces in hydrocarbon systems. Even though a Parachor value has been reported for water, this method is not recommended for the prediction of *IFT* of aqueous interfaces [179,180]. Instead, a more accurate and reliable model for estimating the interfacial tension of hydrocarbon + water systems was proposed by Firoozabadi and Ramey [180]. In their work, the authors successfully correlated the *IFT* between water and hydrocarbons against the density of the contacted phases over a broad range of conditions. Later, Argaud [116] and Sutton [177,178] developed new versions of the original correlation from Firoozabadi and Ramey [180] by readjusting the model to a broader class of compounds and larger database. Although good results were obtained with these approaches, they are limited on their transferability and predictive capabilities.

Other more robust methods, based on statistical thermodynamics, take into account the molecular distribution of species across the interface. Some of these methods include the perturbation theory [181], integral and density functional theories [181–184], the Linear Gradient Theory (LGT) [185,186] and the Square Gradient Theory (SGT) or Density Gradient Theory (DGT) [187,188]. In particular, the latter has been thoroughly applied in the prediction of *IFT* values of a wide class of systems and interfaces. Such systems include pure substances and mixtures containing hydrocarbons [54,61,69,189–200], alcohols [189,201–204], esters [205,206], glycols [207], polymers [208–210], near critical systems [211–214], real petroleum mixtures [196,215] and most recently, aqueous systems containing common gases such as CO_2, CH_4 and N_2 [168,216–223]. It is worth mentioning that several authors have also successfully described this property using Molecular Dynamic (MD) and Monte Carlo (MC) computer simulation approaches [48,117,197,218,223–233].

The accurate estimation of *IFT* values with the methods described above relies on a correct description of both composition and density of the bulk phases by a thermodynamic phase behaviour model. In general, classical cubic equations of state (EoSs) such as the Soave-Redlich-Kwong 1972 (SRK72) EoS [234] and the Peng-Robinson 1978 (PR78) EoS [235] are used for simple systems containing just gases and hydrocarbons. On the other hand, theoretically sound EoSs are preferred for systems containing polar and/or associating compounds such as water, alcohols and glycols, with strong hydrogen bonding interactions. The most popular are the Statistical Associating Fluid Theory (SAFT) [236–238] EoS, and its variants, and the Cubic-Plus-Association (CPA) [239,240] EoS.

In this chapter a brief description of the theoretical approaches used to describe the phase behaviour and *IFT* of reservoir fluids is presented. Aiming at searching for one accurate and general model for predicting the *IFT* of multiphase systems containing both associating and non-associating molecules, the predictive capabilities of the DGT [187,188] are further assessed in this work by comparison with experimental *IFT* data as well as with other theoretical approaches such as the Parachor [42,43], Sutton's correlation [178] and the LGT [185,186].

3.2 Parachor Method

The Parachor model [42,43] and its derivatives are indeed the most successful and widely used approaches in the petroleum industry due to their simplicity and good description of the *IFT* of both simple and complex reservoir mixtures at HPHT conditions. In the Parachor approach, the interfacial tension can be correlated to the bulk density difference of the phases in equilibrium by the equation proposed by Macleod [42] and Sugden [43] for pure substances:

$$IFT^{1/E} = P_{ch}(\rho^L - \rho^V) \qquad \textbf{3.1}$$

where P_{ch} is the Parachor value, ρ^L and ρ^V are the liquid and vapour molar density of the coexisting saturated phases and E is the scaling exponent. The scaling exponent characterises the dependence of *IFT* with the density difference as the latter quantity vanishes near the critical point.

Using the simple molar averaging technique, Weinaug and Katz [41] extended this approach to mixtures:

$$IFT^{1/\mathrm{E}} = \sum_{i=1}^{N_{comp}} P_{ch,i}(\mathrm{x}_i\,\rho^L - y_i\rho^V) \qquad \textbf{3.2}$$

where x_i and y_i are the equilibrium mole fractions of component i in the liquid and vapour phases, respectively, and $P_{ch,i}$ is the Parachor of component i.

A considerable volume of research and review works show in detail modifications for the scaling exponent, with values ranging from 3.45 to 4, and correlations for expressing the Parachor values as function of properties such as molecular weight and specific gravity or critical properties. Reviewed modifications can be found in the work of Ali [241] as well as of Daniel *et al.* [242]. In this work, E is set equal to 4 and the Parachor values of well-defined substances, in units of $(\mathrm{mN.m^{-1}})^{1/4}.(\mathrm{g.cm^{-3}})^{-1}$, are calculated with the correlation regressed by Fanchi [243]:

$$P_{ch,i} = a_0 + a_1V_{c,i} + a_2T_{c,i} + a_3H_i + a_4H_i^{\,2} + a_5H_i^{\,3} + a_6 / H_i \qquad \textbf{3.3}$$

$$H_i = V_{c,i}^{\ 5/6}T_{c,i}^{\ 1/4} \qquad \textbf{3.4}$$

where $T_{c,i}$ and $V_{c,i}$ are the critical temperature (K) and the critical volume ($\mathrm{L.mol^{-1}}$) of component i, respectively. Regressed coefficients a_0 to a_6 are listed in **Table 3.1**. This correlation can be used to calculate the Parachor of *n*-alkanes up to C_{20} as well as of common gases such as CO_2, N_2 and CH_4. In the case of real petroleum fluids, several researches [27,243–245] have recognized that the Parachor of the heaviest fraction (or residue of distillation) exhibits a discontinuity from the other distillation cuts apparently due to the presence of heavy surface active compounds of asphaltic nature. As an attempt to circumvent this problem, and as a way of estimating the Parachor of cuts, Fanchi [243] also suggested linear correlations based on Parachor measurements of high molecular weight (MW) mixtures and of pure compounds including paraffins, CO_2 and N_2. These correlations are defined as follows [243]:

$$P_{ch,i} = 10.0 + 2.92MW_i \text{, recommended for } MW_i < 142 \text{ g.mol}^{-1} \qquad \textbf{3.5}$$

$$P_{ch,i} = 69.9 + 2.30MW_i \text{, recommended for } MW_i > 142 \text{ g.mol}^{-1} \qquad \textbf{3.6}$$

Table 3.1. *Coefficients in* ***Equation 3.3*** [243].

Coefficients	
a_0	176.05005
a_1	-7472.9807
a_2	-0.87458088
a_3	1560.4793
a_4	19.309439
a_5	0.05013801
a_6	-25.691718

3.3 Sutton's Correlation

Sutton [177,178] proposed an improved version of the model originally developed by Firoozabadi and Ramey [180] for estimating the interfacial tension of water + hydrocarbon systems. In their original work, Firoozabadi and Ramey found that a single curve can be used to correlate *IFT* data for methane, propane, *n*-butane, *n*-pentane, *n*-hexane, *n*-octane, *n*-dodecane and benzene against water over a broad range of pressures and temperatures. The correlation was only presented in graphical form, with the curve following a function of the expression given by [180]:

$$f(IFT) = \frac{IFT^{0.25}}{\rho_w - \rho_h} T_r^{\,0.3125} \qquad \textbf{3.7}$$

Danesh [179] and Sutton [177] developed later equations that can reproduce Firoozabadi and Ramey's curve. These equations have the following form:

$$IFT^{Danesh} = 111(\rho_w - \rho_h)^{1.024} T_r^{\,-1.25} \qquad \textbf{3.8}$$

$$IFT^{Sutton} = \left[\frac{1.58(\rho_w - \rho_h) + 1.76}{T_r^{0.3125}} \right]^4 \qquad \textbf{\textit{3.9}}$$

In 2009, Sutton [178] improved the accuracy of his earlier version of the correlation by replacing the exponent 0.3125 with a quadratic function of temperature and readjusting the remaining constants in **Equation 3.9** to a larger database. Data sources comprised *IFT* data used in the original work of Firoozabadi and Ramey [180] as well as more recently published *IFT* data between water and various pure hydrocarbon compounds, including methane through *n*-hexadecane, toluene and benzene. In order to accurately describe the effect of temperature, Sutton [178] also included in the analysis pure water *IFT* data at saturation conditions (*i.e*, surface tension). Supplement *IFT* data of multicomponent gas mixtures against water were also used to test the model. The improved correlation has the following form [178]:

$$IFT = \left[\frac{1.53988(\rho_w - \rho_h) + 2.08339}{T_r^{(0.821976 - 1.83785\times10^{-3}T + 1.34016\times10^{-6}T^2)}} \right]^{3.6667} \qquad \textbf{\textit{3.10}}$$

where ρ_w and ρ_h are the density of the water and hydrocarbon phases in g.cm^{-3}, respectively, T is the temperature of the system in units of R° and T_r is the reduced temperature of the hydrocarbon phase, defined as $T_r = T_c/T$. The critical temperature T_c takes the value of 302.881 for gas–water interfacial tension calculations.

In his approach, Sutton [178] considered the density of the hydrocarbon and water phases to be approximately equal to that of pure compounds determined from multi-parameter models. Therefore, the accuracy of this correlation in predicting *IFT* values can be rather affected by changes from pure density values due to the mutual dissolution of water and hydrocarbons molecules, in particular the increase of water molecules in the oleic phase at high temperatures. Nevertheless, the new model represented in **Equation 3.10** allowed a description of the *IFT* of gas + water and liquid hydrocarbon + water binary mixtures over a wide range of pressure and temperature conditions, with calculated deviations significantly lower than those obtained with **Equations 3.8** and **3.9**. Also, the good results obtained for the interfacial tension between water and gas mixtures including up to 40 mole% CO_2 or up to 49 mole% N_2, showed the potential of the improved model for describing more realistic systems.

3.4 Density Gradient Theory

The Density Gradient Theory (DGT) of fluid interfaces is a more rigorous theoretical approach which has gradually shown to be a good tool for predicting interfacial properties. This theory has its origins in the work of van der Waals [246], but only after the reformulation of Cahn and Hilliard [187] it was found useful in modelling interfacial properties. Accordingly, the DGT approach considers the free energy density of homogeneous fluid (bulk phase) and the influence parameter of inhomogeneous fluid (interface) to determine the density gradient of components across the interface by minimization of the Helmholtz free energy and to compute interfacial tension values. In general, EoSs are used to estimate the equilibrium properties of the bulk phases and to evaluate the energy across the interface. The influence parameters, although they can be derived from theoretical expressions [199,212,247], are usually fitted against surface tension data of pure substances. Since the DGT has already been presented in great detail by several authors in literature, the reader is referred to the studies of Miqueu *et al.* [191,192,194], Davis' book [248], Carey's [249] and Cornelisse's thesis [250] for a comprehensive description of the model; a brief description is now presented.

3.4.1 Theory outline

The basis of the DGT lies on the gradient theory formulated in 1894 by van der Waals [246]. Accordingly, the Helmholtz free energy F of an inhomogeneous system (*e.g.* a flat interface between two phases in equilibrium) in the absence of any external potential (gravitational, electrical, etc.) is given by:

$$F = \int_V f\left[\rho(z)\right] dV \tag{3.11}$$

where $f\,[\rho(z)]$ is the Helmholtz free energy density ($f = F/V$), z denotes the direction normal to the interface and ρ the density of the fluid at the position z.

According to the formalism introduced in 1958 by Cahn and Hilliard [187], the property (*e.g.* density) of an inhomogeneous system can be defined as dependent on both the value of this property at a local position (interface) and the characteristics of this property in the immediate environment (bulk). Under this assumption, the Helmholtz free energy of the inhomogeneous phase can be described by a continuous function of z, from which the density distribution of each component $\rho_i(z)$ can be determined and the *IFT* computed.

In the case of a fluid−liquid system separated by a flat interface, the Helmholtz free energy density of the inhomogeneous phase f can be expanded in a Taylor series around the Helmholtz free energy density of the fluid in a hypothetical homogeneous state f^0 and truncated after the second-order term. This expansion is expressed as follows [187]:

$$f\left[\rho(z)\right] = f^0\left[\rho(z)\right] + \sum_i \sum_j \frac{1}{2} c_{ij} \frac{d\rho_i}{dz} \frac{d\rho_j}{dz} \quad \text{for } i,j = 1\ldots N_{comp} \qquad \textbf{3.12}$$

where $(d\rho_i/dz)$ is the local density gradient of component i in a system of N_{comp} constituents and c_{ij} are the so-called cross influence parameters of the inhomogeneous phase. These parameters relate the response of the density gradients to the local deviations of the chemical potentials from their bulk values and, in turn, the energy of the interface [247–249].

Substituting **Equation 3.12** into **Equation 3.11** gives:

$$F = \int_V f^0\left[\rho(z)\right] + \sum_i \sum_j \frac{1}{2} c_{ij} \frac{d\rho_i}{dz} \frac{d\rho_j}{dz} dV \qquad \textbf{3.13}$$

Thereby, it is evident from **Equation 3.13** that in the absence of any external potential, F is a result of the sum of two contributions: the Helmholtz free energy density $f^0[\rho(z)]$ of a homogenous fluid evaluated at the local density $\rho(z)$ and a corrective term consisting on the influence parameter and the density gradients in the inhomogeneous fluid.

For a given thermodynamic condition, the density distribution of molecules across the interfacial region must be constrained to the condition of phase equilibrium, or minimum Helmholtz free energy F. This minimization, which is performed by applying the Euler-Lagrange theory to **Equation 3.13**, yields a set of partial differential equations defined for planar interfaces of the following form [191,192,194]:

$$\sum_j \frac{d}{dz}\left[c_{ij} \frac{d\rho_j}{dz}\right] - \frac{1}{2} \sum_k \sum_j \frac{\partial c_{kj}}{\partial \rho_i} \frac{d\rho_k}{dz} \frac{d\rho_j}{dz} = \frac{\partial \Omega}{\partial \rho_i} \quad \text{for } i,j,k = 1\ldots N_{comp} \qquad \textbf{3.14}$$

where Ω is the grand thermodynamic potential defined as:

$$\Omega \equiv f^0\left[\rho(z)\right] - \textstyle\sum_i \rho_i \mu_i^{Eq.}. \qquad \textbf{3.15}$$

In the case of planar interfaces, the density dependence of the influence parameters in the inhomogeneous phase can be neglected as showed by Carey *et al.* [189] and McCoy and

Davis [251] and hence, $\partial c/\partial \rho = 0$. Furthermore, since $\mu_i^0 \equiv (\partial f^0/\partial \rho_i)_{T,V,\rho_{j \neq i}}$, the partial derivative of Ω with respect to ρ_i is given by the following expression:

$$\frac{\partial \Omega}{\partial \rho_i} = \mu_i^0 \left[\rho_i(\mathrm{z}) \right] - \mu_i^{Eq.} \qquad \textbf{3.16}$$

where μ_i^0 and $\mu_i^{Eq.}$ correspond to the chemical potential of component *i* evaluated at the position *z* and in the bulk phase, respectively.

After substituting **Equation 3.16** into **Equation 3.14**, the equations governing the density distribution of species across the interfacial region are reduced to a set of non-linear differential equations expressed as follows [248]:

$$\sum_j c_{ij} \frac{d^2 \rho_j}{dz^2} = \Delta \mu_i \quad \text{for } i,j = 1 \ldots N_{comp} \qquad \textbf{3.17}$$

with

$$\Delta \mu_i = \mu_i^0 \left[\rho_1(\mathrm{z}), \ldots, \rho_{N_{comp}}(\mathrm{z}) \right] - \mu_i^{Eq.} \qquad \textbf{3.18}$$

The boundary conditions associated with **Equation 3.17** for a planar interface are: $\rho_i\ (z \rightarrow -\infty) = \rho_i^I$ and $\rho_i\ (z \rightarrow +\infty) = \rho_i^{II}$, where ρ_i^I and ρ_i^{II} correspond to the equilibrium densities of the examined phases in contact (*I: vapour/liquid* and *II: liquid*). Correspondingly, the density gradients will vanish in the bulk phases [248].

Multiplying **Equation 3.17** by $d\rho_i/dz$, summing over *i* and integrating yields the following expression [248]:

$$\sum_i \sum_j \frac{1}{2} c_{ij} \frac{d\rho_i}{dz} \frac{d\rho_j}{dz} = \Delta \Omega \left[\rho(z) \right] \qquad \textbf{3.19}$$

$$\Delta \Omega \left[\rho(\mathrm{z}) \right] \equiv \Omega \left[\rho(\mathrm{z}) \right] + P = f^0 \left[\rho(\mathrm{z}) \right] - \sum_i \rho_i \mu_i^{Eq.} + P \qquad \textbf{3.20}$$

where *P* is the equilibrium pressure and $\Delta\Omega$ is the variation of the grand thermodynamic potential.

Equations 3.19 and **3.20** can be used to eliminate $f^0[\rho(z)]$ from **Equation 3.13** and the following expression is obtained:

$$F = \sum_i \rho_i \mu_i^{Eq.} - P + \int_V \left[\sum_i \sum_j c_{ij} \frac{d\rho_i}{dz} \frac{d\rho_j}{dz} \right] dV \qquad \textbf{3.21}$$

Since $V = A \int dz$, **Equation 3.21** becomes**:**

$$F = \sum_i \rho_i \mu_i^{Eq.} - P + A \int_{-\infty}^{+\infty} \left[\sum_i \sum_j c_{ij} \frac{d\rho_i}{dz} \frac{d\rho_j}{dz} \right] dz \qquad \textbf{3.22}$$

where the upper and lower limits of the integral are extended to ± ∞ because the derivatives $d\rho_i/dz$ go to zero outside the inhomogeneous phase [248].

From the definition of interfacial tension given by **Equation 1.2** and according to the framework of the DGT presented in the foregoing equations, the *IFT* of fluid−liquid interfaces can be computed by [184,247]:

$$IFT = \int_{-\infty}^{+\infty} \left[\sum_i \sum_j c_{ij} \frac{d\rho_i}{dz} \frac{d\rho_j}{dz} \right] dz = \int_{-\infty}^{+\infty} 2\Delta\Omega\left[\rho(z)\right] dz \qquad \textbf{3.23}$$

Alternatively, the spatial variable *z* can be eliminated and the *IFT* computed from [194]:

$$IFT = \int_{\rho_{ref}^{I}}^{\rho_{ref}^{II}} \sqrt{2\Delta\Omega(\rho) \sum_i \sum_j c_{ij} \frac{d\rho_i}{d\rho_{ref}} \frac{d\rho_j}{d\rho_{ref}}} \, d\rho_{ref} \qquad \textbf{3.24}$$

In summary, the only inputs required to compute interfacial tension values with **Equations 3.23** and **3.24** are the influence parameters of the various components in the system considered and the density distribution each component across the interfacial region.

3.4.2 Influence parameter

As stated in the preceding section, the influence parameter relates the response of local gradients to the deviations of properties from their bulk values. Even though the influence parameters of pure substances c_i and c_j can be derived from theoretical expressions, its application to practical systems can be rather complicated as it requires the prior calculation of the radial density distribution function of a pure fluid in the homogeneous state [199,212,247]. To overcome this constraint, these parameters are commonly correlated against *ST* data of pure substances by rewriting **Equation 3.24** for one-component systems:

$$c_i = \frac{1}{2}\left[\frac{ST_{\exp}}{\int_{\rho_i^{vap.}}^{\rho_i^{liq.}} \sqrt{\Delta\Omega(\rho_i)}\ \ d\rho_i}\right]^2 \tag{3.25}$$

The cross influence parameters c_{ij} are related to pure component influence parameters c_i and c_j with the mixing rule suggested by Carey *et al.* [252]:

$$c_{ij} = (1-\beta_{ij})\sqrt{c_i c_j} \tag{3.26}$$

where β_{ij} is the adjustable binary interaction coefficient of influence parameters. When β_{ij} is set to zero, **Equation 3.26** is reduced to the simple geometric mixing rule and this makes the calculation of the interfacial tension with **Equations 3.23** and **3.24** fully predictive. Furthermore, thermodynamic stability of the interface requires the matrix encompassing all of the influence parameters $[c_{ij}]$ to be positive definite *i.e.*, the eigenvalues of the matrix $[c_{ij}]$ should be all non-negative [250,253].

As an example, the influence parameter of *n*-decane computed with the PR78 EoS [235] and CPA EoS [239,240] in combination with the DGT is plotted in **Figure 3.1** as $c_i/(a_i b_i^{2/3})$ as a function of reduced temperature T_r, where a_i and b_i are the energy and co-volume parameters of the pertinent EoS, respectively. From this figure it can be seen that $c_i/(a_i b_i^{2/3})$ values increase slowly with increasing temperature and they are similar in magnitude for both EoSs and at T_r up to 0.8. Beyond this point, PR78 $c_i/(a_i b_i^{2/3})$ values diverge while approaching the critical temperature (ST = 0). This in line with the theoretical definition of the influence parameter [247] and the scaling laws near the critical point [250,254,255]. On the other hand, CPA $c_i/(a_i b_i^{2/3})$ values at $T_r > 0.8$ converge to zero. This difference in behaviour near the critical point is related to the description of the critical properties from these EoSs. In the case of the PR78 EoS, or any other classical cubic EoSs, the coefficients a_i and b_i are calculated directly from critical properties (T_c and P_c). As a result, the temperature dependence of the influence parameter near the critical point is maintained. In the case of the CPA EoS, a_i and b_i are fitted to saturation properties and hence, two different critical temperatures arises: one calculated by the CPA, and the other implicit in the experimental ST data used for calculating the influence parameters (which should be zero at T_c), as reported by Queimada *et al.*[195]. Similar behaviour was also observed by Breure and Peters [199] when combining the DGT with the PC-SAFT EoS.

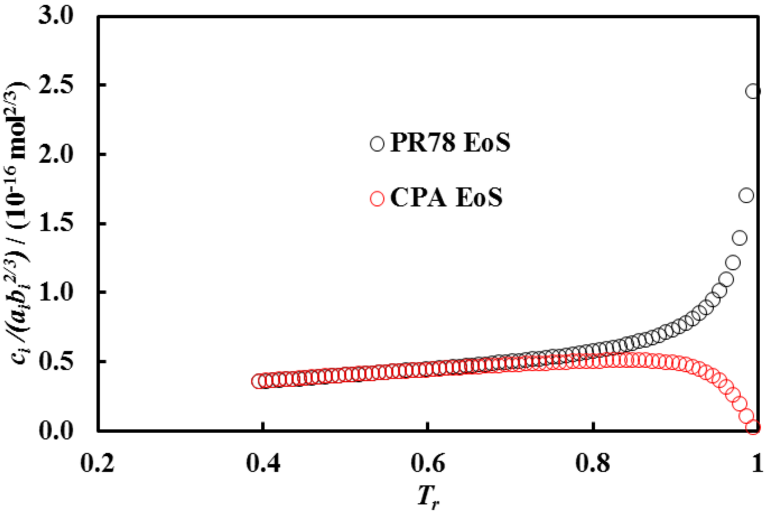

Figure 3.1 *$c_i/(a_ib_i^{2/3})$ values of n-decane computed using two different EoSs.*

For practical purposes, several semi-empirical approaches have been developed and various EoS dependent correlations are reported in literature for the estimation of the influence parameter of pure substances [189–191,195,204,205,250,256]. Most approaches have conserved the temperature dependence of the ratio $c_i/(a_ib_i^{2/3})$ far from the critical point when combining the DGT with several EoSs.

Carey *et al.* [189,249], Cornelisse [250] and Zuo and Stenby [190] were the first to propose a general correlation for the estimation of the influence parameter from pure fluid properties for a wide variety of substances. However, their correlations are based on classical cubic EoSs which are known to poorly represent volumetric properties, in particular liquid phase densities. Consequently, inaccuracies in the prediction of saturated densities were lumped into the values of the influence parameters. In light of these results and to improve density predictions, Miqueu *et al.* [191] and Lin *et al.* [256] derived correlations for the gradient theory influence parameter using the volume-translation concept suggested by Peneloux *et al.* [257] for cubic EoSs. Miqueu *et al.* [191] derived a simple linear correlation for the influence parameter of hydrocarbons, gases and refrigerants as a function of 1-T_r when using a volume-translated version of the PR78 EoS. In turn, Lin *et al.* [256] generalized the influence parameter of a wide number of compounds as function of critical properties, acentric factor and dipole moment based on volume-translated versions of the PR78 EoS and SRK72 EoS. Other authors such as Queimada *et al.* [195] and Oliveira *et al.* [204] combined the DGT with the CPA EoS and developed a quadratic correlation for the influence parameter with reduced temperatures and accurately described the surface tension of water and a series of *n*-alkanes, *n*-perfluoroalkanes and *n*-alkanols for a broad temperature range with global average errors lower than 1 %. This work was also extended to several ester compounds and their mixtures (biodiesels) by the same authors [205,206]. Another approach used by several authors [61,204,216–218] consists of taking the influence parameter as a constant value, usually calculated from surface tension data far from the critical point. Most recently, the findings of Khosharay and co-workers [220,221,258] suggested that an influence parameter dependent on both bulk liquid and vapour densities would produce better results [258], in particular for aqueous systems [220,221].

Due to its simplicity and applicability to reservoir fluids [192,194,196], the expression derived by Miqueu *et al.* [191] is adopted in this work for the estimation of the influence parameter of systems containing non-polar and/or weakly polar substances such as *n*-alkanes and common gases (CO_2, CH_4 and N_2). This expression has the following form [191]:

$$A_i = \frac{-10^{-16}}{1.2326 + 1.3757\omega_i} \tag{3.27}$$

$$B_i = \frac{10^{-16}}{0.9051 + 1.5410\omega_i} \tag{3.28}$$

$$c_i = \left[A_i \left(1 - T_{r,i}\right) + B_i \right] a_i b_i^{2/3} \tag{3.29}$$

$$T_{r,i} = \frac{T_{c,i}}{T} \tag{3.30}$$

where $T_{c,i}$ and ω_i correspond to the critical temperature and acentric factor of component *i*, respectively, and a_i and b_i are the energy and co-volume parameters of the PR78 EoS. This correlation was derived using properties in sub-critical conditions. Thus, the influence parameter of pure fluids at or above supercritical conditions is estimated using the generalized **Equation 3.29** and by setting T_r to a fixed value. In this work, T_r is fixed to the upper limit of temperatures considered by Miqueu *et al.* [191] and hence, the influence parameters of supercritical CO_2, CH_4 and N_2 are estimated for T_r = 0.96, 0.94 and 0.87, respectively. This procedure is adopted from Zuo and Stenby [190].

In contrast, the influence parameters of substances in aqueous systems are estimated using two different approaches. The first consisted on taking the influence parameters to be constant. These parameters are estimated using the empirical correlations regressed by Queimada *et al.* [195] for water and Oliveira *et al.* [204] for *n*-alkanes and calculated for a fixed value of T_r. The influence parameters of CO_2, CH_4 and N_2 are regressed with **Equation 3.25** using surface tension data from REFPROP [99] at one temperature. The influence parameters of some substances of interest estimated with this approach are listed in **Table 3.2** along with the percentage average absolute deviation (%AAD)[2] to *ST* data [99,259].

The second approach consisted on adopting the method suggested by Khosharay and co-workers [220,221,258]. Accordingly, the influence parameters of pure substances calculated from **Equation 3.25** are expressed as function of bulk vapour and liquid molar densities by [220,221,258]:

$$c_i = \left| \frac{\rho^L - \rho^V}{A_i \rho^V + B_i \rho^L} \right| \tag{3.31}$$

where A_i and B_i are the regression coefficients for component *i.*

For multicomponent systems, the influence parameters of component *i* with this approach are calculated from the regressed coefficients (A_i and B_i) and the molar fraction of component *i* in the coexisting bulk phases and are given by:

$$c_i = \left| \frac{\rho^I y_i - \rho^{II} x_i}{A_i \rho^{II} x_i + B_i \rho^I y_i} \right| \tag{3.32}$$

The values of A_i and B_i for substances of interest are obtained by fitting **Equation 3.31** to the influence parameters calculated from **Equation 3.25** using surface tension data. The required *ST* data are taken from REFPROP [99] for water, gases, *n*-hexane and *n*-decane and from the DIPPR database [259] for *n*-hexadecane. Two different sets of coefficients are regressed:

- The first set is fitted against surface tension data over a broad range of reduced temperatures, as done in the works of Khosharay *et al.* [220,221,258];
- For the second set, the influence parameters are considered to be temperature independent and the coefficients fitted against surface tension data at the lowest reduced temperatures. This temperature was selected as opposed to the highest to

---

[2] $\%AAD = 1/NP \times \sum_i^{NP} \left| (X_i^{\mathrm{model}} - X_i^{Exp}) / X_i^{Exp} \right| \times 100$ where *X* is the property under evaluation.

avoid most of the errors that arise from inappropriate prediction of saturated pure densities by the CPA EoS near the critical point [195]; this behaviour is similar to that of classical equation of states, such as cubics and generalised van der Waals' equations, which do not take into account fluctuations of the density of fluids near the vicinity of the critical point [260].

The fitted coefficients A_i and B_i for some substances of interest are given in **Tables 3.3** and **3.4** and, as an example, a comparison between the approaches for water, carbon dioxide and *n*-decane is plotted in **Figure 3.2.**

As can be seen in **Figure 3.2**, all approaches provide a good description of the surface tension of pure components. The lowest deviations were obtained with the method proposed by Khosharay and co-workers and with the coefficients A_i and B_i fitted using surface tension data over a broad range of reduced temperatures, as could be expected, with an overall %*AAD* of 2.0 % (**Table 3.3**). On the other hand, the influence parameters and coefficients A_i and B_i regressed at fixed T_r resulted in an increase of deviations to experimental *ST* data, as listed in **Table 3.2** and **Table 3.4**. This deterioration is partly related to the wide range of temperatures considered, but also to the poor description of the saturation properties by the phase equilibrium model near the critical region [195]. Nonetheless, using a constant influence parameter or as function of bulk densities fitted at low temperatures allowed an estimation of the *ST* of pure fluids with an overall %*AAD* of 5.7 and 4.3 %, respectively.

Table 3.2. *Influence parameter c_i of pure components estimated using correlations or regressed against ST data at fixed T_r with the DGT + CPA EoS approach.*

Pure component	T_r	c_i / (10^{-20} J.m^5.mol^{-2})	**Source**	***AAD%***[a)]
H_2O	0.45	1.80137	Queimada *et al.* [195]	7.0
n-C_6	0.45	41.4546	Oliveira *et al.* [204]	1.6
n-C_{10}	0.45	110.380	Oliveira *et al.* [204]	3.7
n-C_{16}	0.45	279.683	Oliveira *et al.* [204]	11.3
CO_2	0.72	2.84620	This work	5.8
CH_4	0.48	2.09550	This work	5.2
N_2	0.50	1.11750	This work	5.1
			Overall	***5.7***

[a)] *%AAD* to *ST* data [99,259] in the reduced temperature range: $0.45 < T_r < 0.95$ (water), $0.45 < T_r < 0.85$ (*n*-alkanes), $0.71 < T_r < 0.98$ (CO_2), $0.48 < T_r < 0.98$ (CH_4) and $0.50 < T_r < 0.85$ (N_2).

Table 3.3. *Coefficients A_i and B_i (first set) of the bulk density dependent influence parameters regressed against ST data over a wide range of T_r with the DGT + CPA EoS approach.*

Pure component	T_r	A_i / (10^{20}J^{-1}.m^{-5}.mol^2)	B_i / (10^{20}J^{-1}.m^{-5}.mol^2)	***AAD%*** [a)]
H_2O	$0.45 < T_r < 0.95$	2.4479	0.5595	1.8
n-C_6	$0.45 < T_r < 0.85$	0.0095	0.0246	0.4
n-C_{10}	$0.45 < T_r < 0.85$	0.0375	0.0095	0.8
n-C_{16}	$0.45 < T_r < 0.85$	0.1190	0.0040	3.2
CO_2	$0.71 < T_r < 0.98$	0.3208	0.3315	2.7
CH_4	$0.48 < T_r < 0.98$	0.4602	0.5192	2.0
N_2	$0.50 < T_r < 0.98$	-1.2642	0.8436	2.8
			Overall	**2.0**

[a)] Same as in **Table 3.2**.

Table 3.4. *Coefficients A_i and B_i (second set) of the bulk density dependent influence parameters regressed against ST data at fixed T_r with the DGT + CPA EoS approach.*

Pure component	T_r	A_i / (10^{20}J^{-1}.m^{-5}.mol^2)	B_i / (10^{20}J^{-1}.m^{-5}.mol^2)	***AAD%*** [a)]
H_2O	0.45	2.3060	0.5707	2.3
n-C_6	0.15	0.0095	0.0242	0.7
n-C_{10}	0.45	0.0375	0.0091	1.7
n-C_{16}	0.45	0.1190	0.0034	6.4
CO_2	0.71	1.4589	0.3305	10.7
CH_4	0.48	0.4610	0.4767	4.2
N_2	0.50	-1.2678	0.8951	3.9
			Overall	**4.3**

[a)] Same as in **Table 3.2**.

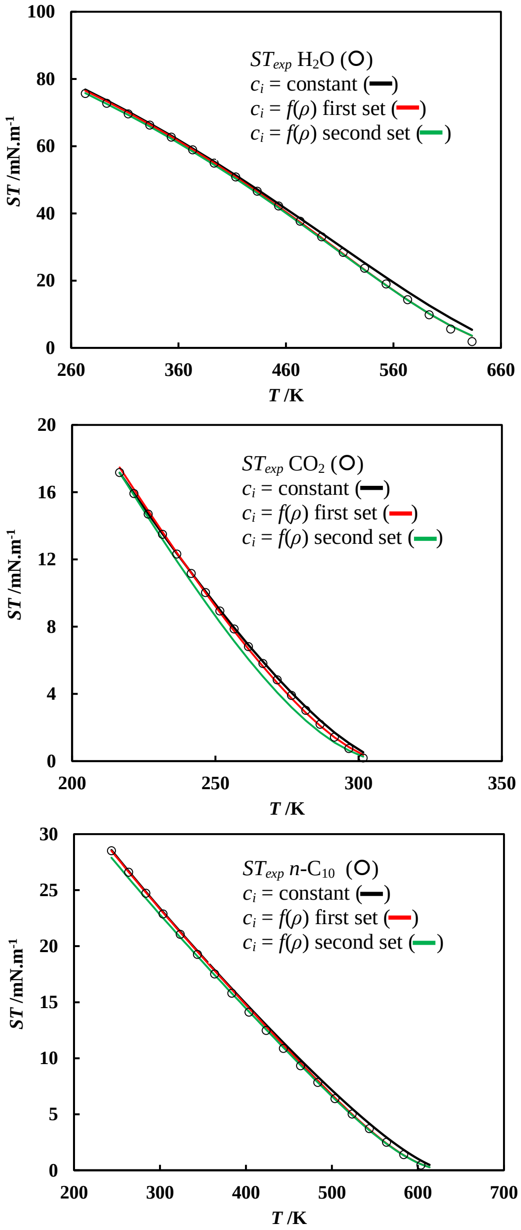

***Figure 3.2**. ST-temperature diagrams of water, carbon dioxide and n-decane. Symbols represent experimental surface tension data from REFPROP [99] and lines represent the DGT + CPA EoS estimations with the different approaches described in the text for the influence parameters.*

3.4.3 Molecular distribution across a planar interface

As shown in **Section 3.4.1**, the minimization of the Helmholtz free energy leads to second order differential **Equations 3.17** from which the distribution of each component through a planar interface can be computed. The different methods for solving numerically these equations are described in great detail in Cornelisse's thesis [250]. **Figure 3.3** sketches possible molecular distributions for the interfacial region between two fluid phases (*I* and *II*) in equilibrium. As can be seen in this figure, the distribution of molecules in the inhomogeneous phase can exhibit a monotonic behaviour and the density profile has a hyperbolic tangent (*tanh*) shape (**Figure 3.3*a***). This profile is typically found in vapour–liquid interfaces of pure fluids, with $\rho(z)$ lying between the density of the bulk homogeneous phases. On the other hand, in the case of mixtures the interaction between molecules of different species (*i* and *j*) can cause the appearance of stationary points ($d\rho/dz = 0$) in the density profiles, as depicted in **Figure 3.3*b*** and ***c***. Accordingly, these points are related to the adsorption (point α: $d^2\rho/dz^2 < 0$) or desorption (point β: $d^2\rho/dz^2 > 0$) of molecules in the interfacial region. In other words, the interfacial activity is governed by the fact that the Helmholtz free energy F is lowered by accumulation or reduction of molecules of one or more species in the interface.

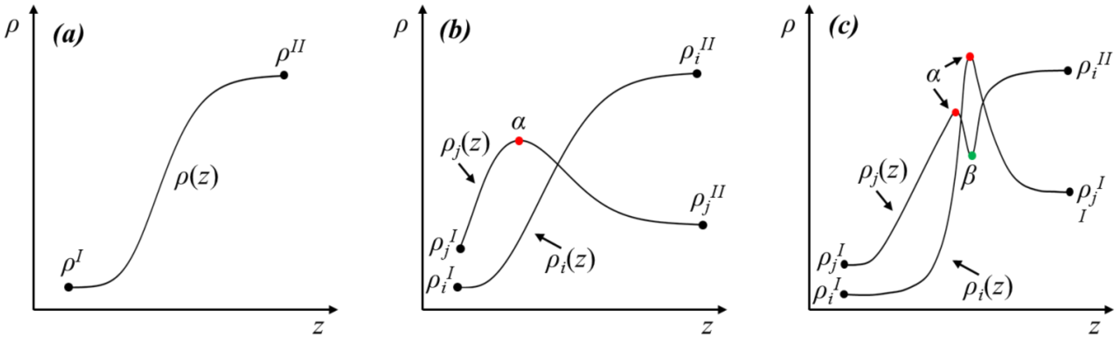

Figure 3.3. *Schematic illustration of possible density profiles (full lines) across the interface between two fluid phases in equilibrium, I and II. Symbols represent the density in the homogeneous phases (●), adsorption (🔴) and desorption (🟢) points. Adapted from Mejía* [261].

In this work, the density profiles are obtained by constraining the set of **Equations 3.17** to a finite domain [0, *L*] and approximating the density boundary conditions to those of the bulk, known as Dirichlet boundary conditions. These conditions are expressed as:

$$\rho_i = \rho_i^{I} \quad \text{at } z = 0 \tag{3.33}$$

$$\rho_i = \rho_i^{II} \quad \text{at } z = L \tag{3.34}$$

in which the superscripts *I* and *II* correspond to the equilibrated phases in contact and *L* is the length of the interface. In this manner, the density profiles can be calculated for a fixed value of *L* and by employing a finite differences scheme for the derivatives of density in space. Accordingly, the interface [0, L] is divided in *N* equidistant grid points and the derivative $d^2\rho_i/dz^2$ is approximated for each z^{th} in the space $0 < z < L$ by:

$$\frac{d^2\rho_i}{dz^2}\left(z^{th}\right)=\frac{1}{\Delta z^2}\left(\rho_i^{z^{th}+1}-2\rho_i^{z^{th}}+\rho_i^{z^{th}-1}\right) \qquad \textbf{3.35}$$

The resultant set of non-linear equations is solved by a Newton-Raphson iteration scheme together with the boundary conditions given in **Equations 3.33** and **3.34**. Since the interface thickness is not known a priori, L is first estimated and subsequently enlarged until the variation of the *IFT* values computed with **Equation 3.23** is lower than 0.1 %. This procedure ensures that only one solution exists. Usually initial values of $L = 0.5$ nm sufficed for the method to converge at each enlargement of the interface. The convergence criterion used for the density profiles at each intermediate value of L is $|\rho_i(z^{th})/d\rho_i(z^{th})| < 10^{-4}$. As suggested by Cornelisse [250], a linear distribution of each component across the interfacial region is used as first guess of the density profiles for the first estimate of L. The number of equations to solve at each enlargement of L is equal to $(N-2)\times N_{comp}$ and hence, N must be selected carefully to avoid not only numerical problems, but also impracticable computation times. In this work, $N = 500$ proven to be sufficient for the type of systems investigated.

The procedure described above allows the computation of the density profiles in a mixture without any prior assumption on the distribution of the components across the interface and is the method of choice if computation time is not a problem. However, taking c_{ij} to be equal to the geometric mean ($\beta_{ij} = 0$) greatly simplifies **Equations 3.17** and the problem to be solved is reduced to a system of algebraic equations defined as [192,194,248,250]:

$$\sqrt{c_i}\left[\mu_{ref}^0(\rho_1,\ldots,\rho_{N_{comp}})-\mu_{ref}^{Eq.}\right]=\sqrt{c_{ref}}\left[\mu_i^0(\rho_1,\ldots,\rho_{N_{comp}})-\mu_i^{Eq.}\right] \qquad \textbf{3.36}$$

where $i = 1\ldots N_{comp}-1$ and the subscript *ref* denotes the reference component of the mixture ($i \neq ref$).

It is clear from the previous simplification that the density profile of each component can be computed as roots of the algebraic **Equations 3.36**, *i.e.*, the density of one component (dependent variable, *i*) can be described as function of the density of the other one, in which the latter is used as an independent (reference, *ref*) variable in a Newton-Raphson root finding scheme. The selection of the reference component density needs to be done with care, as it needs to be a monotonic function of z over the entire interfacial region [192,248,250,262,263]. Since it is not known beforehand whether or not the density of a component has a monotonic behaviour, and in order to avoid problems in finding the roots of **Equations 3.36**, several authors [248,249,263] suggested that the selection of the independent variable can be alternated at each calculation step and the root finding calculation continued over the domain in which the density of the reference component is monotonically changing with *z*. As an example, for a binary mixture this means that if one chooses ρ_1 as reference, a turning point would be foreseen by the approach of the value of $d\rho_1/d\rho_2$ to zero for each increment of ρ_1 and at this point one would merely change the reference variable to ρ_2. More recently, Miqueu *et al.* [192,194,196] concluded that for non-associating compounds and in vapour−liquid interfaces, the criteria for the selection of the reference variable can be done on the basis that the component with the lowest surface tensions would have a tendency to accumulate in the interfacial region, while the density of the less volatile component would pass monotonically from the vapour to the liquid phase and hence, this component can be selected as the reference variable. Consequently, the density profiles calculated with this assumption are equivalent to those obtained by solving directly the differential **Equations 3.17** but with a much lower computational effort. The method has been validated in binary and multicomponent hydrocarbon mixtures containing methane, nitrogen and carbon dioxide [192,194,196,204] and therefore, this method is also adopted in this work for similar systems. A detailed description of the procedure used for casting the roots of the algebraic **Equations 3.36** can be found elsewhere [192,194,248,250].

The coordinates in density space can be transformed to location space and the density profiles represented in the *z* domain by [194]:

$$z = z_0 + \int_{\rho_{ref}(z_0)}^{\rho_{ref}(z)} \sqrt{\frac{\sum_i \sum_j c_{ij} \left(\frac{d\rho_i}{d\rho_{ref}}\right)\left(\frac{d\rho_j}{d\rho_{ref}}\right)}{2\Delta\Omega(\rho_1,\ldots,\rho_{N_{comp}})}}\, d\rho_{ref} \qquad \textbf{3.37}$$

In addition to computing *IFT* values, the distribution of species across the interface can also be used to compute the local adsorption of molecules in the interface. Accordingly, the adsorption of species *i* with respect to species *j* (Γ_{ij}) can be calculated as defined by Gibbs from the following expression [254]:

$$\Gamma_{12} = -\alpha_1 \int_{-\infty}^{+\infty} \Delta C(z) dz \qquad \textbf{3.38}$$

where $\Delta C(z)$ is the symmetrical interface segregation at symmetrical concentrations α_i defined for a binary mixture as [264,265]:

$$\Delta C(\mathrm{z}) = \frac{\rho_2(\mathrm{z}) - \rho_2^{II}}{\alpha_2} - \frac{\rho_1(\mathrm{z}) - \rho_1^{II}}{\alpha_1} \qquad \textbf{3.39}$$

$$\alpha_i = \frac{\rho_i^{II} - \rho_i^{I}}{(\rho_1^{II} + \rho_2^{II}) - (\rho_1^{I} + \rho_2^{I})} \qquad \textbf{3.40}$$

Complementarily, the adsorption isotherms can also be computed directly from experimental *IFT* data and bulk phase density by [254]:

$$\Gamma_{12} = -\frac{\rho_1^{I}\rho_2^{II} - \rho_1^{II}\rho_2^{I}}{(\rho_2^{II} - \rho_2^{I})}\left(\frac{\partial IFT}{\partial P}\right)_T \qquad \textbf{3.41}$$

where the values Γ_{12} can be directly compared with those predicted with **Equation 3.38** and the density profiles computed with the DGT. In **Equations 3.38** and **3.41**, Γ_{12} corresponds to the adsorption (mol.m^{-2}) of component 1 relative to component 2, and thus, the adsorption of component 2 is zero for a particular plane chosen as $\Gamma_2 = 0$.

3.5 Linear Gradient Theory

To overcome the need for solving computationally demanding density profile equations and to speed up *IFT* calculations, Zuo and Stenby [185,186] developed the Linear Gradient Theory (LGT). In the LGT framework, the density of each component across the interface is assumed to be linearly distributed and thus, the density distribution of each species can be readily calculated by:

$$D_i = \frac{d\rho_i(z)}{dz} \qquad \textbf{3.42}$$

$$D_i = \frac{(\rho_i^{I} - \rho_i^{II})}{L} \qquad \textbf{3.43}$$

where D_i is a constant for each component *i* calculated from the density of the coexisting phases (ρ^I and ρ^{II}) separated by an interface of thickness L. With this assumption, the numerical effort inherent to the resolution of a set of equations for finding the density distribution of each component across the interface is eliminated.

Based on the linear distribution of densities across the interface, Zuo and Stenby [185] directly derived the influence parameter of the mixture c from the original DGT:

$$c = \sum_{i}^{N_{comp}} \sum_{j}^{N_{comp}} c_{ij} \frac{\Delta\rho_i}{\Delta\rho_{ref}} \frac{\Delta\rho_j}{\Delta\rho_{ref}} \qquad \textbf{\textit{3.44}}$$

where $\Delta\rho_i$ is the density difference of component i between the coexisting phases and c_{ij} is the cross influence parameter calculated with **Equation 3.26**. However, in a later work [186], the authors opined that the mixing rule in **Equation 3.44** is not suitable for systems at high pressures and hence, suggested the following expression based on the classical van der Waals mixing rule for the energy parameter in cubic EoS:

$$c = \sum_{i}^{N_{comp}} \sum_{j}^{N_{comp}} c_{ij} x_i x_j \qquad \textbf{\textit{3.45}}$$

where x_i and x_j correspond to the molar fraction of components i and j in the bulk liquid phase.

According to the LGT, the *IFT* can be computed as in the DGT by:

$$IFT = \int_{\rho_{ref}^{I}}^{\rho_{ref}^{II}} \sqrt{2c\Delta\Omega(\rho_1, ..., \rho_{Ncomp})}\, d\rho_{ref} \qquad \textbf{\textit{3.46}}$$

The LGT has been applied in the modelling of the *IFT* of both weak and strong associating fluids and complex mixtures [106,185,186,190,258,266–268]. However, the correct description of the *IFT* of several systems required the use of temperature dependent binary interaction coefficients β_{ij} adjusted against experimental mixture data. This is particularly evident in systems such as CO_2 + hydrocarbon [186] and gas + water [106,267–269] where the adsorption of molecules in the interface plays a key role on the *IFT* and thus, the linear distribution of the density profiles together with the mixing rules for the influence parameter given by **Equations 3.44** and **3.45** are unable to accurately describe the energy of the interface. A complementary investigation of these results is also carried out in the present work.

3.6 Phase Behaviour Model

The procedure for modelling interfacial tensions with the models described in the previous section first requires the calculation of the equilibrium properties of the two phases separated by the interface being considered at a given temperature and pressure. These calculations are carried out by applying the criterion of equality of the chemical potentials of each component in the coexisting equilibrium phases [270] in combination with an EoS. Furthermore, the selected EoS is also used to evaluate the energy in the interface within the DGT and LGT framework from fundamental thermodynamic relationships [204,267].

For mixtures containing only hydrocarbons and common gases such as CO_2, CH_4 and N_2, the phase equilibria is predicted with the PPR78 model (Predictive 1978, Peng-Robinson EoS) developed by Jaubert and co-workers [271–275]. The PPR78 EoS relies on the original PR78 EoS [235] as described in **APPENDIX A** and therefore, the simplicity and robustness of the model remains unchanged. However, unlike the classical PR78 EoS [235], where binary interaction coefficients k_{ij} are usually adjusted against vapour−liquid equilibrium (VLE) data for an accurate description of bulk phase compositions, in the PPR78 model these parameters are predicted for each temperature using a group contribution concept. A total of 27 different elementary groups have been established for the time being. The interaction parameters between these groups were adjusted and validated by the authors against an extensive database of VLE measurements [276 and references therein]. In summary, the PPR78 model can be used for estimating the k_{ij} of mixtures involving hydrocarbons, water, mercaptans and common gases (CO_2, N_2, H_2S and H_2) and accurately predicting the VLE over a wide range of experimental conditions. More recently, Jaubert and co-workers [277] extended their method for real petroleum mixtures by proposing an approach to calculate k_{ij} between a *pseudo*-component (PC) and a well-defined component or another PC. PCs are commonly used in the description of real petroleum fluids with the aim of reducing the number of components to be evaluated in engineering calculations. Such procedure involves a characterization scheme in which components of similar nature are lumped together. In the approach of Jaubert and co-workers [277], it is assumed that each PC of a given characterization scheme is made of only three elementary groups (*paraffins* or PAR, *naphthenes* or NAP and *aromatics* or ARO) and k_{ij}s can be calculated based on the occurrence of these functional groups (N_{PAR}, N_{NAP} and N_{ARO}). The occurrence of each functional group is estimated using a group contribution method developed from the critical properties and acentric factors of 174 hydrocarbon substances. Even though no comparison with experimental data was performed, the authors showed that predictions of the phase behaviour of real petroleum fluids with the proposed simplified approach were extremely close to that in which a detailed structure of each PC was considered [277]; in the present work, their method is further assessed by comparison against phase equilibrium data of a real petroleum mixture.

In order to obtain the best prediction possible for the density of the saturated phases with the PPR78 EoS, the volume-translation method is also used. Originally proposed by Martin [278] and later developed by Peneloux *et al.* [257], the volume-translation concept aimed at improving the density predictions of classical cubic EoSs, in particular the density of the saturated liquid phase. The method involves the introduction of a translation factor (volume correction: $v_{c,i}$) for each component within a mixture without any impact on the calculation of the equilibrium phase compositions. Presently, several volume correction methods have been presented for cubic EoSs, with approaches including the use of a constant correction term or temperature and density dependent correlations. For further discussion of these methods one is referred to the works of Abudour *et al.* [279,280]. Considering all approaches, in this work the expression derived by Miqueu *et al.* [191] for the PR78 EoS, and valid for the PPR78 EoS, is used for calculating the volume corrections of all hydrocarbon systems investigated in this work. This correction was chosen because of its simplicity and applicability to a wide range of substances, including the ones in this work. Accordingly, volume corrections are estimated with the following formula [191]:

$$v_{c,i} = \left| \frac{T}{T_{c,i}} - 0.628 \right|^{2.28} - 0.155 + 0.421\omega_i + 0.59e^{28.4\left(\frac{T}{T_{c,i}} - 1\right)} \qquad \mathbf{3.47}$$

On the other hand, for water containing systems, theoretical-based equations of state that explicitly take into account the self- and cross-association interactions between the molecules are the most adequate choice. One of the best known and most successful equations of this kind is the SAFT EoS [236–238] and all its variants. Other association equation of state is the CPA EoS [239,240]. With a much simpler theoretical basis, the CPA EoS combines a physical contribution term accounting for physical forces and an association contribution term accounting for bonding and other chemical forces. The physical contribution term is taken via a classical cubic EoS whereas association effects are accounted from Wertheim’s first-order perturbation theory, as used in SAFT EoS [239,240]. Even though physical interactions can be accounted for with any cubic equation of state, the SRK72 EoS [234] is most commonly used and hence, it is also adopted in this work, as described briefly in **APPENDIX B**. According to the CPA EoS framework, non-associating molecules are defined by three molecular parameters (a_0, c_1 and b) and for associating molecules, two more parameters are included to model the associating interactions (ε: association energy and β_{CPA}: association volume). CPA parameters are typically regressed simultaneously against experimental vapour pressure and saturated liquid density data of pure compounds and thus, a good representation of the volumetric properties of mixtures is usually obtained.

The CPA EoS has been shown to be able to properly describe the phase equilibria of water with alkanes, cycloalkanes and alkenes [281,282], aromatics [282,283], alcohols [284], glycols [285,286], fluoralkanes [287] and common gases such as CO_2 [288], CH_4 [289] and N_2 [290].

With relevance for this work, Tsivintzelis *et al.* [288] and Oliveira *et al.* [291,292] investigated the CPA EoS description of the phase equilibria of CO_2 binary mixtures with water, alcohols, glycols, hydrocarbons, alcohols, esters and acids, over a broad range of temperatures and pressures. Although CO_2 can be regarded as a non-associating compound, the findings of Tsivintzelis *et al.* [288] revealed the importance of taking into consideration the specific strong interactions between CO_2 and water, mainly Lewis electron donor-acceptor type. Accordingly, the best description is obtained when the interactions are accounted for through the procedure proposed by Folas *et al.* [283], where the solvation is taken into account via the modified combining rule CR-1 (**APPENDIX B**), where the cross-association energy is taken as half of the water self-associating association energy and the cross-association volume is regressed from equilibria experimental data along with the binary interaction coefficient, k_{ij}. In this work, the solvation is taken by considering one cross-associating site in the CO_2 molecules and using the binary coefficients regressed against solubility data over the temperature range 298 to 477 K reported in the work of Tsivintzelis *et al.* [288]. Water is modelled as a self-associating fluid with a 4C association scheme (according to the terminology introduced by Huang and Radosz [238]), in which the hydrogen bonding between the hydrogen atoms and the lone pairs of the oxygen are considered. No other type of cross-association or self-associating molecules are considered throughout this work.

The CPA parameters of all substances studied in this work with the CPA EoS are taken from literature [204,288,293–295] and are given in **Table 3.5**, along with *%AAD* to saturation properties [99,259] over a broad range of reduced temperatures.

***Table 3.5**. CPA parameters and modelling results of pure compounds.*

	a_0 / (J.m^3.mol^{-2})	c_1	b / (10^{-5} m^3.mol^{-1})	ε / (J.mol^{-1})	β_{CPA}	**Source**	*%AAD*$^{a)}$		
							P^{Sat}	ρ^{Liq}	ρ^{Vap}
H_2O	0.12277	0.6736	1.45	16655	0.0692	[293]	0.7	1.1	2.4
n-C_6	2.3396	0.8686	10.802			[204]	0.5	0.6	1.6
n-C_{10}	4.7583	1.1121	17.772			[204]	1.3	1.1	2.0
n-C_{16}	9.2020	1.4044	28.964			[204]	1.8	2.2	
CO_2	0.35079	0.7602	2.72			[288]	0.3	1.5	4.5
CH_4	0.2278	0.444	2.84			[294]	0.4	3.4	2.2
N_2	0.4985	0.1372	2.605			[295]	0.7	2.9	1.6
						Overall	**0.8**	**1.8**	**2.4**

a) Same as in **Table 3.2**.

3.7 Summary

The theoretical background of the thermodynamic models considered in this work has been described. The Parachor method and the Sutton’s correlation are semi-empirical/empirical approaches which can be used to predict the interfacial tension of reservoir fluids: the Parachor is suitable for oil−gas interfaces, whereas Sutton’s correlation is suitable for gas−water and oil−water interfaces. On the other hand, the Linear Gradient Theory (LGT) and the Density Gradient Theory (DGT) are models based on the density distribution of components across the interfacial region and on the Helmholtz free energy which are combined to compute *IFT* values. The DGT and LGT can be applied to fluid−liquid interfaces in both hydrocarbon and aqueous systems, as well as in other type of systems (*e.g.*, alcohols, esters and polymers). Of particular interest is the DGT which considers the actual density profile of components obtained through direct minimization of the Helmholtz free energy and thus, besides allowing the computation of macroscopic interfacial properties (*i.e.*, *IFT*), the DGT also provides important information about the microstructure of interfaces such as interface thickness, density profiles and surface/interface activity (adsorption/desorption of molecules at the interface) .

In order to accurately describe the required bulk phase properties, the VT-PPR78 EoS and the CPA EoS have been considered. The first is based on the classical cubic Peng-Robinson 1978 EoS with volume corrections and a predictive feature for the estimation of k_{ij} between mixture components. This EoS is used in **CHAPTER 4** to model the phase equilibria of the hydrocarbon systems examined. The second EoS is suitable for modelling mixtures containing both inert and/or associating molecules. The CPA Eos is used in **CHAPTER 5** to model the phase equilibria of the aqueous systems investigated. Furthermore, both EoSs are also used to evaluate the Helmholtz free energy density of the interface within the DGT and LGT approaches.

CHAPTER 4 – INTERFACIAL TENSION OF HYDROCARBON SYSTEMS

4.1 Introduction

As presented in **CHAPTER 1**, the deployment of more efficient and economical extraction methods and processing facilities of oil and gas requires the accurate knowledge of the interfacial tension of gas + oil systems. Thus, in this chapter an experimental and modelling investigation on the *IFT* and density of oil + gas systems was conducted for binary and multicomponent mixtures composed of *n*-alkanes and common gases such as carbon dioxide, methane and nitrogen.

Aiming at filling the experimental gap found in literature (**Section 1.3.1)**, saturated density and *IFT* measurements of binary systems gas + *n*-decane (gas = CO_2, CH_4 and N_2) were extended for different isotherms (up to 442 K) and pressures up to 69 MPa or near the critical point of each mixture. Measurements were carried out with the experimental setup based on the Capillary Rise technique (**Section 2.2**) and both the equipment and methodology were validated through comparison with selected experimental data available in literature. Densities of the saturated phases were measured with a high pressure densitometer and the data correlated with a thermodynamic phase behaviour model based on the PR78 EoS (**APPENDIX A**). Modelled density data were combined with measured capillary constants to estimate pertinent *IFT* values. Complementarily, measurements were also carried out for three multicomponent synthetic mixtures at a representative reservoir temperature of 393 K. The studied synthetic mixtures comprised systems of up to 9 components which can be used to mimic the behaviour of real gas condensate and petroleum mixtures, particularly during CO_2 injection processes.

The development of predictive models capable of accurately accounting the effect of temperature and pressure on the phase behaviour and *IFT* is necessary for the design of more efficient oil recovery processes. Therefore, the predictive capabilities of the Parachor, LGT and DGT approaches in combination with the VT-PPR78 EoS were assessed by comparison with data measured in this work and gathered from literature for hydrocarbon systems. This means that in the case of the LGT and DGT models the binary coefficient in the mixing rule of the influence parameters was fixed to zero (*i.e.*, $\beta_{ij} = 0$). In total, 16 gas + *n*-alkane binary and 3 multicomponent synthetic mixtures as well as 1 real petroleum fluid were considered. To the author's knowledge, to date only Miqueu *et al.* [196] and Nilssen *et al.* [215] have applied the DGT to predict the *IFT* of real petroleum mixtures. Therefore, in this chapter the impact of critical properties of *pseudo*-components and lumping procedures (*i.e.*, number of *pseudo*-components) on the phase behaviour and *IFT* prediction of a real petroleum mixture was also investigated. Lastly, the impact of the microstructure of the interface on the *IFT* of hydrocarbon systems was investigated with the aid of the density profiles computed by the DGT.

4.2 Experimental Procedure

4.2.1 Materials and sample preparation

The specification and sources of the chemicals used in the experiments described in this chapter are summarized in **Table 4.1**. Toluene and *n*-heptane were used for cleaning purposes only. One certified synthetic multicomponent mixture (MIX-0), with the composition given in **Table 4.2**, was prepared and supplied by BOC. All chemicals were used without further purification.

Three multicomponent mixtures (MIX-1, MIX-2 and MIX-3) were prepared gravimetrically with a Sartorius balance model MSA8202S (resolution 0.01g) and stored in 600 cm^3 sample vessels. MIX-1 and MIX-2 were prepared from pure substances while for MIX-3, MIX-0 saw the gravimetrical addition of *n*-decane and *n*-dodecane. Compositions of the tested multicomponent synthetic mixtures are listed in **Table 4.3**.

Table 4.1. *Suppliers and specification as stated by the supplier of the materials used in this work.*

Chemical Name	Supplier	Mass fraction purity
Carbon dioxide	BOC	0.99995
Methane	BOC	0.99995
Nitrogen	Air Products	0.9999
n-Heptane	RathBurn Chemicals	>0.99
n-Decane	Acros Organic	>0.99
n-Dodecane	Acros Organic	>0.99
n-Tetradecane	Acros Organic	>0.99
Toluene	Fischer Scientific	>0.995

***Table 4.2**. Composition of multicomponent mixture MIX-0 as prepared and certified by BOC.*

Chemical Name	mole%
Methane	7.901 ± 0.040
Nitrogen	6.009 ± 0.031
Ethane	7.015 ± 0.036
Propane	4.968 ± 0.025
n-Butane	2.067 ± 0.001
i-Butane	2.049 ± 0.001
Carbon dioxide	Balance (69.991)

***Table 4.3**. Compositions (mole%) of multicomponent synthetic mixtures prepared in this work.*

Chemical Name	MIX-1 $^{a)}$	MIX-2 $^{b)}$	MIX-3 $^{c)}$
Carbon dioxide	34.26 ± 0.01	73.708 ± 0.004	61.87 ± 0.20
Nitrogen			5.31 ± 0.03
Methane	52.17 ± 0.02	13.41 ± 0.06	6.98 ± 0.04
Ethane			6.20 ± 0.04
Propane			4.39 ± 0.03
n-Butane			1.827 ± 0.001
i-Butane			1.811 ± 0.001
n-Decane	13.57 ± 0.01	9.93 ± 0.01	8.73 ± 0.02
n-Dodecane			2.88 ± 0.04
n-Tetradecane		2.95 ± 0.02	
Total	***100***	***100***	***100***

Predicted saturation pressure with the PPR78 EoS [271–275] at T = 298 K: $^{a)}$23.79 MPa, $^{b)}$9.84 MPa and $^{c)}$10.28 MPa.

4.2.2 Measuring procedure

The entire capillary rise setup was thoroughly cleaned with toluene and *n*-heptane and then dried with compressed air. Once the entire setup had been tested for leaks, it was kept under vacuum at T = 333 K. This cleaning procedure was repeated before loading a new mixture into the system and helped to remove interface active impurities. The desired temperature was set and let to stabilize overnight.

For each binary mixture, *n*-decane was transferred from the sample vessel to the equilibrium cell through port **CR.A$_1$** of the equilibrium cell as depicted in **Figure 2.4**. Sufficient liquid hydrocarbon was introduced into the system until 1/4 to 1/3 of the length of the capillary glass tubes was covered. The desired pressure inside the cell was set by injecting pure gas (*i.e.*, methane, carbon dioxide or nitrogen) into the equilibrium cell and controlling the back pressure of the sample vessel.

On the other hand, for multicomponent mixtures they were loaded into the equilibrium cell by pumping hydraulic fluid behind the piston in the sample vessel containing the testing fluid (MIX-1, MIX-2 or MIX-3) and the pressure inside the equilibrium cell increased at successive steps by controlling the amount of sample transferred. The pressure inside the sample vessel was maintained at values sufficiently higher than the predicted saturation pressure at ambient temperature, *i.e.*, $T \approx 298$ K (**Table 4.3**), to ensure that the tested mixture was in single-phase state at each loading step.

For each pressure and temperature state, valves **CR$_1$**, **CR$_4$** and **CR$_5$** were kept closed and the content of the cell was stirred until pressure and temperature readings were stabilized. Once equilibrium was achieved, normally after 10 min, stirring was stopped and the liquid rise in each capillary tube was measured.

The saturated liquid density was measured by displacing the phase in the equilibrium cell into the densitometer whilst stirring. Opening valve **CR$_5$** and controlling the movement of piston **CR.D** with the aid of the DBR pump, allowed the saturated liquid phase to be displaced from the equilibrium cell into the densitometer, as depicted in **Figure 2.4**. The injection and withdrawal of hydraulic fluid behind piston **CR.D** were performed at a constant rate 100 $\text{cm}^3.\text{h}^{-1}$ with the control software of the pump. The back-flow of fluids from the densitometer to the equilibrium cell was prevented by means of check valves **CR.E$_1$** and **CR.E$_2$**. Generally 4-5 cycles (~5 cm^3/each) allowed a complete renewal of the fluids inside the densitometer with a total pressure change in the system of not more than 0.1 MPa at each stroke, ensuring that the equilibrium conditions were maintained. Following this, the cycling was stopped, valve **CR$_5$** closed and the resonance period of the vibrating tube (τ) recorded after a 5 min period of stabilization.

The measured period of vibration (τ) of a U-tube can be related to the density (ρ) according to:

$$\rho = D_1\tau^2 - D_2 \qquad \textbf{4.1}$$

where D_1 and D_2 are the temperature and pressure dependent densitometer parameters. Similarly, the density of the saturated vapour phase was measured by turning the cell upside down and repeating the procedure described above.

The parameters D_1 and D_2 were calibrated against the density of carbon dioxide, methane, nitrogen and *n*-decane calculated with REFPROP [99] for each pressure and temperature of interest. To check this calibration procedure, the density of the reference fluids was calculated at pertinent conditions with **Equation 4.1** and the percentage average absolute deviation to reference data [99] was found to be 0.26, 0.57, 0.49 and 0.05 %, for carbon dioxide, methane, nitrogen and *n*-decane respectively. Since gases are in general much more compressible and more sensitive to temperature and pressure changes, uncertainties in pressure ($u(P)$ = 0.04 MPa) and temperature ($u(T)$ = 0.1 K) can introduce significant variations on the density measurements. Furthermore, at low pressures it was difficult to obtain a highly reliable and stable reading of τ when the vapour phase of tested mixtures was circulated through the densitometer. This may be due to the retention of micro-droplets of the liquid phase in the densitometer which could not be completely displaced by the flow of the vapour phase alone. Thus, fewer points were obtained for the density of the vapour phase of the systems studied here when compared to the liquid phase. Similar difficulties were highlighted by Chiquet *et al.* [7] when measuring the saturated density of the $CO_2 + H_2O$ system. Overall, taking into account the uncertainties in pressure and temperature measurements, and from observation of dispersion of the density measurements, a combined expanded uncertainty of $U_c(\rho) = 1.5$ kg.m^{-3} and $U_c(\rho) = 7.0$ kg.m^{-3} for the density measurements of the liquid and vapour phases respectively, with a level of confidence of 0.95, were estimated.

The generated densities were correlated with the PR78 EoS described in **APPENDIX A**. Binary interaction coefficients (k_{ij}s) and volume corrections ($v_{c,i}$) were employed for a correct description of the generated data. For multicomponent mixtures, k_{ij}s were fixed to those predicted by the group-contribution method of Jaubert *et al.* [271–275] (*i.e.*, PPR78 EoS) and only volume corrections of key components were regressed against measured density. On the other hand, for binary systems these parameters (k_{ij}s and $v_{c,i}$) were optimized simultaneously for each system and temperature. Optimized parameters are listed in **Tables C.1** and **C.2** in **APPENDIX C** together with the calculated %AAD to measured density data. Subsequently, *IFT* values were calculated with **Equation 2.5** using the square of measured capillary constants a^2 and correlated density data at pertinent pressure and temperature conditions.

4.3 Experimental Results

4.3.1 Binary mixtures

Equilibrium densities: The saturated densities of three binary mixtures CH_4 + *n*-decane, CO_2 + *n*-decane and N_2 + *n*-decane were measured at temperatures of 313, 344, 393 and 443 K and pressures up to 68 MPa or near the critical point of each mixture. The results are presented in **Tables D.1** through **D.3** in **APPENDIX D**. Measured densities were also compared to selected literature data [45–50,52] and correlated densities, as depicted in **Figure 4.1**.

As can be seen in **Figure 4.1**, density measurements from the present work are in good agreement with the data of Sage and co-workers [45,49,50], Nagarajan and Robinson [46], Shaver *et al.* [47], Mejía *et al.* [48] and Jianhua *et al.* [52] within the range of pressure and temperature conditions studied. The largest deviations were observed between measurements performed here and those reported by Reamer and Sage [45] for the density of the saturated vapour phase at high pressures and low temperatures. Indeed, despite the excellent agreement with the density of the saturated liquid phase, results from Reamer and Sage [45] at T = 311 K suggest a lower density for the vapour phase of CO_2 + *n*-decane with increasing pressures. It is worth nothing that no comparison was made with the data measured by Amin and Smith [51] for the saturated density of CH_4 + *n*-decane since quantitative results were not published in their original work nor made available at the time of this study.

The PR78 EoS with binary interaction coefficients and volume corrections listed in **Table C.1** in **APPENDIX C** was capable of correlating the saturated density of the studied systems with relatively low deviations to measured data. As listed in **Table C.1** and depicted in **Figure 4.1**, the highest deviations were obtained for the density of the vapour phases, with a maximum %AAD of 3.6% obtained for the CH_4 + *n*-decane system at the highest temperature. This approach also allowed a correct description of the density of the vapour phase at low pressures, where a limited number of points were measured, as illustrated in **Figure 4.1.** Altogether, the PR78 EoS with adjusted parameters allowed a reproduction of the saturated density with an overall %AAD to measured data between

0.2 and 0.5 % for the liquid phase and between 1.5 and 2.5 % for the vapour phase. These results validate the adequacy of the adopted method for estimating the density difference of these systems.

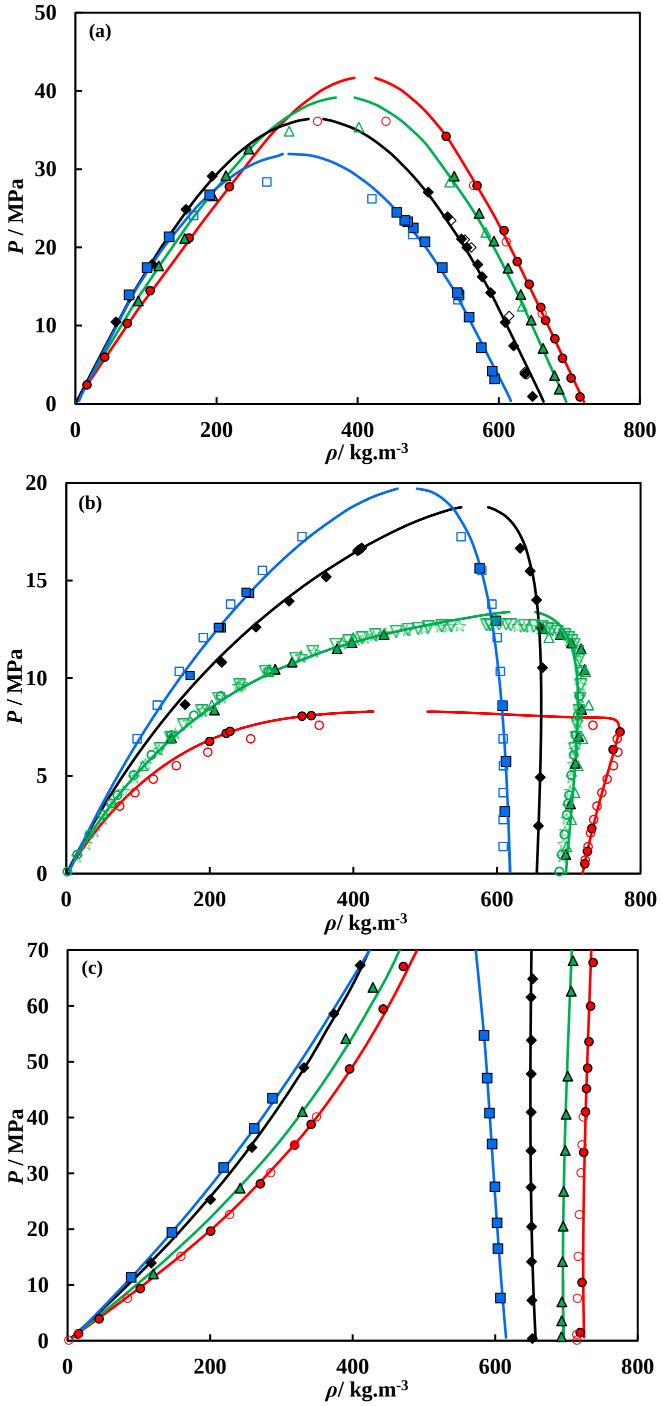

Figure 4.1. *Saturated density−pressure diagrams of* ***(a)*** *n-decane + CH$_4$,* ***(b)*** *n-decane + CO$_2$ and* ***(c)*** *n-decane + N$_2$. Full symbols represent experimental data measured in this work: T = 313 K (●), 343 K (▲), 393 K (◆) and 442 K (■). Empty symbols represent literature data:* ***(a)*** *Reamer et al.* [50], *T = 311 K (○), 344 K (△) and 444 K (□); Sage et al.* [49], *T = 394 K (◇);* ***(b)*** *Reamer and Sage* [45], *T = 311 K (○), 344 K (△) and 444 K (□); Nagarajan and Robinson* [46], *T = 344 K (▽); Shaver et al.* [47], *T = 344 K (☆); Mejía et al.* [48], *T =344 K (○);* ***(c)*** *Jianhua et al.* [52], *T = 313 K (○). Solid lines represent correlated densities with the PR78 EoS and parameters listed in* ***Table C.1*** *in* ***APPENDIX C*** *at pertinent temperatures.*

Interfacial tensions: The capillary constant *a* of three binary mixtures CH_4 + *n*-decane, CO_2 + *n*-decane and N_2 + *n*-decane were measured in the temperature range 313 to 442 K and pressures up to 69 MPa or near the critical point of each mixture, and the results combined with correlated density difference data to estimate the *IFT*. Capillary constants and *IFT* values are listed in **Tables E.1** through **E.3** in **APPENDIX E** for each pressure and temperature condition studied. A comparison between measurements and data available in literature [46–48,51–53,67] is shown in **Figure 4.2**.

As depicted in **Figure 4.2**, *IFT* measurements are in good agreement with those of Amin and Smith [51] and Stegemeier *et al.* [67] for CH_4 + *n*-decane, Nagarajan and Robinson [46], Shaver *et al.* [47], Georgiadis *et al.* [53] and Mejía *et al.* [48] for CO_2 + *n*-decane, and Jianhua *et al.* [52] for N_2 + *n*-decane, validating both the equipment and the experimental procedure followed here. In general, measurements from the present work show that the *IFT* of the studied systems are slightly lower than data reported by others in literature. The largest deviations were obtained between measurements reported here and those from Amin and Smith [51] at low pressures for CH_4 + *n*-decane. However, data points from Amin and Smith [51] at low pressures have been brought to question as the slope of their results suggest an *IFT* for this system at ambient pressure significantly higher than surface tension of *n*-decane at pertinent temperatures. As an example, their measurements at T = 311 K are plotted in the insert of **Figure 4.2*a*** (*n*-decane *ST* = 22.18 $mN.m^{-1}$ at T = 311 K [99]). Moreover, it is worth mentioning that data measured by Georgiadis *et al.* [53] for CO_2 + *n*-decane at T = 344 and 443 K were recalculated using the approach adopted in this work for the density difference between the equilibrated phases and plotted in **Figure 4.2*b***. It was found that the absolute difference between the recalculated and the original *IFT* data [53] had an average of 0.18 $mN.m^{-1}$ (%AAD = 3.7 %) and reached a maximum of 0.48 $mN.m^{-1}$ (%AAD = 17.7%) at the highest temperature and pressure, where the density difference between the equilibrated phases reached the lowest value within the range studied. The impact of the approximation to pure substance density on the *IFT* values is further evaluated in **CHAPTER 5**.

From **Figure 4.2** it can also be seen that the pressure increase leads to a reduction of the interfacial tension values in all systems investigated, more pronounced for the CO_2 + *n*-decane system. On the other hand, the temperature increase leads to a decrease of the *IFT* in the CH_4 + *n*-decane and N_2 + *n*-decane systems over the entire pressure range, whereas a crossover was observed in the CO_2 + *n*-decane system for pressures ranging from 5 to 10 MPa, where the impact of temperature on the *IFT* is less marked. In general, the *IFT* dependence on temperature is more pronounced at low pressures and gradually decreases with increasing pressures.

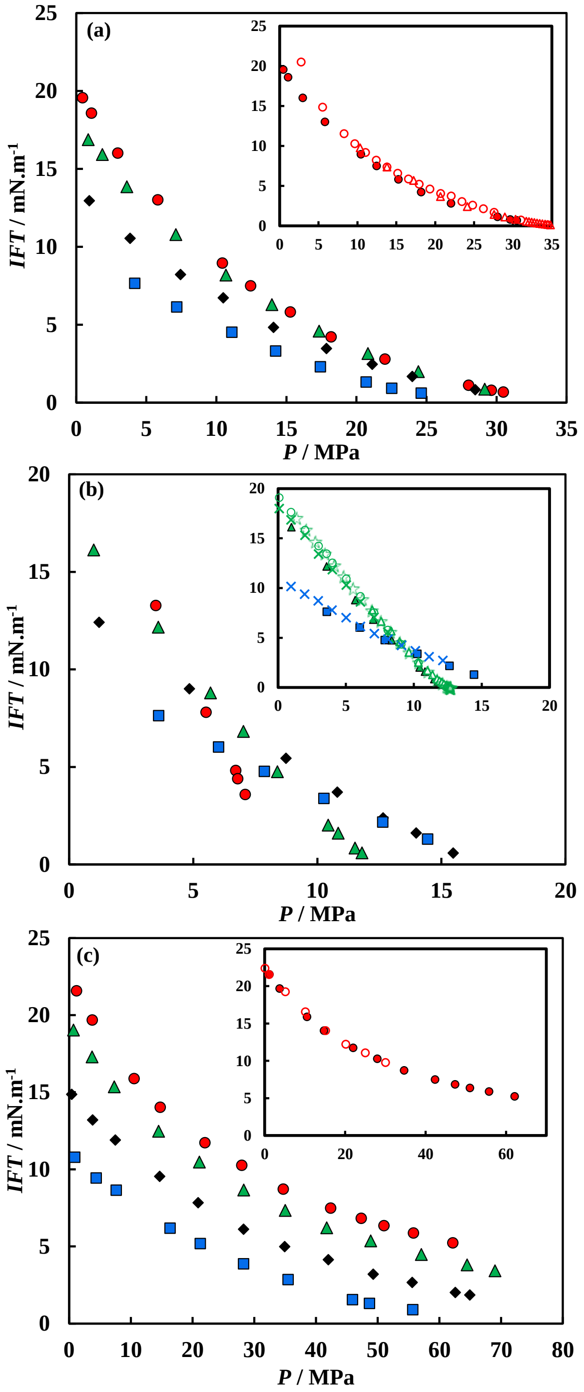

Figure 4.2. *IFT−pressure diagrams of* ***(a)*** *n-decane + CH$_4$,* ***(b)*** *n-decane + CO$_2$ and* ***(c)*** *n-decane + N$_2$. Full symbols represent experimental data measured in this work: T = 313 K (●), 343 K (▲), 393 K (◆) and 442 K (■). Empty symbols represent literature data:* ***(a)*** *Stegemeier et al.* [67], *smoothed data T = 311 K (△); Amin and Smith* [51], *T = 311 K (○);* ***(b)*** *Nagarajan and Robinson* [46], *T = 344 K (△); Shaver et al.* [47], *T = 344 K (☆); Georgiadis et al.* [53], *T = 344 K (✕) and 443 K (✕); Mejía et al.* [48], *T =344 K (○);* ***(c)*** *Jianhua et al.* [52], *T = 313 K (○). Data from Georgiadis et al.* [53] *were recalculated using the approach adopted in this work for the density difference between the equilibrated phases.*

4.3.2 Multicomponent mixtures

Equilibrium densities: The saturated densities of three multicomponent synthetic mixtures (of compositions given in **Table 4.3**) were measured at T = 393 K and pressures in the vapour–liquid region. The results are presented in **Tables D.4** through **D.6** in **APPENDIX D** and plotted in **Figure 4.3**. For comparison purposes, correlated saturated densities of the CO_2 + *n*-decane and CH_4 + *n*-decane systems together with the ones computed with the PPR78 EoS and appropriate volume corrections (**Table C.2**) for each multicomponent mixture are also shown in **Figure 4.3**.

As expected, the saturated densities of the synthetic multicomponent mixtures investigated in this work exhibited a behaviour which lies between that of the binary mixtures CO_2 + *n*-decane and CH_4 + *n*-decane at pertinent temperatures, as shown in **Figure 4.3**. With the highest content in methane, MIX-1 showed two-phase equilibrium pressures higher than those of MIX-2 and MIX-3, in which CO_2 is the predominant component (73.708 and 61.87 mole%, respectively). From **Figure 4.3** it can also be observed that by using the PPR78 EoS and appropriate volume corrections, a good description of the effect of pressure on the saturated densities of the multicomponent mixtures is obtained, with an overall %AAD to measured liquid and vapour data of 0.4 and 4.1 %, respectively (**Table C.2**). These results demonstrate that this model can be used to adequately estimate the density difference of studied synthetic mixtures at other pressure conditions.

Interfacial tensions: The capillary constant a of three synthetic mixtures MIX-1, MIX-2 and MIX-3 were measured at T = 393 K and pressures up to 23 MPa or near the complete vapour–liquid miscibility pressures, and the results combined with correlated density difference data to estimate the *IFT*. Capillary constants and *IFT* values are listed in **Tables E.4** through **E.6** in **APPENDIX E** and compared in **Figure 4.4** to *IFT* data of CO_2 + *n*-decane and CH_4 + *n*-decane.

As can be seen from **Figure 4.4** and similar to what was observed in the binary systems, the pressure increase leads to a decrease of the interfacial tension, with *IFT* values for the multicomponent mixtures lying between those of the binary systems CO_2 + *n*-decane and CH_4 + *n*-decane. The results also show that increasing the mixtures CO_2 content generally resulted in lower interfacial tension values at fixed pressure.

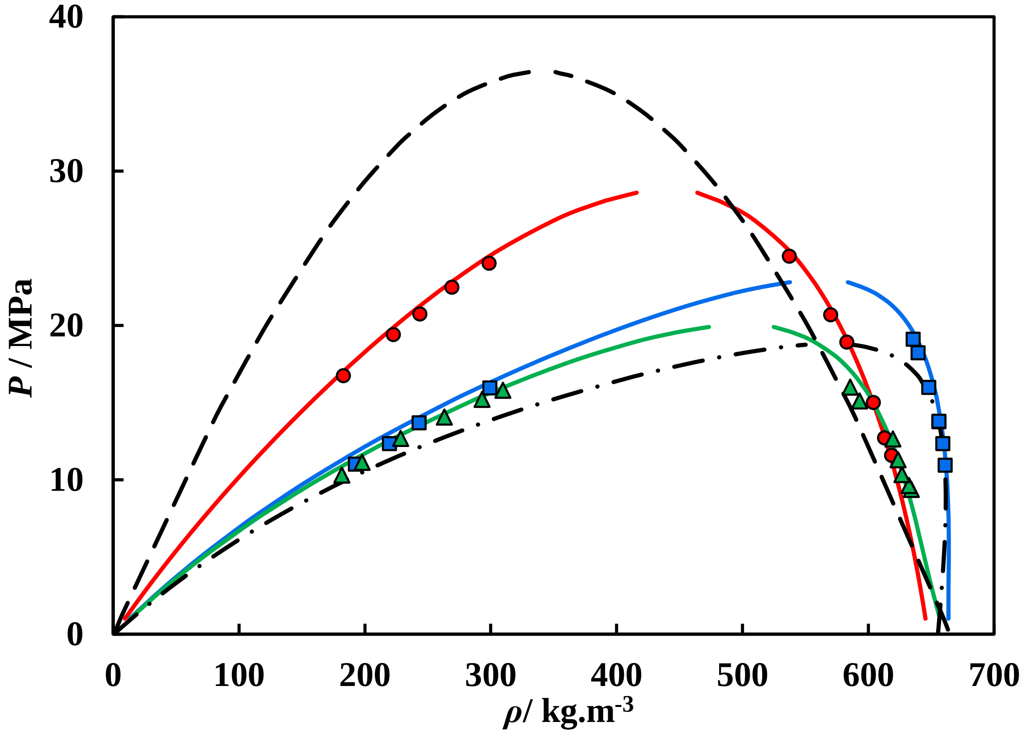

Figure 4.3. *Saturated density−pressure diagrams of multicomponent synthetic mixtures. Full symbols represent experimental data measured in this work at T = 393 K: MIX-1 (●), MIX-2 (■) and MIX-3 (▲). Solid lines represent correlated densities with the PPR78 EoS and volume corrections listed in* ***Table C.2*** *in* ***APPENDIX C****. Dashed and dotted-dashed lines correspond to the correlated densities of the binary mixtures* CH_4 *+ n-decane and* CO_2 *+ n-decane at T = 393 K, respectively, calculated with the PR78 EoS and optimized parameters (*k_{ij}*s and* $v_{c,i}$*) listed in* ***Table C.1****.*

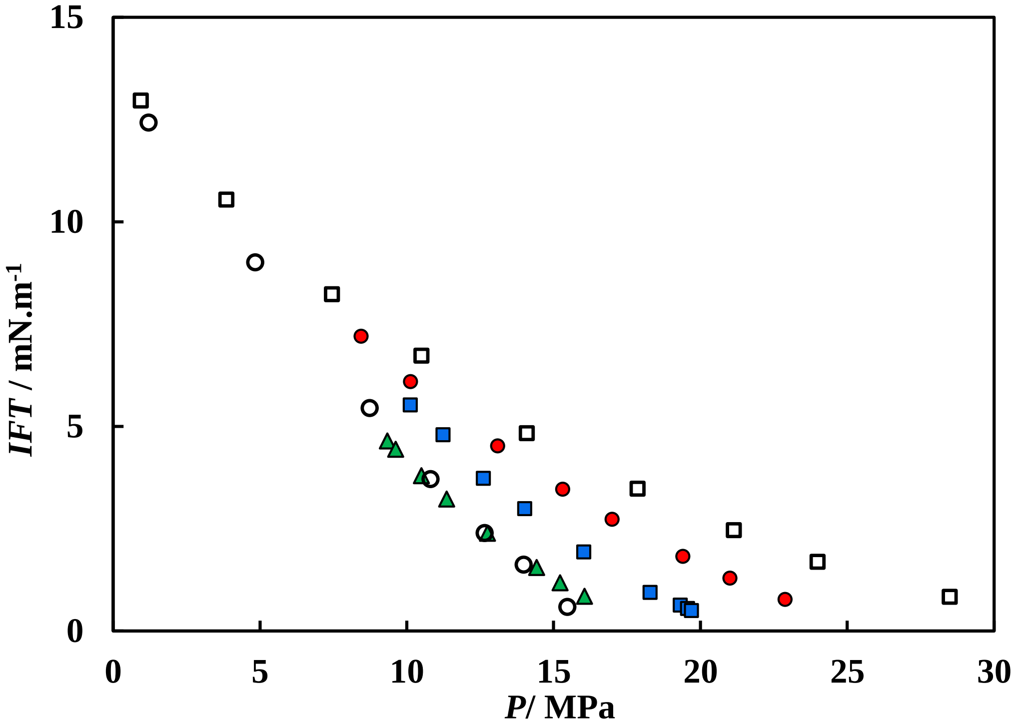

Figure 4.4. *IFT−pressure diagrams of binary and multicomponent synthetic mixtures measured in this work at T = 393 K: MIX-1 (●), MIX-2 (■), MIX-3 (▲),* CH_4 *+ n-decane (☐) and* CO_2 *+ n-decane (○).*

4.3.3 Experimental uncertainties

The measurement of any thermophysical property is always susceptible to uncertainties which affect the overall accuracy of experimental data. In this work, the combined expanded uncertainties in the interfacial tension measurements, U_c (*IFT*), with the differential CR method are assessed by considering the effect of uncertainties on the measured capillary constants, U_1 (*IFT*), and uncertainties on the estimation of the density of the equilibrated phases, U_2 (*IFT*).

U_1 (*IFT*) can be estimated by considering the impact of uncertainties of the cathetometer and dispersion of the measured difference of the liquid rise height in the capillary tubes, Δh. It was estimated a combined expanded uncertainty for Δh of 0.010 cm for measurements ranging from 1.876 to 0.129 cm, with a level of confidence of 0.95. The calculation of the expanded uncertainty of a^2 depends not only of the ID of the capillary tubes, but also of the magnitude of Δh and, in turn, of the total pressure of the system. For measurements performed with the CR setup, the combined expanded uncertainty of a^2 was found to be $U_c(a^2) = 0.000331$ cm^2, with a level of confidence of 0.95, yielding expanded relative uncertainties for this parameter between 0.5 and 0.7 % at low pressures and up to 8 % for pressures close to the complete vapour−liquid miscibility, where Δh reached the lowest values. Using the law of propagation of errors [296], U_1 (*IFT*) can be estimated as follows:

$$U_1(IFT) = \left(\left(\frac{\partial IFT}{\partial a^2} \right)^2 U_c(a^2)^2 \right)^{1/2} \qquad \textbf{4.2}$$

$$U_c(a^2) = \left(\left(\frac{\partial a^2}{\partial \Delta h} \right)^2 U_c(\Delta h)^2 \right)^{1/2} \qquad \textbf{4.3}$$

The second contribution, U_2 (*IFT*), can be estimated by considering the deviations between correlated and measured density data for each system, phase and temperature of interest (**Tables C.1** and **C.2** in **APPENDIX C**). The impact of uncertainties in temperature ($u(T)$ = 0.1 K) and pressure ($u(P)$ = 0.04 MPa), as well as mixtures composition on the estimation of the density of the saturated phases, are somewhat suppressed by the deviations of the model to measured data and hence, were not considered. The expression for estimating U_2 (*IFT*) has the following form [296]:

$$U_2(IFT) = \left(\left(\frac{\partial IFT}{\partial \rho^L} \right)^2 U_c(\rho^L)^2 + \left(\frac{\partial IFT}{\partial \rho^V} \right)^2 U_c(\rho^V)^2 \right)^{1/2} \tag{4.4}$$

The combined expanded uncertainties in the *IFT* measurements estimated with a confidence level of 0.95, are shown in **Tables E.1** through **E.6** for each system and experimental condition, with values averaging 0.13, 0.12 and 0.14 mN.m^{-1} for CO_2 + *n*-decane, CH_4 + *n*-decane and N_2 + *n*-decane, respectively, and 0.10, 0.14 and 0.12 mN.m^{-1} for MIX-1, MIX-2 and MIX-3, respectively. Overall, the combined expanded uncertainty of the *IFT* measurements increased with pressure, with relative expanded uncertainties lower than 1.5% at low pressures and up to 11.3 % near the complete miscibility conditions, where *IFT* values are very low (< 1.5 mN.m^{-1}).

4.4 Modelling

4.4.1 Binary and multicomponent synthetic mixtures

In this section the predictive capabilities of the VT-PPR78 EoS and *IFT* models to represent the experimental data of the studied synthetic hydrocarbon systems were evaluated. This analysis was also extended to binary mixtures containing CH_4, CO_2 and N_2 and other *n*-alkanes by comparing the *IFT* predictions against selected literature data [41,52,54,59,61,63,64,68,69,74].

Classical cubic equations of state have been extensively applied in previous studies available in literature in combination with *IFT* methods to model the interfacial tension of gas + *n*-alkane systems [173,185,186,190,192,194,196,213–215,250,256,263,266]. Unlike most of these studies, where volume corrections and/or binary interaction coefficients within the EoS framework were adjusted to bulk phase property data in order to obtain a good representation of the phase behaviour of the mixtures, here the most reliable bulk phase properties are obtained in a fully predictive manner with the VT-PPR78 model. This approach for computing the phase behaviour is an improvement over the methodology adopted by Miqueu *et al.*[192,194,196] when modelling the *IFT* of some of the systems also considered in this work.

Differences between measured and predicted bulk phase properties of the studied systems in terms of %AAD are given in **Tables C.1** and **C.2** and, as an example, a comparison at T = 343 K for the binary systems gas + *n*-decane is plotted in **Figure 4.5**. The deviations between measured and predicted *IFT* with the Parachor, LGT and DGT approaches for the binary systems gas + *n*-decane as well as for other gas + *n*-alkanes mixtures are listed in **Tables 4.4** and **4.5**. A graphical representation of the results for selected systems and conditions is depicted in **Figures 4.6** and **4.7**. It should be noted that *IFT* values computed for these systems with the LGT were obtained using the mixing rule given in **Equation 3.45**, as followed by Zuo and Stenby [186] when modelling synthetic mixtures containing hydrocarbons and gases.

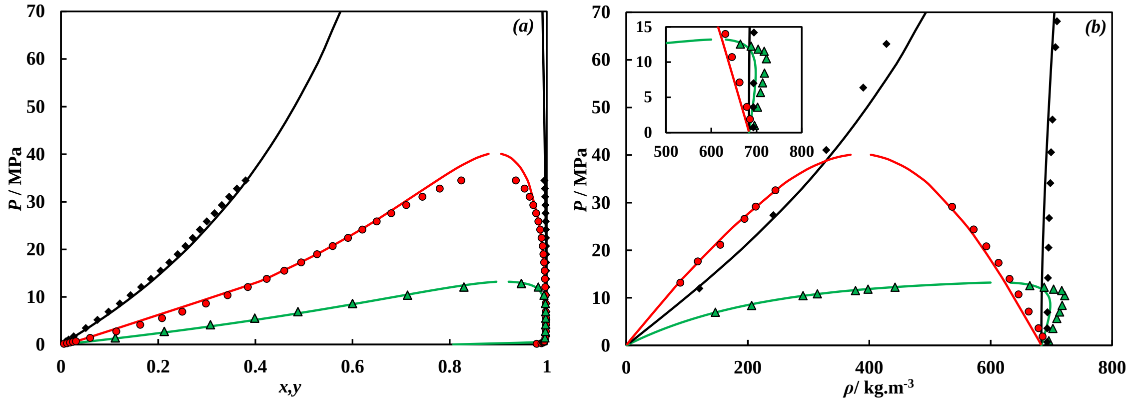

*Figure 4.5. **(a)** Pressure−composition and **(b)** pressure−density diagrams of n-decane + CH_4 (red), n-decane + CO_2 (green) and n-decane + N_2 (black). Symbols in **(a)** represent solubility data taken from literature: Reamer et al.* [50], *T = 344 K (●), Reamer and Sage* [45], *T = 344 K (▲) and Azarnoosh and McKetta* [297], *smoothed data T = 344 K (◆). Symbols in **(b)** represent density data measured in this work at T = 343 K. Solid lines represent predictions from VT-PPR78 EoS.*

As can be seen in **Figure 4.5,** the VT-PPR78 predictions are in good agreement with experimental solubility and density data. Moreover, as listed in **Tables C.1** and **C.2**, the VT-PPR78 EoS allowed a prediction of the saturated density data measured in this work, with an overall %AAD between 1 to 2.9 % for the liquid phase and between 3.2 to 7.4 % for the vapour phase. A complementary graphical representation of the predictive capabilities of this EoS for other systems of interest is plotted in **Figure F.1** in **APPENDIX F**. Overall, deviations from predicted densities to measured data are only slightly higher than those obtained with correlated density data, validating the adequacy of the VT-PPR78 EoS for predicting the effect of pressure and temperature on the phase behaviour of the hydrocarbon systems studied here.

Table 4.4 and **Figure 4.6** show that the DGT approach gave the best predictions of the *IFT* of binary systems composed of *n*-alkane and either methane, carbon dioxide or nitrogen, with an overall %AAD to measured data of 8.3, 5.5 and 4.9 %, respectively. In general, the highest deviations were observed near the critical point, where *IFT* values are rather low (*IFT* < 1.5 mN.m^{-1}) and experimental uncertainties considerable. In this region, the overall deviations of predictions with all models to measured data ranged between 15.9 to 54.9 %. These discrepancies may be related to the inappropriate description of the equilibrium properties by the selected phase behaviour model near the critical point, as depicted in **Figure 4.5** and **F.1**. In this sense, the computation of more accurate interfacial tensions near critical point would require a refinement of the phase behaviour model. The performance of the phase behaviour model near critical point can be improved by the use of the crossover approach. In such approach, the transition from classical to non-classical behaviour near the critical region is captured by a crossover equation and thereby, the equilibrium properties in this region are successfully described. The crossover approach was already incorporated to the PR78 EoS by others in previous studies in literature [298,299]. However, this treatment requires the fitting of additional parameters which characterise the critical region and thus, aiming at keeping the model predictive, it was decided not to implement this approach here. All things considered, the VT-PPR78 + DGT results are in good agreement with other DGT studies [48,54,61,69,300] in which more complex and molecular-based equations of state, such as SAFT and its derivatives, are used for the description the bulk saturated properties and the Helmholtz free energy density of the fluid across the interfacial region.

It can be seen in **Table 4.4** that the LGT model outperforms in general the Parachor method for systems in methane and nitrogen atmospheres. Overall, the LGT allowed a prediction of the *IFT* of CH_4 + *n*-alkane and N_2 + *n*-alkane systems far from the critical point (*i.e., IFT* > 1.5 mN.m^{-1}) with an overall %AAD of 10.1 and 7.7 %, respectively, whereas deviations to measured data with the Parachor method were 14.5 and 13.9 %, respectively. On the other hand, a significant underprediction of the *IFT* was obtained for the systems containing carbon dioxide with the LGT at moderate pressures, as depicted in **Figure 4.6*b*,** resulting in an overall %AAD of 20.3 %, whereas overall deviations with the Parachor method yield only 9.3%. These findings are agreement with the modelling results of Zuo and Stenby [186], in which a large and negative binary interaction coefficient for the cross influence parameter was necessary for correct description of the *IFT* of systems containing CO_2 with the LGT model.

At this point it is important to note that the Parachor method can be shown to describe correctly the *IFT* vs density difference behaviour near the critical point of pure components [242]. However, the results obtained in this work with the Parachor method for binary mixtures indicate a poor description of the *IFT* of such mixtures, with overall %AADs higher than 23.8 % for *IFT* < 1.5 mN.m^{-1}. On the one hand, these results can be traced back to the inability of the phase behaviour model for describing the bulk properties in this region. On the other hand, predictions with the Parachor are influenced by the scaling exponent chosen *i.e.*, by the value of E in **Equation 3.2**, which normally ranges between 3.45 and 4. In the regime of low interfacial tension, lower exponents seem often more suitable, whereas exponents approaching $E = 4$ (scaling exponent used in this work) work better for intermediate and high interfacial tension [242]. The selection of a scaling exponent $E \neq 4$ would also require a recalculation of the Parachor values used in this work (*i.e.*, via **Equation 3.3**).

In line with what was described for the binary mixtures, **Table 4.5** and **Figure 4.7** show that the largest deviations to experimental *IFT* data of the studied multicomponent synthetic mixtures were also obtained with the LGT, in particular for MIX-2 and MIX-3 where CO_2 is the predominant component, with an overall %AAD of 28.3% for *IFT* > 1.5 mN.m^{-1} and of 48.1% for *IFT* ≤ 1.5 mN.m^{-1}. As depicted in **Figure 4.7**, the DGT predictions are superior to that of the Parachor method, with the latter slightly underpredicting the *IFT* of these systems. All in all, the DGT predictions for these systems deviated from measured *IFT* data with an overall %AAD at moderate and high pressures of 4.2 and 18.2 %, respectively, whereas the Parachor averaged deviations were of 11.8 and 34.5 % in the same pressure range.

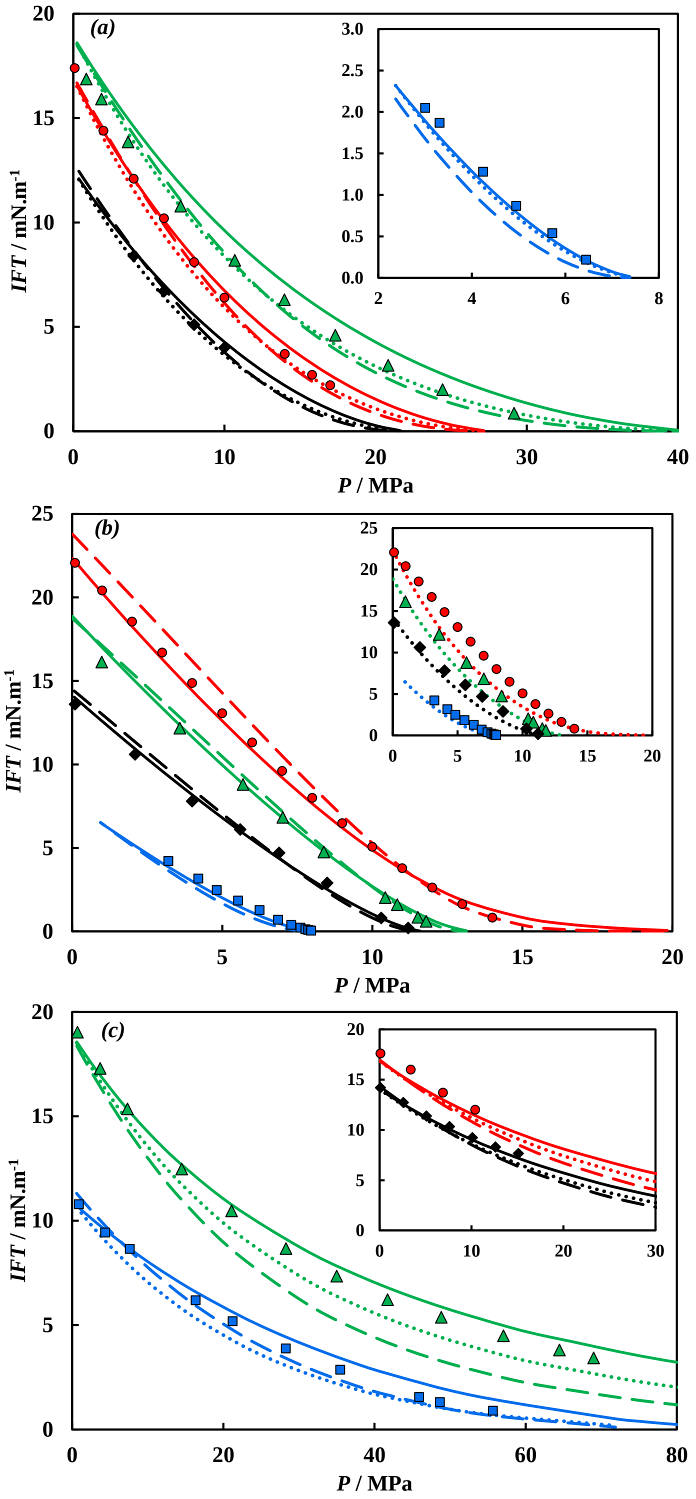

Figure 4.6. *IFT−pressure diagrams of **(a)** n-alkane + CH_4, **(b)** n-alkane +CO_2 and **(c)** n-alkane +N_2. Symbols in **(a)** represent experimental IFT data of CH_4 and: propane taken from Weinaug and Katz* [41], *T = 338 K (■); n-hexane taken from Niño-Amézquita et al.* [61], *T = 350 K (◆); n-heptane taken from Jaeger et al.* [64], *T = 323 K (●) and n-decane from this work, T = 343 K (▲). Symbols in **(b)** represent experimental IFT data of CO_2 and: n-butane taken from Hsu et al.* [68], *T = 344 K (■); n-heptane taken from Jaeger et al.*[63], *T = 353 K (◆); n-decane from this work, T = 343 K (▲) and n-tetradecane taken from Cumicheo et al.* [54], *T = 344 K (●). Symbols in **(c)** represent experimental IFT data of N_2 and: n-hexane taken from Garrido et al.* [74], *T = 333 K (◆); n-heptane taken from Niño-Amézquita et al.* [69], *T = 323 K (●) and n-decane from this work, T = 343 K (▲) and 442 K (■). Dashed, dotted and solid lines represent predictions from the Parachor, LGT and DGT approaches, respectively, in combination with the VT-PPR78 EoS.*

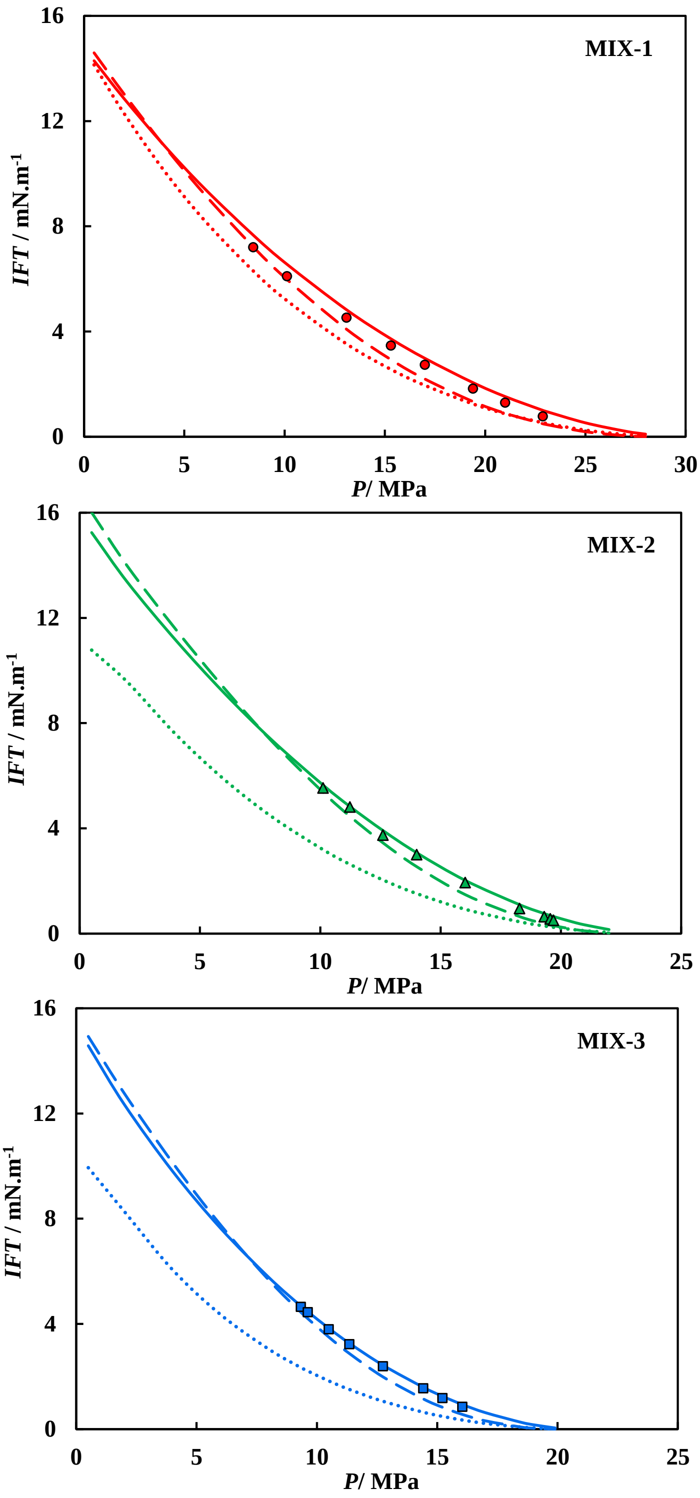

Figure 4.7. *IFT−pressure diagrams of multicomponent synthetic mixtures investigated at T = 393 K. Symbols correspond to IFT data measured in this work. Dashed, dotted and solid lines represent predictions from the Parachor, LGT and DGT approaches, respectively, in combination with the VT-PPR78 EoS.*

Table 4.4. *Summary of %AADs between measured and predicted IFT using the VT-PPR78 EoS in combination with the Parachor, LGT and DGT models for several gas + n-alkanes binary systems. NP = number of data points.*

System	**Data Source**	***T* / K**	**NP**	***%AAD* a)**			**NP**	***%AAD* a)**		
				IFT > 1.5 mN.m^{-1}				**$IFT \leq$ 1.5 mN.m^{-1}**		
				Parachor	**LGT**	**DGT**		**Parachor**	**LGT**	**DGT**
Methane +										
propane	Weinaug and Katz [41]	258 to 338	26	26.0	10.4	4.8	15	29.7	13.4	11.3
n-butane	Pennington and Hough [59]	311 to 344	4	25.2	19.3	4.0	11	29.5	19.4	4.3
n-hexane	Niño-Amézquita *et al.* [61]	300 to 350	9	5.4	6.4	8.2				
n-heptane	Jaeger *et al.* [63,64]	298 to 323	18	6.1	6.8	10.1				
n-decane	This work	313 to 442	31	10.0	7.4	14.4	8	30.5	14.9	59.8
		Overall	***88***	***14.5***	***10.1***	***8.3***	***34***	***29.9***	***15.9***	***25.1***
Carbon dioxide +										
n-butane	Hsu *et al.* [68]	319 to 377	14	18.2	24.6	10.2	24	74.1	66.4	40.9
n-heptane	Jaeger *et al.* [63]	323 to 353	10	7.9	18.0	5.7	4	40.8	54.7	11.5
n-decane	This work	313 to 442	23	10.0	23.7	3.7	4	10.5	19.6	30.9
n-dodecane	Cumicheo *et al.* [54]	344	12	7.8	14.6	5.9				
n-tridecane	Cumicheo *et al.* [54]	344	13	3.6	20.3	3.7	1	10.0	4.1	67.7
n-tetradecane	Cumicheo *et al.* [54]	344	14	6.9	20.5	3.9	1	4.8	1.0	63.1
		Overall	***86***	***9.1***	***20.3***	***5.5***	***34***	***28.0***	***29.2***	***42.8***
Nitrogen +										
n-pentane	Jianhua *et al.* [52]	313	6	16.6	6.3	5.0				
n-hexane	Garrido *et al.* [74]	303 to 333	28	7.2	5.3	2.9				
n-heptane	Niño-Amézquita *et al.* [69]	295 to 373	11	9.8	8.9	7.1				
n-octane	Jianhua *et al.* [52]	313	8	14.0	5.2	1.1				
n-decane	This work	313 to 442	44	21.9	12.7	8.5	2	23.8	22.4	54.9
		Overall	***97***	***13.9***	***7.7***	***4.9***	***2***	***23.8***	***22.4***	***54.9***

a) $\%AAD = 1/NP \times \sum_i^{NP} \left| \left(IFT_i^{Model} - IFT_i^{Exp} \right) / IFT_i^{Exp} \right| \times 100$

***Table 4.5**. Summary of %AADs between measured and predicted IFT using the VT-PPR78 EoS in combination with the Parachor, LGT and DGT models for synthetic multicomponent systems. NP = number of data points.*

System	T / K	NP	%AAD $^{a)}$ $IFT > 1.5$ mN.m^{-1} Parachor	LGT	DGT	NP	%AAD $^{a)}$ $IFT \leq 1.5$ mN.m^{-1} Parachor	LGT	DGT
MIX-1	393.1	6	12.3	22.7	8.3	2	33.7	32.0	23.7
MIX-2	393.2	5	11.2	46.9	3.0	4	37.9	53.0	23.0
MIX-3	393.4	6	11.8	53.2	1.4	2	31.9	59.1	8.1
Overall		***17***	***11.8***	***28.3***	***4.2***	***8***	***34.5***	***48.1***	***18.2***

$^{a)}\ \%AAD = 1/NP \times \sum_i^{NP} \left| (IFT_i^{Model} - IFT_i^{Exp}) / IFT_i^{Exp} \right| \times 100$

4.4.2 Real Black oil

Complementarily, in this section the adequacy of these models for predicting the phase behaviour and *IFT* of real petroleum fluids is assessed. Predictions were compared to compositional, volumetric and *IFT* data measured for multiple contact experiments performed on a Real Black oil (RFS-1) at T = 373 K and P = 34.58 MPa, as part of a reservoir studies project conducted in our laboratories (1990−1993) [301].

Multiple contact experiments are designed to simulate gas injection processes in oil reservoirs and involve multiple contacts of injection/equilibrium gas with original/equilibrium reservoir oil. They can be divided into forward- and backward-multiple contact tests (FMC and BMC, respectively), as illustrated schematically in **Figure 4.8**. In the FMC test, the injection gas is mixed with the reservoir oil and the equilibrium gas used in the next contacts with fresh oil; this simulates the leading edge of a gas displacement within an oil reservoir. On the other hand, in the BMC test, equilibrated oil is contacted in subsequent stages with fresh injection gas, simulating the zone close to where the injection gas would emerge into the oil reservoir.

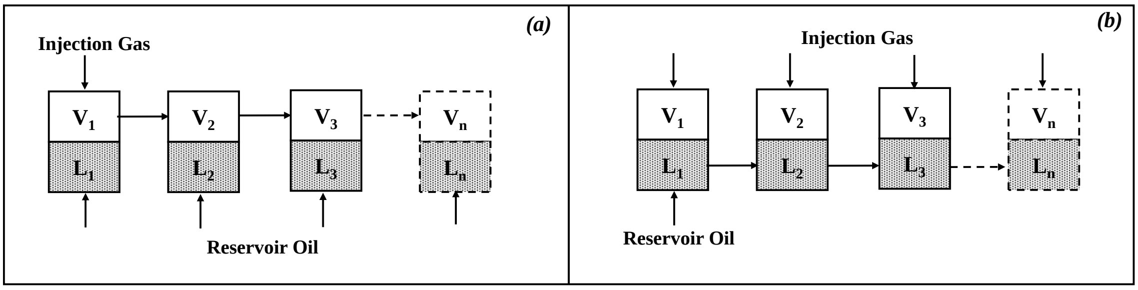

***Figure 4.8**. Flow diagram in FMC **(a)** and BMC **(b)** tests.*

For the studies examined here, methane was used as the injection gas and two series of multiple contact tests were performed on RFS-1: a three stages FMC and a four stages BMC. At each stage, the composition of the equilibrated phases was determined by direct sampling method and subsequent gas chromatography analysis, the density measured with a densitometer and the *IFT* between phases estimated with the selected plane method in pendant drops. Results of these studies are reported in Dandekar's thesis [302]. Single phase composition and physical properties of RFS-1 are listed in **Table 4.6**. Molecular weight (MW) and specific gravity (SG) of *pseudo*-components (C_6 to C_{20+}) were not originally reported in Dandekar's thesis [302] and thus, they were taken from the final report of the project [301] and are also listed in **Table 4.6**.

***Table 4.6**. Single phase composition and physical properties of RFS-1* [301,302].

Component	Mole%	MW / g.mol^{-1}	SG (at T = 288.7 K)
Methane	23.979		
Ethane	3.978		
Propane	5.647		
i-Butane	1.998		
n-Butane	4.118		
i-Pentane	2.090		
n-Pentane	2.890		
C_6	4.104	85	0.666
C_7	6.248	96	0.714
C_8	6.552	105	0.738
C_9	5.197	119	0.761
C_{10}	4.059	133	0.776
C_{11}	3.308	147	0.790
C_{12}	2.638	162	0.801
C_{13}	2.357	173	0.815
C_{14}	2.179	188	0.831
C_{15}	1.947	203	0.837
C_{16}	1.615	220	0.844
C_{17}	1.283	233	0.849
C_{18}	1.265	248	0.856
C_{19}	1.046	262	0.863
C_{20+}	11.503	483	0.947
Temperature / K		373	
Saturation Pressure (P^{Sat}) / MPa		9.41	
Saturation Density (ρ^{Sat}) / kg.m^{-3}		715	

The computation of the phase behaviour of a real petroleum fluid with classical cubic EoSs requires the estimation of the critical properties (T_c and P_c) and acentric factor (ω) of the *pseudo*-components as they are directly used in the calculation of the EoS parameters (**APPENDIX A**). A common approach for the characterisation of each PC (to estimate T_c, P_c and ω) is based on the use of correlations and from the knowledge of characteristic properties such as MW and SG. A review of the recommended correlations for the estimation of these data in petroleum fractions can be found in Riazi's book [303] and Whitson and Brulé's monograph [304].

In the particular case of the VT-PPR78 EoS, the required critical properties and acentric factor are also necessary for the calculation of the EoS volume corrections with **Equation 3.47** and the occurrence estimation of functional groups in each PC and, in turn, of the k_{ij} values (**Section 3.6**). Influence parameters calculated within the framework of the DGT and the LGT with **Equation 3.29** also depend on the values of T_c and ω of PCs. Therefore, the selection of the correlations to be used for the estimation of T_c, P_c and ω of PCs should be made with care.

The predictive capability of the VT-PPR78 EoS for describing the phase behaviour of RFS-1 was tested using four different estimated sets of T_c, P_c and ω for each PC. The different characterisation methods used as well as the calculated %AAD of predictions to measured saturation pressure and density of RFS-1 at T = 373 K are listed in **Table 4.7**. A graphical representation of the phase envelopes computed with the four sets is given in **Figure 4.9**. As shown in **Table 4.7**, all sets allowed a good prediction of the experimental saturation pressure with %AADs ranging from 1.9 to 5.0 %, whereas deviations to measured saturation density were slightly higher with %AADs ranging from 6.0 to 9.5 %. Such overprediction of the saturated density with all sets may be due to the fact that the correlation used for estimating volume corrections was originally regressed using *n*-alkanes up to *n*-hexadecane, among other lighter substances [191], and hence it may fail when applied to heavy petroleum fractions. In light of these results it was decided to use T_c, P_c and ω estimated with the characterisation methods of Set 1 and, as an attempt to improve the description of the density, volume corrections of PCs computed with **Equation 3.47** were calibrated to match the saturation density of RFS-1 by a factor of 0.1 (*i.e.*, $v_c = 0.1 \times v_c^{Miqueu}$).

***Table 4.7**. Prediction of saturations properties of RFS-1 at T = 373 K using the VT-PPR78 EoS and different methods for the estimation of T_c, P_c and ω of PCs.*

Set	**Method for T_c and P_c**	**Method for ω**	**VT-PPR78 EoS**			
			P^{Sat} / MPa	**%AAD**	**ρ^{Sat} / kg.m^{-3}**	**%AAD**
1	Riazi and Daubert	Edmister *	9.59	1.9	768.7	7.5
2	Lee and Kesler *	Lee and Kesler *	9.13	2.9	758.4	6.1
3	API Extended **	Lee and Kesler **	9.89	5.0	783.0	9.5
4	Twu **	Lee and Kesler **	9.65	2.6	757.8	6.0

[*] Normal boiling point calculated from MW and SG using Riazi and Daubert's correlation [305].

[**] Normal boiling point calculated from MW and SG using Riazi and Daubert's correlation [305] for MW ≤ 300 g.mol^{-1} and extended version [303] for MW > 300 g.mol^{-1}.

Sources: Riazi and Daubert [305]; Edmister [306]; Lee and Kesler [307,308]; API Extended [303]; Twu [309].

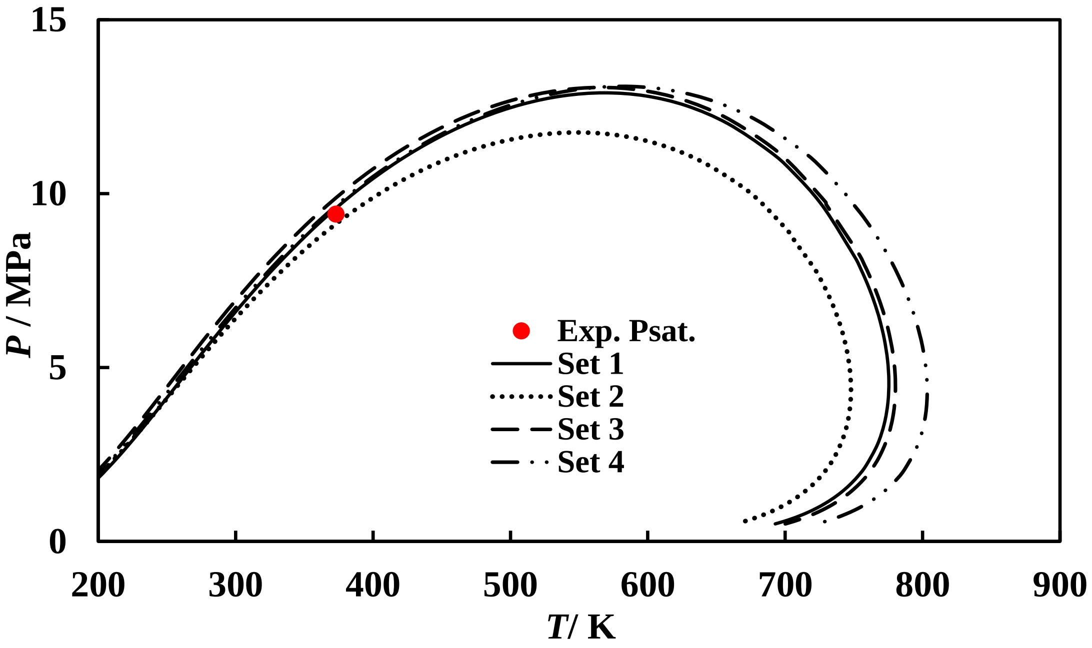

***Figure 4.9.** Predicted phase envelopes of RFS-1 using the VT-PPR78 EoS and different methods for the estimation of T_c, P_c and ω of PCs (**Table 4.7**).*

As depicted in **Figure 4.10** and **Figure 4.11**, by using the selected characterisation method (Set 1) and calibrated volumes corrections, the VT-PPR78 EoS allowed a good prediction of the composition and density of the equilibrated phases in both FMC and BMC tests. The largest deviations were obtained for the vapour phase in the 1st and 3rd stages of the BMC and FMC tests, respectively, where the EoS predicted a lighter phase, with a lower composition in intermediate (C_2-C_{10}) and heavy (C_{11+}) components, as depicted in **Figure 4.11**. These results may be related to the characterisation of the *pseudo*-components and, in turn, of the k_{ij}s computed through the group contribution approach. Furthermore, asphaltene precipitation was observed during the 2nd and 3rd stages of the FMC test [301], meaning that a third solid phase was formed and hence, the success of the two-phase model to predict correctly this change in behaviour (2 fluids + 1 solid phase) is limited. Nonetheless, these results stand out as very good, considering that no adjustable parameters were used in the prediction of the phase behaviour of the multiple contact studies, and they also confirm the adequacy of the method used for estimating the k_{ij}s. Overall, calculated %AAD of the predicted saturated density to experiments was of 1.0 and 3.1 % for the liquid and vapour phases in the BMC test, respectively, and of 1.2 and 5.9 % for liquid and vapour phases in the FMC test, respectively.

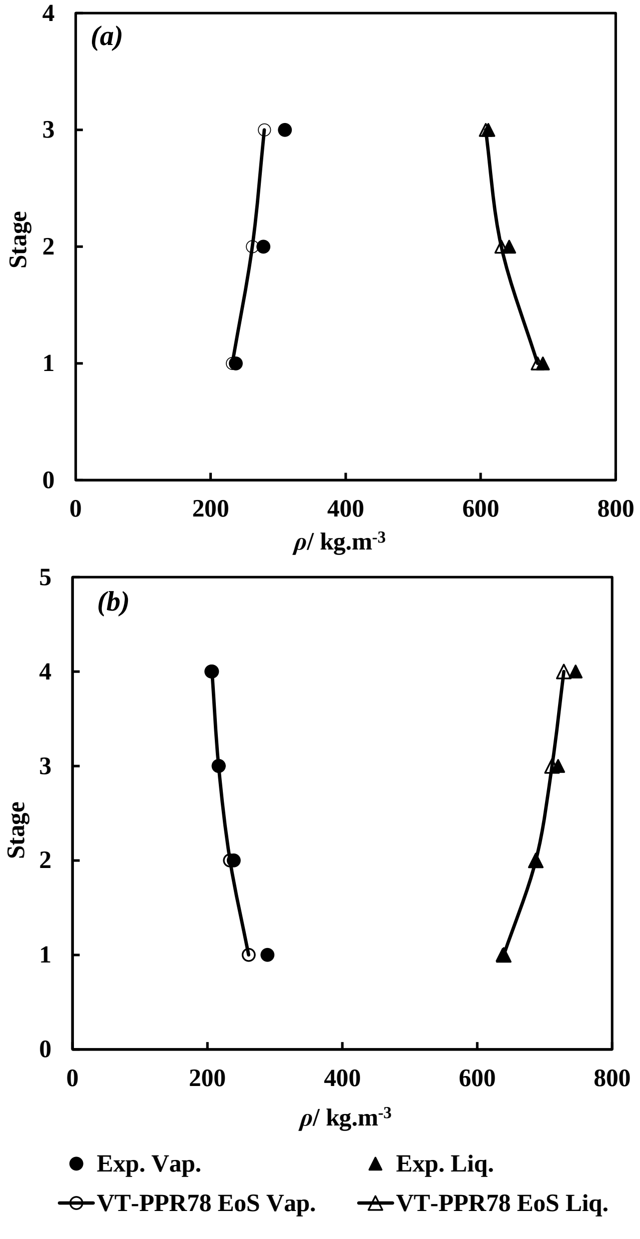

Figure 4.10. *Predicted and experimental phase densities of multiple contact studies performed on RFS-1 at T = 373 K and P = 34.58 MPa:* ***(a)*** *FMC and* ***(b)*** *BMC. Experimental data were taken from Dandekar's thesis* [302]. *Predictions were obtained with the VT-PPR78 EoS and using Set 1 (****Table 4.7****) and calibrated volume corrections.*

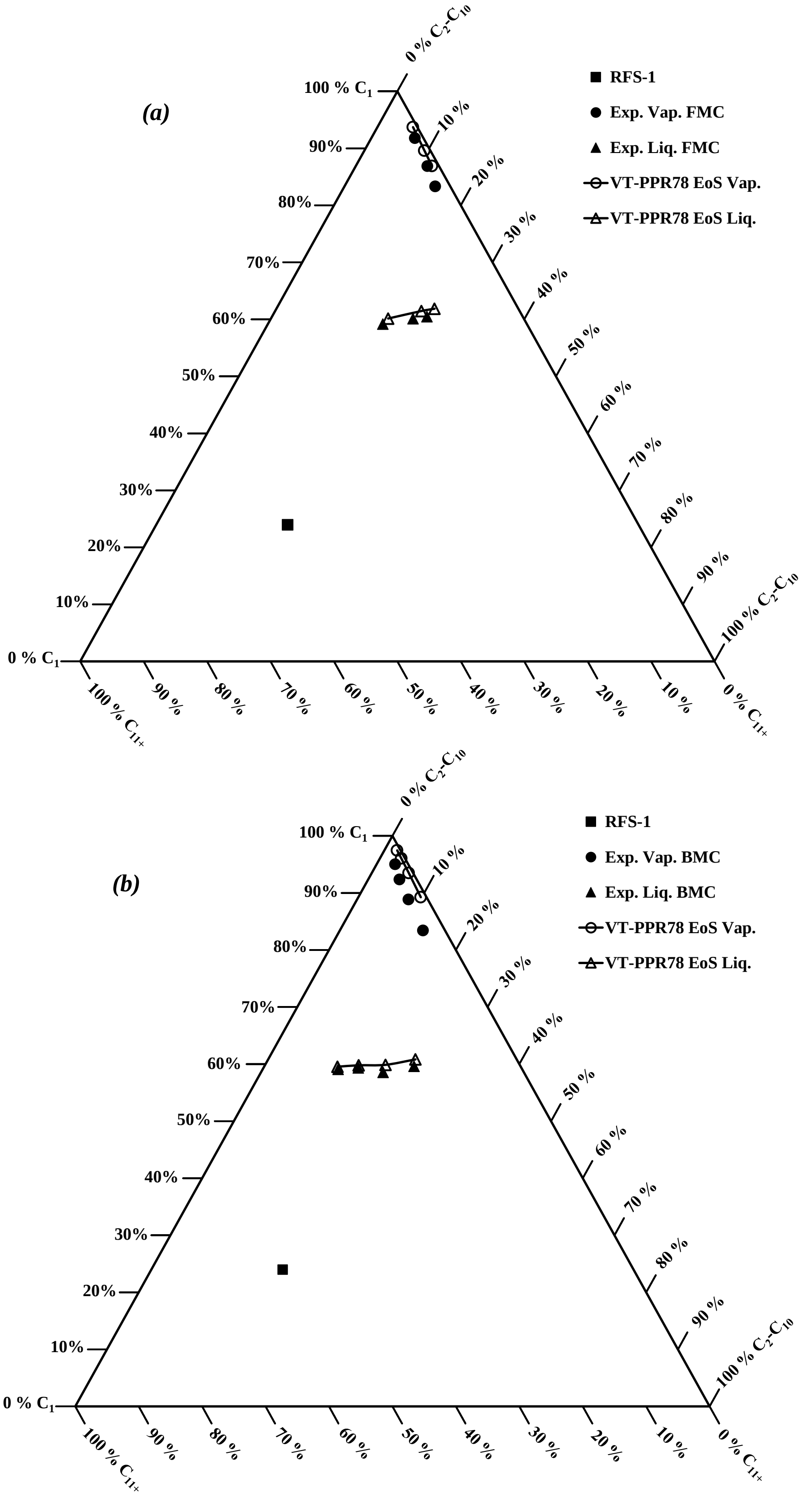

Figure 4.11. *Predicted and experimental phase compositions of multiple contact studies performed of RFS-1 at T = 373 K and P = 34.58 MPa:* ***(a)*** *FMC and* ***(b)*** *BMC. Experimental data were taken from Dandekar's thesis* [302]. *Predictions were obtained with the VT-PPR78 EoS and using Set 1 (****Table 4.7****) and calibrated volume corrections.*

Measured interfacial tensions between the vapour and liquid phases of the BMC and FMC tests are compared to predictions from the Parachor, the LGT and the DGT approaches in **Figure 4.12**. From this figure it can be seen that the Parachor underpredicted the *IFT* measured in both FMC and BMC tests for all stages with an overall %AAD of 49.4 and 62.2 %, respectively. Such under predictions are in line with the results obtained by Miqueu *et al.* [196] and Nilssen *et al.* [215] when predicting the interfacial tension of real petroleum mixtures with the Parachor method. Parachor values of well-defined components (methane through *n*-pentane) were estimated using **Equation 3.3**, whereas **Equations 3.5** and **3.6** were used for the Parachor values of PCs (C_6 through C_{20+}). The LGT also underpredicted the measured *IFT*, with deviations to experimental data higher than that of the Parachor (AAD% > 70 %). Although these mixtures did not include CO_2 in their composition, the results demonstrate the limitations of considering a linear density distribution of components in the interface and of using **Equation 3.45** as the mixing rule of influence parameters. In fact, computed *IFT* values with the LGT are rather sensitive to the selected mixing rule of the influence parameters. This is demonstrated also in **Figure 4.12** by plotting the *IFT* values computed with the LGT and using the mixing rule of influence parameters given by **Equation 3.44**. Such results make the selection of the mixing rule of influence parameters case dependent and hence, the predictive feature of the LGT is significantly reduced.

As shown in **Figure 4.12**, there are some important differences between measured and predicted *IFT* values with the DGT. In the case of the BMC test (**Figure 4.12*a***), the DGT allowed a good prediction of the *IFT* with a %AAD to experimental data of 11.9%. DGT prediction was also very close to measured *IFT* for the 1st stage of the FMC test (**Figure 4.12*b***). However, predicted values started to diverge from measured ones in the 2nd and 3rd stages of the FMC test, where asphaltene precipitation was noticed during experiments, resulting in an overall %AAD of 55.4%. The presence of asphaltene material will not only change the phase behaviour of the system [310], but it will also affect the *IFT* between the vapour and liquid phases. In fact, recently Doryani *et al.* [311] investigated the impact of asphaltene on the *IFT* between methane and synthetic oil, and observed a profound change of the *IFT* values when in the presence of these solids, in particular at high pressures. Asphaltene precipitation and its impact on the phase behaviour and *IFT* is an interesting subject which is beyond the scope of this work.

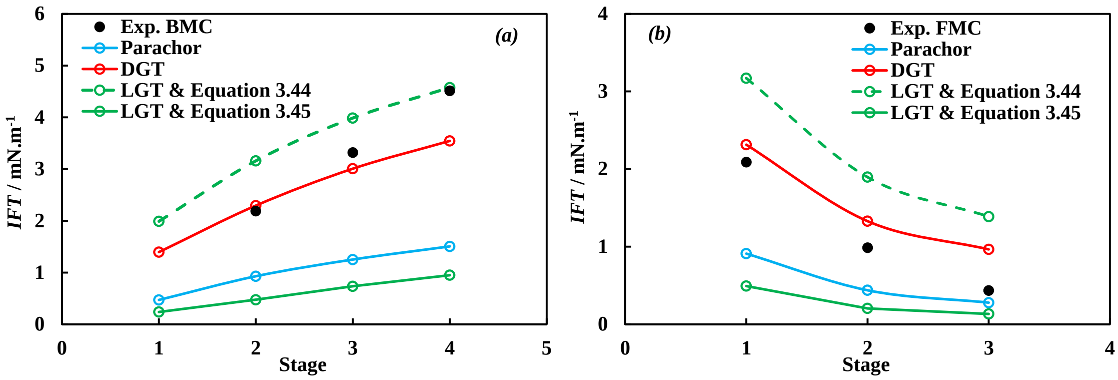

Figure 4.12. *Predicted and experimental IFT of multiple contact studies performed on RFS-1 at T = 373 K and P = 34.58 MPa. Experimental data were taken from Dandekar's thesis* [302]. *Predictions were obtained with the VT-PPR78 EoS in combination with the Parachor, LGT and DGT models.*

Another important aspect to consider is related to the applicability of the correlation used to estimate the influence parameter of PCs, in particular of the heavy end. In the work of Miqueu *et al.* [196], DGT predictions obtained for five petroleum mixtures using **Equation 3.29** for the influence parameters appeared to be in good agreement with experimental *IFT* data. Although no limitations in the use of this correlation for PCs were reported by the authors, it is important to point out that **Equation 3.29** was regressed using pure substances only, with *n*-hexadecane as the heaviest component considered. Therefore, to test the sensitivity of *IFT* values computed with the DGT and LGT to the influence parameter of the heaviest fraction (C_{20+}), predictions with these models for the BMC test were repeated using a value for the influence parameter of C_{20+} adjusted to -30, -15, 15 and 30 % of the value estimated using Miqueu's correlation [191]. As indicated in **Figure 4.13**, predictions with the LGT and DGT are to some extent sensitive to the value of the influence parameter of C_{20+}. In all cases, the increase or decrease of the influence parameter of the heavy end resulted in a shift of predictions to higher or lower *IFT* values. As a result, deviations of predictions to experimental *IFT* may be due to an underestimation/overestimation of this parameter. Indeed, as way of improving *IFT* predictions of real oil and gas condensate systems with the LGT in combination with the SRK72 EoS, Zuo and Stenby [266] presented an expression for the influence parameters of PCs regressed against experimental *IFT* data of cuts from a selected crude oil. Additionally, experimental uncertainties must also be taken into consideration. Dandekar [302] estimated an overall uncertainty of 1.9% for these *IFT* measurements by accounting the impact of uncertainties in both density measurements and characteristic drop dimensions; however, due to the complexity of both the experimental setup and studied fluids, uncertainties that arise from sampling as well as the repeatability of measurements may also lead to higher experimental uncertainties. Nevertheless, all things considered, it is clear that the predictions from the DGT are superior to that of the LGT and the Parachor.

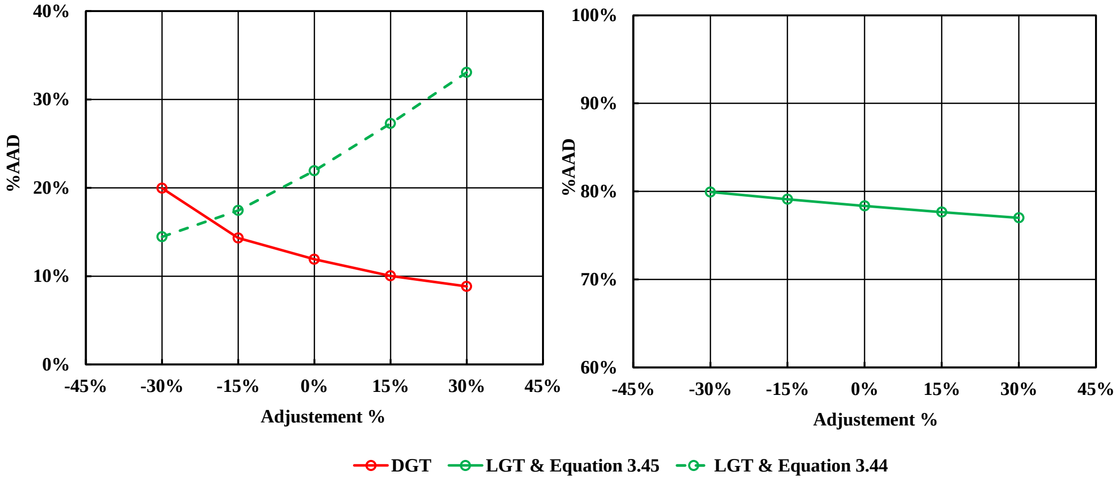

Figure 4.13. *Percentage average absolute deviations (%AAD) of predictions with the DGT and LGT models to measured IFT data of the BMC test as function of the adjustment of the influence parameter of the heavy end (*C_{20+}*).*

All predictions described above were obtained using full component phase behaviour and *IFT* models, *i.e.*, all 22 components and *pseudo* components listed in **Table 4.6** were considered during the calculations. A common practice in reservoir and engineering calculations involves the lumping (or grouping) of components as calculation time generally increases with the number of groups (or components = N_{comp}); particularly for the DGT, where a minimum of $N_{comp} - 1$ equations needs to be solved at each grid point across the interface, as explained in **Section 3.4.3**. Aiming at testing the impact of different lumping schemes, the phase behaviour and *IFT* predictions for the BMC test were repeated using different lumping schemes, as listed in **Table 4.8**. For each scheme, critical properties, acentric factor, volume correction, Parachor and influence parameter of groups were calculated as weight means of the corresponding property of the individual component fractions. Subsequently, k_{ij}s were recalculated for each group based on the *new* T_c, P_c and ω. As depicted in **Figure 4.14**, the number of groups can be reduced up to 5, within the lumping schemes considered, with no significant overall variation (< 4%) in the predictions of the phase densities with the VT-PPR78 EoS and of the *IFT* with the LGT & **Equation 3.44** as well as with the DGT. This in agreement with the modelling results of Miqueu *et al.* [196] with the DGT. On the other hand, the Parachor and the LGT & **Equation 3.45** appear to be more sensitive to the lumping procedures. It is worth noticing that such lumping procedures resulted into a significant reduction of calculation time, in particular with the DGT. As an example, *IFT* calculations considering full component scheme with the DGT showed an average timespan of 5 min, whereas the same calculations considering lumping scheme 4 (**Table 4.8**) were obtained in approximately 0.5 s. These results, together with its superior predictive capability, confirm the suitability of the DGT for modelling real petroleum mixtures.

***Table 4.8**. Lumping schemes for RFS-1.*

Scheme 1	Scheme 2	Scheme 3	Scheme 4	Scheme 5
Methane	Methane	Methane	Methane	Methane
Ethane	Ethane	Ethane − *n*-Pentane	Ethane − *n*-Pentane	Ethane − *n*-Pentane
Propane	Propane	$C_6 - C_9$	$C_6 - C_{14}$	$C_6 - C_{14}$
i-Butane	*i*-Butane − *n*-Pentane	$C_{10} - C_{14}$	$C_{15} - C_{19}$	C_{15+}
n-Butane	$C_6 - C_9$	$C_{15} - C_{19}$	C_{20+}	
i-Pentane	$C_{10} - C_{14}$	C_{20+}		
n-Pentane	$C_{15} - C_{19}$			
$C_6 - C_9$	C_{20+}			
$C_{10} - C_{14}$				
$C_{15} - C_{19}$				
C_{20+}				
11 groups	8 groups	6 groups	5 groups	4 groups

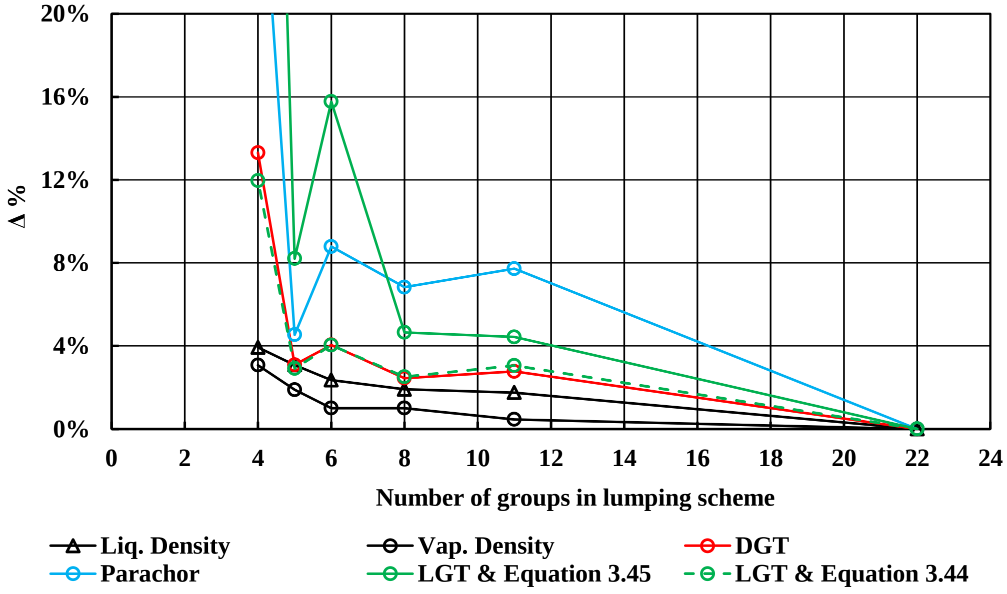

***Figure 4.14.** Overall absolute variations (Δ%) of predictions of the BMC test as function of the number of groups considered in each lumping scheme for RFS-1. Overall absolute variations were calculated relative to predictions obtained with the full compositional phase behaviour and IFT models (i.e., considering all components and pseudo-components in **Table 4.8**).*

4.5 Microstructure of Interfaces

One key advantage of the DGT over the other modelling approaches considered in this work is that it provides valuable information about the molecular distribution of components across the interface. As an example, the density profiles and adsorption isotherms obtained with the DGT are plotted in **Figure 4.15** and **Figure 4.16** at T = 344 K for gas + *n*-decane systems. The profiles show an enrichment of the interface in gas molecules, as reflected by the observation of a peak in the density profiles of methane, carbon dioxide and nitrogen (**Figure 4.15**). This is in agreement with other DGT studies [48,54,61,69,192,197,214,256,300,312,313] and Molecular Dynamic simulation and Monte Carlo approaches [48,74,197,227]. Additionally, this relative enrichment seems to decrease with increasing pressure as the relative height of the peaks of all three light components decreases and moves towards the liquid surface and the interface thickness is enlarged. These results are supported by the adsorption isotherms plotted in **Figure 4.16** and calculated via **Equation 3.41** together with experimental *IFT* data from literature [47] and measured in this work. Accordingly, the adsorption of gas molecules at the interface increases with pressure and reaches a maximum for all three gases, suggesting a saturation limit for the relative adsorption of gas molecules, as also concluded by others [48,54,197,254]. It is worth mentioning that similar results were obtained for the multicomponent mixtures, with an enrichment of the interface in light components.

Furthermore, the slope in the adsorption curves is more pronounced for CO_2 + *n*-decane when compared to that of the CH_4 + *n*-decane and N_2 + *n*-decane systems. This behaviour can help explaining the high pressure dependence of the *IFT* of hydrocarbon systems containing CO_2, in which the large adsorption of CO_2 leads to a higher reduction of the *IFT*. These results also demonstrate the inadequacy of the approximation of the mixture influence parameter given by **Equation 3.45,** together with the linear density assumption under the LGT framework, and explain the poor *IFT* predictions obtained with this model for systems containing carbon dioxide.

In summary, the good agreement between both theoretical and experimental approaches for the calculation of Γ_{12} at low and moderate pressures validates to some extent the density profiles calculated with the DGT approach. The results also confirm the capability of the model to provide a perspective of the distribution of species across the interfacial region and its impact on the *IFT*. However, for pressures near the critical point, the theoretical approach yields values significantly different from those obtained with

Equation 3.41 as depicted in **Figure 4.16**. Deviations between the two approaches are related in part to large uncertainties in the calculation of the derivative $(\partial IFT/\partial P)_T$ in **Equation 3.41** and in limitations of the phase behaviour model near the critical point.

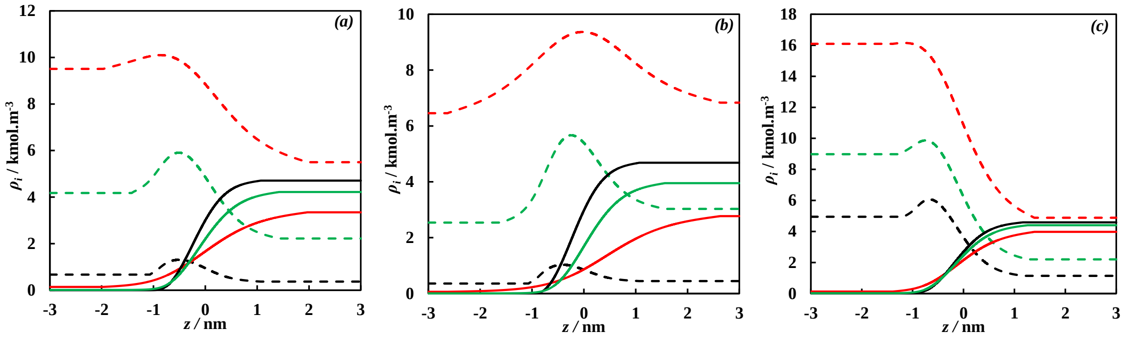

Figure 4.15. Density profiles across the interface as function of pressure computed with the DGT ($\beta_{ij} = 0$) + VT-PPR78 EoS approach for ***(a)*** *n-decane + CH_4,* ***(b)*** *n-decane + CO_2 and* ***(c)*** *n-decane + N_2 at T = 343 K: n-decane (solid lines) and gas (dashed lines).* ***(a)*** *P = 1.87 MPa (black), 10.69 MPa (green) and 24.43 MPa (red).* ***(b)*** *P = 0.99 MPa (black), 5.69 MPa (green) and 10.43 MPa (red).* ***(c)*** *P = 14.50 MPa (black), 28.29 MPa (green) and 64.47 MPa (red).*

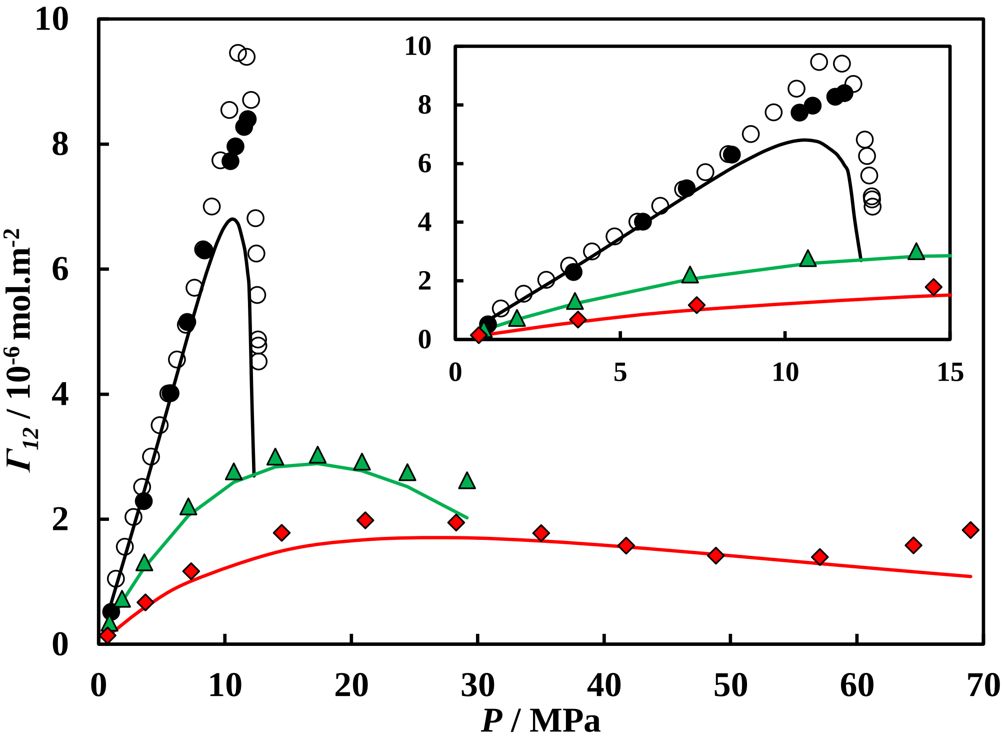

Figure 4.16. Gas adsorption (Γ_{12})−pressure diagram of n-decane + CH_4 (green), n-decane + CO_2 (black) and n-decane + N_2 (red) at T = 343 K. Symbols represent the gas adsorption calculated with ***Equation 3.41*** *and experimental IFT data measured in this work (solid symbols) and from literature [47] (empty symbols). Solid lines represent the gas adsorption calculated with* ***Equation 3.38*** *and density profiles predicted with the DGT ($\beta_{ij} = 0$) + VT-PPR78 EoS approach.*

4.6 Summary

Interfacial tension and saturated density data of three gas + *n*-decane binary mixtures as well as of three multicomponent hydrocarbon systems have been measured over a broad range of conditions (temperatures up to 442 K and pressures up to 69 MPa). Saturated density data were correlated with the PR78 EoS and combined with measured capillary constants to estimate the *IFT* of the studied systems. Measurements performed here for the binary systems were found to be in good agreement with selected literature data, validating both the methodology and the experimental procedure followed. The results showed that generally the *IFT* decreased with increasing temperatures and pressures; a crossover pressure region was observed between isotherms for the CO_2 + *n*-decane system. Moreover, for systems containing CO_2, low interfacial values were achieved at significantly lower pressures, readily showing that CO_2 is an effective agent in the reduction of interfacial forces and thus, in increasing oil recovery. Both density and *IFT* measurements complement the experimental gap found in literature and extend these measurements to reservoir conditions.

The coupling of the VT-PPR78 EoS with the Parachor, the LGT and the DGT approaches was applied and their predictive capabilities evaluated by comparison with density and *IFT* data measured in this work and from literature. The evaluated systems included binary and multicomponent synthetic hydrocarbon systems as well as one real petroleum fluid. The phase behaviour model showed very good capabilities for predicting the effect of pressure and temperature on the equilibrium phase compositions and densities of the hydrocarbon systems, considering that no adjustable parameters to mixtures were used. The poorest predictions were obtained close to the critical region, where classical cubic EoSs generally fail. Furthermore, some deviations were also observed between predicted and measured phase behaviour data of the 2nd and 3rd stages of the forward multiple contact test performed on the real petroleum fluid; asphaltene precipitation, noticed during experiments, has been pointed out as the potential cause. In general, the best *IFT* predictions were obtained with the DGT model with an overall %AAD between 4.9 and 8.3 % to data of binary systems, and between 1.4 and 8.3 % to multicomponent systems data at low and moderate pressures (*IFT* > $1.5 \mathrm{mN.m^{-1}}$). In the case of the multiple contact tests, the DGT allowed predictions of the *IFT* of the BMC test with a %AAD of 11.9% to experimental data, whereas for the FMC test, a significant overprediction of the *IFT* was obtained in the stages where precipitation of asphaltene occurred, resulting in a

%AAD of 55.4 %. Predictions with the LGT showed to be very sensitive to the selected influence parameters mixing rule and, for systems with high content in CO_2 the Parachor method performed better than the LGT. For low interfacial tension values (*IFT* < 1.5 $mN.m^{-1}$), all *IFT* models considered deviated significantly to measured data. This can be attributed in part to the experimental uncertainties in this region, but also to the deviations of the VT-PPR78 EoS to the bulk properties of the equilibrium phases. Lastly, an investigation of the impact of different grouping schemes showed that phase behaviour and *IFT* predictions of the BMC test with the VT-PPR78 EoS + DGT approach remained practically unaffected when five or more groups were used in the fluid description. The use of such lumping schemes resulted in a significant reduction of the computation time, specifically for the DGT, which makes this model a good candidate for industrial applications and reservoir engineering calculations.

The DGT, through the calculation of the distribution of components in the interfacial region, showed a local enrichment and relative adsorption of gas molecules in the interfacial region, which increased with pressure and reached a saturation limit. This behaviour was more pronounced for CO_2 which seems to explain the high pressure dependence of the *IFT* values of CO_2 + *n*-alkane systems when compared to that of N_2 + *n*-alkane and CH_4 + *n*-alkane systems. These results may also explain the large negative deviations obtained with the LGT for systems with CO_2, in which the assumption of a linear density distribution of components in the interfacial region proved inadequate. This show the need for adjusting binary interaction coefficients within the LGT framework as a way of improving computed *IFT* values. Altogether, the good agreement observed between calculated and experimental Gibbs adsorption isotherms confirms the adequacy of the DGT for describing the complex microstructures that arise from fluid interfaces and their impact on the *IFT* values.

CHAPTER 5 – INTERFACIAL TENSION OF AQUEOUS SYSTEMS

5.1 Introduction

Water is ubiquitously present in many industrial processes and often in contact with a multitude of fluid and/or solid phases. In the context of reservoir engineering, water is always present in the pore spaces of reservoir rocks (either as residual or injected water), with a characteristic salinity. In this sense, accurate knowledge of the interfacial tension between water/brine and concurrent reservoir fluids, such as liquid hydrocarbons and common gases (CO_2, CH_4 and N_2), is essential not only for the deployment of enhanced oil recovery schemes, but also for the safe geological storage of CO_2, as briefly explained in **CHAPTER 1**. Therefore, this chapter focusses on addressing some discrepancies and filling in some experimental gaps found in literature for the *IFT* of systems composed of carbon dioxide and water (**Section 1.3.2**) as well as testing the capabilities of models for describing the *IFT* of aqueous systems at conditions representative of those in underground formations.

First, the saturated phase densities of the $CO_2 + H_2O$ system were investigated with a vibrating U-tube densitometer and the results were compared to both selected literature data and pure component density data. A correlation, for accurately estimating the density of the CO_2-saturated liquid phase at pressure and temperature conditions of interest, was regressed against experimental data. Then, the ADSA method and the setup based on the Pendant Drop technique (**Section 2.3**) were used for investigating CO_2−H_2O *IFT* at temperatures ranging from 298 to 469 K and pressures up to 69 MPa. Additionally, the impact of small quantities of sparingly soluble gases in water as well as that of water salinity was investigated. This was done by measuring the *IFT* between water and two CO_2-rich mixtures (CO_2 composition > 90 mole%) and between pure CO_2 and NaCl brines of molalities $m = 0.98$ and 1.98 mol.kg^{-1}, for temperatures and pressures up to 423 K and 69 MPa, respectively. Furthermore, the implications of these studies on the geological storage of CO_2, in terms of capillary-sealing efficiency of the caprock, were also discussed.

The capabilities of the DGT for modelling the *IFT* of aqueous systems were investigated by comparison of the computed values with those of the LGT, Parachor and Sutton's correlation as well as with experimental data measured in the present work and gathered from literature. *IFT* models were coupled with the CPA EoS for a correct description of the bulk phase properties and the energy associated with the interface. The systems tested included binary and multicomponent aqueous mixtures composed of CO_2, CH_4 and N_2 as well as liquid hydrocarbons or salts. Conditions at which one aqueous phase and two fluid phases were simultaneously present were also studied. Finally, the density profiles computed with the DGT were analysed and the impact of the microstructure of the interface on the *IFT* was discussed.

5.2 Experimental Procedure

5.2.1 Materials and sample preparation

The specification and sources of the chemicals used in the experiments described in this chapter are summarized in **Table 5.1**. Toluene and *n*-heptane were used for cleaning purposes only. Two certified CO_2-rich mixtures (MIX-4 and MIX-5), with compositions given in **Table 5.2**, were supplied by BOC. The water used has better specifications than double-distilled water (electrical conductivity < 0.02 µS/cm at T = 298 K). Two NaCl aqueous solutions of molalities 0.98 and 1.98 mol.kg^{-1} were prepared gravimetrically by adding the salt (dried in an oven at T = 373 K for 24h) to water. The mass of salt was determined using a Mettler Toledo balance (model PB3002) with a resolution of 0.001 g and hence, the relative uncertainty in the molality of the NaCl aqueous solutions is taken equal to the purity of the salt (0.5%). The water and brines were degassed by means of an ultra-sonic bath during 30 min before they were transferred to the hand pump **PD.C** (**Figures 2.7** and **2.10**).

***Table 5.1**. Suppliers and specification as stated by the supplier of the materials used in this work.*

Chemical name	Supplier	Mass fraction purity	Chemical analysis
Carbon dioxide	BOC	0.99995	
Toluene	Fischer Scientific	>0.995	
n-Heptane	RathBurn Chemicals	>0.99	
Sodium Chloride	Fischer Scientific	>0.995	
Water	Sigma-Aldrich		≤0.01 ppm silicate ≤0.4 ppm Cl^- ≤0.4 ppm NO_3^- ≤1.0 ppm PO_4^{3-} ≤1.0 ppm SO_4^{2-} ≤0.01 ppm heavy metals (as Pb)

***Table 5.2**. Composition of CO_2-rich mixtures MIX-4 and MIX-5 as prepared and certified by BOC.*

Chemical Name	MIX-4 (mole%)	MIX-5 (mole%)
Nitrogen	2.028 ± 0.041	5.05± 0.04
Hydrogen	0.605 ± 0.012	
Oxygen	0.783 ± 0.016	3.07± 0.10
Argon	0.611 ± 0.012	2.05 ± 0.06
Carbon dioxide	Balance (95.97)	Balance (89.93)

5.2.2 Measuring procedure

Each piece of the pendant drop setup including glassware, hand pump, sample cylinders and high-pressure cell were extensively cleaned by using alternately toluene and *n*-heptane. After being drained, deionized water was circulated through all components and the system was dried with compressed air. Once the entire setup had been tested for leaks, it was placed under vacuum at T = 333 K. This procedure was repeated before loading a new system into the setup and helped to minimise the presence of surfactant-like impurities during the experiments. The desired temperature was set and let to stabilise overnight.

The view cell was filled with either pure CO_2 or CO_2-rich mixtures (MIX-4 and MIX-5) through the bottom or the side valve of the PD cell (*i.e.*, **PD_2** in **Figure 2.7** or **PD_4** in **Figure 2.10**, respectively) and the desire pressure set by means of the hydraulic pump connected to the gas sample cylinder. Before the start of experiments, water/brine was introduced inside the view cell until a liquid phase was visible on the bottom of the cell and the system was left to reach equilibrium, *i.e.*, for the CO_2-rich phase to be saturated with H_2O. Thereafter, water/brine drops were created by opening the top valve **PD_1** and turning the hand pump. For each pressure and temperature state, valves **PD_1**, **PD_2** and **PD_4** were kept closed and a minimum of 3 consecutive drops were recorded during at least 900s and the software was set to capture pictures every 10 seconds. The *IFT* data point was obtained by taking the average value calculated from pictures taken within the 300th and 600th second. According to mass transfer models [91] and experimental observation this interval is sufficient for the system to reach equilibrium by diffusion mechanisms alone and to obtain a steady value for the *IFT*. As an example, the *IFT* versus time for isotherms at T = 298, 374 and 469 K is depicted in **Figure 5.1**.

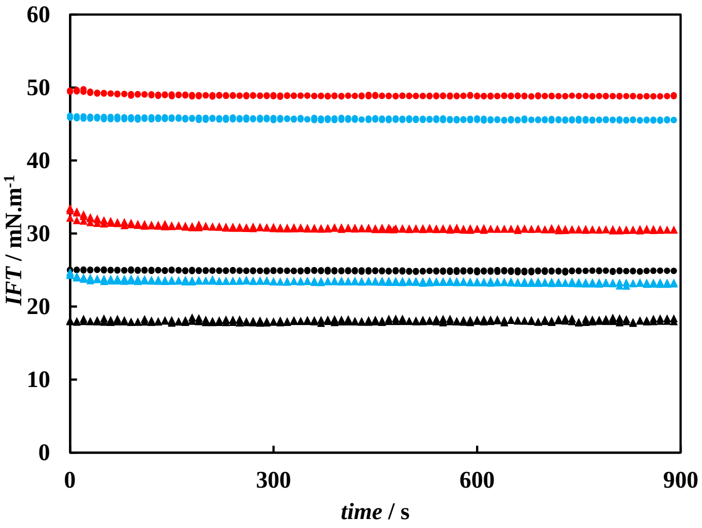

Figure 5.1. *IFT-time diagram of the CO_2 + H_2O system at T = 298 K: P = 3.68 MPa (●) and 10.63 MPa (▲); at T = 374 K: P = 5.60 MPa (●) and 69.12 MPa (▲) and at T = 469 K: P = 14.91 MPa (●) and 29.97 MPa (▲).*

The saturated phase densities of the CO_2 + water system were measured by loading the binary mixture into the thermostated equilibrium cell from the CO_2 and H_2O sample vessels, as depicted in **Figure 2.9**. The desired pressure was set by controlling the amount of fluids injected. The density values of the CO_2-saturated liquid were determined by purging the mixture at constant pressure and flowing this phase through the densitometer. A magnetic stirrer positioned at the bottom of the cell together with a high ratio of volume of system to volume of purge ($V_{system}/V_{purge} \approx 500cm^3/2.2cm^3$) helped to ensure that equilibrium conditions were maintained throughout measurements. The density of the water-saturated CO_2 phase was also studied by turning the equilibrium cell vertically and repeating the procedure described above. On the other hand, in the case of the systems including water and MIX-4 or MIX-5, the density of the saturated water-rich phase was measured in-situ for each pressure and temperature state by transferring this phase from the pendant drop cell to the vibrating U-tube densitometer at constant pressure (**Figure 2.10**).

In the same way, the measured period of vibration can be related to the density of the fluid using **Equation 4.1**. The densitometer parameters were calibrated against pure densities of water and carbon dioxide [99] for each pressure and temperature of interest. This calibration procedure allowed a reproduction of the density of pure H_2O and CO_2 with a %AAD to reference data [99] of 0.01 and 0.41 %, respectively. Standard uncertainties in pressure ($u(P)$ = 0.04 MPa) and temperature ($u(T)$ = 0.1 K) can introduce significant variations on the density measurements, particularly for CO_2 in the vicinity of the phase transition and critical point. Therefore, taking into account all uncertainties and from experimental observation of dispersion of measurements, the estimated combined expanded uncertainties are $U_c(\rho)$ = 0.7 kg.m^{-3} and $U_c(\rho)$ = 6.7 kg.m^{-3} for the density measurements in the water- and carbon dioxide-rich phases, respectively, with a level of confidence of 0.95 within the pressure and temperature range studied with the setup illustrated in **Figure 2.9**. On the other hand, a slightly higher dispersion of density values of the water-rich phase was observed when using the setup depicted in **Figure 2.10**; the estimated combined expanded uncertainty of in-situ density measurements is $U_c(\rho)$ = 3.0 kg.m^{-3}, with a level of confidence of 0.95.

5.3 Experimental Results

5.3.1 *CO_2 and H_2O*

Equilibrium densities: The saturated densities of the CO_2 + H_2O system were measured at T = 298, 333, 373, 393 and 423 K using the experimental setup illustrated in **Figure 2.9**, and at T = 323 K using the setup depicted in **Figure 2.10**, and for pressures up to 69 MPa. The results are listed in **Tables D.7** and **D.8** in **APPENDIX D** and plotted in **Figure 5.2** along with selected data available in literature [87,93,95–97,314] and pure component densities [99].

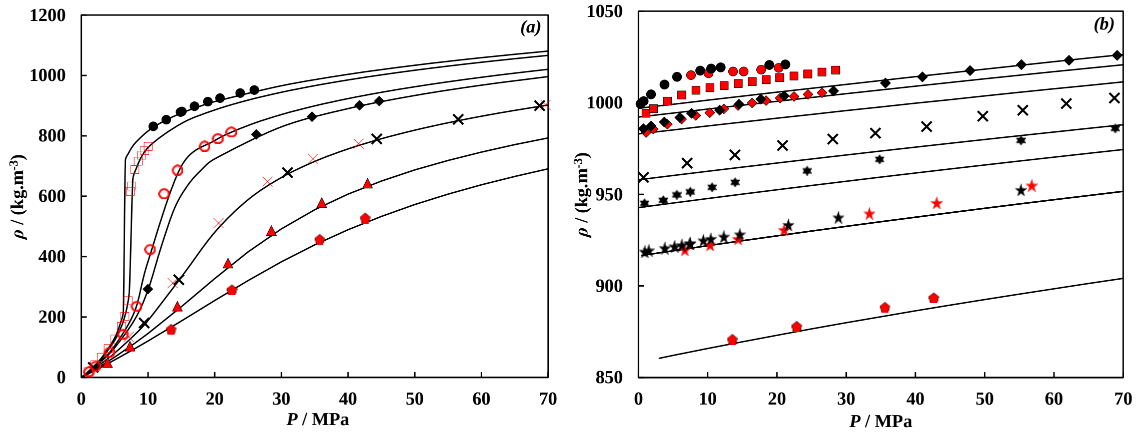

Figure 5.2*. Density−pressure diagrams of* ***(a)*** *water-saturated and* ***(b)*** *CO_2-saturated phases of the CO_2 + H_2O system. Black symbols represent the experimental data measured in this work: T = 298 K (●), 333 K (◆), 373 K (✕), 393 K (✱) and 423 K (★). Red symbols represent literature data: King et al.* [314], *T = 298 K (●); Yaginuma et al.* [95], *T = 304 K (□); Hebach et al.* [96], *T = 313 K (■) and 333 K (◆); Kvamme et al.* [87], *T = 323 K (○); Tabasinejad et al.* [97], *T = 423 K (▲); Shariat et al.* [93], *T = 373 K (✕), 423 K (★) and 477 K (⬟). Solid lines represent pure density of* ***(a)*** *CO_2 and* ***(b)*** *water at pertinent temperatures obtained from REFPROP* [99]*. Data from Shariat et al.* [93] *were read from graphs.*

As can be seen in **Figure 5.2**, for all isotherms the density of the water-saturated CO_2 phase is very close to that of pure CO_2 within the experimental uncertainty. This is also in agreement with what was already reported by several authors in literature [7,87,93,96,97,314] and hence, the density of this phase can be fairly approximated to that of pure CO_2 [99]. On the other hand, the increase in density of the CO_2-saturated water phase with pressure exceeds that of pure water for all isotherms investigated and it is in good agreement with the data gathered from open literature [93,96,97,314]. This increase can be divided into two regions: whether CO_2 is gaseous or liquefied/supercritical. The density increase in the CO_2-saturated water phases is more pronounced when in contact with gaseous CO_2 and moderate for liquefied/supercritical CO_2, and must be associated with the well-known decrease in solubility of CO_2 molecules in the water-rich phase [315]. The deviation between the pure and measured CO_2-saturated water densities is larger at low temperatures and high pressures, with a maximum relative density difference of 1.7% (17 kg.m^{-3}) obtained at T = 298.5 K and P = 11.89 MPa.

Despite the overall low relative deviation observed between the pure and CO_2-saturated water densities in **Figure 5.2**, the density approximation of this phase to that of pure water can result in significantly different overall density difference (*i.e.*, $\Delta\rho$) between the two equilibrated fluids for interfacial tension estimations (**Equation 2.9**). In particular, this is the case close to the density inversion conditions where the lowest values for $\Delta\rho$ are obtained. The approximation of the density of the CO_2-saturated water phase to that of pure water would result in lower values for $\Delta\rho$ and therefore, in an underestimation of the *IFT* values. This behaviour has also been reported by Chiquet *et al.* [7] who estimated a $\Delta\rho$ up to 1.7 times smaller than the one obtained from experiments when pure density assumption for the equilibrated phases is used at T = 308 K and P = 45 MPa.

In order to estimate the density of the CO_2-saturated water phase at pertinent experimental conditions, the correlation proposed by Hebach *et al.* [96] was extended in this work to higher temperatures and pressures by using saturated phase density data measured here and available in literature, as listed in **Table 5.3**. Accordingly, this correlation is expressed as follows:

$$\rho_{H_2O}^{Correlation} = a_0 + a_1P + a_2T + a_3P^2 + a_4T^2 + a_5TP + a_6P^3 + a_7T^2P + a_8P^2T \qquad \textbf{5.1}$$

where a_0 through a_8 are the regressed parameters listed in **Table 5.4,** and P and T are in MPa and K, respectively. The regression displays a low relative deviation to the experimental data as depicted in **Figure 5.3** and ensures calculated densities values for the CO_2-saturated water phase with a quality of reproduction above 99.60 % and a %AAD of 0.11 % in the range studied. The density values of the water-saturated CO_2 phase were assumed to be equal to that of pure CO_2 under the same P and T conditions, without significant loss of accuracy in the estimation of the interfacial tension values. As an example, the density difference data measured by Kvamme *et al.* [87] at $T = 323$ K were reproduced with a %AAD of 0.15 %, confirming to some extent the validity of the selected method for estimating the density difference between the phases of the H_2O + CO_2 system.

***Table 5.3**. Experimental data used in the regression of parameters in **Equation 5.1**. Data from Shariat et al.* [93] *were read from graphs.*

Source	*P* /MPa	*T* /K	Data points
King *et al.* [314]	6.6 to 21.8	293,298	16
Yaginuma *et al.* [95]	1 to 10.0	304	15
Hebach *et al.* [96]	1.1 to 28.6	293, 313, 333	44
Kvamme *et al.* [87]	1.1 to 22.5	322	11
Chiquet *et al.* [7]	5.0 to 45.0	308, 323, 343, 363, 383	33
Shariat *et al.* [93]	6.9 to 75.3	323, 422, 477	18
This work	0.73 to 69.1	298, 333, 373, 393, 423	61
		Total	**198**

***Table 5.4**. Regressed parameters in **Equation 5.1**.*

Parameter	$\rho_{CO_2}^{pure} \leq 467.8$ kg.m^{-3}	$\rho_{CO_2}^{pure} > 467.8$ kg.m^{-3}
a_0 / kg.m^{-3}	1025.0	1018.4
a_1/ kg.m^{-3}.MPa^{-1}	2.7452	3.5183×10^{-1}
a_2/ kg.m^{-3}.K^{-1}	3.1077×10^{-1}	4.4627×10^{-1}
a_3/ kg.m^{-3}.MPa^{-2}	-3.0731×10^{-1}	2.3878×10^{-3}
a_4/ kg.m^{-3}.K^{-2}	-1.3197×10^{-3}	-1.5628×10^{-3}
a_5/ kg.m^{-3}.MPa^{-1}.K^{-1}	9.6245×10^{-3}	0
a_6/ kg.m^{-3}.MPa^{-3}	-9.8222×10^{-4}	0
a_7/ kg.m^{-3}.MPa^{-1}.K^{-2}	-3.6286×10^{-5}	0
a_8/ kg.m^{-3}.MPa^{-2}.K^{-1}	7.9860×10^{-4}	0

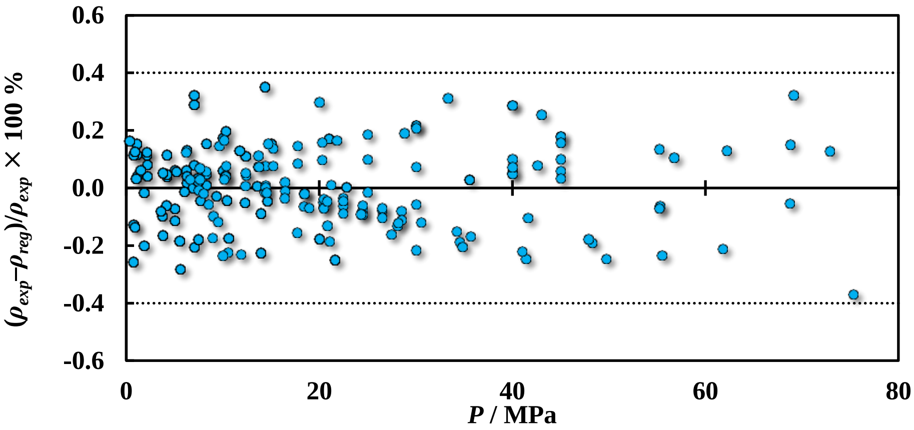

Figure 5.3. *Relative deviation between densities of the CO_2-saturated water phase estimated from* ***Equation 5.1*** *and experimental data from studies listed in* ***Table 5.3****.*

Interfacial tensions: The interfacial tension of the CO_2 + H_2O system was measured for temperatures ranging from 298 to 469 K and pressures from 0.34 to 69.14 MPa. The results are listed in **Table E.7** in **APPENDIX E**.

Although interfacial tension data for the CO_2 + H_2O system are widely available in literature [7,76–94], only the studies of Park *et al.* [84], Kvamme *et al.* [87], Chiquet *et al.* [7], Bachu and Bennion [89], Chalbaud *et al.* [90], Bikkina *et al.* [92] and Shariat *et al.* [93] have considered the effect of CO_2 dissolution on the density of the aqueous phase and taken the values of density from experiments or models. The effect of considering pure substance densities [99] in the experimental determination of CO_2−H_2O *IFT* was evaluated and the relative difference to the *true IFT* (*i.e.*, considering the density change in the water-rich phase by **Equation 5.1**) were calculated by:

$$\Delta IFT_i = IFT_i^{pure} - IFT_i^{true} \qquad \textbf{5.2}$$

and the results plotted in **Figure 5.4**. As expected, the lower values for the density difference due to the higher density of the CO_2-saturated water phase when compared to the density of pure water, resulted in lower interfacial tension values, as depicted in **Figure 5.4**. These results are in agreement with the findings of Chiquet *et al.* [7]. The underestimation of CO_2−H_2O *IFT* generally increased with pressure for all isotherms, with the highest underestimations obtained at the lowest temperatures for constant pressures. For the conditions examined here, a maximum difference of -7.28 $mN.m^{-1}$ (%AAD = 27.8 %) was calculated at T = 333.15 K and P = 59.91 MPa. These conditions also correspond to the lowest calculated density difference $\Delta\rho$ = 55.8 kg.m^{-3}, as listed in **Table E.7**.

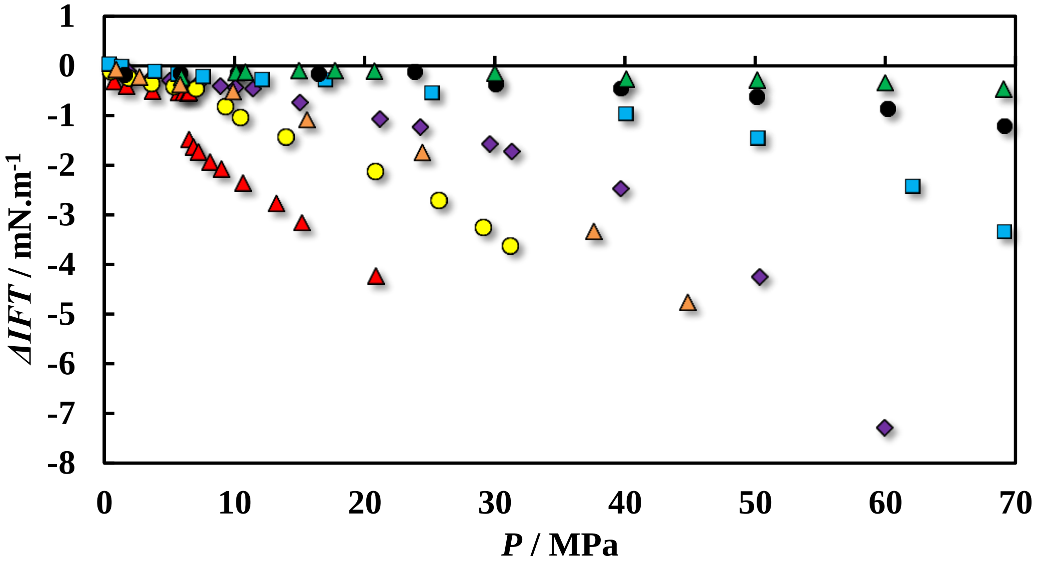

Figure 5.4. *ΔIFT−pressure diagram of the CO_2 + H_2O system: T = 298 K (▲), 313 K (●), 324 K (▲), 333 K (◆), 374 K (■), 424 K (●) and 469 K (▲).*

In light of these results, the *IFT* values reported by Hebach *et al.* [82] and Georgiadis *et al.* [91] were recalculated applying the approach followed here for the density difference and the results were plotted against measurements from this work and the ones from Park *et al.* [84], Chiquet *et al.* [7], Bachu and Bennion [89], Kvamme *et al.* [87], Bikkina *et al.* [92] and Shariat *et al.* [93], as depicted in **Figure 5.5**. The isotherms in the figures are not exactly identical, but sufficiently close for comparison purposes. As can be observed, measurements performed here are in good agreement with the data reported by the different authors within the range studied, with the exception of the data reported by Park *et al.* [84], Bikkina *et al.* [92] and Bachu and Bennion [89] at temperatures ranging from 298 to 323 K (**Figure 5.5*a*** through ***c***), where significant deviations are observed in the region where CO_2 is in the liquid or supercritical state. *IFT* data from Bikkina *et al.* [92] persisted in being lower than *IFT* measured here and by others at *T* = 333 K (**Figure 5.5*d***). Overall, the small deviations obtained to the data from Hebach *et al.* [82], Chiquet *et al.* [7], Kvamme *et al.* [87], Georgiadis *et al.* [91] and Shariat *et al.* [93] validate both the equipment and methodology adopted here, showing these to be adequate for investigating the *IFT* of this system over a wide range of conditions.

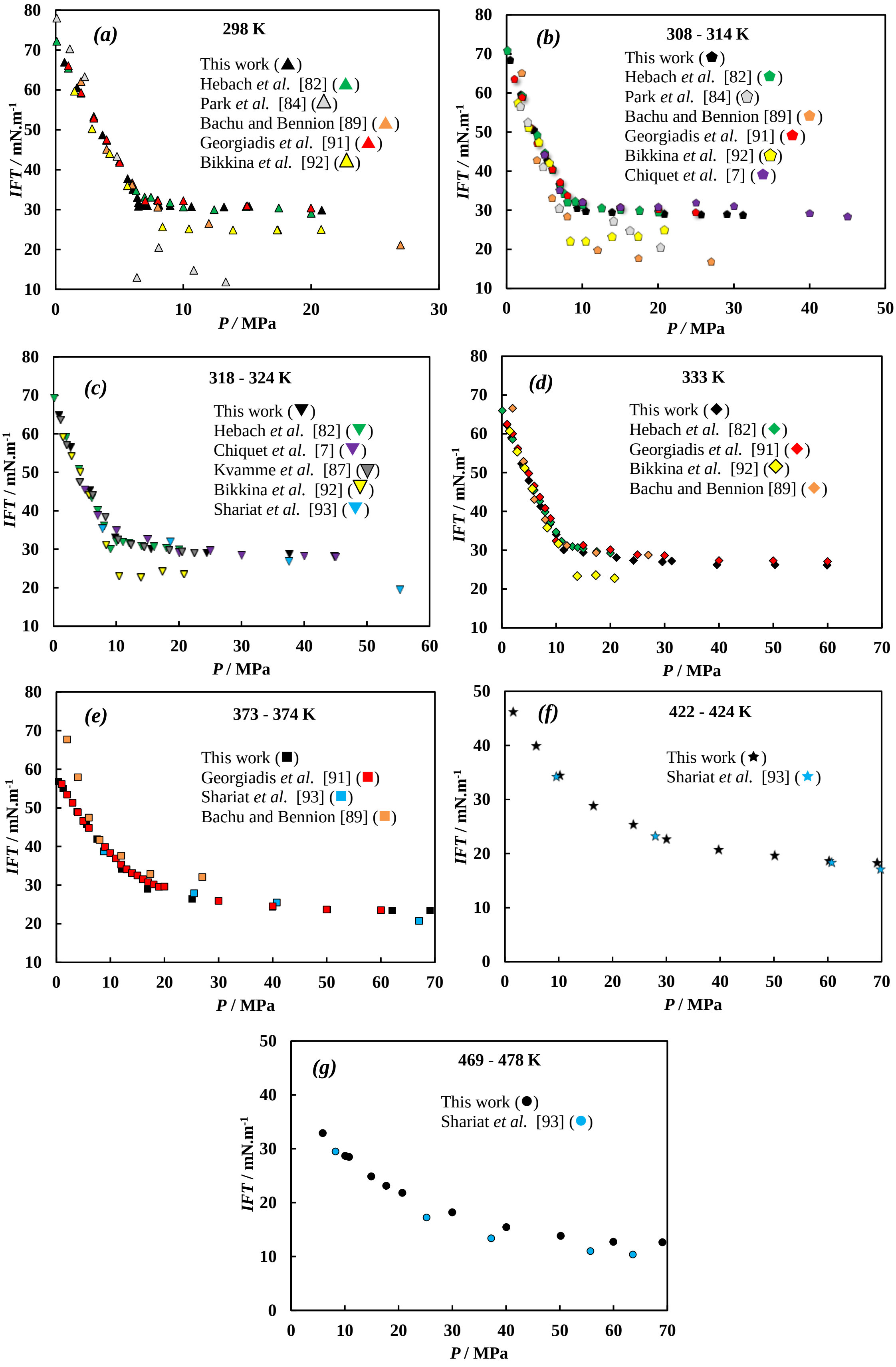

Figure 5.5. *IFT−pressure diagrams of the* CO_2 + H_2O *system. IFT data reported by Hebach et al.* [82] *and Georgiadis et al.* [91] *were recalculated using the correlation developed in this work for estimating the density of the* CO_2*-saturated water phase. Data from Shariat et al.* [93] *were read from graphs.*

As described by others [225,316,317], the system CO_2 + H_2O exhibits a type III phase behaviour, according to the classification of Scott and Konynenburg [318,319]. Consequently, this system presents a very rich interfacial behaviour characterised by the appearance of different type of interfaces. For temperatures below the upper critical end point (UCEP), approximately equal to the critical temperature of CO_2 (T_c ~ 304 K) [316], the system displays a vapour−liquid region at low pressures and a liquid−liquid region at higher pressures, separated by the appearance of a vapour−liquid−liquid phase equilibria at the three-phase equilibrium pressure line. On the other hand, for temperatures higher than that of the UCEP, and depending on the pressure, liquid water may be in contact with gaseous or supercritical CO_2.

As depicted in **Figure 5.6**, two regions are distinguishable in the *IFT*−pressure projections for the four lowest temperatures investigated: a low pressure region where *IFT* decreases rather rapidly and a high pressure region where *IFT* decreases but in a much less pronounced rate, corresponding to the isothermal phase transition of CO_2 from vapour/gaseous to liquid/supercritical. Such pressure dependence of *IFT* has been attributed by different authors [81,91] to the isothermal compressibility of CO_2 and its impact on the free energy density of the interface. At low pressures, the free energy density changes significantly with pressure and therefore the decrease of the interfacial tension values is more pronounced [81]. On the other hand, at high pressures the CO_2-rich phase becomes less compressible as it reaches a *liquid-like* behaviour and the interfacial tension values decrease gradually [91]. Even though these two regions also appear to be present in the other studied isotherms (374, 424 and 469 K), the transition seems to become smoother with increasing temperature. The dependence of the *IFT* on temperature is less marked. The results plotted in **Figure 5.7** show a general decrease of the interfacial tension isobars with increasing temperature for temperatures greater than 373 K, and an apparent tendency inversion for lower temperatures, similar to what was reported by others [93]. This change should be closely linked with the isobaric minimum of CO_2 solubility in water [320]. For pressures ranging from about 5 to 15 MPa, the *IFT* values measured at T = 374 and 424 K are similar or greater than the ones measured for lower isotherms, supporting the evidence of the *IFT* dependence on CO_2 dissolution. Furthermore, as shown in **Table E.7**, a point in the vapour−liquid−liquid line was observed and three equilibrium phases were present at T = 298.6 K and P = 6.49 MPa (a CO_2-rich vapour phase, a CO_2-rich liquid phase and a water-rich liquid phase). The appearance conditions of this point are in agreement with measurements performed by others [316,321]. The interfacial tension values for the vapour CO_2–water and liquid CO_2–water interfaces were found to amount 31.69 and 30.79 $mN.m^{-1}$, respectively, and are in reasonable agreement with the values obtained from MD simulations [225]. The complex behaviour of CO_2–H_2O *IFT* as well as the *IFT*s at the three-phase equilibrium pressure are discussed in more detail in terms of the microscopic characteristics of the interface in **Section 5.5** using the density profiles computed with the DGT.

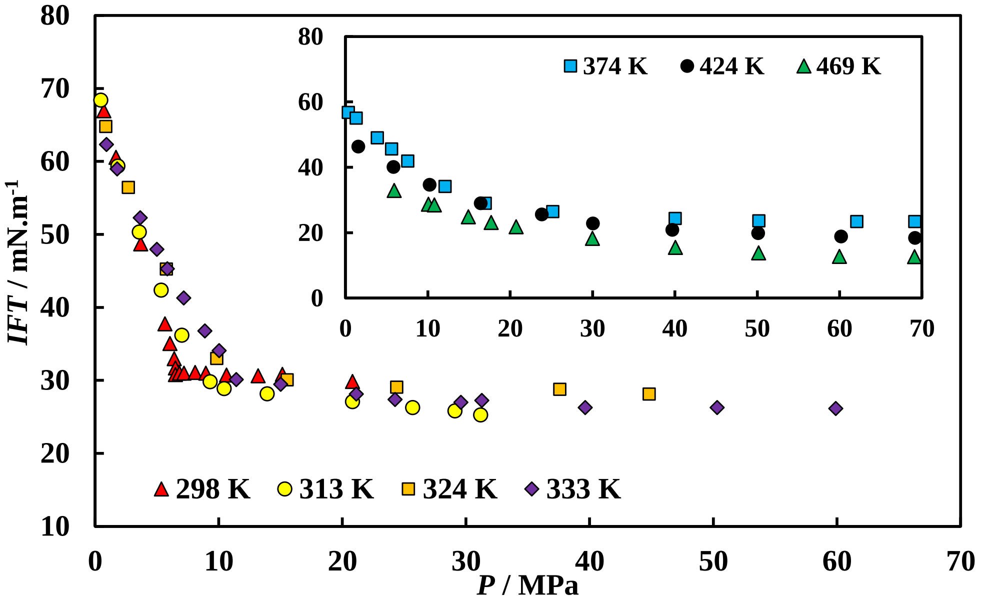

Figure 5.6. *IFT–pressure diagram of CO_2 + H_2O. Symbols represent data measured in this work.*

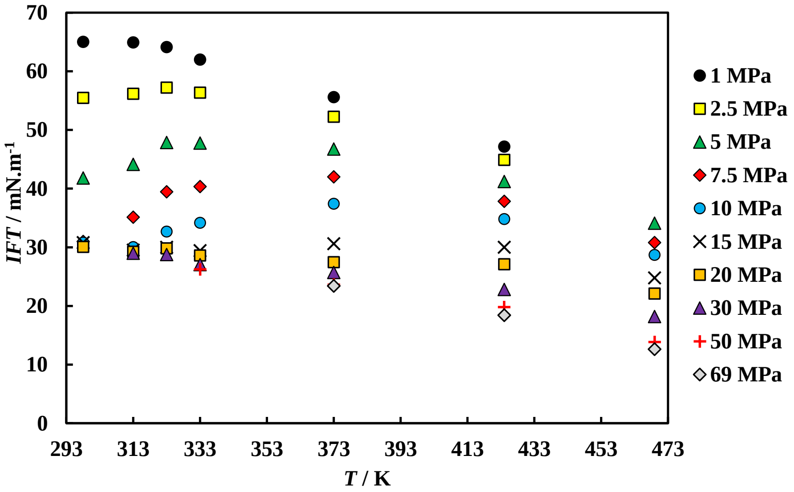

Figure 5.7. *IFT–temperature diagram of CO_2 + H_2O. Symbols represent isobars correlated from data measured in this work.*

5.3.2 CO_2-rich mixtures and water

Equilibrium densities: Considering the density results obtained for the CO_2 + H_2O system, the saturated density of the CO_2-rich phase was taken equal to that of the dry density of MIX-4 and MIX-5 previously measured in our laboratory [322,323]. On the other hand, the density of the water-rich phase was measured in-situ (**Figure 2.10**) at temperatures ranging from 298 to 423 K and pressures up to 69.06 MPa. The results are listed in **Table D.9** in **APPENDIX D**. **Figure 5.8** shows the impact of 4 and 10 % of diluent gases on the density of the phases when compared to that of the CO_2 + H_2O system. As can be seen in **Figure 5.8*a***, the presence of small quantities of light diluent gases (*i.e.*, MW < MW CO_2) such as N_2, Ar, O_2 and H_2, resulted in a density reduction from that of pure CO_2 [99], more marked with increasing content in diluent gases *i.e.*, from MIX-4 to MIX-5. This effect was considerably more pronounced at low temperatures and for pressures close to the mixture phase transition/critical point (**Figure 5.8*a***). As an example, the maximum density reduction calculated at T = 323 K was 20.1 and 33.9 % for MIX-4 and MIX-5, respectively, for pressures around 11 MPa [323]. The analysis of the effect of diluent gases on the aqueous phase (**Figure 5.8*b***) shows also a reduction in the density but with density values laying mostly within the experimental uncertainties; this may be due to the considerable lower solubility of the diluent gases in water when compared to CO_2 making the density readings less sensitive to variations.

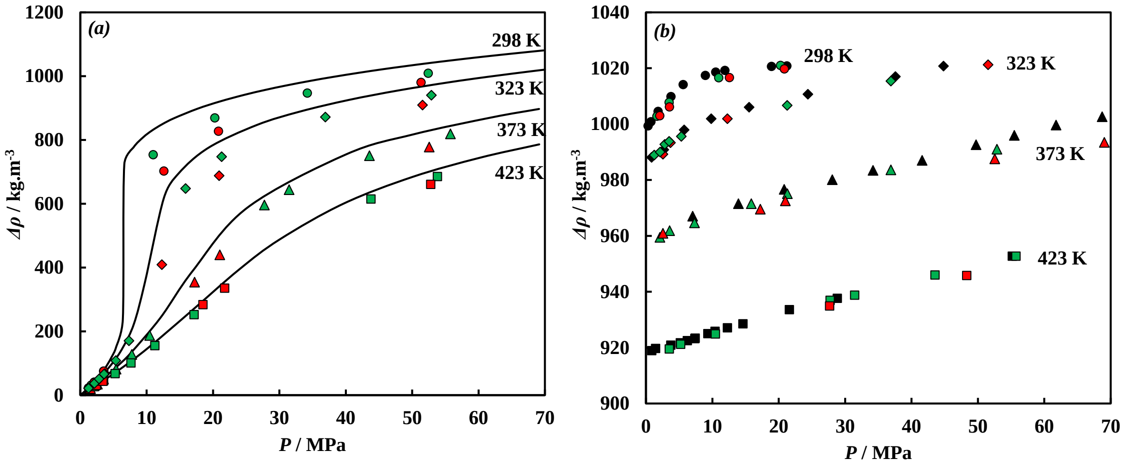

Figure 5.8. *Density−pressure diagrams of the **(a)** CO_2-rich and **(b)** water-rich phases of H_2O + CO_2 (black), H_2O + MIX-4 (green) and H_2O + MIX-5 (red). Solid lines in **(a)** represent the density of pure CO_2* [99]. *Coloured symbols in **(a)** represent the dry density of MIX-4 (green) and MIX-5 (red) measured in our laboratory* [323]. *Coloured and black symbols in **(b)** represent the density of the water-rich phase measured in this work.*

Interfacial tensions: The interfacial tension of the MIX-4 + H_2O and MIX-5 + H_2O systems were measured at T = 298, 323, 373 and 423 K and pressures up to 55.75 MPa using the density values described in the foregoing paragraph and correlated whenever necessary. The results are listed in **Tables E.8** and **E.9** in **APPENDIX E**. A comparison of the results with CO_2–H_2O *IFT* and density difference is plotted in **Figure 5.9**.

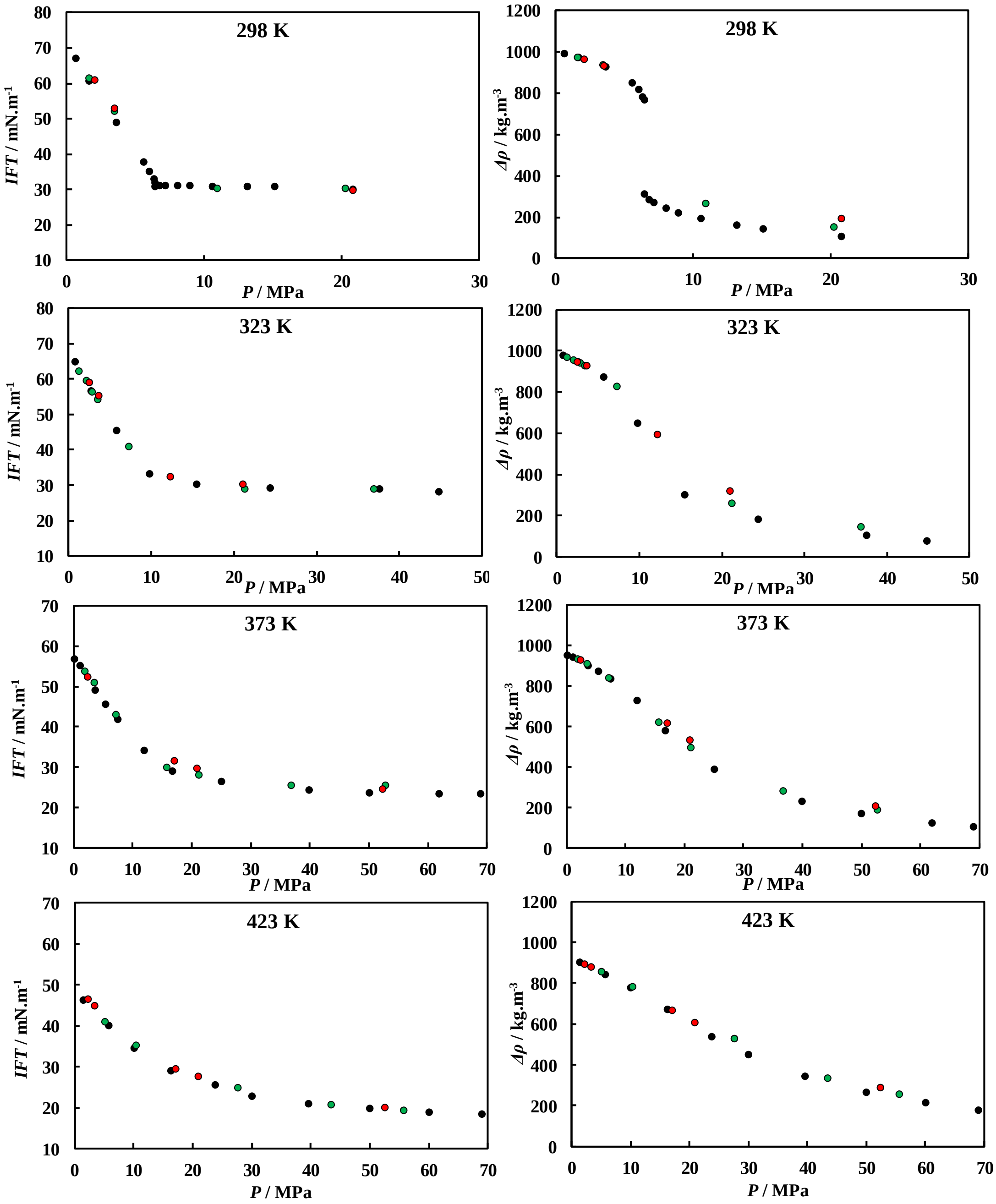

Figure 5.9. IFT–pressure and density difference–pressure diagrams of CO_2 + H_2O (black), MIX-4 + H_2O (green) and MIX-5 + H_2O (red). Symbols represent data measured in the present work.

From **Figure 5.9** can be seen that the presence of light diluent gases resulted in an overall increase of the density difference between the contacted phases as well as of the *IFT* when compared to that of the $CO_2 + H_2O$ system, over the range of temperature and pressure examined. The observed increase of the *IFT* values from those of CO_2−H_2O *IFT* is in agreement with the observations from others [105,106], taking into account that the quantity of diluent gases studied here was much lower. The calculation of the relative change of *IFT* from that of $CO_2 + H_2O$ for each isotherm (**Figure 5.10**) shows an overall increase in *IFT* with increasing content in diluent gases *i.e.*, from MIX-4 to MIX-5, as it could be expected. However, calculated variations for each isotherm also seem to lie close to the experimental uncertainties of measurements (**Section 5.3.4**); in average, the relative increase from CO_2−H_2O *IFT* was 2.1% (0.69 mN.m^{-1}) for MIX-4 and 4.1% (1.47 mN.m^{-1}) for MIX-5, over the pressure range investigated. The type and content of diluent gases investigated allows to deduce the potential impact of light gaseous impurities on the geological storage of CO_2-rich streams, as further discussed in **Section 5.3.5**.

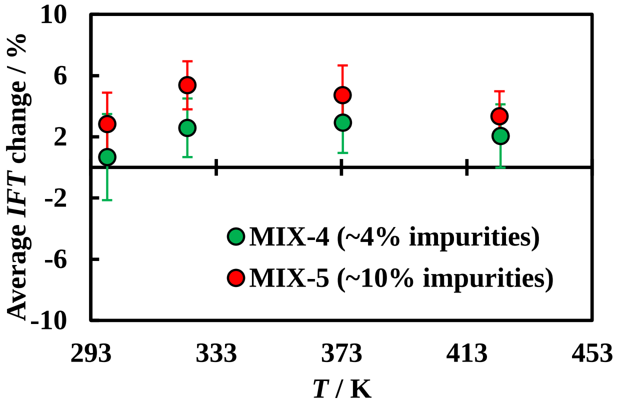

Figure 5.10. *Average IFT change−temperature diagram of MIX-4 + H_2O and MIX-5 + H_2O. IFT change was calculated relative to CO_2−H_2O IFT values correlated from measurements performed in this work and averaged over the pressure range investigated. Error bars correspond to averaged uncertainties of experimental measurements (**Tables E.8** and **E.9**).*

5.3.3 CO_2 and NaCl brines

Equilibrium densities: Considering the effect of CO_2 solubility on the density difference of the $CO_2 + H_2O$ system and, in turn, the impact on the experimental determination of *IFT* values, it becomes also important to properly account for the effect of CO_2 dissolution on the density of NaCl solutions. Experimental CO_2-saturated liquid density data of NaCl brines were reported by Yan *et al.* [324]. In their work, the densities of CO_2-saturated solutions with NaCl molalities of 1 and 5 mol.kg^{-1} were measured using a vibrating U-tube densitometer at temperatures in the range 323 to 413 K and pressures up to 40 MPa. In order to estimate the density of the CO_2-saturated brine phase at pertinent pressure and temperature conditions, and salt molalities, the model developed by Duan *et al.* [325] was used (through computer programs mentioned therein). Accordingly, this model is a multi-parameter correlation based on the Duan *et al.* [326] EoS, and improved versions of the model [320,327], and on the theory of Pitzer [328]. The Duan model is expected to be capable of predicting the CO_2-saturated brine density of CO_2 + NaCl(aq) systems for temperatures and pressures up to 573 K and 100 MPa, respectively, and NaCl molalities up to 4.5 mol. kg^{-1}. To check the validity of this approach, deviations of the Duan *et al.* [325] model to CO_2-saturared water and brine density data measured in this work and by Yan *et al.* [324] were calculated and the results plotted in **Figure 5.11**. As can be seen, the model allows a reproduction of the density of the aqueous phase of the CO_2 + H_2O and CO_2 + NaCl(aq) systems above 99.50% and 99.75%, respectively, with a %AAD to experimental data of 0.13 and 0.06 %, respectively, confirming to some extent the validity of this approach. On the other hand, and similar to the CO_2 + H_2O system, the density of the water-saturated CO_2 phase was taken to be equal to that of pure CO_2 [99] under analogous pressure and temperature conditions.

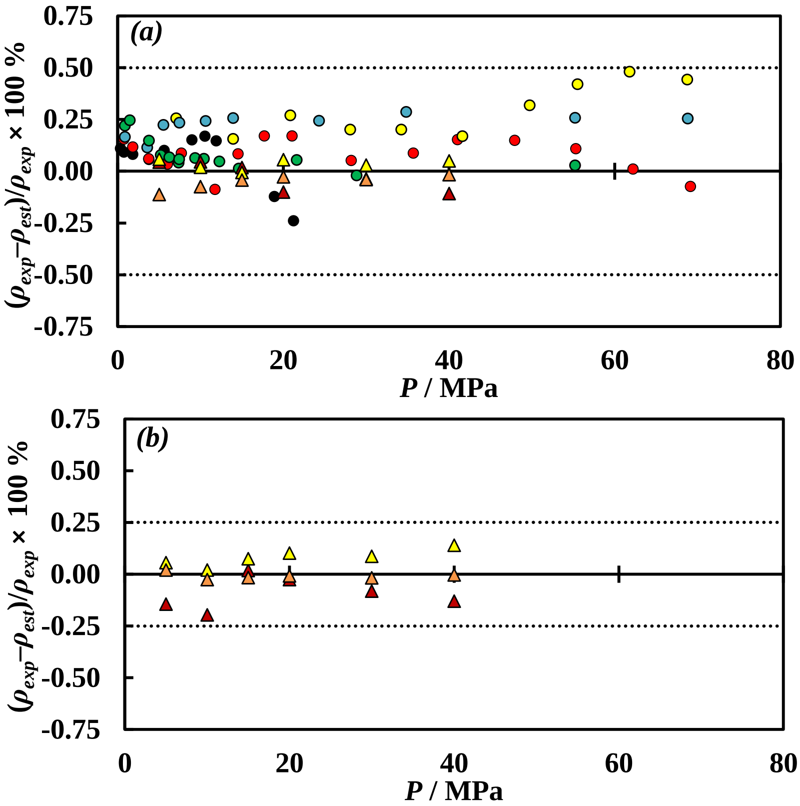

Figure 5.11. *Relative deviation−pressure diagrams of* ***(a)*** *CO_2 + H_2O and* ***(b)*** *CO_2 + NaCl(aq) systems. Symbols represent deviations of CO_2-saturated liquid densities estimated using the Duan et al.* [325] *model to measured data from: this work, T = 298 K (●), 333 K (●), 373 K (○), 393 K (●) and 423 K (●); Yan et al.* [324], *T = 323 K (▲), 373 K (△) and 413 K (▲). Deviations in* ***(b)*** *were calculated only for data reported by Yan et al.* [324] *for NaCl solutions with molality m= 1 $mol.kg^{-1}$.*

Interfacial tensions: The interfacial tension of CO_2 + NaCl(aq) systems were measured at temperatures ranging from 298 to 423 K and pressures up to 69.51 MPa and salt molalities 0.98 and 1.98 mol.kg^{-1}. The results are listed in **Tables E.10** and **E.11** in **APPENDIX E** and plotted in **Figure 5.12**. It can be observed that the addition of NaCl resulted in an increase of the *IFT* for all pressure and temperature conditions investigated. This effect appeared to be less marked at T = 298 K and below the saturation pressure of CO_2, where *IFT* varies rapidly with pressure. On the other hand, measurements at higher pressures and temperatures suggest that the increment in *IFT* due to the presence of NaCl was approximately constant and nearly doubled with salt molality. Indeed, the average relative increase observed on the *IFT* values from that of the CO_2 + H_2O system, over the pressure range investigated, was found to amount 7.2 % (2.01 mN.m^{-1}) and 13.2 % (3.73 mN.m^{-1}) at T = 333, 373 and 423 K, and around 4.4 % (1.42 mN.m^{-1}) and 7.8 % (2.67 mN.m^{-1}) at T = 298 K, for NaCl molalities 0.98 and 1.98 mol.kg^{-1}, respectively, as depicted in **Figure 5.13**.

Although the impact of NaCl on the *IFT* of the CO_2 + H_2O system was already studied in literature (**Table 1.5**), only measurements from Liu *et al.* [128] permit a fairly direct comparison with the values presented in this work at T = 298 K. To allow some discussion at other temperatures, data from Chalbaud *et al.* [90] at T = 373 K and different NaCl molalities are also plotted in **Figure 5.12**, along with data from Li *et al.* [115] at T = 373 and 423 K for a brine composed of 0.864 (mole fraction) NaCl and 0.136 (mole fraction) KCl, and total salt molalities 0.98 and 1.98 mol.kg^{-1}. From this figure it can be observed that the data measured in this work are in good agreement with those of Liu *et al.* [128], but in reasonable agreement with those of Chalbaud *et al.* [90]. In fact, CO_2−NaCl(aq) *IFT* data from Chalbaud *et al.* [90] at T = 373 K and NaCl molalities m = 0.09 and 0.87 mol.kg^{-1} are generally lower than CO_2−H_2O *IFT*, similar to what was already described in **Section 1.3.2** at T = 298 K. Regarding the data from Li *et al.* [115], despite the discrepancies observed at T = 298 K (**Figure 1.5**), comparison with the isotherms at T = 373 and 423 K indicates that Na^+ and K^+ ions have similar impact on the *IFT* values as their data are very close to CO_2−NaCl(aq) *IFT* measured in this work at identical pressure, temperature and brine molality. It is also important to note that, even though higher water salinities than those investigated in the present work can be found in deep reservoirs [89], *IFT* is expected to increase linearly with salt molality

[113,115,119,129,130] and thus, the *IFT* reported here can be extrapolated to systems with higher NaCl content with fairly good confidence.

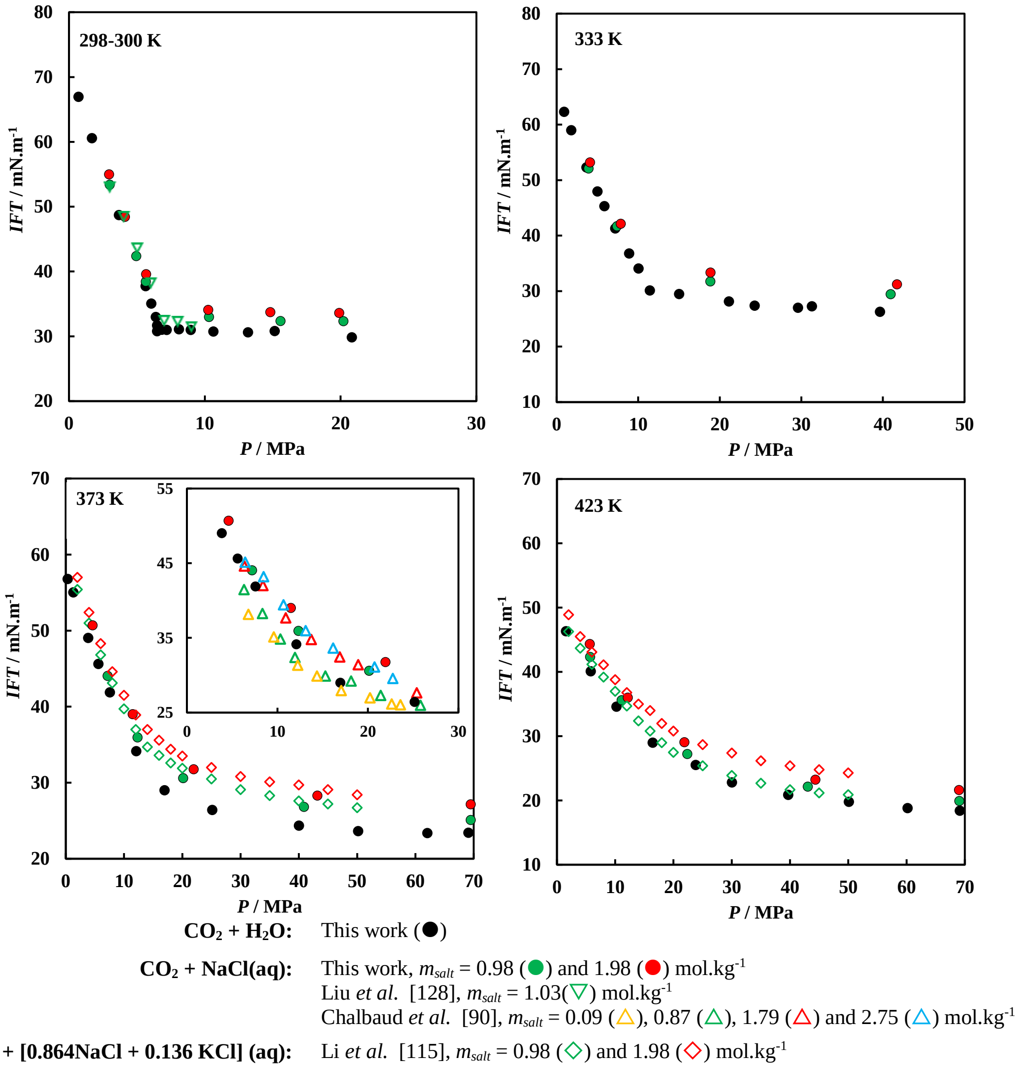

***Figure 5.12**. IFT−pressure diagrams of CO_2 + H_2O and CO_2 + brine systems.*

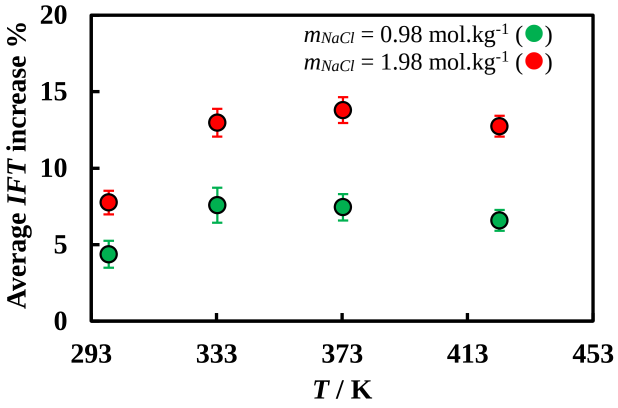

***Figure 5.13**. Average IFT increase−temperature diagram of CO_2 + NaCl(aq) systems. IFT increase was calculated relative to CO_2−H_2O IFT values correlated from measurements performed in this work and averaged over the pressure range investigated. Error bars correspond to averaged experimental uncertainties (**Tables E.10** and **E.11**).*

5.3.4 Experimental uncertainties

The combined expanded uncertainties in the interfacial tension measurements, U_c (*IFT*), are assessed by combining the uncertainties on the drop shape analysis for each recorded image, U_1 (*IFT*), and uncertainties on the estimation of the density difference for the equilibrated phases, U_2 (*IFT*). The first contribution can be estimated, to some extent, by the standard deviation of the interfacial tension values calculated from the recorded images at each experimental condition. This statistical standard error includes the errors and uncertainties from the use of the Laplace equation, vibrations and reproducibility of the measurements. The effect of uncertainties in pressure and temperature in determining the density of the saturated phases used in the interfacial tension calculations can be evaluated by the law of propagation of errors as follows [296]:

$$U_2(IFT) = \left(\left(\frac{\partial IFT}{\partial \rho_{H_2O}} \right)^2 U_c(\rho_{H_2O})^2 + \left(\frac{\partial IFT}{\partial \rho_{CO_2}} \right)^2 U_c(\rho_{CO_2})^2 \right)^{1/2} \quad \mathbf{5.3}$$

$$U_c(\rho) = \left(\left(\frac{\partial \rho}{\partial P} \right)^2 u(P)^2 + \left(\frac{\partial \rho}{\partial T} \right)^2 u(T)^2 \right)^{1/2} \quad \mathbf{5.4}$$

The combined expanded uncertainties in the *IFT* measurements, estimated with a confidence level of 0.95, are shown in **Tables E.7** through **E.11** for each system and experimental condition. It can be observed that in general, the uncertainties caused by the density of the phases are greater than the uncertainties that arise from the ASDA method. Overall, the combined expanded uncertainty averaged 0.31 $mN.m^{-1}$ for the CO_2 + H_2O system, 0.67 $mN.m^{-1}$ for the MIX-4 + H_2O and MIX-5 + H_2O systems, and 0.27 $mN.m^{-1}$ for the CO_2 + NaCl(aq) systems. A maximum uncertainty of 1.87 $mN.m^{-1}$ was estimated at the three-phase equilibrium point of the CO_2 + H_2O system for the *IFT* value between the CO_2-rich liquid and the water-rich liquid phases.

5.3.5 Implications on the geological storage of CO_2

Considering the wide range of experimental conditions investigated in the foregoing sections, it is now possible to study the impact of interfacial tension on the geological storage of CO_2. This analysis was performed by deducing the impact of temperature and pressure, as well as of fluids properties, on the column of CO_2 that can be trapped beneath a caprock due to variations on CO_2−H_2O *IFT* via **Equation 1.8** (structural trapping). For the sake of simplicity and as a first approximation, some considerations, based on the works of others [7,33], have been made:

- Type of reservoir: aquifer;
- Reservoir fluids: carbon dioxide and water;
- The caprock is considered to be fully water wet ($\cos \theta = 1$) and with pores of cylindrical shape and average radius $R = 0.1$ μm;
- The values of porosity and residual water saturation of the reservoir are assumed to be $\phi = 0.3$ and $S_w = 0.1$;
- The aforementioned properties of the caprock and reservoir are assumed to be evenly distributed and constant with depth;
- Pores above the caprock are considered to be filled with water, thus the pressure felt in the caprock is deduced using a hydrostatic gradient of 10 MPa.km^{-1};
- Temperature felt in the caprock is deduced using two geothermal gradients: 30 and 40 K.km^{-1};
- The density of CO_2, calculated with REFPROP [99] at the caprock's temperature and pressure, is considered to be constant throughout the reservoir (*i.e.*, along H). The density of water is calculated using **Equation 5.1**. The dissolution of CO_2 in the aquifer below the reservoir is not considered;
- The maximum amount of CO_2 that can be trapped beneath the caprock is estimated using CO_2-H_2O *IFT* values correlated from the isotherms investigated in this work.

Under these assumptions, the column of CO_2 that the caprock can safely sustain and, in turn, the CO_2 storage capacity (in millions of tons per km^2 *i.e.*, Mt.km^{-2}) of an underlying reservoir are estimated via **Equation 1.9** as function of caprock depth. Estimations were performed considering two different field scenarios: onshore, with a surface temperature and pressure of 288 K and 0.1 MPa, respectively, and offshore, with a seabed temperature and pressure of 277 K and 10 MPa, respectively. **Figure 5.14** shows schematically some of the foregoing assumptions. The results are plotted in **Figures 5.15** and **5.16** along with the variation of CO_2-H_2O *IFT* and CO_2 density with caprock depth.

The results plotted in **Figure 5.15*a*** suggest that CO_2 storage capacity in an onshore field increases with caprock depths up to 2 km and levels off for depths up to 4 km. This behaviour is in good agreement with that described by Chiquet *et al.* [7] for a caprock and reservoir with the same characteristics as well as the same pressure/temperature gradients and depth range. However, for depths greater than 4 km, results in **Figure 5.15*a*** clearly indicate a decrease of the trapping potential (*i.e.*, *H*) of deep caprocks and, consequently, of the CO_2 storage capacity, contrasting with the view of constant CO_2 storage capacity for greater depths, as it could be suggested by the results from Chiquet *et al.*[7] alone. The impact of depth and, in turn, of pressure and temperature on the calculated storage capacity can be interpreted in terms of the variation of CO_2-H_2O *IFT* and CO_2 density, as depicted in **Figure 5.15*b***. From this it can be seen that CO_2 density increases rather rapidly in the first 2 km due to phase transition from vapour/gaseous to liquid/supercritical, corresponding to the sharp increase in CO_2 storage capacity, and then slowly for greater depths; in contrast, CO_2-H_2O *IFT* decreases for all depths, and thus the sealing capillary pressure is reduced, and so also the CO_2 trapping potential of the caprock.

In dealing with an offshore field, the results in **Figure 5.16*a*** show that CO_2 storage capacity is reduced progressively with caprock depth. For this case, both CO_2-H_2O *IFT* and CO_2 density curves (**Figure 5.16*b***) show a decreasing trend as a result of the overall higher pressures and lower temperatures when compared to those of the onshore scenario for a fixed caprock depth. Nevertheless, by comparing these two field scenarios, it is evident that caprocks in offshore fields can potentially trap significantly higher quantities of CO_2.

From these results it can be also deduced that the increase in *IFT* due to the presence of salts and/or sparingly soluble gaseous impurities would result in an increase of the sealing capillary pressure by a factor equal to the relative increase in *IFT* from that of CO_2 + H_2O *i.e.*, $\gamma_{new}/\gamma_{CO_2-H_2O}$. In terms of gas storage capacity, the analysis of the impact of salts and sparingly soluble gaseous and light (comparing to CO_2) impurities should be made with care. Water salinity increases not only the *IFT*, but also the hydrostatic head pressure; this results in a translation of the curve describing the dependence of CO_2 storage capacity with caprock depth (**Figures 5.15** and **5.16**) to the right and upward. In other words, greater CO_2 storage capacities could be obtained at shallower caprock depths. In the case of a CO_2-rich stream containing sparingly soluble gaseous and light impurities like the ones investigated in this work, the observed density reduction from that of pure CO_2, specifically near CO_2 phase transition/critical point, would result in a reduction of the storage capacity of a stream with these characteristics. Nevertheless, the fact that the interfacial tension of the $CO_2 + H_2O$ system increases with increasing content in gaseous impurities (sparingly soluble in water) as well as with water salinity indicates that safer storage conditions (*i.e.*, better capillary-sealing efficiencies) would be obtained under such conditions. Furthermore, from **Figures 5.15** and **5.16** it becomes evident that CO_2 storage capacities are negatively affected by higher temperatures.

It is worth mentioning that the assumptions considered in the calculation of the CO_2 storage capacity only allowed to study the impact of variations on the properties of fluids (CO_2 and H_2O) and did not consider the lithology and heterogeneity of geological formations, nor the effect of depth on reservoir and caprock characteristics (*e.g.*, wettability, porosity, shape and size of pores). For example, porosity is expected to decrease with depth which, in turn, would have a negative impact on the CO_2 storage capacity (**Equation 1.9**). On the other hand, at higher depths, caprocks most probably would exhibit pores with smaller radius, increasing CO_2 trapping potential (**Equation 1.8**). The designed injection pressure of a CO_2 project should also take into consideration the pressure at which the caprock would be fractured (*i.e.*, mechanical failure) [33].

It is also important to note that the assumption of constant density of CO_2 along the reservoir can also lead to quite different estimations, specifically for conditions near CO_2 phase transition/critical point [7]. Nonetheless, all things considered, the analysis performed here still provides important insights on the effect of *IFT* on the CO_2 storage capacity based on the capillary-sealing efficiency of the caprock.

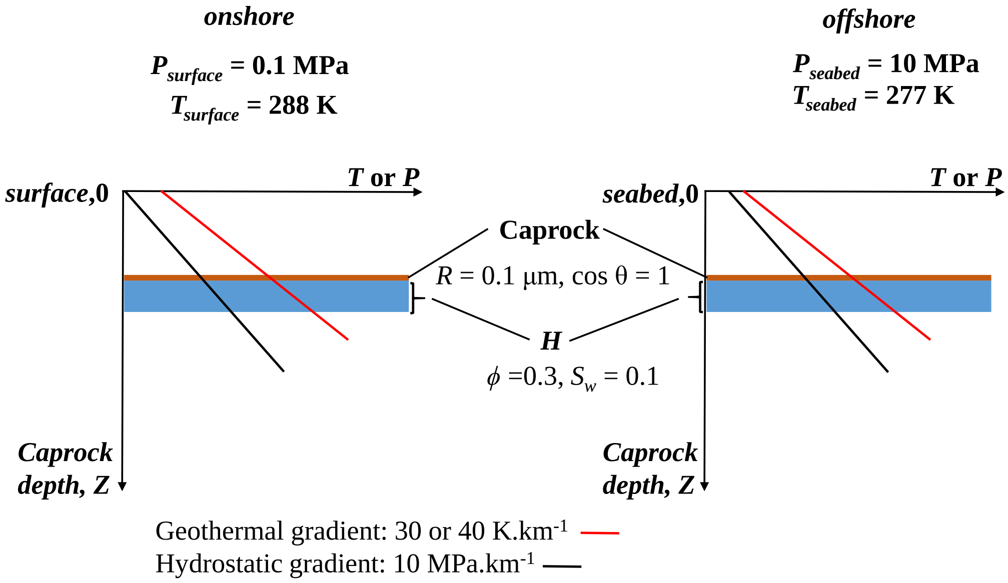

Figure 5.14. *Schematic representation of the two field scenarios considered for CO_2 storage.*

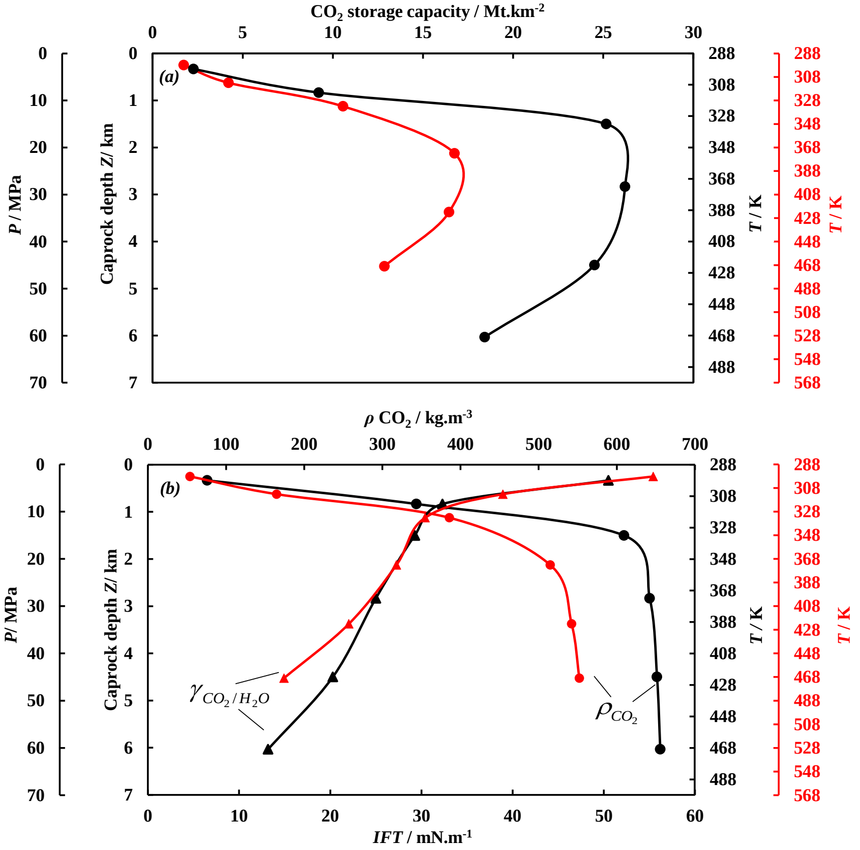

Figure 5.15. ***(a)*** *CO₂ storage capacity−caprock depth and* ***(b)*** *IFT/ρCO₂−caprock depth diagrams for an onshore field. Lines correspond to estimations using a geothermal gradient of 30 (black) and 40 K.km^{-1} (red). Temperature at reference depth (surface) is taken equal to T = 288 K. Pressure is deduced using a hydrostatic gradient of 10 MPa.km^{-1}.*

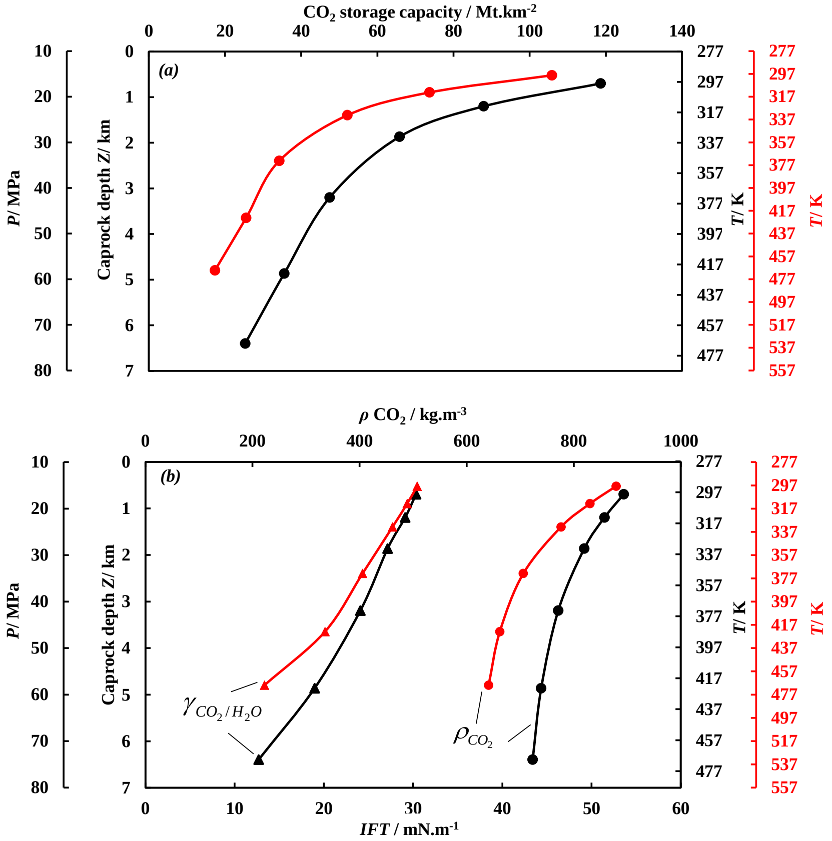

Figure 5.16. ***(a)*** *CO₂ storage capacity−caprock depth and* ***(b)*** *IFT/ρCO₂−caprock depth diagrams for an offshore field. Lines correspond to estimations using a geothermal gradient of 30 (black) and 40 K.km^{-1} (red). Temperature at reference depth (surface) is taken equal to T = 277 K. Pressure is deduced using a hydrostatic gradient of 10 MPa.km^{-1}.*

5.4 Modelling

5.4.1 *Binary mixtures*

In this section the DGT was coupled with the CPA EoS and its ability to describe both bulk phase and interfacial properties of binary aqueous systems was evaluated by comparison with experimental data from the present work and gathered from literature. Modelling results were also compared to *IFT*s computed using Sutton's correlation and the LGT. The systems investigated included two-phase interfacial tensions of common gases (CO_2, N_2 and CH_4) and *n*-alkanes (*n*-C_6, *n*-C_{10} and *n*-C_{16}) against water over a broad range of pressure and temperature conditions. For the thermodynamic conditions examined, the type of interfaces analysed comprised a liquid water phase in contact with gases in subcritical and/or supercritical conditions, as well as with liquid hydrocarbons.

In order to provide a correct description of the composition of the phases, binary interaction coefficients within the CPA EoS framework (k_{ij}s) were used. The k_{ij} values were taken from previous works, except for N_2 + H_2O and *n*-C_{16} + H_2O systems, which were regressed against solubility data for the aqueous phase and used to predict the behaviour of the gas/*n*-alkane-rich phase. Correlated aqueous phase data of N_2 + H_2O for pressures up to 60 MPa from the work of Mao and Duan [329] and experimental *n*-C_{16} solubility data in the aqueous phase at P = 5 MPa reported in Bergin's thesis [330] were used as regression data. In the case of the gas + water systems, the dependence of k_{ij} values on temperature was preserved, whereas for each *n*-alkane + water system, a single k_{ij} value, temperature independent, was used. All non-aqueous components were modelled as inert molecules and only cross-association (solvation) between CO_2 and H_2O was explicitly incorporated in the model (**Section 3.6** and **APPENDIX B**). The k_{ij}s values used in this work are summarized in **Table 5.5** along with the temperature range of experimental/calculated solubility data used in their regression.

Figures 5.17*a* through **5.19*a*** show that the CPA EoS is capable of providing a good description of both gas solubility and water content of the studied gas + water systems over a broad range of pressures and temperatures, including near and at CO_2 supercritical conditions. For the *n*-alkane + water systems, mutual solubility data at high pressures are scarce, with experimental studies frequently carried at atmospheric conditions or at three-phase equilibrium pressures [331–333], hence comparison with solubility data at elevated pressures was not performed. From **Figure 5.20** it can be observed that one single, temperature independent, k_{ij} value is enough to adequately describe the considerably low mutual solubilities of such systems with the CPA EoS. The highest model deviations are obtained for the *n*-alkane solubility in the aqueous phase at low temperatures, where the CPA EoS fails to describe the well-known minimum *n*-alkane solubility [334]. These deviations were attributed by Oliveira *et al.* [282] to limitations of this EoS to account for hydrophobic interactions between water and hydrocarbon molecules. Accordingly, the appearance of a temperature at which the hydrocarbon solubility is minimum (T_{min}) is usually interpreted in terms of the enthalpy of solution. The enthalpy of solution includes a positive contribution due to cavitation effects and negative contribution due to hydrophobic effects. These two contributions cancel out each other at $T = T_{min}$, with the hydrophobic effects predominating over cavitation effects for $T < T_{min}$ and vice-versa for $T > T_{min}$. Based on these observations, the hydrophobic effects can be somewhat accounted for through the use of a new mixing rule for the energy parameter of the physical term of the CPA EoS in combination with one extra binary interaction coefficient, as recently proposed by Medeiros [335]. However, aiming at using a minimum number of adjustable parameters to mixtures, and since reservoir temperatures normally exceed those of the case in point, it was decided not to incorporate here the approach of Medeiros [335].

Regarding the description of the phase densities, CPA EoS predictions are plotted in **Figures 5.17*b*** through **5.19*b*** as well as in **Figure 5.21** in terms of density difference between the contacted phases. From these it can be observed that by considering only the CPA parameters adjusted to pure component saturation properties (**Table 3.5**) and k_{ij} values fitted against solubility data (**Table 5.5**), the CPA EoS allows a good prediction of the effect of both pressure and temperature on the density difference of the gas + water systems. However, in the case of the *n*-alkane + water systems, although the effect of pressure seems to be relatively well described, the CPA EoS predicts a higher temperature dependence of the density difference. Nevertheless, all things considered, both phase composition and density predictions of the aqueous systems with the CPA EoS appear adequate considering the asymmetry (large + small molecules) and highly non-ideal character (different intermolecular forces) of such systems as well as the wide spectrum of miscibility and broad range of pressure and temperature conditions examined.

***Table 5.5**. Binary interaction coefficients k_{ij} used for H_2O (1) + gas/n-alkane (2) systems within the CPA EoS framework. Temperature, T, is in Kelvin.*

(2)	k_{ij}	Source	Temperature range / K
CO_2	$-0.15508 + 0.000877\ T$	Tsivintzelis *et al.* [288]	298 to 478
CH_4	$-1.18\times10^{-5}\ T^2 + 0.0102\ T - 1.9668$	Haghighi *et al.* [289]	273 to 393
N_2	$-1.14\times10^{-5}\ T^2 + 0.0137\ T - 2.5289$	This work	273 to 483
n-C_6	0.044	Oliveira *et al.*[282]	310 to 473
n-C_{10}	-0.054	Oliveira *et al.* [282]	374 to 576
n-C_{16}	-0.16	This work	303 to 473

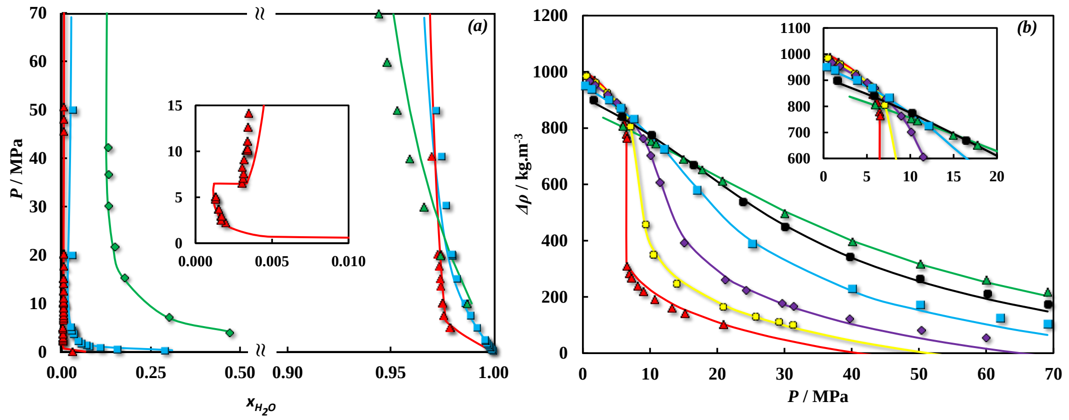

***Figure 5.17.** **(a)** Pressure−composition and **(b)** Δρ−pressure diagrams of the CO_2 + H_2O system. Symbols in **(a)** represent solubility data: Spycher et al.* [336], *T= 298 K (▲) and 373 K (■); Takenouchi and Kennedy* [337], *T =473 K (▲); Tabasinejad et al.* [290], *T = 478 K (◆). Symbols in **(b)** represent the density difference used in the calculation of the experimental IFT values given in **Table E.7**: T = 298 K (▲), 313 K (●), 333 K (◆), 373 K (■), 424 K (●) and 469 K (▲). Solid lines represent CPA EoS estimates and predictions.*

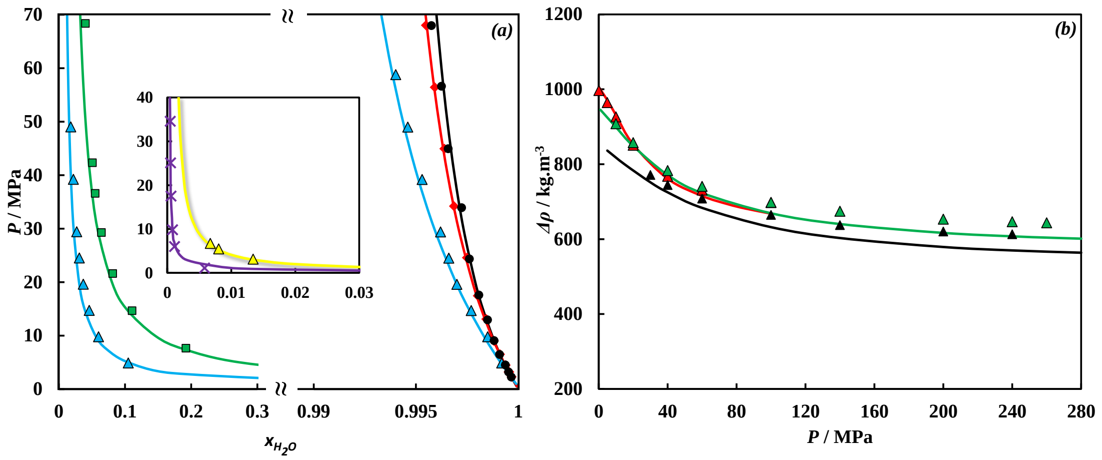

***Figure 5.18.** **(a)** Pressure−composition and **(b)** Δρ−pressure diagrams of the CH_4 + H_2O system. Symbols in **(a)** represent solubility data: Chapoy et al.* [338], *T = 308 K (×); Culberson and McKetta* [339], *T = 344 K (●) and 378 K (◆); Sultanov et al.* [340], *T = 423 K (▲); Rigby and Prausnitz* [341],*T=348 K (△); Tabasinejad et al.* [290], *T = 461 K (■). Symbols in **(b)** represent the density difference between CH_4 and H_2O taken from Weygand and Franck* [100]*: T = 298 K (▲), 373 K (▲) and 473 K (▲). Solid lines represent CPA EoS estimates and predictions.*

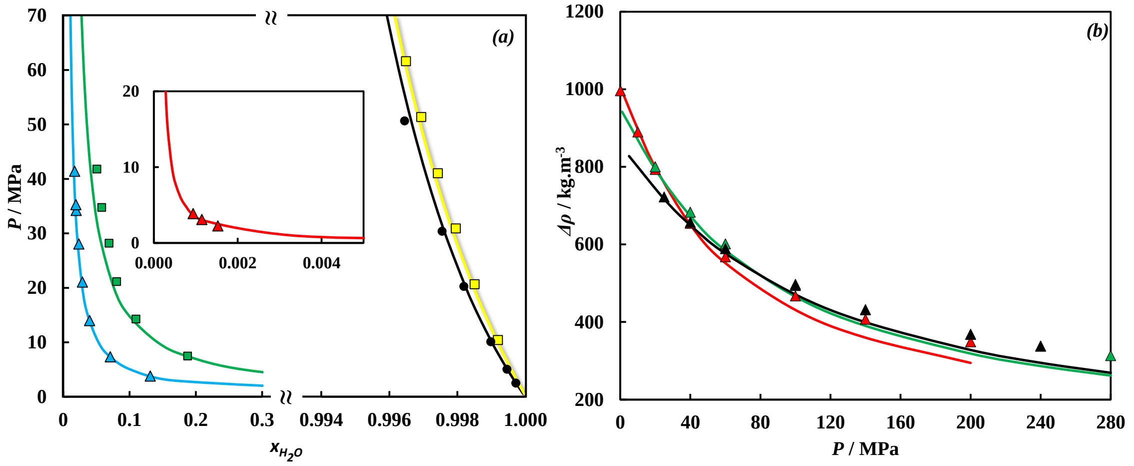

Figure 5.19. ***(a)*** *Pressure−composition and* ***(b)*** *Δρ−pressure diagrams of the N_2 + H_2O system. Symbols in* ***(a)*** *represent solubility data: Wiebe et al.* [342], *T = 298 K (●); O'Sullivan and Smith* [343], *T =398 K (□); Rigby and Prausnitz* [341], *T = 298 K (▲); Tabasinejad et al.* [290], *T = 422 K (▲) and 461 K (■). Symbols in* ***(b)*** *represent the density difference between N_2 and H_2O taken from Wiegand and Franck* [100]*: T = 298 K (▲), 373 K (▲) and 473 K (▲). Solid lines represent CPA EoS estimates and predictions.*

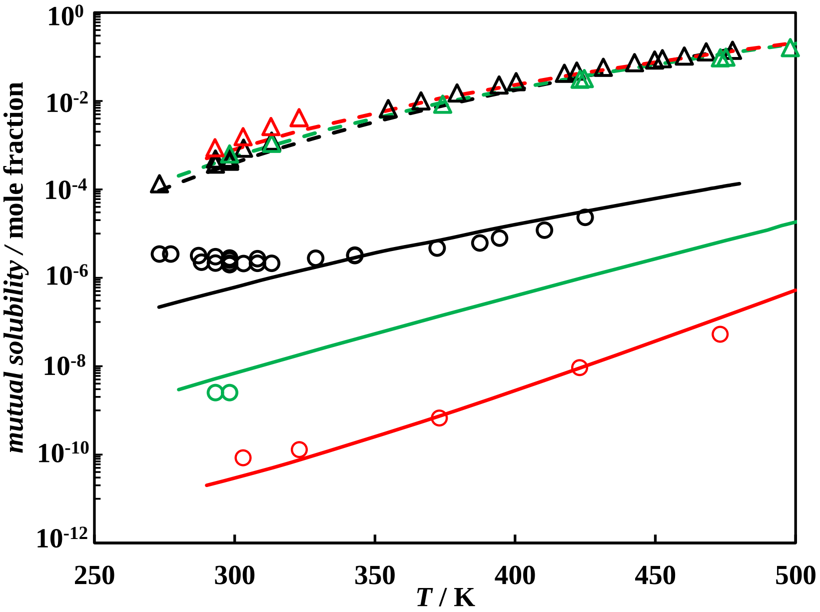

Figure 5.20. *Mutual solubility−temperature diagram of the n-alkane + H_2O systems at atmospheric/three-phase pressure conditions: n-C_6 + H_2O (black), n-C_{10} + H_2O (green) and n-C_{16} + H_2O (red). Symbols and lines represent experimental solubility data taken from literature* [330–333] *and CPA EoS estimates, respectively: solubility of water in the hydrocarbon-rich phase (triangles and dashed lines); solubility of hydrocarbon in the water-rich phase (circles and solid lines).*

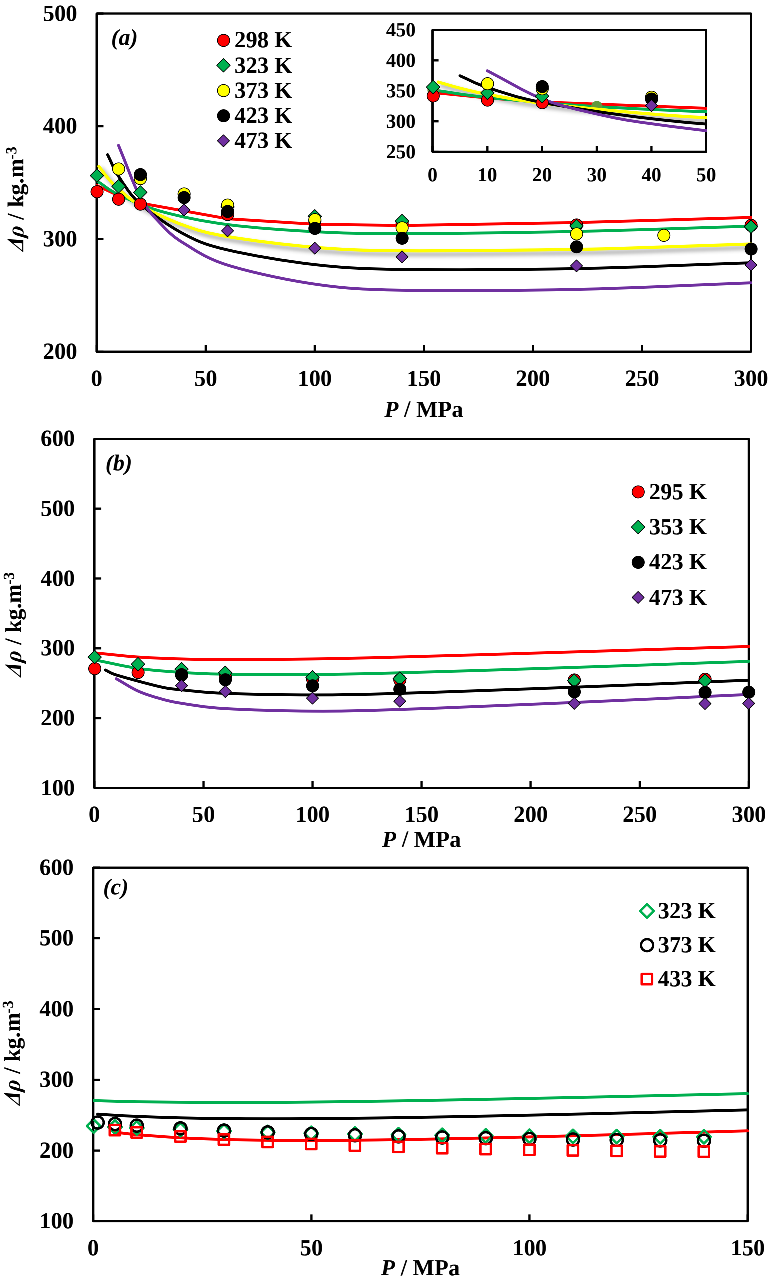

Figure 5.21. *Δρ−pressure diagrams of* ***(a)*** *n-C_6 + H_2O,* ***(b)*** *n-C_{10} + H_2O and* ***(c)*** *n-C_{16} + H_2O. Symbols and lines represent pure component density difference data between the n-alkane and water taken/calculated from* [99,100,344] *and CPA EoS predictions, respectively.*

Having demonstrated the adequacy of the CPA EoS for describing the bulk phase properties, it is now possible to couple this EoS with the LGT and DGT and investigate their capabilities for modelling the *IFT* of such aqueous systems. Aiming at analysing the impact of using constant influence parameters (**Table 3.2**) and bulk density dependent influence parameters (**Tables 3.3** and **3.4**), CO_2−H_2O and CH_4−H_2O *IFT*s at *T* = 298 and 373 K, and *n*-C_{10}−H_2O *IFT* at *T* = 374 K were computed with the DGT and LGT and the results compared to experimental data measured in the present work and from literature

[31,100], as depicted in **Figure 5.22**. In the case of the LGT, calculations were performed using the mixing rule for influence parameters derived directly from the DGT *i.e.*, as given by **Equation 3.44**.

Similar to what was done for hydrocarbon systems (**CHAPTER 4**), and as a first approach, the binary interaction coefficient in the mixing rule of influence parameters within the LGT and DGT framework were fixed to zero (*i.e.*, $\beta_{ij} = 0$) and the *IFT*s computed in a fully predictive manner. However, in the case of the n-C_{10} + H_2O system, a small binary coefficient $\beta_{ij} = 0.02$ within the DGT approach was found to be necessary for numerical stability of the method used for casting the solution of the equations governing the density profiles across the interface; yet, this value is small enough to allow comparison between the DGT and LGT with $\beta_{ij} = 0$. Furthermore, as can be observed in **Figure 5.22** for CO_2 + H_2O and CH_4 + H_2O, the DGT calculations showed a strange behaviour at $T = 298$ K, as denoted by the appearance of kink in the *IFT* curves at low pressures. Such results are believed to be associated with the appearance of an infinitely steep density profile for the adsorbed species when using a value of $\beta_{ij} = 0$, as discussed in **Section 5.5**.

The agreement between computed values and experimental data for CO_2 + H_2O and n-C_{10} + H_2O seemed to improve when using bulk density dependent influence parameters, whereas for CH_4 + H_2O similar *IFT* values were computed with both constant and bulk density dependent influence parameters. These variations appear to be associated with the magnitude of the values for the pure component influence parameters, as they were taken to be either constant or calculated through bulk density dependent functions. Accordingly, influence parameters for water and methane estimated using both the *first set* (**Table 3.3)** and the *second set* (**Table 3.4)** of coefficients for the bulk density dependent functions yielded values of the same magnitude as those of the constant influence parameters (**Table 3.2**). As a result, both LGT and DGT calculations remained approximately the same for CH_4 + H_2O. On the other hand, influence parameters estimated for carbon dioxide using the *second set*, and influence parameters for *n*-decane using both the *first set* and the *second set* of coefficients for the bulk density dependent function, yielded influence parameters smaller by one order of magnitude than those of pure component constant tension influeuce parameters; this effect seems to have helped correct not only the underestimation of the interfacial values for CO_2 + H_2O and n-C_{10} + H_2O, but also the behaviour described for the *IFT* curve of CO_2 + H_2O at low pressures with the DGT. Indeed, by using no more than pure component influence parameters obtained through the use of bulk density dependent functions and coefficients listed in **Table 3.4**, the DGT is capable of predicting CO_2−H_2O *IFT* with an overall %AAD of 4.5% to the data measured in the present work [118]. In the case of the LGT, even though the influence parameters are not used in the calculation of the density profiles, their impact on the energy of the interface and, in turn, on the *IFT* values seems to be captured by the mixing rule examined, as calculation with the LGT followed the same trend described for the DGT; yet, the LGT still failed to capture the high pressure dependence of *IFT* values at T = 298 K and below the saturation pressure of CO_2.

It is important to point out that the *first set* of coefficients regressed for CO_2 using the bulk density dependent function (**Table 3.3**) also led to influence parameters smaller than that of the constant value (**Table 3.2**) at T **=** 298 K and for low pressures, with values becoming of the same magnitude as that of the constant value for higher pressures, as obtained for the isotherm at T = 373 K and over the range of pressures investigated. In this manner, the kink on calculations with the DGT for CO_2−H_2O *IFT* at T = 298 K and low pressures was also corrected with the *first set*, whereas at higher pressures as well as for the isotherm at T = 373 K, computed CO_2−H_2O *IFT* values were approximately the same as those obtained using constant influence parameters, as depicted in **Figure 5.22**. It is important to note that for the temperature examined (T = 298 K), CO_2 density varies rapidly with pressure and thus, influence parameters calculated through density dependent functions are greatly affected by such variations.

The impact of the magnitude of the influence parameters described in the foregoing paragraphs appears to be in qualitative agreement with the observations of Carey [249]. Accordingly, computed *IFT* values are strongly dependant on the particular choice of the influence parameters for the components with surface/interfacial activity, specifically CO_2 and CH_4, as shown in **Section 5.5**.

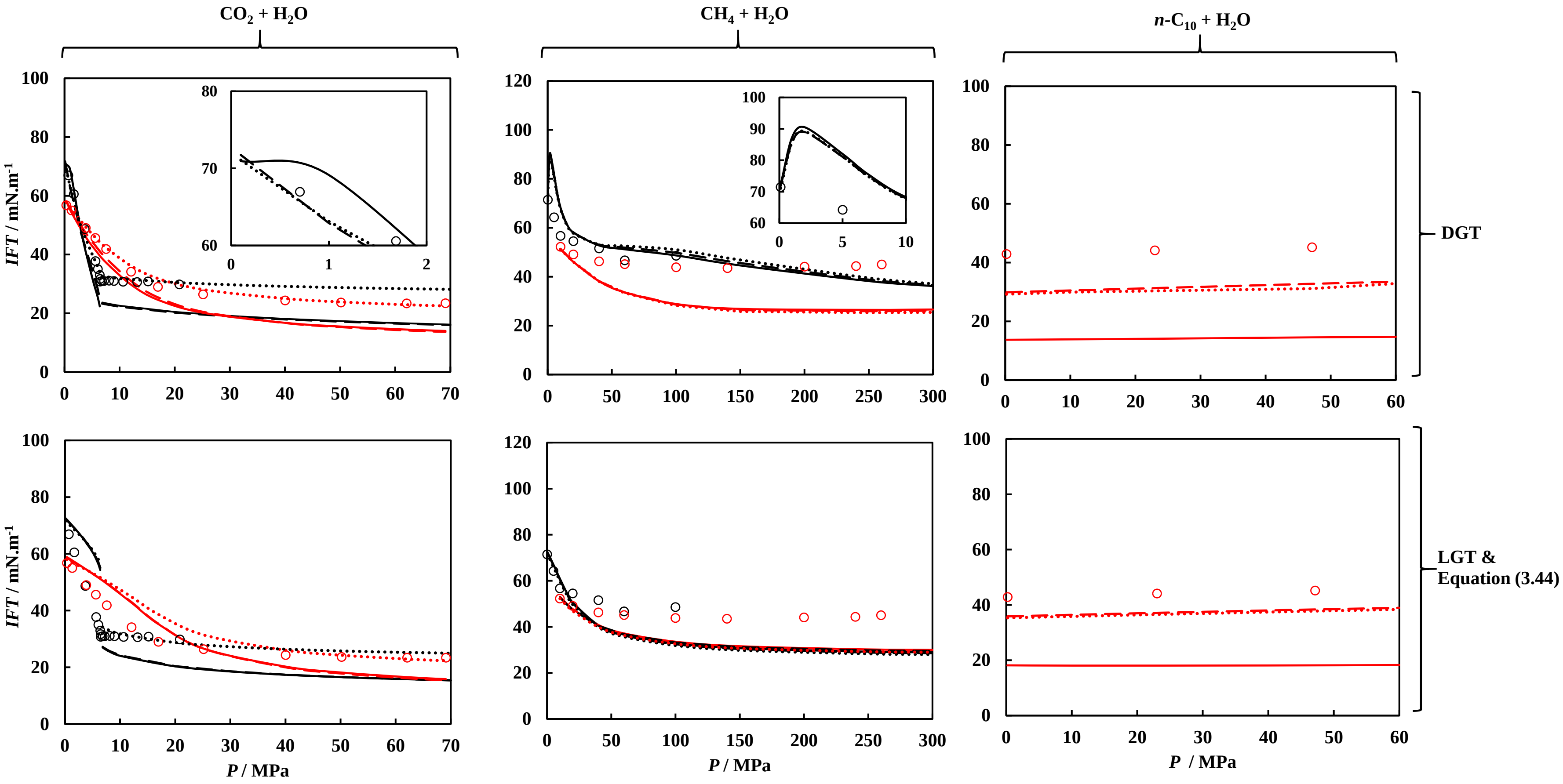

Figure 5.22. *IFT−pressure diagrams of aqueous systems of interest. Symbols represent experimental data measured in this work and gathered from literature* [31,100] *at T = 298 (black) and 373−374 K (red). Lines represent values computed with the DGT and LGT using either constant pure component influence parameters listed in **Table 3.2** (solid lines) or estimated through bulk density dependent functions and coefficients listed in **Table 3.3** (dashed lines) or **3.4** (dotted lines). β_{ij}s were fixed to 0 except for computing the IFT of the n-C_{10} + H_2O system with the DGT (β_{ij}= 0.02; see text).*

Based on what has been described, the better agreement of DGT and LGT calculations to experimental data appears to be intrinsically associated with the value of influence parameters of the non-aqueous components. In the case of CO_2 and n-C_{10}, they were positively estimated through the use of bulk density dependent functions together with specific set of coefficients regressed against surface tension data. Furthermore, the influence parameters were estimated using pure component properties in the subcritical region which, in turn, may not be enough for providing an accurate representation of the influence parameters at/or above supercritical conditions, specifically for CO_2 (T_c ~ 304 K) and CH_4 (T_c ~ 190 K). As a result, the characteristics of the interface as well as the *IFT* are not correctly described. To circumvent this constraint, it was decided to use henceforth only constant values for the influence parameters of all pure components (**Table 3.2**) and the *IFT* of binary systems corrected using a value for $\beta_{ij} \neq 0$. This procedure is in line with that followed by many others [217–219,222,250] when modelling such challenging systems.

In order to keep the number of adjustable parameters at a minimum, β_{ij}s were estimated with the help of one experimental *IFT* data point of each of the binary systems examined, at moderate pressure and temperature conditions, and then used to compute the *IFT* at other conditions. The values of β_{ij} used are listed in **Table 5.6** along with the %AAD of computed values with the DGT and LGT to experimental *IFT* data. A graphical representation of the results is provided in **Figures 5.23** and **5.24** for selected isotherms. Calculations using Sutton’s correlation have also been included in the figures to allow some discussion as well as deviations to experimental *IFT* data in **Table 5.6**; under this approach, the required density difference was calculated from pure component density [99,344], as followed by Sutton [178]. Even though Sutton [178] did not use *IFT* data for $CO_2 + H_2O$ and $N_2 + H_2O$ in his model development, deviations from this approach to *IFT* experiments for these systems are also provided.

From **Figures 5.23** and **5.24** it can be observed that the DGT gave the best *IFT* estimations, with an overall %AAD to experiments of 4.2% (**Table 5.6**). The use of a single binary interaction coefficient between influence parameters helped to improve significantly *IFT* estimations as well as to correct the behaviour described at low pressures (*i.e.*, kink). These modelling results are in agreement with that of others. For example, Niño-Amezquita and co-workers [219,222] coupled the DGT with the PC-SAFT EoS and modelled the *IFT* of $CO_2 + H_2O$, up to T = 333 K and P = 25 MPa, using β_{ij} = 0.75 and of $CH_4 + H_2O$, up to $T = 373$ K and $P = 50$ MPa, using $\beta_{ij} = 0.45$. Miqueu and co-workers [217,218] have applied the SAFT-VR Mie EoS and by considering $\beta_{ij} = 0.085$ for CO_2−H_2O and $\beta_{ij} = 0.25$ for CH_4−H_2O, they captured the behaviour of *IFT* of $CO_2 + H_2O$, up to $T = 318$ K and $P = 20$ MPa, as well as of $CH_4 + H_2O$, up to $T = 473$ K and $P = 260$ MPa. Cornelisse *et al.* [201] attempted to describe *n*-$C_6 + H_2O$ interfacial tensions using $\beta_{ij} = 0.53$ and 0.48 with the DGT in combination with the Associated Perturbed Anisotropic Chain Theory (APACT) and the PR78 EoS, respectively. In comparison, the binary interaction coefficients used in this work were $\beta_{ij} = 0.27$ for CO_2−H_2O, $\beta_{ij} = 0.39$ for CH_4−H_2O and $\beta_{ij} = 0.34$ for *n*-C_6−H_2O (**Table 5.6**). The differences in the values of β_{ij} may be linked to the different EoSs used to describe the energy of the interface and bulk properties. Despite some deviations, the results with the DGT + CPA EoS approach stand out as very good considering the broad range of pressure/temperatures conditions and the type of interfaces examined (vapour−liquid, liquid−liquid and supercritical fluid−liquid). Furthermore, this modelling approach also seems to capture the appearance of a minima in the *IFT* curve of the $CH_4 + H_2O$ and $N_2 + H_2O$ systems. *IFT*s computed by the DGT for the $CO_2 + H_2O$ system at the three-phase equilibrium line are described in detail in **Section 5.5**.

By tanking the profiles to be linearly distributed across the interface and with the aid of a single $\beta_{ij} \neq 0$, it can be observed in **Figures 5.23** and **5.24** that the LGT also allowed a good description of the *IFT* of all aqueous systems examined, except for $CO_2 + H_2O$ where significant overestimation of the *IFT* was obtained for pressures up to approximately 20 MPa. This clearly indicates that the linear density profile assumption, together with the mixing rule described in **Equation 3.44** and $\beta_{ij} = 0.21$, is not capable of providing a correct representation of the energy associated with the interface and, in turn, of the *IFT*. Similar behaviour was described by Yan *et al.* [106] when modelling CO_2−H_2O *IFT* at $T = 313$ K with the LGT in combination with the SRK72 EoS. As an attempt to improve the description of CO_2−H_2O *IFT* with the LGT, other values for β_{ij} were tested here and the mixing rule described in **Equation 3.45** was also considered; however, calculations did not show a significant overall improvement in the description of CO_2−H_2O *IFT*. In contrast, modelling results from Khosharay and Varaminian [268] suggested that, by considering temperature dependent β_{ij}s, the LGT + CPA EoS approach was capable of providing good qualitative and quantitative estimation of CO_2−H_2O *IFT;* from their work, however, it is not evident which mixing rule for the influence parameters was used. Nevertheless, all things considered, the results from the present work showed that a single, temperature independent, binary interaction coefficient $\beta_{ij} \neq 0$ is enough for providing *IFT* estimations of the examined aqueous systems with an overall %AAD to experiments of 5.1 % (**Table 5.6**).

As expected, the correlation proposed by Sutton performed well when estimating the *IFT* of hydrocarbon + water systems, with an overall %AAD to experiments of 5.4 %, as listed in **Table 5.6**. In his work, Sutton [178] also demonstrated the ability of this correlation for predicting the *IFT* of natural gas/methane mixtures containing up to 40 mole% CO_2 or up to 49 mole% N_2. However, predictions performed here for CO_2 + H_2O and N_2 + H_2O systems showed the limited transferability of this correlation for estimating the *IFT* of such systems, with %AADs exceeding 25% (**Table 5.6**). These systems appeared to follow a different dependence of *IFT*s with phase density difference data and reduced temperature when compared to that of hydrocarbon + water systems. Moreover, in the case of CO_2 + H_2O, as observed experimentally, the *IFT* values have a strong dependence on pressure and temperature, hence more correlating parameters would be needed to describe correctly this system. In addition, at this point it is also important to mention that *IFT* values predicted with Sutton's correlation for *n*-for alkanes + water systems decrease with increasing pressure, which seems to contradict the trend experimentally obtained (**Figure 5.24**).

***Table 5.6**. Summary of %AADs between measured and calculated IFT using Sutton's correlation as well as the CPA EoS in combination with the LGT and DGT models for $H_2O(1)$ + gas(2) and $H_2O(1)$ + n-alkane(2) systems. Binary interaction coefficients used within the LGT and DGT framework i.e., β_{ij}, as described in **Equation 3.26**, are given in parenthesis. NP = number of data points*

(2)	**Data Source**	***T* / K**	**NP**	***%AAD* [a] (β_{ij})**				
				Sutton's Correlation	**LGT**		**DGT**	
CO_2	This work	298 to 469	86	- [b]	16.5	(0.21)	6.5	(0.27)
CH_4	Wiegand and Franck [100]	298 to 473	23	8.6	4.4	(0.36)	3.6	(0.39)
	Tian *et al.* [104]	298 to 473	15	5.3	4.2		3.8	
	Ren *et al.* [105]	298 to 373	30	1.7	1.3		3.9	
	Khalil *et al.* [103]	311 to 473	31	5.0	3.6		3.1	
N_2	Wiegand and Franck [100]	298 to 473	23	- [c]	5.7	(0.23)	6.2	(0.27)
	Tian *et al.* [104]	298 to 473	16	- [d]	5.2		5.8	
n-C_6	Wiegand and Franck [100]	298 to 473	37	8.3	5.3	(0.28)	5.8	(0.34)
n-C_{10}	Georgiadis *et al.* [31]	298 to 443	15	5.2	2.9	(0.35)	2.4	(0.44)
n-C_{16}	Cai *et al.* [101]	298 to 353	13	3.9	1.4	(0.43)	1.1	(0.54)
	Overall		***289***	***5.4***	***5.1***		***4.2***	

[a] $\%AAD = 1/NP \times \sum_{i}^{NP} \left| \left(IFT_i^{Model} - IFT_i^{Exp} \right) / IFT_i^{Exp} \right| \times 100$

[b] 28.0, [c] 39.0 and [d] 25.3; not included in the calculation of overall *%AAD*

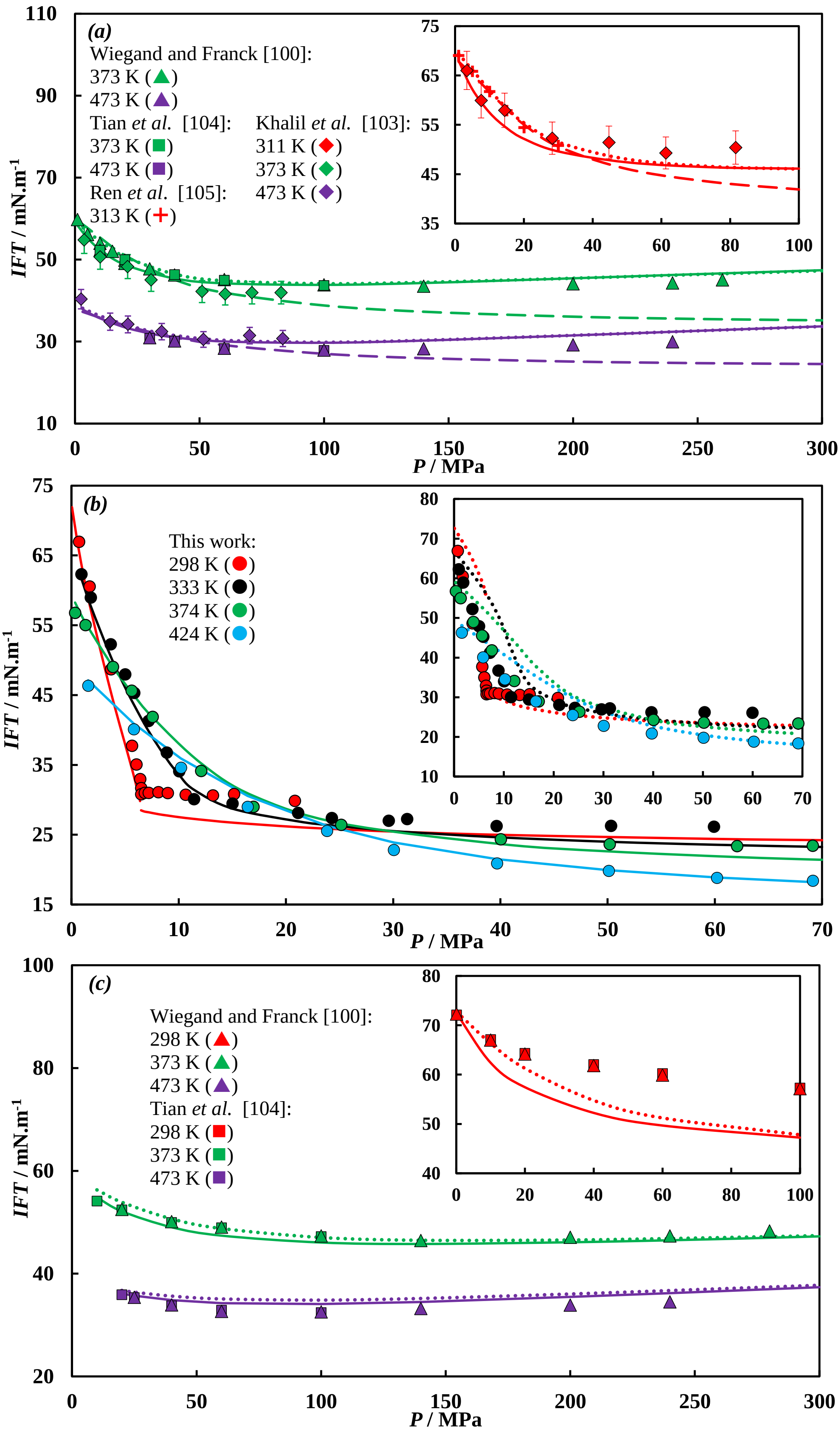

Figure 5.23. *IFT−pressure diagrams of* ***(a)*** *$CH_4 + H_2O$,* ***(b)*** *$CO_2 + H_2O$ and* ***(c)*** *$N_2 + H_2O$. Symbols represent experimental IFT data. Dashed, dotted and solid lines represented represent estimations using Sutton's correlation, LGT and DGT approaches, respectively, at pertinent conditions. See* ***Table 5.6*** *for β_{ij} used within the LGT and DGT framework.*

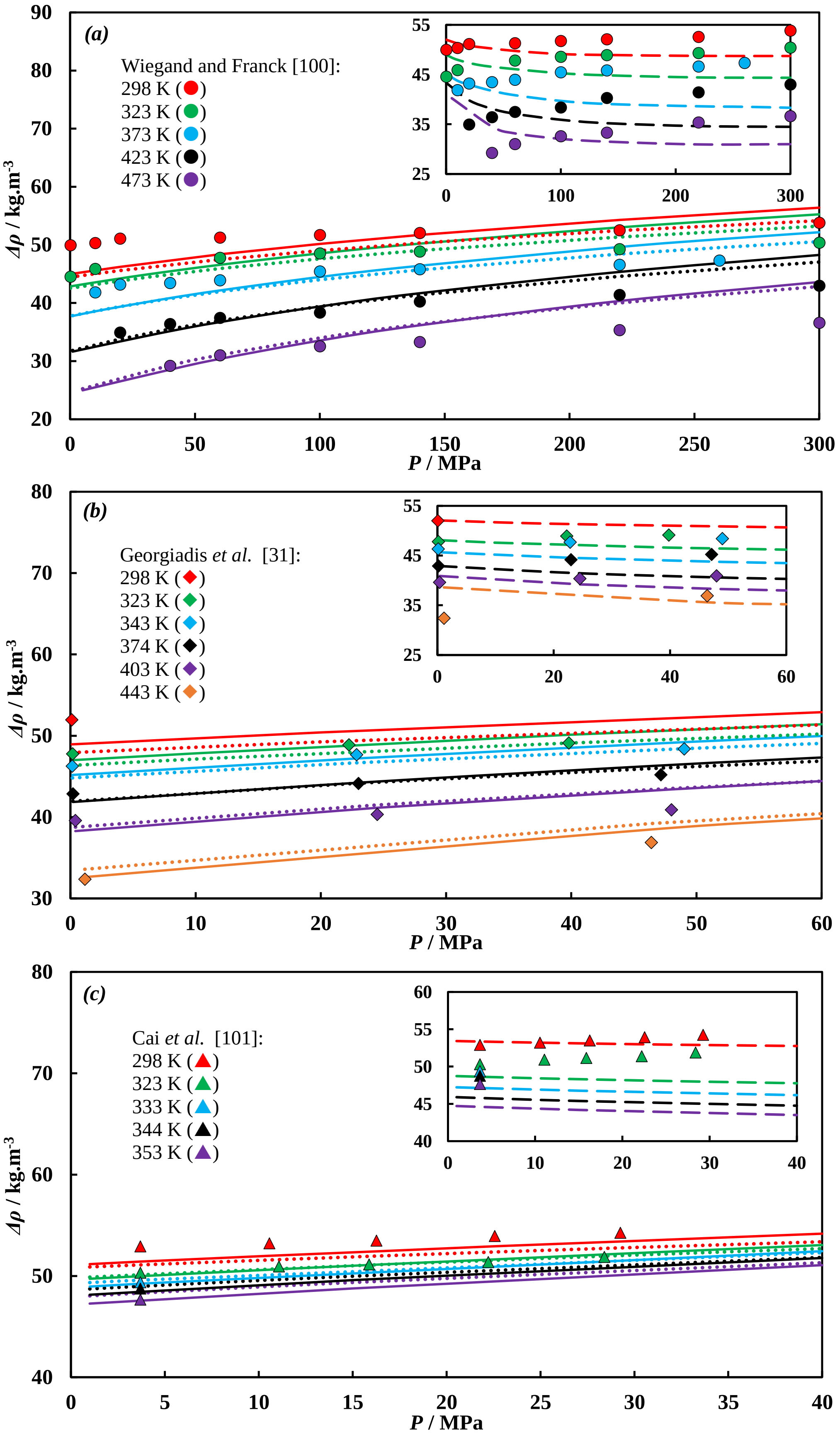

Figure 5.24. *IFT−pressure diagrams of **(a)** n-C_6 + H_2O, **(b)** n-C_{10} + H_2O and **(c)** n-C_{16} + H_2O. Symbols represent experimental IFT data. Dashed, dotted and solid lines represented represent estimations using Sutton's correlation, LGT and DGT approaches, respectively, at pertinent conditions. See **Table 5.6** for β_{ij} used within the LGT and DGT framework.*

5.4.2 Multicomponent mixtures

In this section the ability of the DGT in combination with the CPA EoS to describe fluid−liquid *IFT*s of multicomponent aqueous systems is investigated. The modelling results were compared to experimental *IFT* data as well as to phase equilibrium data whenever available and to predictions from semi-empirical/empirical models (Parachor and Sutton's correlation) and the LGT. The systems CO_2 + n-C_{10} + H_2O, CH_4 + n-C_{10} + H_2O, CH_4 + n-C_{16} + H_2O and CO_2 + CH_4 + H_2O were studied as models of CO_2 + oil/natural gas + water mixtures. In addition, *IFT* of CO_2 + brine systems were modelled with the DGT through the study of *IFT* data for single and mixed salt solutions of NaCl, KCl and $CaCl_2$ against CO_2.

CO_2 + oil/natural gas + water: Although very limited in their number of components, the systems CO_2 + n-C_{10} + H_2O, CH_4 + n-C_{10} + H_2O and CH_4 + n-C_{16} + H_2O are of key relevance as they provide insights on the behaviour of fluids phases (gaseous, oil and aqueous) present during oil and gas processes, particularly in EOR operations. On the other hand, the system CO_2 + CH_4 + H_2O can be used to mimic the variations on the interfacial tension that may occur during CO_2 storage in a depleted natural gas reservoir. For these systems, vapour−liquid and liquid−liquid *IFT* data at two- and/or three-phase equilibrium conditions are available in literature (**Section 1.3.2**). Therefore, the extension of calculations to these systems represent an important leap in the sense that one single model (DGT as well as LGT) will be used to compute the *IFT* of all interfaces involved *i.e.*, vapour−water-rich liquid (V−L_1), vapour−hydrocarbon-rich liquid (V−L_2) and water-rich liquid−hydrocarbon-rich liquid (L_1−L_2). At this point it is important to note that, in this section, the phase denoted as vapour/V corresponds to a fluid phase rich in light components, namely CO_2 and CH_4, and not necessarily to its physical state.

The multicomponent systems aforementioned include some of the binary mixtures already modelled with the CPA EoS and hence, binary interaction coefficients k_{ij} listed in **Tables 5.5** were incorporated in the calculations of the present systems. As an attempt to ensure that the best predictions of the phase compositions were obtained with the EoS, binary interaction coefficients between non-aqueous components, temperature independent, have also been used. They were estimated with the help of VLE data of corresponding binary mixtures available in literature for selected isotherms [45,50,345,346]. The binary interaction coefficients used amount: k_{ij} = -0.03 for CH_4−n-

C_{10}, k_{ij} = -0.01 for CH_4–*n*-C_{16}, k_{ij} = 0.09 for CH_4–CO_2 and k_{ij} = 0.10 for CO_2–*n*-C_{10}. Modelling results using a $k_{ij} = 0$ and $k_{ij} \neq 0$ for the corresponding binary mixtures are plotted in **Figures F.2**, **F.3** and **F.4** in **APPENDIX F**. From these it can be observed that, despite some deviations, a single k_{ij} value helped to improve the description of the phase behaviour of the binary mixtures with the CPA EoS.

Similar to what was done in previous section, it is important to assess first the ability of the selected EoS for describing the bulk properties. Unfortunately, experimental phase composition and density data for the present multicomponent systems are rather scarce in literature. Ghafri *et al.* [347], and other authors mentioned therein, measured phase equilibrium compositions of the CO_2 + CH_4 + H_2O system under multiphase conditions, including two-phase equilibria data (*i.e.*, a [CO_2 + CH_4]-rich phase and a water-rich phase), for water and an equimolar dry gas mixture at T = 323, 373 and 423 K. Forte *et al.* [348] investigated the three-phase equilibrium compositions of the CO_2 + *n*-C_{10} + H_2O system at temperatures ranging from 323 to 413 K and pressures up to the point at which the CO_2-rich and *n*-decane-rich phases became miscible. However, to the author's knowledge, experimental phase composition data for CO_2 + *n*-C_{10} + H_2O in the two-phase region as well as for CH_4 + *n*-C_{10} + H_2O and CH_4 + *n*-C_{16} + H_2O, at conditions similar to those of the *IFT* experiments examined here, were not available in literature. Regarding the effect of pressure and temperature on the density of mutually saturated phases, only data for the systems CH_4 + *n*-C_{10} + H_2O and CH_4 + *n*-C_{16} + H_2O [124] were available at the time of this work.

As an example, **Figure 5.25** shows a comparison between experimental [347] and CPA EoS predicted equilibrium constants K of each component in a [$0.5CO_2$ + $0.5CH_4$] (molar fraction) + H_2O mixture at T = 323 K. K values are defined as $K_i = y_i/x_i$, where y corresponds to the mole fraction of component i in the [CO_2 + CH_4]-rich phase and x corresponds to the mole fraction of component i in the water-rich phase. Because the overall feed composition of this mixture was not known, CPA EoS predictions plotted in **Figure 5.25** correspond to the average of predictions computed considering two different global aqueous fractions (feed), zH_2O = 0.1 and zH_2O = 0.9. As can be observed, predicted K values of CH_4 and CO_2 are in good agreement with those determined using experimental solubility data, whereas K values of H_2O are generally underpredicted by the CPA EoS.

To allow some discussion, *K* values of water in $CO_2 + H_2O$ and $CH_4 + H_2O$ mixtures, under two-phase equilibrium conditions, computed through the models of Duan and co-workers [320,349] are also plotted in **Figure 5.25**. Comparison of *K* values of water obtained through the models of Duan and co-workers [320,349] for the constituent binaries to *K* values calculated using experimental data from Ghafri *et al.* [347] for $[0.5CO_2 + 0.5CH_4] + H_2O$ [347] suggests that water distribution between the $[CO_2 + CH_4]$-rich and water-rich phases are only slightly affected by the presence of approximately 50 mole% of methane, as the *K* values of water approach more closely to those in the $CO_2 + H_2O$ system.

In contrast to the above, as depicted in **Figure 5.26**, water content measurements performed in a $[0.9469CO_2 + 0.0531CH_4]$ (molar fraction) + H_2O mixture [350] at T = 323 K suggest a different behaviour. Accordingly, water solubility in the $[CO_2 + CH_4]$-rich phase is considerable reduced due to the presence of approximately 5 mole% of methane, as the water content values for this mixture approach more closely to those in the $CH_4 + H_2O$ system; this behaviour appears to be adequately predicted by the CPA EoS. Moreover, from **Figure 5.26** it can also be observed that experimental water content values reported by Ghafri *et al.* [347] for the $[0.5CO_2 + 0.5CH_4] + H_2O$ mixture at low pressures significantly exceed those predicted by the CPA EoS as well as those of the model of Duan and co-workers [320,349] in the constituent binary aqueous mixtures, which should approach to the ideal behaviour as pressure is decreased. The estimated experimental uncertainties reported by Ghafri *et al.* [347] for the measurements in the $[0.5CO_2 + 0.5CH_4] + H_2O$ mixture are relatively small and therefore, they do not have a significant impact on the reported solubility values. In this sense, the differences encountered between predictions from the CPA EoS and experimental data from Ghafri *et al.* [347] may be partially due to the experimental difficulties associated with this type of measurements, in particular the water content in the $[CO_2 + CH_4]$-rich phase.

To conclude the analysis of the capabilities of the CPA EoS for describing the phase behaviour of the examined ternary aqueous systems, density predictions were compared to measured density data of the $CH_4 + n\text{-}C_{10} + H_2O$ and $CH_4 + n\text{-}C_{16} + H_2O$ systems [124], as depicted in **Figure 5.27**. The horizontal dashed line in **Figure 5.27*b*** represents the dew point pressure of the hydrocarbon-rich phase (P_{dew} = 49.97 ± 0.07 MPa [124]) and separates the two- and three-phase regions. Despite the limited number of density measurements, it can be observed that the CPA EoS appears to adequately predict the effect of pressure on the density of all phases, with an overall AAD% to experiments of 7.3%, validating to some extent, the selection of this EoS for modelling the bulk properties of the present mixtures.

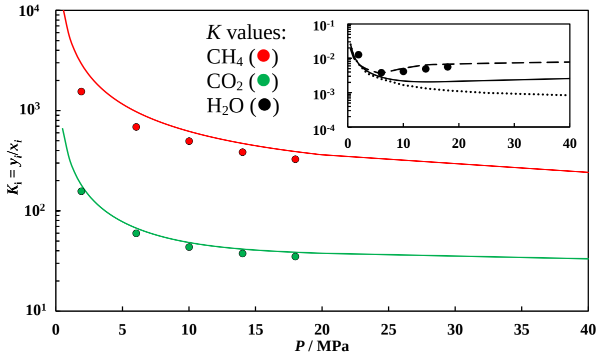

Figure 5.25. *K values−pressure diagram of [0.5CO_2 + 0.5CH_4] + H_2O at T = 323 K. Solid symbols represent K values calculated using experimental vapour−liquid equilibrium data from Ghafri et al.* [347]. *Solid lines represent K values predicted by CPA EoS. Dashed and dotted lines represent K values of H_2O in CO_2 + H_2O and CH_4 + H_2O systems, respectively, calculated using solubility data predicted by the model of Duan and co-workers* [320,349].

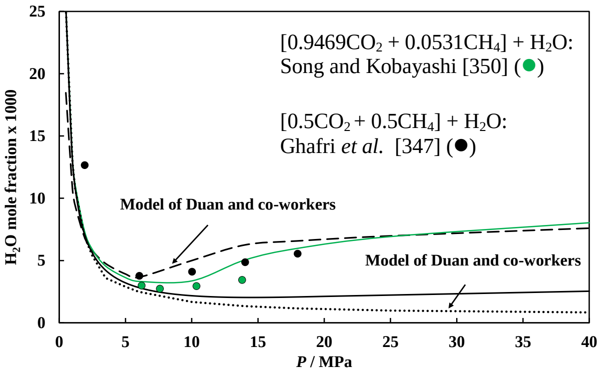

Figure 5.26. *Water content−pressure diagram of CO_2 + CH_4 + H_2O mixtures at T = 323 K. Solid lines represent CPA EoS predictions for the CO_2 + CH_4 + H_2O mixtures at pertinent compositions.*

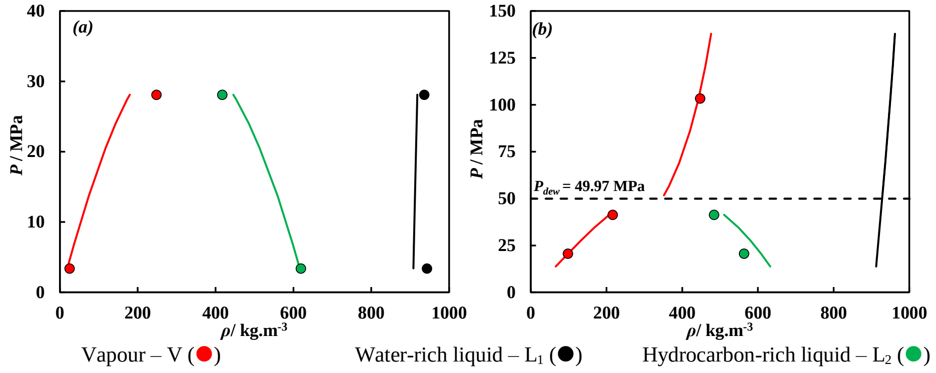

Figure 5.27. *Pressure−density diagrams of the* ***(a)*** *CH_4 + n-C_{10} + H_2O and* ***(b)*** *CH_4 + n-C_{16} + H_2O systems at T=423 K. Symbols represent experimental density data* [124]. *Solid lines represent CPA EoS predictions. Dashed horizontal line in* ***(b)*** *represent the dew point pressure of the hydrocarbon-rich phase determined experimentally* [124]*; the overall molar composition of this mixture is: 0.4353CH_4 +0.0333 n-C_{16} + 0.5314H_2O.*

The %AADs between experimental *IFT* data of the ternary aqueous systems and *IFT*s computed using the LGT and DGT approaches in combination with the CPA EoS are listed in **Table 5.7**. Again, the mixing rule given by **Equation 3.44** was used in the LGT model. The β_{ij} coefficients have been taken equal to those estimated for the corresponding binary mixtures with the LGT and DGT (**Table 5.6**). However, in the case of the framework of the DGT, an additional correction was necessary for the matrix of influence parameters ($[c_{ij}]$) of the present ternary mixtures to be positive definite *i.e.*, for thermodynamic stability of the interface. Following Cornelisse's approach [250], this problem was circumvented by readjusting one of the β_{ij}. For the systems examined here it was decided to consider a binary interaction coefficient $\beta_{ij} \neq 0$ between non-aqueous components. The smallest values that turned the matrix $[c_{ij}]$ positive definite within each ternary mixture were found to amount: $\beta_{ij} = 0.002$ for CH_4−*n*-C_{10}, $\beta_{ij} = 0.016$ for CH_4−*n*-C_{16}, $\beta_{ij} = 0.014$ for CO_2−CH_4 and $\beta_{ij} = 0.025$ for CO_2−*n*-C_{10}. It is important to remember that, as shown in **CHAPTER 4**, the DGT was capable of predicting (*i.e.*, $\beta_{ij} = 0$) the interfacial tension of CO_2 + *n*-alkane and CH_4 + *n*-alkane mixtures with remarkably low deviations to experimental data and hence, the new binary interaction coefficients were only used to ensure that the eigenvalues of the matrix $[c_{ij}]$ are non-negative [250]. In this sense, *IFT*s computed for ternary mixtures with the DGT are also regarded henceforth as predictions. A graphical comparison between *IFT* predictions and experimental data is shown in **Figures 5.28** through **5.31**. For comparison purposes, V−L_1 and L_1−L_2 *IFT* predictions using Sutton's correlation and V−L_2 *IFT* predictions using the Parachor approach were also included in these figures and deviations to experimental data listed in **Table 5.7**. The required bulk phase properties (compositions and densities) were also predicted with the CPA EoS. As followed in **CHAPTER 4**, the Parachor of non-aqueous components were estimated using Fanchi's correlation, whereas for H_2O a Parachor value of 52 was used [171]. Calculations for CO_2 + *n*-C_{10} + H_2O correspond to the average of predictions computed considering two different aqueous fractions (feed), $zH_2O = 0.1$ and $zH_2O = 0.5$. Two-phase *IFT* data reported by Jennings and Newman [123] for CH_4 + *n*-C_{10} + H_2O were not included in this analysis as the *IFT* data reported therein for *n*-C_{10} + H_2O were observed to be lower than that reported by other authors [31,101].

As can be observed from **Figures 5.28** through **5.31**, the best *IFT* predictions were obtained with the DGT, with an overall %AAD to experiments of 9.7% (**Table 5.7**). The largest deviations were observed between predicted V−L_2 *IFT* and that experimentally determined for CH_4 + n-C_{10} + H_2O (%AAD = 22.8 %) . In this region, *IFT* values are rather small as the saturation pressure of the hydrocarbon-rich phase is approached (complete miscibility between the vapour and hydrocarbon-rich liquid phases). Despite the increase on the associated experimental uncertainties, and similar to what was described for CO_2/CH_4/N_2 + hydrocarbon systems in **CHAPTER 4**, it seems that the DGT + CPA EoS approach is also not capable of adequately describing such low *IFT* values. Nonetheless, when dealing with high V−L_1 and L_1−L_2 interfacial tensions, the DGT outperformed all other models examined, in particular for the CH_4 + n-C_{10} + H_2O (**Figure 5.30**) and CH_4 + n-C_{16} + H_2O (**Figure 5.31**) systems at pressures near the complete miscibility between the V and L_2 phases. Furthermore, as can be observed in **Figures 5.28** and **5.29**, the DGT was capable of effectively accounting for the decrease on the *IFT* values due to the presence of CO_2 which, in turn, further confirms the robustness of this model.

The performance of the LGT is not as good as that described previously for the DGT, with LGT predictions showing an overall %AAD to experiments of 17.8% (**Table 5.7**). The largest deviations were generally obtained between predictions and experimentally determined V−L_1 and V−L_2 *IFT*, as depicted in **Figures 5.28**, **5.30** and **5.31,** with %AADs ranging between 15.4 and 32.7 %. As explained in the next section with the aid of density profiles computed with the DGT, the inaccuracy of *IFT* predictions obtained with the LGT is believed to be associated with the accumulation of species in the interfacial region. Furthermore, although the pressure dependence of L_1−L_2 *IFT* of the CO_2 + n-C_{10} + H_2O system appeared to be adequately described, the LGT consistently overpredicted the *IFT* of this system, as depicted in **Figure 5.29**.

By using the CPA EoS predicted phase compositions and densities, Sutton’s correlation yielded V−L_1 and L_1−L_2 *IFT* values with an overall %AAD to experiments of 19.4 %, whereas an overall %AAD of 20.1% was obtained between experiments and predicted V−L_2 *IFT* values with the Parachor method, as listed in **Table 5.7**. The largest deviations with Sutton’s correlation were observed between predicted and experimental V−L_1 *IFT* values of the CH_4 + n-C_{10} + H_2O system (%AAD = 50.4 %), and with the Parachor method between predicted and experimental V−L_2 *IFT* values of the CH_4 + n-C_{16} + H_2O system (%AAD = 31.4 %). Moreover, despite showing low %AADs, Sutton’s correlation was unable to describe the decrease of V−L_1 *IFT* values of the CO_2 + CH_4 + H_2O system with increasing content in CO_2, at low pressures (**Figure 5.28**), as well as the correct pressure dependence of L_1−L_2 *IFT* values of the CO_2 + *n*-C_{10} + H_2O system, at high temperatures (**Figure 5.29**). Even though a comparison with more systems is recommended, these results help to highlight the limited transferability of empirical models such as the Parachor method and Sutton's correlation.

***Table 5.7**. Summary of %AADs between measured and predicted IFT using the CPA EoS in combination with Sutton's correlation, Parachor, LGT and DGT models for ternary aqueous systems. NP = number of data points.*

System	Data Source	*T* / K	NP	%AAD $^{a)}$			
				Sutton's correlation	Parachor	LGT	DGT
CO_2 + CH_4 + H_2O	[105]	333					
V−L_1			24	8.8		15.4	6.2
CO_2 + *n*-C_{10} + H_2O	[31]	323 to 443					
L_1−L_2			21	8.9		16.0	8.0
CH_4 + *n*-C_{10} + H_2O	[125]	423					
V−L_1			4	50.4		23.6	8.0
V−L_2 $^{b)}$			4		8.8	37.2	22.8
L_1−L_2			4	20.8		16.1	15.7
CH_4 + *n*-C_{16} + H_2O	[126]	423					
V−L_1			11	17.5		6.5	5.3
V−L_2 $^{b)}$			4		31.4	23.3	8.2
L_1−L_2			4	10.4		4.5	3.7
Overall			***76***	***19.4***	***20.1***	***17.8***	***9.7***

$^{a)}$ $\%AAD = 1/NP \times \sum_i^{NP} \left| \left(IFT_i^{Model} - IFT_i^{Exp} \right) / IFT_i^{Exp} \right| \times 100$

$^{b)}$ Only *IFT* data > 1.5 $mN.m^{-1}$ was considered.

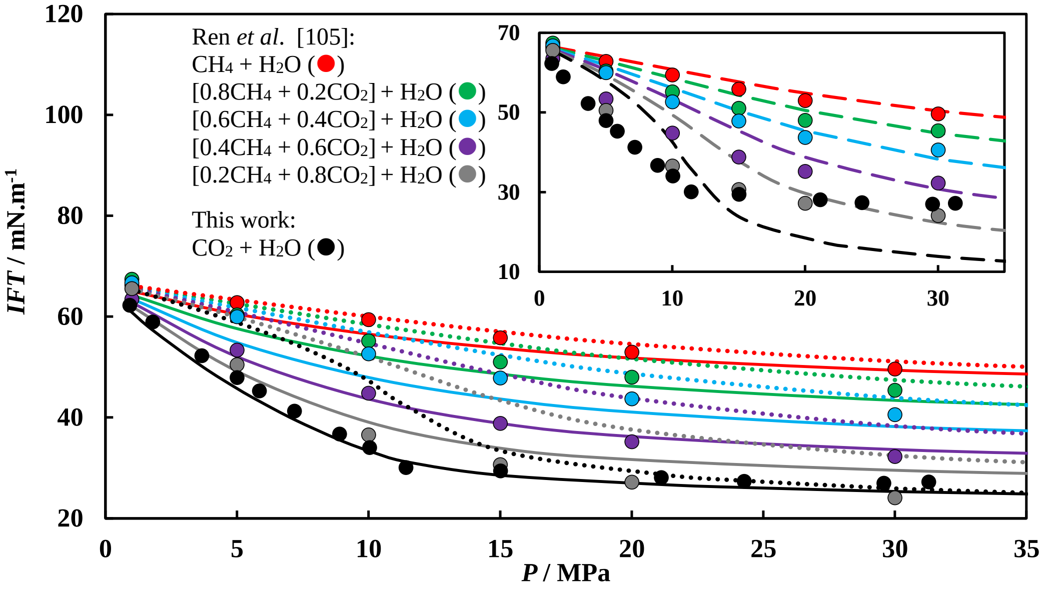

***Figure 5.28.** IFT−pressure diagram of CO_2 + CH_4 + H_2O mixtures at T = 333 K. Symbols represent experimental V−L_1 IFT data from Ren et al.[105] and from the present work. Lines represent predicted IFT values with Sutton's correlation (dashed lines), LGT (dotted lines) and DGT (solid lines) in combination with the CPA EoS.*

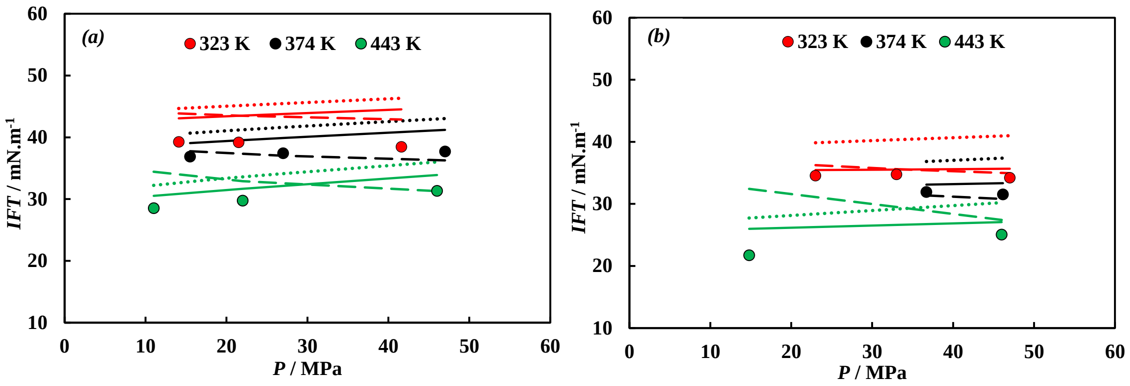

Figure 5.29. *IFT−pressure diagrams of* ***(a)*** *[0.2 CO_2 + 0.8n-C_{10}] + H_2O and* ***(b)*** *[0.5 CO_2 + 0.5n-C_{10}] + H_2O* ***(b)*** *mixtures. Solid symbols represent experimental L_1−L_2 IFT data* [31]. *Lines represent predicted IFT values with Sutton's correlation (dashed lines), LGT (dotted lines) and DGT (solid lines) models in combination with the CPA EoS.*

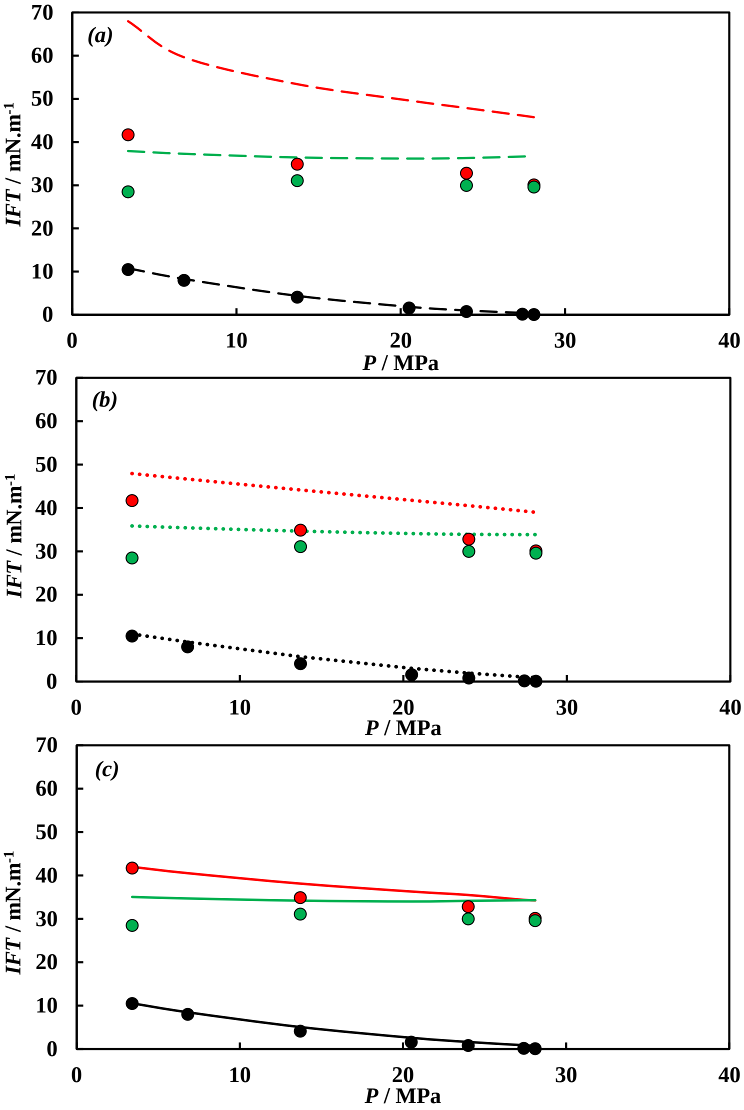

Figure 5.30. *IFT−pressure diagrams of the CH_4 + n-C_{10} + H_2O system at T = 423 K. Solid symbols represent experimental IFT data* [125]*: V−L_1 (red), V−L_2 (black) and L_1−L_2 (green). Lines represent predicted IFT values with* ***(a)*** *Sutton's correlation + Parachor,* ***(b)*** *LGT and* ***(c)*** *DGT models in combination with the CPA EoS.*

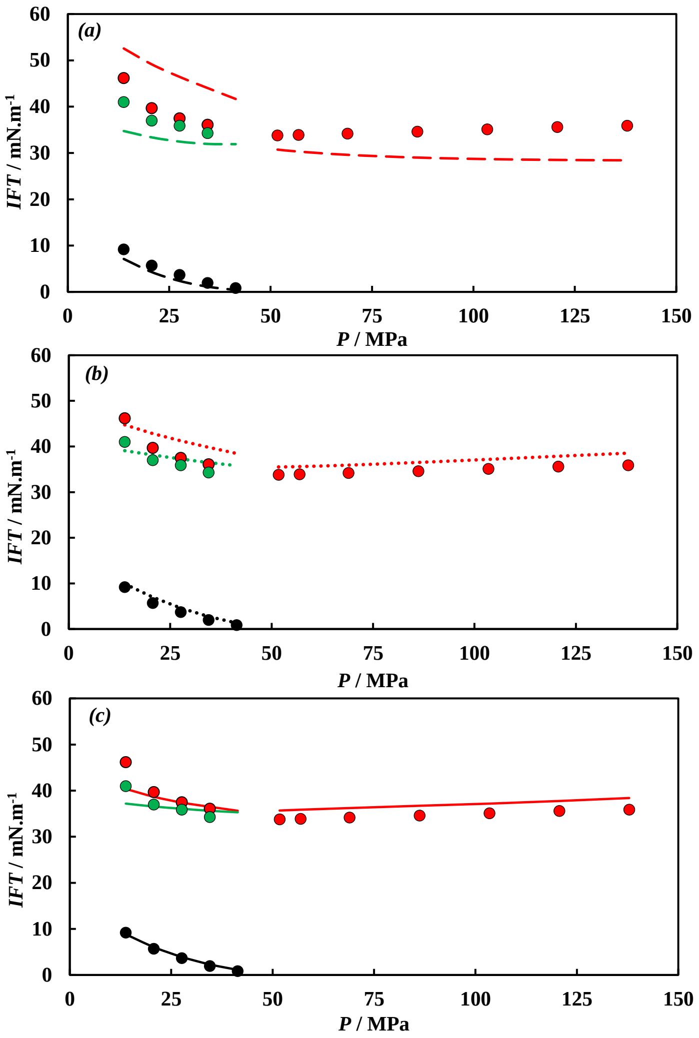

Figure 5.31. *IFT−pressure diagrams of the CH_4 + n-C_{16} + H_2O system at T = 423 K. Solid symbols represent experimental IFT data* [126]*: V−L_1 (red), V−L_2 (black) and L_1−L_2 (green). Lines represent predicted IFT values with* ***(a)*** *Sutton's correlation + Parachor,* ***(b)*** *LGT and* ***(c)*** *DGT models in combination with the CPA EoS*

CO_2 + water + salt: The modelling of the effect of salts on CO_2−H_2O *IFT* is of key importance for the successful design and optimisation of CO_2 sequestration projects. The development of a predictive tool capable of adequately estimating CO_2−brine *IFT* would help overcoming the cost as well as the difficulties associated with the experimental determination of this property.

As explained in **Section 1.3.2**, the increase in *IFT* upon the addition of salts appears to be related to their effect on the bulk properties as well as to the negative surface excess of ions at the interface. Based on this, it is now explored the idea of predicting the *IFT* between CO_2 and brines solutions by considering only the *IFT* increase due to effects associated with changes on the phase equilibria. In this approximated approach, the impact of salts on the bulk properties are modelled via the CPA EoS combined with an electrolyte model and the accompanying *IFT* predicted via the density profiles of CO_2 and H_2O in a hypothetical salt-free system computed using the DGT. In other words, the change in *IFT* is modelled by considering the salting-out effect and its influence on the energy of both bulk phases and interface in a salt-free system. Such approach does not account for the depletion of ions at the interface; however, initial results showed [103] that this method lead to successful predictions of the *IFT* of CH_4 + NaCl(aq) systems with salt molalities up to 1.91 $mol.kg^{-1}$. In this section, the model is extended to CO_2 + brine systems and the validity of such idea (approximation) is tested for higher salt molalities.

The impact of salts on the composition of the equilibrated phases has been considered by using the method introduced by Aasberg-Petersen *et al.*[351] and extended to the CPA EoS by Haghighi *et al.* [352]. Accordingly, the shift in the equilibrium conditions (*i.e.*, $\mu_i^V = \mu_i^L$) is evaluated by the addition of an electrostatic contribution to the fugacity coefficient of components in the aqueous phase [351]:

$$\ln \phi_i = \ln \phi_i^{EoS} + \ln \gamma_i^{EL} \tag{5.5}$$

where ϕ_i^{EoS} is the fugacity coefficient of component *i* computed by the CPA EoS and γ_i^{EL} is the Debye-Hückel activity coefficient expressed as [351]:

$$\ln \gamma_i^{EL} = \frac{2Ah_{is}M_m}{B^3} f(BI^{1/2}) \tag{5.6}$$

where M_m is the salt-free mixture molecular weight, h_{is} is the adjustable interaction coefficient between the salt and non-electrolytic components and, *A* and *B* are parameters expressed as function of temperature and the dielectric constant of water. The parameters *A* and B were transferred directly from the work of Aasberg-Petersen *et al.* [351] whereas coefficients h_{is}, specifically optimised for CPA EoS, were used.

Water–salt interaction coefficients ($h_{water-salt}$) were taken equal to those of the work of Haghighi *et al.* [87] and CO_2–salt coefficients (h_{CO_2-salt}) were regressed here against solubility data of CO_2 in single salt systems for salt molalities up to 5 $mol.kg^{-1}$. The regressed coefficients, assumed to be function only of temperature, are listed in **Table 5.8** for three salts (NaCl, KCl and $CaCl_2$) along with the range of salinity and temperature conditions of the experimental data used. The extension of calculations to mixed salt solutions was performed by employing the approach suggested by Patwardhan and

Kumar [353], and further tested by Tohidi-Kalorazi [354] and Haghighi [352]. Accordingly, the activity of a mixed salt solution (a_w) can be evaluated by considering the activity of the corresponding single salt solutions and calculated as follows [353]:

$$\log a_w = \sum_i^{salt} y_i \log a_{w,i}^0 \tag{5.7}$$

where $a_{w,i}^0$ represents the activity of a single electrolyte solution of the same ionic strength ($I = 0.5 \sum_j m_j z_j^2$, m_i and z_j correspond to the molality and charge of the j^{th} ion, respectively) as that of the mixed electrolyte solution and y_i represents the ionic strength fraction of the electrolyte *i*. The expression above does not include any empirical constants and thus, the contribution of the electrostatic term for mixed salt solutions is obtained in a fully predictive manner.

***Table 5.8**. Optimised CO_2−salt interaction coefficients.*

Salt	**Data Source**	**Salt molality m_{salt} / mol.kg^{-1}**	***T* / K**	h_{CO_2-Salt}
NaCl	[324,355–357]	0.3 to 5.0	293 to 473	$-3.6813\times10^{-6}\ T^2 + 2.8025\times10^{-3}\ T - 0.4808$
KCl	[358,359]	1.0 to 4.5	313 to 433	$-1.4933\times10^{-6}\ T^2 + 1.0512\times10^{-3}\ T - 0.1624$
$CaCl_2$	[359,360]	0.3 to 5.0	309 to 424	$-1.2369\times10^{-6}\ T^2 + 8.5643\times10^{-4}\ T - 0.1155$

As an example, a comparison between model estimates and experimental data for the solubility of CO_2 in NaCl and $CaCl_2$ solutions is provided in **Figures F.5** and **F.6** in **APENDIX F**. From these it can be observed that the CPA EoS + Electrolyte model can successfully account for the decrease in CO_2 solubility over a broad range of salt molalities. Moreover, as can be seen in **Figures F.7** through **F.9** in **APENDIX F**, the use of the regressed CO_2−salt coefficients (**Table 5.8**) allowed a good prediction of the water content in the CO_2-rich phase of CO_2 + brine systems as well as of CO_2 solubility in mixed salt solutions composed of NaCl, KCl and $CaCl_2$. It is important to note that the value of k_{ij} used for CO_2−H_2O throughout the present calculations was the same as that calculated using the expression listed in **Table 5.5**.

Having shown the capabilities of the CPA EoS + Electrolyte model for describing the phase equilibria of CO_2 + brines systems, it is now possible to combine this model with the DGT and to compute the density profiles of CO_2 and H_2O in a hypothetical salt-free system and, in turn, the associated *IFT*. By keeping the binary interaction coefficient β_{ij}

= 0.27 for CO_2–H_2O within the DGT framework (**Table 5.6**), the *IFT* of CO_2 + brines systems was predicted and the results compared to experimental data measured in the present work as well as to that gathered from literature (**Section 1.3.2**). Results are plotted in **Figures 5.32** and **5.33** for selected isotherms.

As shown in **Figures 5.32** and **5.33,** the model can adequately predict the increase in *IFT* due to the presence of salts such as NaCl, KCl and $CaCl_2$ as well as their mixtures; good agreement with experimental data measured here for CO_2 + NaCl(aq) at T = 333 and 373 K and salt molalities up to 1.98 mol.kg^{-1} is observed. In addition, as substantiated experimentally [113,115,119,129,130], predicted *IFT* values increase linearly with salt molalities; as an example, results for CO_2 + [0.864 NaCl + 0.136 KCl](aq) at T = 373 K and selected isobars are plotted in **Figure 5.34**. However, for very concentrated brines, and depending on the computed CO_2–H_2O *IFT* for the examined isotherm, the model appears to overpredict severely the *IFT* of CO_2 + brine systems, in particular for brines containing $CaCl_2$. It is important to note that *IFT* data measured by Aggelopoulos *et al.* [129,130] for diluted brines containing $CaCl_2$ persisted in being lower than CO_2–H_2O *IFT* measured in the present work (**Figures 5.32*b*** and **5.33*b***), similar to what was described previously for *IFT* data reported by others (**Sections 1.3.2** and **5.3.3**); yet, the differences between predicted and experimentally determined *IFT* values at higher salt concentrations cannot be attributed to the inconsistencies in the experiments alone. In turn, such overprediction of *IFT* values may be most probably due to the strong salting-out effect of $CaCl_2$ compared to NaCl or KCl, which is intrinsically related to the ionic strength of the brine. Based on these observations and on the modelling results for the examined brines, it can be argued that such approximated treatment of the rise in *IFT* due the presence of salts (via solubility change) appears to be adequate only for brines with low and medium ionic strength (up to I = 2.7 mol.kg^{-1} or 0.9 $m_{\mathrm{CaCl_2}}$) under the temperature conditions examined.

The modelling results explained above are better interpreted by means of the Gibbs adsorption equation. Accordingly, the change in CO_2–brine *IFT* ($d\gamma$) can be related to the chemical potentials (μ) of CO_2 and ions as follows [361]:

$$-d\gamma = \Gamma_{CO_2}\mu_{CO_2} + \Gamma_{cation}\mu_{cation} + \Gamma_{anion}\mu_{anion} \qquad \text{at constant } T \qquad \textbf{\textit{5.8}}$$

where Γ_i is the surface/interfacial excess (or adsorption) of species *i*. By convention, a dividing surface is chosen such that $\Gamma_{H_2O} = 0$. From this equation it can be shown that changes on CO_2–brine *IFT* are related to the individual contribution of each species in the system: increasing the chemical potential of a species with positive surface excess (such as CO_2) would result in a decrease in *IFT*, whereas increasing the chemical potential of a species with negative surface excess (such as the ions examined) would result in an increase in *IFT*. Therefore, it can be concluded that the differences between predictions and experimental *IFT* data for CO_2 + brines are due to the fact that in the model only the salting-out effects were accounted for (*i.e.*, decrease in the chemical potential of CO_2) while the contribution of ions to the *IFT* has been neglected.

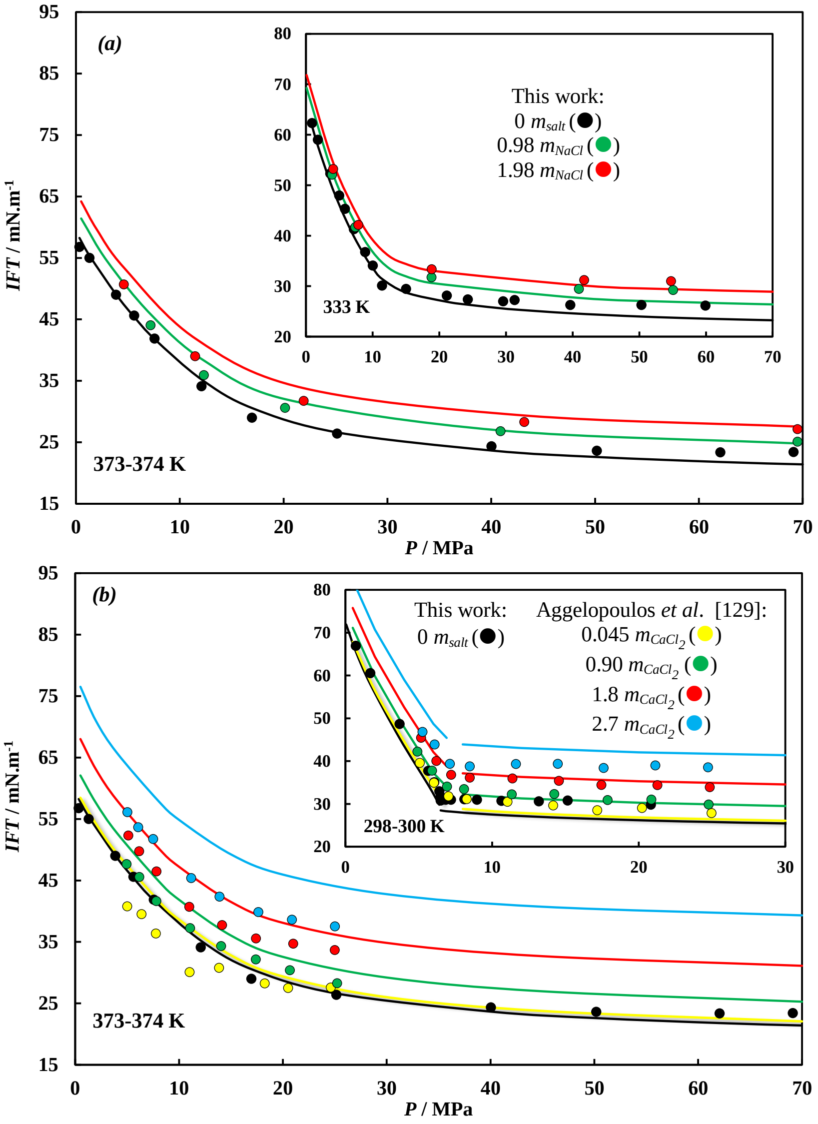

Figure 5.32. *IFT–pressure diagrams of **(a)** CO_2 + NaCl(aq) and **(b)** CO_2 + $CaCl_2$(aq) systems. Solid lines represent DGT predictions at pertinent salt molalities and temperatures. Predictions were obtained using a binary interaction coefficient β_{ij} = 0.27, as estimated for the CO_2 + H_2O system (**Table 5.6**).*

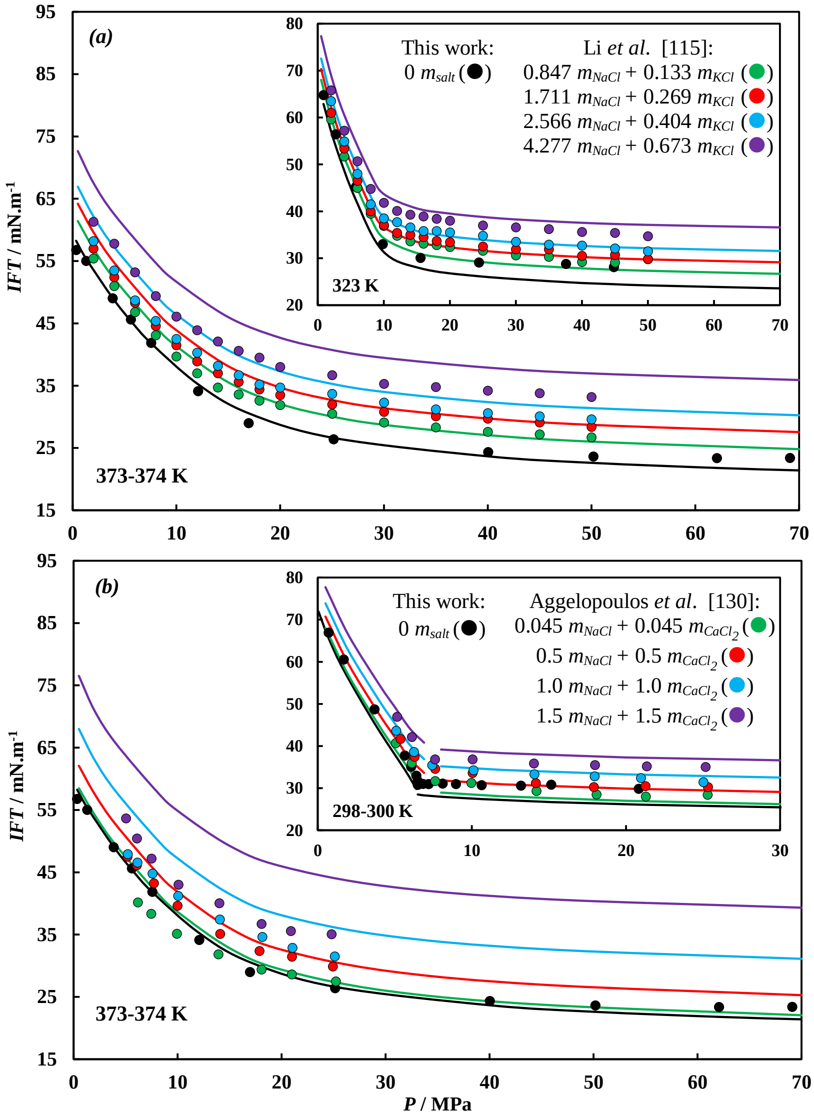

Figure 5.33. *IFT−pressure diagrams of **(a)** CO_2 + [NaCl + KCl](aq) and **(b)** CO_2 + [NaCl + $CaCl_2$](aq) systems. Solid lines represent DGT predictions at pertinent salt molalities and temperatures. Predictions were obtained using a binary interaction coefficient β_{ij} = 0.27, as estimated for the CO_2 + H_2O system (**Table 5.6**).*

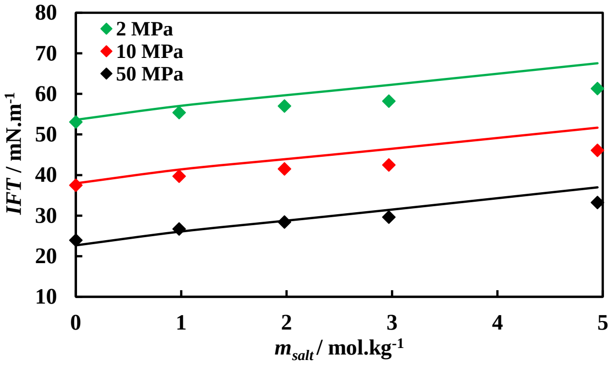

Figure 5.34. *IFT−total salt molality diagram of CO_2 +[0.864 NaCl + 0.136 KCl](aq) systems at T = 373 K. Symbols represent experimental data from Li et al. [115] for fixed pressure. IFT data points for zero salt molality were interpolated from measurements performed in this work. Full lines represent DGT predictions.*

5.5 Microstructure of Interfaces

As done in **Section 4.5** for the hydrocarbon systems, the density profiles of the aqueous systems computed using the DGT are analysed in the present section and the impact of the microstructure of the interface on the *IFT* is discussed.

First, the effect of using a binary interaction coefficient $\beta_{ij} \neq 0$ is described. As an example, the density profiles computed using different values for β_{ij} are plotted in **Figures 5.35**, **5.36** and **5.37** for the systems CO_2 + H_2O, CH_4 + H_2O and n-C_{10} + H_2O at selected temperatures and pressures. The density profiles of the CO_2 + H_2O (**Figure 5.35**) and CH_4 + H_2O (**Figure 5.36**) systems show a local enrichment of the interface in CO_2 and CH_4 molecules, as noticed by the appearance of adsorption peaks in the density profiles of CO_2 and CH_4, whereas the density profile of water follows the usual *tanh* shape, increasing monotonically from the CO_2/CH_4-rich phase to the water-rich phase. It can also be observed from these figures that the use of $\beta_{ij} = 0$ leads to the computation of very sharp peaks (infinitely steep) at the interface; interfacial tensions associated with these profiles are those plotted in **Figure 5.22**, where a kink in the *IFT*−pressure diagram was observed. The appearance of such steep gradients creates some numerical convergence problems which are rather difficult to overcome [250]. A simple way of avoiding these problems is by using a value for $\beta_{ij} \neq 0$. For the CO_2 + H_2O and CH_4 + H_2O systems, the use of positive and increasing values of β_{ij} results in a reduction of the maximum concentration of the components with interfacial activity which, in turn, leads to a better agreement between the accompanying *IFT* and that experimentally determined, as previously described.

Density profiles of the n-C_{10} + H_2O system computed using $\beta_{ij} = 0.02$ suggest some degree of adsorption of n-C_{10} in the interface, as depicted in the insert of **Figure 5.37**; however, the use of the optimal value for *IFT* estimation ($\beta_{ij} = 0.44$) leads to the computation of less steep and broader density profiles for n-C_{10} and H_2O and apparently reduces the amount of n-C_{10} in the interface. The effect of broadening the interface would lead to a decrease in *IFT*, whereas the removal of n-C_{10} molecules from the interface would result in increase in *IFT*. Since better agreement with experimental *IFT* data was achieved using higher values of β_{ij}, the withdrawal of n-C_{10} molecules from the interface appears to have a stronger influence on the computed *IFT* values at the thermodynamic conditions examined.

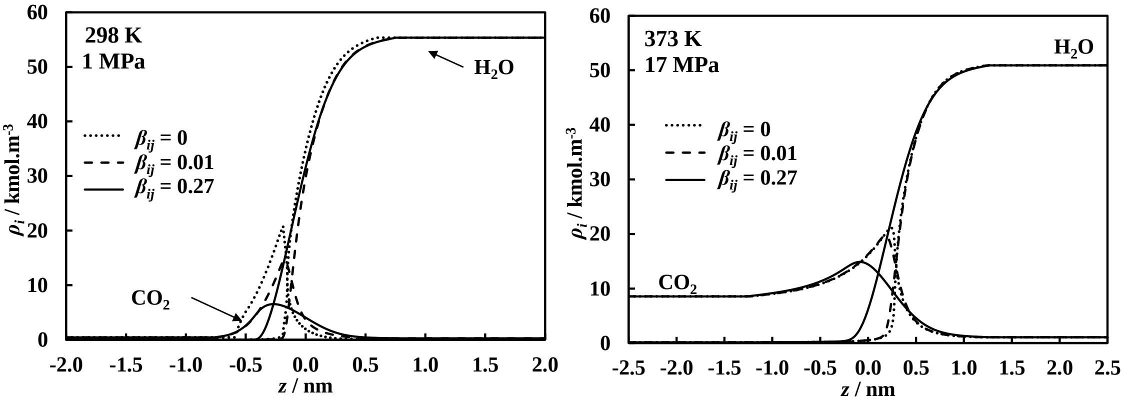

Figure 5.35. *Density profiles across the interface as computed by the DGT + CPA EoS approach for CO_2 + H_2O using different values for β_{ij}.*

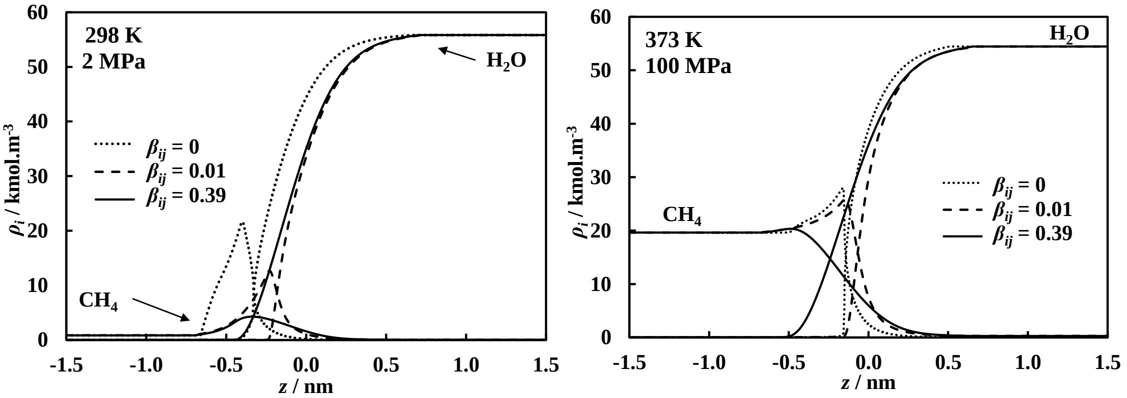

Figure 5.36. *Density profiles across the interface as computed by the DGT + CPA EoS approach for CH_4 + H_2O using different values for β_{ij}.*

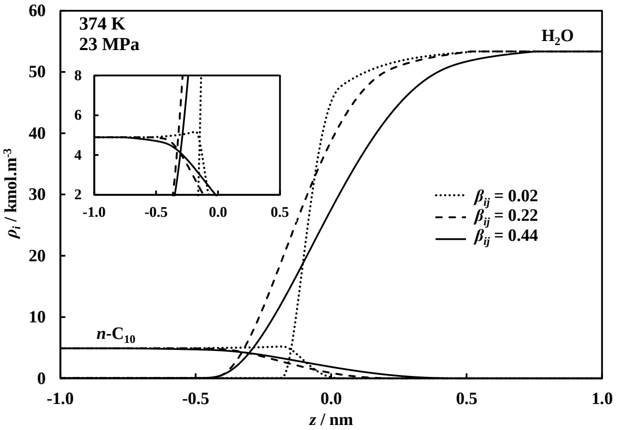

Figure 5.37. *Density profiles across the interface as computed by the DGT + CPA EoS approach for n-C_{10} + H_2O using different values for β_{ij}.*

Figure 5.38 shows the density profiles computed for these binary mixtures at T = 298 K and for two pressures using the optimal values for β_{ij} (**Table 5.6**). The selected pressures and systems allow the study of interfaces involving the contact between liquid water and either vapour/liquid CO_2, gaseous/supercritical CH_4 and liquid *n*-C_{10}. As can be observed, the microstructure of the CO_2−H_2O and CH_4−H_2O interfaces show a decrease in the relative height of CO_2 and CH_4 adsorption peaks with increasing pressures, whereas H_2O exhibits the monotonic behaviour previously described, with no significant change from that of the hyperbolic tangent function at the thermodynamic conditions examined. The adsorption peaks are located on the CO_2/CH_4-rich side of the interface, due to the low solubility of CO_2/CH_4 in the water-rich phase, and the position of the peaks seems to move towards the CO_2/CH_4-rich phase with increasing pressures. The thickness of the CO_2−H_2O interface was observed to increase and to decrease slightly for the CH_4−H_2O interface with higher pressures. The results for these systems are in agreement with the findings reported by other authors when coupling the DGT with SAFT-type EoSs [216–219,222,223] as well as through MC and MD approaches [218,223,225,230,231]. At this point it is worth mentioning that density profiles computed for the N_2 + H_2O system also showed a local accumulation of N_2 at the N_2−H_2O interface. In the case of the *n*-C_{10}−H_2O interface, no changes from the usual *tanh* shape were observed in the density profiles of *n*-decane and water at the thermodynamic conditions examined, but the thickness of the interface was observed to change slightly; this is in agreement with the idea that the small pressure dependence of *n*-C_{10}−H_2O *IFT* is related to the thickness of the liquid−liquid interface [362].

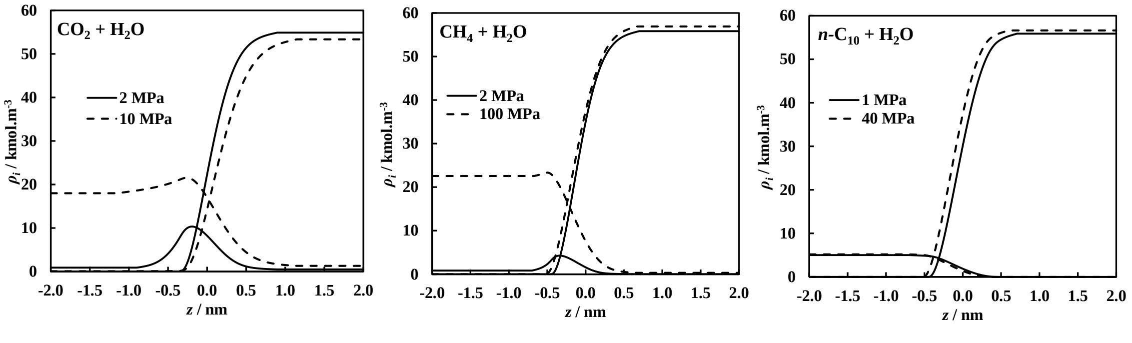

Figure 5.38. *Density profiles across the interface as computed by the DGT + CPA EoS approach for CO_2 + H_2O, CH_4 + H_2O and n-C_{10} + H_2O at T = 298 K and for two pressures.*

To better understand the pressure and temperature dependence of CO_2−H_2O *IFT*, and as a way of assessing the consistency of the computed density profiles, the relative adsorption Γ_{12} of CO_2 molecules at the CO_2−H_2O interface calculated using the density profiles *i.e.*, through **Equation 3.38**, was compared to that determined using experimental *IFT* data *i.e.*, through **Equation 3.41**. Γ_{12}−pressure diagrams were generated for three temperatures: T = 298 K, where *IFT* was observed to decrease rapidly and with an abrupt change in slope for higher pressures, T = 333 K, where *IFT* shows an intermediate behaviour, and finally T = 373 K, where *IFT* was observed to decrease continuously but in a less pronounced rate for higher pressures. These results along with experimental CO_2−H_2O *IFT* values, and *IFT* estimated using the DGT (β_{ij} = 0.27), are plotted in **Figure 5.39**.

As previously described, the $CO_2 + H_2O$ system is characterised by the appearance of different type of interfaces. Considering the range of temperatures and pressures, and global compositions (excess water) examined, liquid water (L_1) may be in contact with either vapour/gaseous CO_2 (V), liquid CO_2 (L_2) and supercritical CO_2 (SC); for brevity, the interfaces corresponding to these contacts are denoted as V−L_1, L_2−L_1 and SC−L_1, respectively. The selection of the isotherms plotted in **Figure 5.39** is not random, as it allows the study of the *IFT* of the different interfaces that arise in this system, in particular for temperatures near ambient conditions, where the regions corresponding to the contacts V−L_1 and L_1−L_2 are separated by the three-phase contact V−L_1−L_2, as depicted in the insert of **Figure 5.39*b***.

Examination of the experimental adsorption isotherms in **Figure 5.39** confirms a close relationship between the microstructure of the CO_2−H_2O interface and the behaviour of *IFT*. Accordingly, at T = 298 K and for pressures ranging from 0.1 to 6.4 MPa, corresponding to a V−L_1 interface, the relative adsorption of CO_2 increases rather rapidly while *IFT* decreases sharply (with an approximated slope of -5.89 nm or -5.89 $mN.m^{-1}.MPa^{-1}$). For pressures above that of the three-phase equilibrium pressure, carbon dioxide adsorption at the L_2−L_1 interface is significantly lower and remains approximately constant with increasing pressures. On the other hand, at T = 373 K CO_2 adsorption increases for first the pressure steps ($P < P_c$ CO_2) with an important slope, corresponding to the decrease of V−L_1 *IFT*, reaches a maximum adsorption around 17 MPa and then decreases for higher pressures, gradually approaching zero for pressures up to 70 MPa, corresponding to the weak variation of SC−L_1 *IFT* with increasing pressures. The appearance of a maximum in the adsorption isotherm suggests the existence of a saturation limit, similar to what has been described for $CH_4 + H_2O$ [103,218] as well as for $N_2/CH_4/CO_2$ + *n*-alkane systems in the present work. Finally, the intermediate adsorption isotherm (T = 333 K) also shows an important enrichment of the interface in CO_2 molecules at low and moderate pressures, corresponding to a marked decrease in *IFT*, whereas at higher pressures, CO_2 adsorption appears to lie within the adsorption values calculated using CO_2-H_2O *IFT* data at T = 298 and 373 K.

The close agreement observed between CO_2 adsorption isotherms experimentally determined and those calculated using computed density profiles, as depicted in **Figure 5.39*a***, validates the computed density profiles and confirms the capability of the DGT for describing the complex microstructure of the CO_2-H_2O interface over a broad range of thermodynamic conditions. Furthermore, these results clearly indicate that CO_2 activity in the CO_2-H_2O interface has an important impact on the behaviour of the *IFT* which, in turn, can help to explain the large deviations of the values computed with the LGT to experimental CO_2-H_2O *IFT* data, in particular at low temperatures and for low/moderate pressures. It is worth nothing that the adsorption isotherm computed with the DGT at T = 298 K and for the $V-L_1$ interface is in excellent agreement with the theoretical calculations of Lafitte *et al.* [217].

As previously explained, the slope of interfacial tension versus pressure, used in the calculation of the adsorption values through **Equation 3.41**, can have large uncertainties. For the present system, the largest uncertainties are expected at low temperatures and near the vicinity of pressures where the *IFT* behaviour abruptly changes. This may lead to significant deviations between calculated (*i.e.*, using density profiles) and experimentally determined adsorption values and to an “apparent discontinuity” in the experimentally determined adsorption isotherm at T = 333 K, as depicted in **Figure 5.39*a***.

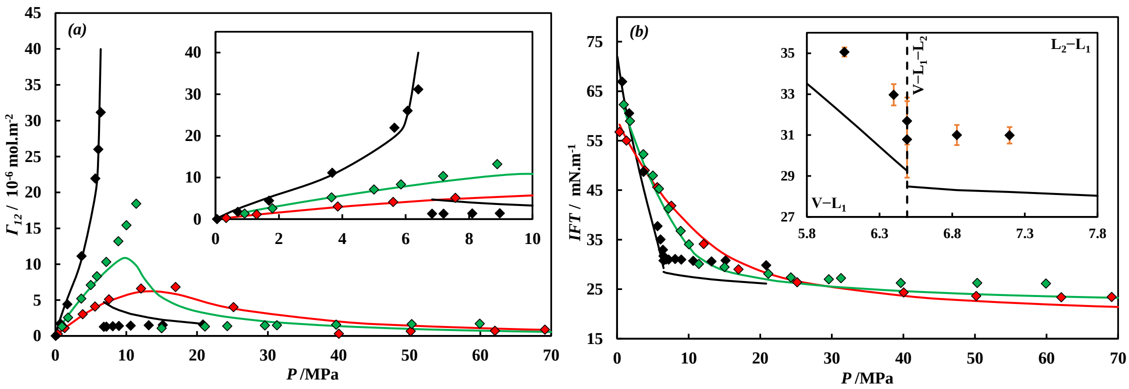

Figure 5.39. ***(a)*** *CO_2 adsorption (Γ_{12})−pressure and* ***(b)*** *IFT−pressure diagrams of CO_2 + H_2O at T = 298 K (black), 333 K (green) and 373 K (red). Symbols in* ***(a)*** *represent CO_2 adsorption in the interface calculated with* ***Equation 3.41*** *and using IFT data measured in this work. Symbols in* ***(b)*** *represent experimental IFT data measured in this work. Solid lines in* ***(a)*** *represent the CO_2 adsorption calculated with* ***Equation 3.38*** *and using density profiles computed by the DGT approach (β_{ij} = 0.27). Solid lines in* ***(b)*** *represent DGT estimations. Error bars (orange) in the inserted graph* ***(b)*** *represent the combined experimental uncertainties listed in* ***Table E.7*** *and the dashed line represents the three-phase equilibrium pressure line at T = 298.6 K.*

In addition to the above, the DGT can also be used to study the microstructure of interfaces, and associated *IFT*s, that arise at the three-phase equilibrium line of the CO_2 + H_2O system. As previously described, a point in the three-phase line was observed in the present work at T = 298.6 K and for a pressure of 6.49 MPa (approximately equal to CO_2 vapour pressure [99] and in agreement with experimental data [316]) and the *IFT* of the V−L_1 and L_2−L_1 interfaces were experimentally determined. Recalling the values reported in **Table E.7**, V−L_1 and L_2−L_1 *IFT*s were found to amount 31.69 ± 1.15 and 30.79 ± 1.87 mN.m^{-1}, respectively. On the other hand, the DGT estimations at the three-phase point yield: V−L_1 *IFT* = 29.25 mN.m^{-1}, L_2−L_1 *IFT* = 28.49 mN.m^{-1} and V−L_2 *IFT* = 0.88 mN.m^{-1}. The close agreement between V−L_1 and L_2−L_1 *IFT*s experimentally determined and those estimated using the DGT stands out as very good, considering the relatively high experimental uncertainties and that the β_{ij} value used (**Table 5.6**) was estimated with the aid of an experimental *IFT* data point at higher temperatures. Furthermore, the estimated V−L_2 *IFT* is approximately equal to the surface tension of CO_2 under analogous conditions (*ST* CO_2 = 0.50 mN.m^{-1} [99]), and the difference between them may be related, to some extent, to mutual solubility effects.

Interfacial tensions of systems at three-phase equilibrium conditions are interrelated via the following expressions [255]:

$$\gamma_{V-L_1} < \gamma_{L_2-L_1} + \gamma_{V-L_2} \tag{5.9}$$

$$\gamma_{V-L_1} = \gamma_{L_2-L_1} + \gamma_{V-L_2} \tag{5.10}$$

where the inequality given by **Equation 5.9**, known as Neumman's inequality, corresponds to the situation in which the L_2 phase partially wets the V−L_1 interface. On the other hand, the equality given by **Equation 5.10**, known as Antonow's rule, corresponds to the situation in which the L_2 phase spreads at (completely wets) the V−L_1 interface. For the CO_2 + H_2O system and the examined three-phase point, the summation of L_2−L_1 and V−L_2 *IFT*s, computed using the DGT, yields a tension of 29.37 mN.m^{-1}, which is nearly equal to the interfacial tension computed for the V−L_1 interface (29.25 mN.m^{-1}). The slight difference between the computed values is believed to be associated with the method used for casting the solution of the density profiles, which is based on the gradual enlargement of the width of the interfacial region by a constant rate.

Figure 5.40 shows the density profiles as computed by the DGT for the interfaces corresponding to the three-phase equilibria in the CO_2 + H_2O system. From this can be observed that the phases V (CO_2-rich vapour) and L_1 (water-rich liquid) are separated by the formation of a layer of the phase L_2 (CO_2-rich liquid), which perfectly wets the $V-L_1$ interface. Examination of the density profile of CO_2 for pressures just below that of the saturation pressure of CO_2 shows that carbon dioxide gradually accumulates at the $V-L_1$ interface as the three-phase equilibrium pressure is approached, as depicted in **Figure 5.41**. This is in agreement with the idea of the formation of a CO_2 film which progressively grows thicker, corresponding to a prewetting transition [363], as also reported by Lafitte *et al.* [217]. On the other hand, as depicted in **Figure 5.40**, the profiles at the L_2-L_1 interface show a local enrichment of the interface in CO_2 molecules, whereas the profiles at the $V-L_2$ interface show that the density of CO_2 and H_2O increases monotonically from the phase V to the phase L_2. It is worth nothing that $V-L_2$ *IFT* is expected to continuously decrease as the system approaches the UCEP, corresponding to the broadening of the density profiles and to the decrease in the density difference between the phases V and L_2. These observations as well as the behaviour described for the three-phase equilibria are in agreement with the MD simulations of Müller and Mejía [225] for CO_2 + H_2O, as well as with the findings of Miqueu *et al.* [218] for CH_4 + H_2O and Míguez *et al.* [223] for CO_2 + CH_4 + H_2O, for conditions along the three-phase equilibrium line.

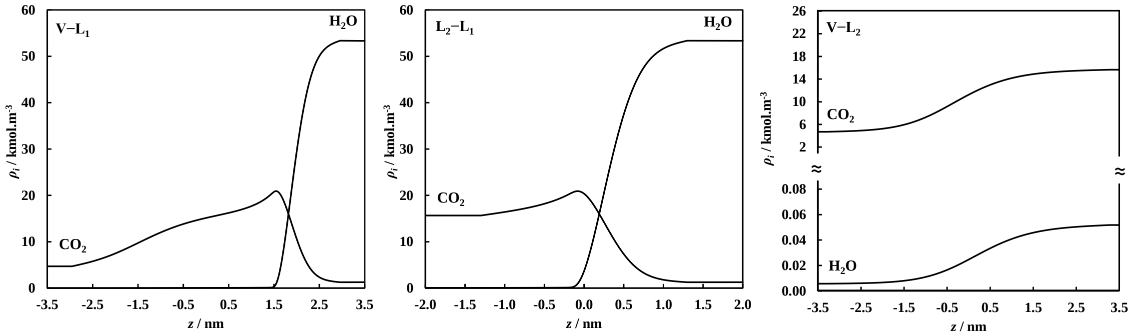

***Figure 5.40**. Density profiles across the interface as computed by the DGT + CPA for CO_2 + H_2O at T = 298.6 K and for the three-phase equilibrium pressure.*

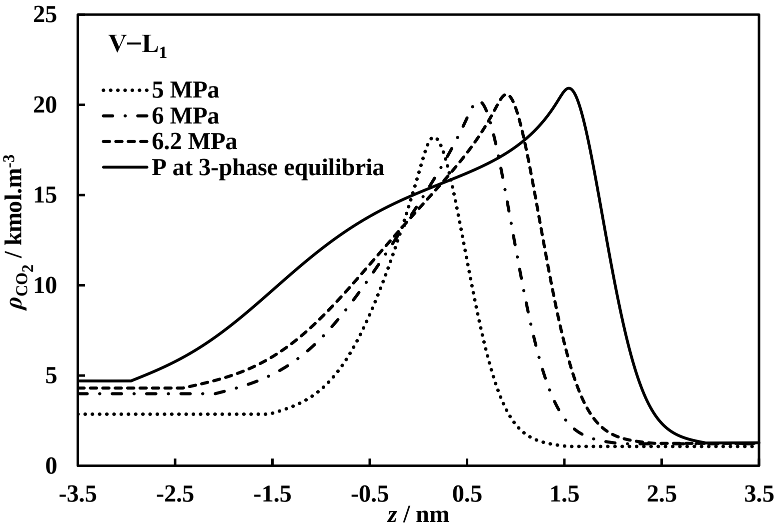

***Figure 5.41**. Density profiles of CO_2 across the V−L_1 interface as computed by the DGT + CPA for CO_2 + H_2O at T = 298.6 K and for pressures approaching the three-phase equilibrium pressure.*

Complementarily, and as an example of the microstructure of the interface in ternary aqueous mixtures, the density profiles across the interface of the CO_2 + CH_4 + H_2O and CO_2 + *n*-C_{10} + H_2O systems, at fixed pressure and temperature conditions, and for increasing values in the global molar composition of CO_2, are plotted in **Figures 5.42** and **5.43**. The density profiles correspond to the equilibrium of two fluid phases: a [CO_2 + CH_4]/[CO_2 + *n*-C_{10}]-rich phase and a water-rich liquid phase. From these figures it can be observed that CO_2 adsorbs strongly at the interface and this effect is most marked at higher concentrations of carbon dioxide which, in turn, lead to the computation of lower interfacial tensions for fixed pressure and temperature. As already described for the CH_4 + H_2O system, methane also shows some degree of adsorption at the interface of the CH_4 + CO_2 + H_2O system, whereas no interfacial activity is observed for water and *n*-decane at the interface of the corresponding systems at the conditions examined. This analysis further highlights the capability of the DGT as a tool not only for computing interfacial tensions, but also for providing important insights about the microscopic behaviour of the interface. Additionally, the results also help to explain the poor predictive capabilities shown by the LGT when applied to systems that exhibit high interfacial activity. In other words, the microstructure of such interfaces and, in turn, of the associated energy are not adequately accounted for by the use of linear density profiles together with the examined mixing rules of influence parameters with the LGT approach.

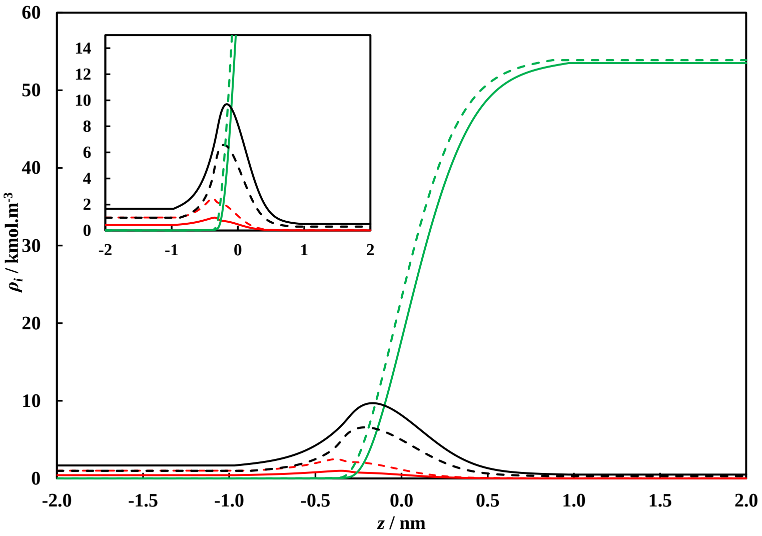

Figure 5.42. *Density profiles of CO_2 (black), CH_4 (red) and H_2O (green) across the interface as computed by the DGT + CPA for [0.5CO_2 + 0.5CH_4] + H_2O (dashed) and [0.8CO_2 + 0.2CH_4] + H_2O (solid) mixtures at T = 333 K and P = 5 MPa.*

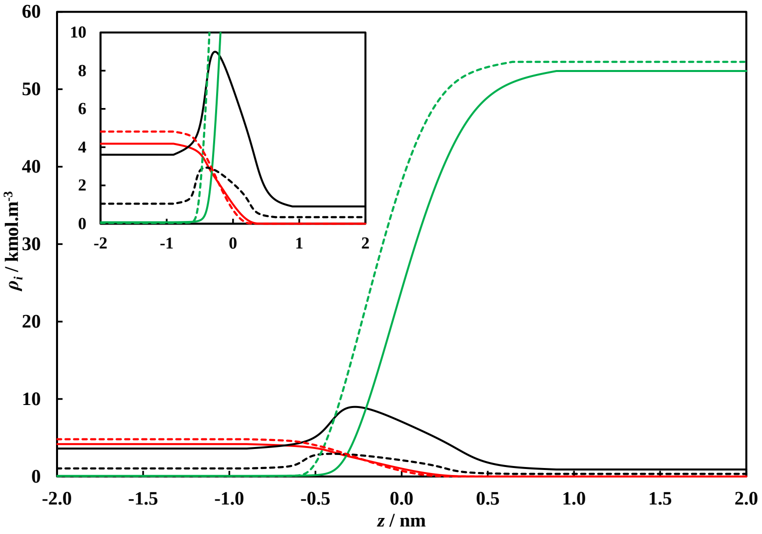

Figure 5.43. *Density profiles of CO_2 (black), n-C_{10} (red) and H_2O (green) across the interface as computed by the DGT + CPA for [0.2CO_2 + 0.8n-C_{10}] + H_2O (dashed) and [0.5CO_2 + 0.5n-C_{10}] + H_2O (solid) mixtures at T = 373 K and P = 60 MPa.*

5.6 Summary

Interfacial tension and saturated density data of the CO_2 + H_2O system have been measured over the temperature range 298 to 469 K and for pressures up to 69 MPa. Interfacial tensions were measured by applying the axisymmetric drop shape analysis method in pendant drops and density measurements were carried out in a vibrating U-tube densitometer. Both the equipment and methodology were validated through comparison of measurements with selected literature data. The data reported helped filling in the experimental gap found in literature and allowed the study of the behaviour of CO_2−H_2O *IFT* over a broad range of pressure and temperature conditions, including those of relevance for EOR and CO_2 storage processes.

The density results showed that the approximation of the density of the CO_2-rich phase to that of pure CO_2, as followed by most authors in literature, is in fact valid within the experimental uncertainty. However, CO_2 dissolution in water with increasing pressure lead to density values higher than those of pure water, in particular in the region where CO_2 is in the liquefied or supercritical state. The use of pure component densities for the water-rich phase would, therefore, lead to an underestimation of the *IFT* values, with this being more severe close to the phase density inversion conditions. Indeed, a maximum underestimation of CO_2−H_2O *IFT* was calculated at T = 333.15 K and P = 59.91 MPa, where the difference between the *true IFT* and that estimated by using the pure component approximation for the aqueous phase was of 7.28 $mN.m^{-1}$ (%AAD = 27.8 %). In this context, a correlation was proposed to readily determine the density of the CO_2-saturated water phase at conditions of interest. This helped to improve the overall precision of the reported *IFT* values. For a given isotherm, CO_2−H_2O *IFT*s exhibited a marked pressure dependence, with values decreasing sharply at low and moderate (~10 to 15 MPa) pressures, but in a less pronounced rate at higher pressures. The change in slope of the *IFT* versus pressure projections was noticeably abrupt at T = 298, 313, 323 and 333 K, but smooth for higher temperatures. On the other hand, for a given isobar, CO_2−H_2O *IFT*s generally decreased with increasing temperatures for temperatures greater than 373 K, with an apparent tendency inversion for isotherms lower than 373 K.

In addition to the above, the effect of gaseous impurities (sparingly soluble in water) as well as the presence of salts in the water phase on CO_2−H_2O *IFT* were investigated for four isotherms and pressures up to 69 MPa. This was done by measuring the *IFT* between water and two CO_2-rich mixtures (> 90 mole% CO_2) and between CO_2 and two NaCl(aq) solutions, with NaCl molalities m_{NaCl} = 0.98 and 1.98 $mol.kg^{-1}$. The results showed an increase of the interfacial tension from that of the CO_2 + H_2O system with increasing content in diluent gases (N_2, H_2, O_2 and Ar) as well as with increasing the water salinity. For the type and content of gases examined, the *IFT* increase due to the presence of diluent gases was observed to lie mostly within the experimental uncertainty. On the other hand, for CO_2−NaCl(aq) systems, the *IFT* was observed to always exceed the CO_2−H_2O *IFT*, resolving some of the inconsistencies observed for data reported in previous studies. The increase in interfacial tension averaged an amount between 1.42 and 2.01 mN.m^{-1} for m_{NaCl} = 0.98 mol.kg^{-1} and between 2.67 and 3.73 mN.m^{-1} for m_{NaCl} = 1.98 mol.kg^{-1}. This corresponds to an average relative increase from CO_2−H_2O *IFT* between 4.4 and 13.2%, over the range of pressures, temperatures and salt molalities examined here.

A brief discussion of the impact of CO_2−H_2O *IFT* on the capillary-sealing efficiency of caprocks was presented. The results suggest the existence of an optimal caprock depth for the storage of CO_2 in reservoirs located onshore, whereas for reservoirs located offshore, CO_2 trapping potential appeared to decrease progressively with increasing caprock depth. Nonetheless, by comparing these two scenarios, it was evident that caprocks in offshore fields can potentially trap significantly higher quantities of CO_2. In addition to this, the analysis of the impact of gaseous sparingly soluble impurities and water salinity indicated that they would have a positive effect on the capillary-sealing efficiency of caprocks.

The interfacial tension of binary and multicomponent aqueous systems measured in the present work as well as reported by others in literature were compared to theoretical calculations obtained with the DGT in combination with the CPA EoS. Comparison to calculations with the LGT approach and empirical methods, such as the Parachor and Sutton's correlation, was also performed. The systems investigated included conditions at which one aqueous phase was simultaneously in contact with one or two fluid phases. The results showed that by using constant influence parameters and a single, temperature independent, binary interaction coefficient adjusted to one *IFT* data point at moderate conditions, the DGT was capable of describing the *IFT* of two- and three-phase aqueous systems over a broad range of pressure and temperature conditions, with deviations to experimental data lower than that obtained using other *IFT* models. The DGT performed significantly well when describing the complex behaviour of the CO_2 + H_2O system, namely the high pressure dependence of the interfacial tension. Moreover, the impact of salts was also adequately replicated, up to a certain limit of ionic strength, by modelling the salting-out effect and computing the *IFT* associated with the density profiles in a hypothetical salt-free system. Overall, the DGT in combination with the CPA EoS was capable of accounting for the *IFT* variations in aqueous systems of relevance for EOR and CO_2 storage processes due to changes in composition, temperature and pressure.

Further to the above, the density profiles computed with the DGT were examined and the impact of the microstructure of the interface on the *IFT* was discussed. The use of $\beta_{ij} \neq 0$ helped to circumvent the numerical difficulties encountered in the solution of the equations governing the density profiles of aqueous systems; the appearance of infinitely steep density profiles was pointed out as a possible cause. The use of the optimal values of β_{ij} for interfacial tension estimations showed a tendency of CO_2, CH_4 and N_2 molecules to accumulate at the interface of aqueous systems, as reflected by the appearance of adsorption peaks in the density profiles. In the case of the $CO_2 + H_2O$ system, a good agreement between the Gibbs adsorption isotherms computed using the density profiles and those computed using experimental $CO_2{-}H_2O$ *IFT* was found. This validates to some extent the computed density profiles and confirms the adequacy of the DGT for describing the complex microstructure of aqueous interfaces. Particular attention was given to the $CO_2{-}H_2O$ interface near the vicinity of the three-phase equilibrium line, with density profiles showing the formation of a thin CO_2 film as the saturation pressure of CO_2 was approached. This behaviour was found to be in agreement with the findings reported by others in previous studies available in literature. Furthermore, density profiles computed for the ternary systems $CO_2 + n\text{-}C_{10} + H_2O$ and $CO_2 + CH_4 + H_2O$ showed an increasing enrichment of the fluid−liquid interface in CO_2 molecules by increasing the global content in CO_2, readily linking the reduction of interfacial tension to the interfacial activity of CO_2. Together, these results also helped to explain the poor modelling results obtained with the LGT for aqueous interfaces. Accordingly, it appears that the energy of such interfaces and, in turn, the *IFT* are not adequately described by the use of linear density profiles together with the mixing rules of influence parameters examined within the framework of the LGT.

CHAPTER 6 – CONCLUSIONS AND RECOMMENDATIONS FOR FUTURE WORK

6.1 Introduction

In this thesis the interfacial tension of reservoir fluids in the context of enhanced oil recovery processes and CO_2 storage in underground formations has been investigated. The investigations covered both experimental and modelling aspects of the interfacial tension of fluid−liquid interfaces in hydrocarbon and aqueous systems over a broad range of conditions (from ambient up to 473 K and 300 MPa). The examined systems comprised binary and multicomponent synthetic mixtures including *n*-alkanes, water, salts and gases, as well as one real petroleum fluid. Though most of the systems studied here were simple in terms of the number of components, they are not devoid of complexities as obtainable in real reservoirs. Interfacial tensions were observed to span from near complete miscibility (low *IFT* values) to immiscible (high *IFT* values) two- and three-phase equilibria conditions. Moreover, as well as complementing and extending the range of experimental data sets available in literature, the data measured in this thesis (and by others) were used for testing the capability of theoretical tools for replicating the *IFT* variations in reservoir fluids due to changes in composition, temperature and pressure. More specific details on the experimental and modelling achievements and results of this thesis are briefly outlined below. Recommendations for future investigations are also described in this chapter.

6.2 Experimental Investigation

Two new HPHT apparatus were constructed and used to measure the interfacial tension between fluid phases. One was based on the Differential Capillary Rise method and was suitable for measuring the interfacial tension of hydrocarbon systems, where low tension values can be attained at sufficiently high pressure and temperature conditions. The other, used for aqueous systems, was based on the Pendant Drop method and the axisymmetric drop shape analysis technique. The measurement of *true IFT* values requires the accurate estimation of the density of the phases in contact. Therefore, saturated phase density data were measured using a vibrating U-tube densitometer and the generated densities used directly or as correlating data for the experimental determination of *IFT* values.

The interfacial tension and saturated density of gas + oil systems were measured for three binary mixtures CH_4 + *n*-decane, CO_2 + *n*-decane and N_2 + *n*-decane as well as for three multicomponent synthetic mixtures composed of CH_4, CO_2, N_2 and *n*-alkanes, in a total of up to 9 components. These properties were investigated in the binary mixtures for four isotherms 313, 344, 393 and 443 K and pressures up to 69 MPa or near the critical point of each mixture. Good agreement with literature data at pertinent conditions was observed, validating both the equipment and methodology as well as extending the range of conditions available from previous studies. The multicomponent mixtures were investigated at a representative reservoir temperature of 393 K and pressures up to 23 MPa. The results for the hydrocarbon systems showed a clear decreasing trend of *IFT* with increasing pressures, more pronounced for systems with higher CO_2 content, and with the values vanishing as the contacted fluid phases became completely miscible. The increase of temperature resulted in a decrease in the interfacial tension, more markedly at low pressures and only moderately at higher pressures for the CH_4 + *n*-decane and N_2 + *n*-decane systems. For CO_2 + *n*-decane, a crossover pressure region between the examined isotherms was observed. Measured interfacial tensions for these systems ranged from 21.58 down to 0.50 mN.m^{-1}.

The interfacial tension and saturated density of the CO_2 + water system were measured for temperatures ranging from 298 to 469 K and pressures up to 69 MPa. Density measurements showed that the density of the CO_2-rich phase can be fairly approximated to that of pure CO_2, whereas the use of pure water density for the water-rich phase can lead to significant underestimation of the interfacial tension values, in particular in the vicinity of phase density inversion conditions. Indeed, a maximum underestimation of 7.28 mN.m^{-1} for CO_2–H_2O *IFT* was estimated at T = 333.15 K and P = 59.91 MPa, corresponding to a relative deviation from the *true IFT* value of 27.8%. In order to readily determine the density of the CO_2-saturated water phase, a correlation was proposed and *IFT* values were corrected accordingly. The good agreement observed between the data generated in this work and that from previous studies in literature for CO_2 + H_2O validated the capability of the apparatus and the experimental procedure adopted for measuring these properties in aqueous systems. CO_2–H_2O *IFT* was observed to decrease with a marked slope at low and moderate (~10 to 15 MPa) pressures, and then in a less pronounced rate with further increase in pressure. The temperature dependence of CO_2–H_2O *IFT* was less marked. For a given isobar, the results showed a moderate increase of CO_2−H_2O *IFT* with increasing temperatures up to 373 K, and then a reversed behaviour for higher temperatures. Measurements were performed throughout the two-phase region where, depending on the pressure and temperature, water was in contact with vapour/gaseous, liquid or supercritical CO_2. A point in the three-phase equilibrium pressure line was observed at T = 298.6 K and interfacial tensions between the aqueous and the two CO_2-rich phases were measured. Overall, CO_2−H_2O *IFT*s were observed to span from 68.52 down to 12.65 $mN.m^{-1}$.

Further to above and aiming at studying more realistic systems, the impact of gaseous impurities (sparingly soluble in water) and salts were investigated by measuring the *IFT* between water and two CO_2-rich mixtures (> 90 mole% CO_2), and between CO_2 and two NaCl(aq) brines (m_{NaCl} = 0.98 and 1.98 $mol.kg^{-1}$). Measurements were carried out at temperatures in the range 298 to 423 K and pressures up to 69 MPa. Results showed an increase from CO_2−H_2O *IFT* values, more pronounced due to the presence of salts. These measurements bridge the experimental gap found for studies concerning the impact of small quantities of gaseous impurities on CO_2−H_2O *IFT*, and helped to resolve the inconsistencies observed in CO_2−NaCl(aq) *IFT* data available in literature, while extending both pressure and temperature conditions from previous maximum (45 MPa and 373 K).

The implications of measurements performed here were analysed in terms of the impact of CO_2−H_2O *IFT* on the storage of CO_2 in deep aquifers. By deducing the caprock temperature and pressure with depth, the CO_2 trapping potential of caprocks located onshore and offshore were estimated and the CO_2 storage capacity of the underlying reservoirs calculated. The reservoir and caprock characteristics (porosity, wettability, etc.) were taken equal to that used previously by others in similar studies and were assumed to remain constant with depth. The results indicated a progressive increase of CO_2 trapping potential of caprocks and, in turn, of CO_2 storage capacity with increasing depth for reservoirs located onshore. A maximum CO_2 trapping potential was estimated for caprock depths approximately between 2 and 4 km, point from which CO_2 storage capacity is expected to decrease with further increase in depth due to the negative impact of CO_2−H_2O *IFT* on the capillary-sealing efficiency at higher pressures and temperatures. On the other hand, the results for caprocks located offshore showed that they can trap significantly higher quantities of CO_2 compared to those located onshore, but CO_2 trapping potential was observed to continuously decrease with increasing caprock depth.

Complementarily, it was possible to deduce that the increase of *IFT* due to the presence of gaseous impurities, sparingly soluble in water, as well as with water salinity would lead to an increase of the capillary-sealing efficiency with respect to the gas and, thereby, to safer storage conditions.

6.3 Modelling Investigation

Having generated and gathered from literature experimental data, this work set out upon testing the capabilities of theoretical methods for modelling the interfacial tension of mixtures of relevance for reservoir engineering processes. The modelling approaches tested included a standard method used in the petroleum industry (Parachor method), an empirical correlation (Sutton) and a more robust approach, based on the density distribution of components across the interfacial region, called the Density Gradient Theory (DGT). The DGT requires the numerical resolution of a set of differential/algebraic equations governing the density profiles across the interface before the *IFT* can be computed. This can lead to high computation times, in particular for multicomponent mixtures. Therefore, a simplified version of the DGT, the Linear Gradient Theory (LGT), with a much lower computational effort, was also considered. In the framework of the LGT density profiles are assumed to be linearly distributed and thus, the need for solving time-consuming density profile equations is removed. Both DGT and LGT rely on the use of influence parameters. These parameters account for the non-homogenous nature of the interface and were adjusted here against surface tension data of pure substances or calculated using correlations available in literature. The DGT and the LGT can be used to compute interfacial tension values of gas−oil, gas−water and oil−water interfaces and therefore, the studies performed here showcase the possibility of using one single method for modelling fluid−liquid *IFT*s of systems in multiphase conditions.

The *IFT* models were coupled with equations of state in order to compute the required phase equilibrium properties of the homogenous fluids (bulk composition and density) as well as the energy of the interface. Hydrocarbon systems were modelled with the VT-PPR78 EoS whereas aqueous systems were modelled with the CPA EoS. These EoSs were capable of adequately describing the phase equilibria and densities of the systems examined at HPHT conditions. The poorest descriptions were observed near the critical point of mixtures or near the region where the bulk phases become miscible with one another.

The modelling results showed that the DGT provided the lowest deviations to experimental *IFT* data, outperforming the other theoretical approaches examined. The tested systems included a number of synthetic mixtures as well as one real petroleum fluid, with temperatures and pressures ranging from ambient up to 473 K and 300 MPa, respectively. In the absence of water, *IFT* calculations with the DGT were performed in a fully predictive manner, with no adjustable parameters to mixtures. For aqueous systems, the use of a single binary interaction coefficient, adjusted against one *IFT* data point at moderate conditions, and constant influence parameters was enough for the DGT to accurately describe the complex interfacial tension behaviour of binary and multicomponent systems, including both two- and three-phase equilibria conditions. The largest deviations were obtained for low *IFT* values, corresponding to near complete miscibility conditions, where experimental uncertainties are high and the selected phase behaviour models failed to adequately describe the bulk properties. Overall, deviations between experimental and calculated *IFT* with the DGT for synthetic mixtures and $IFT > 1.5$ mN.m^{-1} ranged between 4.2 and 9.7 %. These modelling results confirm the robustness of the DGT for accurately describing the interfacial tension of reservoir fluid systems. In addition to this, the fact that the DGT can handle lumping schemes without significantly changing the magnitude of the computed *IFT* values, as tested here for the real petroleum fluid, makes this model more attractive for reservoir engineering calculations.

Though the computation time of *IFT* values is significantly lower with the LGT, the performance of this model was not as good as the DGT, in particular for systems with high content in CO_2. For these systems, the use of binary interaction coefficients, temperature dependent, may be necessary for the computation of more accurate *IFT* values. Nonetheless, the LGT was observed to perform better than the Parachor method and Sutton’s correlation for some systems, namely CH_4 + *n*-alkane, N_2 + *n*-alkane, CH_4 + *n*-decane + H_2O and CH_4 + *n*-C_{16} + H_2O.

Furthermore, taking advantage of the good modelling capabilities of the DGT, an approach for predicting the impact of salts on the magnitude of the interfacial tension of gas + brine systems was developed and analysed. The modelling approach was based on accounting for the salting-out effect on the solubility of the gas, via the CPA EoS in combination with an electrolyte model, and subsequent computation of density profiles and *IFT* in a hypothetical salt-free system with the DGT. Though the distribution of dissolved salt ions between the interface and the bulk aqueous phase was neglected in the model, predicted CO_2−brine interfacial tensions yield good agreement with values experimentally determined here and gathered from literature for single and mixed salt solutions with low and medium ionic strength (up to $I = 2.7$ mol.kg^{-1}).

Additionally, the density profiles computed with the DGT were analysed and the impact of the microstructure of the interface on the interfacial tension was discussed. Density profiles showed a local enrichment of the hydrocarbon and aqueous interfaces in gas molecules such as CO_2, CH_4 and N_2. For increasing pressures and temperatures, the relative height of the adsorption peaks were observed to decrease and the interface thickness to generally increase. To better understand the pressure and temperature dependence of *IFT* values, Gibbs adsorption isotherms were calculated using experimental *IFT* data and the results compared to theoretical adsorption isotherms obtained with the density profiles. The good agreement between theoretical and experimental adsorption isotherms confirms, to some extent, the validity of the density profiles computed through the framework of the DGT. Moreover, these results further confirm the suitability of this model for providing insights into the microstructure of fluid−liquid interfaces. It is worth noting that the modelling results obtained here with the DGT and the examined EoSs were found to be in agreement with Molecular Dynamics and Monte Carlo investigations available in literature as well as with other DGT studies in which equations of state with a sound theoretical background, such as SAFT, were used.

Finally, theoretical *IFT* methods tested in this study were implemented in the in-house PVT software of the Gas Hydrates, Flow Assurance and Phase Equilibria research group at Heriot-Watt University (HWPVT).

6.4 Recommendations for Future Work

Although this thesis contributed with a considerable amount of experimental *IFT* data of relevance for EOR and CO_2 storage projects and encouraging results towards the development of a robust *IFT* model for reservoir engineering calculations were obtained with the DGT, experimental gaps still exist and refinement of this model in some areas is still needed. Based on the results and findings of this thesis, several aspects concerning the experimental measurement and modelling of *IFT* of reservoir fluids can be mentioned as subjects for further study.

With respect to the experimental measurement of reservoir fluids, in this thesis great effort was put into the design, construction and validation of two apparatus suitable for measuring fluid−liquid interfacial tensions over a broad range of pressure and temperature conditions. One of the apparatus was specifically developed to measure this property in hydrocarbon systems and the other was intended for aqueous systems including corrosive fluids, such as brines. Therefore, taking into account the capabilities of these apparatus, it is worth ensuring their continued use in making experimental measurements for systems whose experimental data remains yet unavailable, namely binary systems gas + *n*-alkane and CO_2 + brine. The study of binary gas + *n*-alkane *IFT* would be necessary for modelling purposes. For instance, the generated *IFT* data would be necessary for the tuning of binary interaction coefficients as a way of improving the description of gas−oil *IFT* with the LGT. In the case of CO_2−brine *IFT*, data for single and binary salt systems are still scarce, with only a few number of salts studied to date and in a narrow range of pressures and temperatures. Consequently, the extension of measurements to other single salt systems would allow a better understanding of the specific influence of each salt on the interfacial tension.

In addition to the above, it would be interesting to study the impact of pH of solution on the interfacial tension at reservoir conditions. For the type of aqueous systems investigated in this thesis, pH can be expected to be acidic due to the dissolution of CO_2 at high pressures and formation of carbonic acid. Under low pH levels, the dissociation of carbonic acid is negligible. However, for alkaline solutions (high pH levels), the dissolution of CO_2 and concentration of ionic species (bicarbonate, carbonate and proton) in solution can be significantly affected which, in turn, can have an impact on the interfacial tension values. Another case to point out is the impact of pH on the interfacial tension between crude oil and water. As an example, for alkaline pH levels interfacial active agents present in the oil can be formed at the interface (natural surfactant generation or saponification) and low or even ultra-low oil−water *IFT* values ($IFT < 0.1$ $mN.m^{-1}$) can be attained [364,365]. In this sense, the study of the impact of pH would allow a better understanding of the *IFT* variations in reservoir engineering processes.

The experimental methods applied here for measuring the *IFT* require the accurate estimation of the density of the equilibrated phases. In this thesis, saturated density data were measured in-situ or in parallel experiments with a vibrating U-tube densitometer. A key aspect in the in-situ measurement of the density of the saturated phases is a steady circulation of fluids in the densitometer while maintaining the pressure and temperature conditions throughout the system. Here, the circulation of fluids from the *IFT* cell to the densitometer was made by using two check valves and a movable piston. However, it is suggested for future studies the use of a circulation pump and two densitometers, one for the vapour phase and another for the liquid phase. In this manner, stable density readings would be more easily attained and phase densities near critical complete miscibility conditions could be measured. The use of a gas chromatograph sampling system, connected to the *IFT* cell, would also greatly benefit this type of experiments as it would allow an integrated investigation of the composition of the contacted phases, in addition to the density and *IFT*. It is worth noting that increasing the complexity of the equipment would also make measurements more prone to the presence of impurities which can have a significant impact in the *IFT* measurements. Therefore, a thorough cleaning of all parts of the apparatus with different solvents is crucial so surface/interface active impurities can be kept at a minimum.

In dealing with the modelling of *IFT*, it was clear from this study, as well as from previous studies in literature, that the DGT shows an excellent capability for describing fluid−liquid interfacial tensions while providing other microscopic properties which characterise the interface such as density profiles, interface thickness and surface/interface activity. For hydrocarbon systems, *IFT* calculations are usually made in a fully predictive manner ($\beta_{ij} = 0$), whereas the *IFT* of aqueous interfaces can be accurately described using a single, temperature independent, binary interaction coefficient with the DGT. Nevertheless, a drawback of this model may be pointed to the computational effort required for solving the equations governing the density profiles across the interface, in particular when using $\beta_{ij} \neq 0$. Moreover, although the computation time can be reduced by using lumping methods without a significant change in the computed *IFT* values, the development of more efficient numerical algorithms for solving these equations would be necessary for the use of the DGT in practical engineering calculations. Studies towards this direction were recently published by Larsen *et al.* [366] and Kou and co-workers [367–369]. By constructing a linear transformation of the

Euler-Lagrange equations and introducing a weighted molar density function, monotonically varying across the interface, Kou and co-workers [368,369] proposed a numerical algorithm to find the density profiles when using $\beta_{ij} = 0$ without the need for selecting a reference component. This treatment makes the method for finding the density profiles more general as for some systems it may be difficult to know, beforehand, which component should be used as reference or the system may not have any monotonic component. As an attempt to speed up calculations, Larsen *et al.* [366], as well as Kou and Sun [367,369], proposed adaptive refinement techniques for the number of grid points considered in the discretization of the interface with no loss of accuracy on the prediction of the *IFT* of mixtures ($\beta_{ij} = 0$). Furthermore, Larsen *et al.* [366] also proposed a method to reduce the number of calls to the EoS while solving the density profiles, which can be very beneficial in terms of computation speed when modelling multicomponent systems.

Finally, another area which can also be improved in the model is the description of low interfacial tension values. As shown in this thesis, the DGT in combination with the selected EoSs was not capable of providing a good description of the behaviour of systems near critical complete miscibility conditions. The correct representation of such low *IFT*s is key for the optimisation of miscible (or near miscible) gas injection enhanced oil recovery mechanisms. In this sense, the use of a phase behaviour model with proper scaling behaviour near the critical point (crossover) could potentially improve the description of the *IFT* in this region. Crossover versions of the PR78 EoS and the CPA EoS have already been proposed by others in studies available in literature [298,299,370,371]. The coupling of the DGT with other EoSs such as SAFT could also help extending the modelling of *IFT* to systems with highly non-ideal behaviour such as alcohols, acids, glycols, etc.

APPENDIX A − Peng-Robinson 1978 Equation of State

The Peng-Robinson 1978 EoS [235] can be expressed in terms of pressure as:

$$P = \frac{RT}{v-b} - \frac{a(T)}{v(v+b)+b(v-b)} \tag{A.1}$$

$$a(T) = \frac{0.45724 R^2 T_c^2}{P_c} \left[1 + m(1-\sqrt{T_r})\right]^2 \tag{A.2}$$

$$m = 0.37464 + 1.54226\omega - 0.26992\omega^2 \qquad \text{for } \omega<0.49 \tag{A.3}$$

$$m = 0.3796 + 1.485\omega - 0.1644\omega^2 + 0.01667\omega^3 \qquad \text{for } \omega\geq 0.49 \tag{A.4}$$

$$b = 0.07780 \frac{RT_c}{P_c} \tag{A.5}$$

where *a* and *b* are the EoS energy and co-volume parameters, respectively, obtained from critical data, T_c and P_c, and the acentric factor, ω.

When dealing with the volume-translated version of this EoS, the corrected molar volume v_{VTPR} is given by [257]:

$$v_{VTPR} = v_{PR} - v_c \tag{A.6}$$

where v_{PR} and v_c are the untranslated molar volume and the volume correction, respectively.

For mixtures, the energy and co-volume parameters are calculated by employing the conventional van der Waals one-fluid mixing rules, with one binary interaction coefficient k_{ij} for the energy parameter, and the linear mixing rule is used for the mixture volume correction. They have the following form:

$$a = \sum_i \sum_j x_i x_j (1-k_{ij}) \sqrt{a_i a_j} \tag{A.7}$$

$$b = \sum_i x_i b_i \tag{A.8}$$

$$v_c = \sum_i x_i v_{c,i} \tag{A.9}$$

APPENDIX B − Cubic-Plus-Association Equation of State

The CPA EoS [239,240] can be expressed in terms of pressure as :

$$P = P^{SRK72} + P^{Association} \qquad \textbf{B.1}$$

$$P^{SRK72} = \frac{RT}{v-b} - \frac{a(T)}{v(v+b)} \qquad \textbf{B.2}$$

$$P^{Association} = -\frac{1}{2}\frac{RT}{v}\left(1+\rho\frac{\partial \ln g}{\partial \rho}\right)\sum_i x_i \sum_{A_i}(1-X_{A_i}) \qquad \textbf{B.3}$$

where a is the energy parameter, b is the co-volume parameter, g is the simplified radial distribution function, X_{Ai} is the mole fraction of pure component i not bounded at site A and x_i is the mole fraction of component i.

The CPA energy parameter has a Soave-type reduced temperature dependence defined as:

$$a(T) = a_0\left[1+c_1(1-\sqrt{T_r})\right]^2 \qquad \textbf{B.4}$$

For mixtures, the energy and co-volume parameters in the physical term (SRK72) are calculated by employing the conventional van der Waals one-fluid mixing rules, with one binary interaction coefficient k_{ij} for the energy parameter, expressed as:

$$a = \sum_i \sum_j x_i x_j (1-k_{ij})\sqrt{a_i a_j} \qquad \textbf{B.5}$$

$$b = \sum_i x_i b_i \qquad \textbf{B.6}$$

X_{A_i} is related to the association strength $\Delta^{A_iB_j}$ between two sites belonging to two different molecules, *e.g.* site A on molecule i and site B on molecule j, and it is found by solving the following equation:

$$X_{A_i} = \frac{1}{1+\rho\sum_j x_j \sum_{B_j} X_{B_j}\Delta^{A_iB_j}} \qquad \textbf{B.7}$$

For a self-associating molecule (*e.g.* water), $\Delta^{A_iB_i}$ is given by:

$$\Delta^{A_iB_i} = g(\rho)\left[\exp\left(\frac{\varepsilon^{A_iB_i}}{RT}\right)-1\right]b_{ii}\beta_{CPA}^{A_iB_i} \qquad \textbf{B.8}$$

where $\varepsilon^{A_iB_i}$ and $\beta_{CPA}^{A_iB_i}$ are the energy and volume association parameters, respectively, and the radial distribution function is calculated by:

$$g(\rho) = \frac{1}{1-1.9\eta} \text{ where } \eta = \frac{1}{4}b\rho \qquad \textbf{B.9}$$

For sites belonging to two different associating molecules, the Elliot's combining rule is used:

$$\Delta^{A_iB_j} = \sqrt{\Delta^{A_iB_i}\Delta^{A_jB_j}} \qquad \textbf{B.10}$$

In summary, non-associating components such as *n*-alkanes, CO_2, CH_4 and N_2 are modelled with three pure component parameters (a_0, c_1 and b) while two more parameters ($\varepsilon^{A_iB_i}$ and $\beta_{CPA}^{A_iB_i}$) are added in the model for associating fluids. The pure component parameters are generally regressed simultaneously from vapour pressure and liquid density data.

Water is the only self-associating fluid considered in this work. It is modelled using the well-known 4C association scheme, where two proton donors and two proton acceptors are assumed on every H_2O molecule.

Carbon dioxide is assumed to be able to cross-associate with water (solvation). Following the findings of Tsivintzelis *et al.* [288], interactions between H_2O and CO_2 molecules are taken into account by considering one cross-associating site in the CO_2 molecules. The cross-association energy and volume are calculated via the modified CR-1 (mCR-1) mixing rule [288]:

$$\varepsilon^{A_iB_j} = \frac{\varepsilon_{H_2O}^{A_iB_i}}{2} = 8328\ J.mol^{-1} \qquad \textbf{B.11}$$

$$\beta_{CPA}^{A_iB_j} = 0.1836 \text{ (fitted against experimental solubility data along with } k_{ij}\text{)} \qquad \textbf{B.12}$$

APPENDIX C − Optimized Binary Interaction Coefficients and Volume Corrections for the Correlation of Saturated Density Data with the PR78 EoS

Table C.1*. Calculated percentage absolute deviation (%AAD) of correlated and predicted saturated density to measured data of binary mixtures. Correlated data were obtained with the PR78 EoS and optimized binary interaction coefficients (k_{ij}) and volume corrections ($v_{c,i}$). Predicted data were obtained with the VT-PPR78 EoS described in* ***Section 3.6****.*

System	***T* / K**	***k***	**$v_{c,i}$ / 10^{-6} m^3.mol^{-1}**			**%AAD $^{a)}$**			
						Correlated		***Predicted***	
			Gas	***n-decane***		***ρ^L***	***ρ^V***	***ρ^L***	***ρ^V***
CH_4 + *n*-decane	313.1	0.046	-1.47	16.35		0.2	1.8	1.6	2.6
	343.3	0.038	-0.67	14.33		0.6	2.2	1.4	2.1
	392.9	0.040	-2.46	15.26		0.7	2.3	1.0	3.0
	442.8	0.050	-1.46	14.69		0.7	3.6	1.5	5.0
					Overall	***0.5***	***2.5***	***1.4***	***3.2***
CO_2 + *n*-decane	313.4	0.105	3.427	15.61		0.1	1.2	2.8	2.6
	343.3	0.105	1.565	14.08		1.1	1.5	2.3	1.6
	393.0	0.110	6.284	12.23		0.3	2.4	3.6	5.4
	443.1	0.112	6.868	14.73		0.4	1.9	3.1	3.6
					Overall	***0.5***	***1.7***	***2.9***	***3.3***
N_2 + *n*-decane	313.2	0.112	-3.83	17.22		0.3	2.4	1.6	5.4
	343.5	0.112	-3.24	14.19		0.2	2.1	1.2	5.0
	393.3	0.090	-5.09	12.84		0.2	1.0	0.5	5.0
	443.2	0.052	-5.15	13.83		0.1	0.6	0.7	4.0
					Overall	***0.2***	***1.5***	***1.0***	***4.8***

a) $\%AAD = 1/NP \times \sum_i^{NP} \left| (\rho_i^{Model} - \rho_i^{Exp}) / \rho_i^{Exp} \right| \times 100$

Table C.2*. Calculated percentage absolute deviation (%AAD) of correlated and predicted saturated density to measured data of multicomponent mixtures at T = 393 K. Correlated data were obtained with the PPR78 EoS and optimized volume corrections ($v_{c,i}$) of key components. Predicted data were obtained with the VT-PPR78 EoS described in* ***Section 3.6****.*

System	**$v_{c,i}$ / 10^{-6} m^3.mol^{-1}**					**%AAD $^{a)}$**			
						Correlated		***Predicted***	
	CO_2	***CH_4***	***n-decane***	***n-dodecane***	***n-tetradecane***	***ρ^L***	***ρ^V***	***ρ^L***	***ρ^V***
MIX-1	4.56	6.24	9.54			0.3	2.8	2.2	6.7
MIX-2	7.23	2.55	11.00		27.73	0.3	5.7	2.7	8.9
MIX-3	7.46	4.30	11.57	21.99		0.7	3.8	2.2	6.5
					Overall	***0.4***	***4.1***	***2.7***	***7.4***

a) Same as in **Table C.1**

APPENDIX D − Saturated Density Data

Standard uncertainties

- $u(P)$ = 0.04 MPa
- $u(T)$ = 0.1 K

Combined expanded uncertainties (confidence level of 0.95)

Hydrocarbon systems:

- $U_c(\rho)$ = 1.5 kg.m^{-3} for the liquid phase and $U_c(\rho)$ = 7.0 kg.m^{-3} for the vapour phase

Aqueous systems:

- $U_c(\rho)$ = 0.7 kg.m^{-3} for the water-rich phase and $U_c(\rho)$ = 6.7 kg.m^{-3} for the CO_2-rich phase.
- $U_c(\rho)$ = 3.0 kg.m^{-3} for in-situ measurements of the water-rich phase performed with the setup depicted in **Figure 2.10**.

***Table D.1**. Measured saturated density data of liquid (L) and vapour (V) phases of the CH_4 + n-decane system.*

P / MPa	**ρ / kg.m^{-3}**	**Phase**	**P / MPa**	**ρ / kg.m^{-3}**	**Phase**
	T = 313.1 K			**T = 392.9 K**	
0.89	715.1	*L*	0.94	647.8	*L*
3.29	702.4	*L*	3.83	636.9	*L*
5.83	690.3	*L*	7.42	620.9	*L*
8.31	679.5	*L*	10.40	609.0	*L*
10.67	666.2	*L*	14.21	588.5	*L*
12.34	659.4	*L*	16.23	576.3	*L*
15.29	642.9	*L*	17.80	570.0	*L*
18.17	626.2	*L*	19.98	554.9	*L*
22.15	607.4	*L*	21.07	547.1	*L*
27.89	569.2	*L*	23.90	527.3	*L*
34.19	525.2	*L*	27.05	499.9	*L*
2.43	16.3	*V*	10.46	57.3	*V*
5.98	41.5	*V*	13.64	76.6	*V*
10.29	73.4	*V*	17.85	108.7	*V*
14.47	105.8	*V*	24.85	156.7	*V*
21.17	160.8	*V*	29.11	193.7	*V*
21.17	160.8	*V*			
27.75	218.0	*V*		**T = 442.8 K**	
			3.19	593.9	*L*
	T = 343.3 K		4.17	590.7	*L*
1.87	685.6	*L*	7.18	575.3	*L*
3.62	678.8	*L*	11.09	557.8	*L*
7.10	662.7	*L*	13.91	543.5	*L*
10.70	645.9	*L*	14.21	541.2	*L*
13.98	631.1	*L*	17.41	519.9	*L*
17.33	613.1	*L*	20.71	495.1	*L*
20.79	592.9	*L*	22.48	478.8	*L*
24.36	572.1	*L*	23.27	470.8	*L*
29.10	536.7	*L*	23.47	466.6	*L*
13.16	89.0	*V*	24.48	455.4	*L*
17.63	117.8	*V*	13.94	75.8	*V*
21.13	154.8	*V*	17.43	101.5	*V*
26.58	194.7	*V*	21.34	132.7	*V*
29.16	213.3	*V*	26.72	190.1	*V*
32.56	245.5	*V*			

Table D.2. *Measured saturated density data of liquid (L) and vapour (V) phases of the CO_2 + n-decane system.*

P / MPa	ρ / kg.m^{-3}	Phase	P / MPa	ρ / kg.m^{-3}	Phase
	T = 313.4 K			**T = 393.0 K**	
0.49	722.1	*L*	2.43	657.8	*L*
1.13	725.8	*L*	4.92	660.2	*L*
2.30	731.8	*L*	10.53	663.2	*L*
6.34	761.6	*L*	12.58	660.6	*L*
7.25	771.3	*L*	14.00	655.2	*L*
6.75	199.8	*V*	15.48	646.1	*L*
7.17	222.7	*V*	16.64	632.3	*L*
7.27	228.1	*V*	8.64	165.6	*V*
8.05	328.4	*V*	10.81	216.5	*V*
8.07	341.3	*V*	12.61	264.3	*V*
			13.93	310.4	*V*
	T = 343.3 K		15.18	362.2	*V*
0.98	695.7	*L*	16.52	406.0	*V*
3.56	702.5	*L*	16.59	408.8	*V*
5.64	708.8	*L*	16.64	410.8	*V*
7.02	713.7	*L*	16.66	411.6	*V*
8.40	717.7	*L*			
10.43	722.0	*L*			
11.51	717.2	*L*		**T = 443.1 K**	
11.80	703.7	*L*	3.16	610.8	*L*
12.22	688.0	*L*	5.73	612.4	*L*
12.53	664.4	*L*	8.58	607.7	*L*
6.94	146.7	*V*	12.93	598.4	*L*
8.36	206.5	*V*	15.62	575.7	*L*
10.45	291.1	*V*	10.14	172.4	*V*
10.82	314.6	*V*	12.57	216.0	*V*
11.50	377.3	*V*	12.60	213.0	*V*
11.81	398.0	*V*	12.59	212.0	*V*
12.23	442.5	*V*	14.33	255.3	*V*

Table D.3. *Measured saturated density data of liquid (L) and vapour (V) phases of the N_2 + n-decane system.*

P / MPa	**ρ / kg.m^{-3}**	**Phase**	**P / MPa**	**ρ / kg.m^{-3}**	**Phase**
	T = 313.2 K			**T = 393.3 K**	
1.46	719.3	*L*	0.41	652.2	*L*
10.44	721.8	*L*	7.24	651.5	*L*
33.74	724.1	*L*	14.16	650.9	*L*
41.03	726.6	*L*	20.45	650.9	*L*
45.18	728.1	*L*	27.48	650.2	*L*
48.83	729.7	*L*	34.03	650.3	*L*
53.57	731.5	*L*	40.96	650.4	*L*
59.94	733.8	*L*	47.81	650.6	*L*
67.77	737.4	*L*	53.83	650.6	*L*
1.25	15.3	*V*	61.53	650.3	*L*
3.91	44.1	*V*	64.83	652.5	*L*
9.32	102.0	*V*	13.93	117.3	*V*
19.64	200.6	*V*	25.29	200.5	*V*
28.12	270.3	*V*	34.63	258.5	*V*
35.04	318.5	*V*	48.92	331.5	*V*
38.76	341.7	*V*	58.58	373.5	*V*
48.69	395.5	*V*	67.27	410.5	*V*
59.43	442.7	*V*			
67.05	471.0	*V*		**T = 443.2 K**	
			7.65	607.2	*L*
	T = 343.5 K		16.51	603.8	*L*
0.71	693.0	*L*	21.11	602.7	*L*
3.57	693.2	*L*	27.58	599.5	*L*
6.96	693.5	*L*	35.23	595.7	*L*
14.16	694.4	*L*	40.78	591.9	*L*
20.54	695.4	*L*	47.06	588.7	*L*
26.74	696.1	*L*	54.70	584.3	*L*
34.09	698.4	*L*	11.36	89.2	*V*
40.58	699.4	*L*	19.41	146.3	*V*
47.42	701.9	*L*	31.05	218.8	*V*
62.65	706.7	*L*	38.02	261.9	*V*
68.08	709.2	*L*	43.45	287.4	*V*
11.97	120.3	*V*			
27.33	242.1	*V*			
41.05	329.3	*V*			
54.15	390.1	*V*			
63.31	428.4	*V*			

Table D.4. *Measured saturated density data of liquid (L) and vapour (V) phases of MIX-1.*

P / MPa	**ρ / kg.m^{-3}**	**Phase**
	T = 393.1 K	
11.57	618.6	*L*
12.71	613.0	*L*
15.00	604.1	*L*
18.90	583.0	*L*
20.68	570.2	*L*
24.47	537.3	*L*
16.73	183.0	*V*
19.39	222.6	*V*
20.73	243.9	*V*
22.47	269.3	*V*
24.01	298.9	*V*

Table D.5. *Measured saturated density data of liquid (L) and vapour (V) phases of MIX-2.*

P / MPa	**ρ / kg.m^{-3}**	**Phase**
	T = 393.2 K	
10.94	661.1	*L*
12.33	659.4	*L*
13.75	656.2	*L*
13.78	656.1	*L*
15.97	648.1	*L*
18.22	639.6	*L*
19.10	635.7	*L*
11.00	192.5	*V*
12.33	219.7	*V*
13.68	243.1	*V*
15.94	299.5	*V*

Table D.6. *Measured saturated density data of liquid (L) and vapour (V) phases of MIX-3.*

P / MPa	**ρ / kg.m^{-3}**	**Phase**
	T = 393.4 K	
9.36	634.4	*L*
9.61	632.3	*L*
10.33	626.7	*L*
11.30	623.7	*L*
12.63	619.6	*L*
15.10	593.1	*L*
16.00	585.7	*L*
10.29	181.9	*V*
11.11	197.9	*V*
12.67	228.5	*V*
14.05	263.2	*V*
15.20	293.2	*V*
15.78	309.7	*V*

Table D.7. *Measured density of the water-saturated CO_2 phase of the CO_2 + H_2O system. L, G, SC stand for liquid, gaseous and supercritical state, respectively.*

T **/ K**	***P*** **/ MPa**	**Phase**		***ρ*** **/ kg·m^{-3}**
		H_2O	**CO_2**	
298.3	10.78	*L*	*L*	830.9
298.3	12.75	*L*	*L*	853.2
298.3	14.88	*L*	*L*	878.5
298.3	15.08	*L*	*L*	880.5
298.3	16.97	*L*	*L*	897.7
298.3	18.96	*L*	*L*	912.7
298.3	20.79	*L*	*L*	924.6
298.3	23.83	*L*	*L*	941.3
298.3	25.93	*L*	*L*	951.4
333.4	9.96	*L*	*SC*	292.3
333.2	26.23	*L*	*SC*	804.6
333.1	34.59	*L*	*SC*	863.0
332.9	41.70	*L*	*SC*	900.9
332.7	44.66	*L*	*SC*	914.8
373.2	1.78	*L*	*G*	33.0
373.2	9.41	*L*	*SC*	180.3
373.2	14.60	*L*	*SC*	323.2
373.5	30.90	*L*	*SC*	678.0
373.5	44.28	*L*	*SC*	789.7
373.7	56.49	*L*	*SC*	854.4
373.7	68.71	*L*	*SC*	900.0

Table D.8. *Measured density of the CO_2-saturated water phase of the CO_2 + H_2O system. L, G, SC stand for liquid, gaseous and supercritical state, respectively.*

T **/ K**	***P*** **/ MPa**	**Phase**		***ρ*** **/ kg·m^{-3}**	***T*** **/ K**	***P*** **/ MPa**	**Phase**		***ρ*** **kg·m^{-3}**
		H_2O	**CO_2**				**H_2O**	**CO_2**	
298.5	0.32	*L*	*G*	999.3	373.7	7.04	*L*	*G*	967.0
298.5	0.75	*L*	*G*	1000.8	373.2	13.93	*L*	*SC*	971.5
298.4	1.82	*L*	*G*	1004.5	373.5	20.82	*L*	*SC*	976.6
298.4	3.77	*L*	*G*	1009.8	373.4	28.07	*L*	*SC*	980.1
298.4	5.6	*L*	*G*	1014.1	373.4	34.22	*L*	*SC*	983.4
298.5	8.95	*L*	*L*	1017.4	373.3	41.61	*L*	*SC*	987.0
298.4	10.52	*L*	*L*	1018.6	373.3	49.73	*L*	*SC*	992.6
298.4	11.89	*L*	*L*	1019.2	374.1	55.50	*L*	*SC*	995.9
298.4	18.91	*L*	*L*	1020.6	374.1	61.79	*L*	*SC*	999.6
298.3	21.23	*L*	*L*	1020.8	374.1	68.73	*L*	*SC*	1002.6
323.8	0.86	*L*	*G*	988.1*	393.3	0.86	*L*	*G*	945.2
323.9	2.69	*L*	*G*	990.8*	393.6	3.56	*L*	*G*	947.0
323.9	5.77	*L*	*G*	997.9*	393.5	5.50	*L*	*G*	949.8
323.9	9.83	*L*	*SC*	1001.9*	393.5	7.45	*L*	*G*	951.5
323.9	15.54	*L*	*SC*	1006.0*	393.5	10.60	*L*	*SC*	954.0
323.9	24.41	*L*	*SC*	1010.7*	393.5	13.92	*L*	*SC*	956.6
323.8	37.58	*L*	*SC*	1016.9*	393.4	24.31	*L*	*SC*	962.9
323.9	44.82	*L*	*SC*	1020.7*	393.4	34.81	*L*	*SC*	969.2
					393.2	55.19	*L*	*SC*	979.6
333.4	0.73	*L*	*G*	985.8	393.2	68.80	*L*	*SC*	986.2
333.4	1.82	*L*	*G*	987.2					
333.4	3.74	*L*	*G*	989.4	423.7	0.87	*L*	*G*	918.9
333.4	5.99	*L*	*G*	991.9	423.7	1.46	*L*	*G*	919.7
333.4	7.67	*L*	*G*	994.2	423.7	3.75	*L*	*G*	920.9
333.5	11.73	*L*	*SC*	995.9	423.5	5.18	*L*	*G*	921.7
333.5	14.52	*L*	*SC*	999.2	423.5	6.23	*L*	*G*	922.5
333.4	17.68	*L*	*SC*	1001.9	423.5	7.36	*L*	*G*	923.2
333.5	21.05	*L*	*SC*	1003.7	423.5	7.42	*L*	*G*	923.4
333.4	28.17	*L*	*SC*	1006.4	423.5	9.33	*L*	*SC*	925.0
333.4	35.68	*L*	*SC*	1010.7	423.5	10.41	*L*	*SC*	925.8
333.4	41.01	*L*	*SC*	1014.1	423.5	12.28	*L*	*SC*	927.1
333.5	47.9	*L*	*SC*	1017.5	423.5	14.61	*L*	*SC*	928.5
333.5	55.29	*L*	*SC*	1020.8	423.5	21.60	*L*	*SC*	933.6
333.5	62.19	*L*	*SC*	1023.2	423.3	28.82	*L*	*SC*	937.6
333.4	69.13	*L*	*SC*	1025.8	423.2	55.20	*L*	*SC*	952.7

*Measured in-situ during *IFT* measurements with setup depicted in **Figure 2.10**.

Table D.9. *Measured (in-situ) density of the water-rich phase of the MIX-4 + H_2O and MIX-5 + H_2O systems.*

MIX-4 + H_2O				**MIX-5 + H_2O**			
P / MPa	**ρ / kg·m^{-3}**	**P / MPa**	**ρ / kg·m^{-3}**	**P / MPa**	**ρ / kg·m^{-3}**	**P / MPa**	**ρ / kg·m^{-3}**
T = 298.2 K		**T = 323.8 K**		**T = 298.2 K**		**T = 323.8 K**	
1.65	1002.8	1.24	988.9	2.09	1003.0	2.57	989.2
3.50	1007.7	2.12	989.9	3.54	1006.1	3.70	993.3
10.96	1016.6	2.82	992.7	12.58	1016.6	12.28	1001.9
20.27	1020.9	3.50	993.8	20.84	1019.7	51.54	1021.2
		5.33	995.6				
		21.29	1006.7				
		36.91	1015.4				
T = 373.4 K		**T = 423.7 K**		**T = 373.4 K**		**T = 423.1 K**	
2.11	959.4	3.51	919.5	2.56	960.9	27.68	934.9
3.57	961.8	5.24	921.2	17.22	969.5	48.33	945.8
7.32	964.6	10.45	924.9	21.01	972.5		
15.86	971.5	27.74	936.9	52.56	987.5		
21.29	975.0	31.45	938.8	69.06	993.4		
36.91	983.6	43.54	946.0				
52.88	991.0	55.75	952.7				

APPENDIX E − Interfacial Tension Data

Standard uncertainties
- *u*(*P*) = 0.04 MPa
- *u*(*T*) = 0.1 K

Combined expanded uncertainties (confidence level of 0.95)
- $U_c\,(a^2)$ = 0.000331 cm^2
- $U_c\,(IFT)$ is estimated and listed in tables for each pressure and temperature state

Table E.1. *Measured interfacial tension data of the CH_4 + n-decane system. The density difference between equilibrated phases corresponds to correlated data using the PR78 EoS and parameters listed in* ***Table C.1***.

P **/ MPa**	a^2 **/ cm²**	$\Delta\rho$ **/ kg.m⁻³**	***IFT*** **/ mN.m⁻¹**	**Experimental Error / mN.m⁻¹**		
				U_1	U_2	$U_c=U_1+U_2$
			T **= 313.3 K**			
0.45	0.055604	716.8	19.56	0.12	0.04	0.16
1.08	0.053354	709.6	18.58	0.12	0.04	0.16
2.97	0.047465	687.4	16.01	0.11	0.03	0.14
5.83	0.040651	652.2	13.01	0.11	0.03	0.14
10.43	0.030826	592.2	8.96	0.10	0.03	0.13
12.46	0.027056	565.0	7.50	0.09	0.03	0.12
15.28	0.022493	526.8	5.81	0.09	0.03	0.12
18.20	0.017667	487.0	4.22	0.08	0.02	0.10
22.04	0.013141	434.3	2.80	0.07	0.02	0.09
28.02	0.006550	349.2	1.12	0.06	0.01	0.07
29.64	0.005008	324.8	0.80	0.05	0.01	0.06
30.50	0.004485	311.5	0.69	0.05	0.01	0.06
			T **= 343.2 K**			
0.86	0.049980	687.8	16.87	0.11	0.09	0.20
1.87	0.047895	677.1	15.92	0.11	0.09	0.20
3.62	0.042900	658.1	13.86	0.11	0.08	0.19
7.11	0.035523	618.5	10.78	0.10	0.07	0.17
10.69	0.028974	575.7	8.19	0.09	0.06	0.15
13.97	0.023981	534.9	6.30	0.09	0.05	0.14
17.34	0.019055	491.4	4.60	0.08	0.04	0.12
20.83	0.014462	444.4	3.15	0.07	0.03	0.10
24.43	0.010336	393.0	1.99	0.06	0.02	0.08
29.16	0.005532	318.3	0.86	0.05	0.01	0.06
			T **= 392.6 K**			
0.94	0.040320	654.9	12.96	0.11	0.09	0.20
3.85	0.034366	624.8	10.54	0.10	0.07	0.17
7.45	0.028610	585.7	8.22	0.10	0.06	0.16
10.50	0.024874	550.9	6.73	0.09	0.05	0.14
14.08	0.019385	507.9	4.83	0.08	0.04	0.12
17.86	0.015420	459.4	3.48	0.07	0.03	0.10
21.14	0.012118	413.9	2.46	0.07	0.03	0.10
23.99	0.009248	371.1	1.68	0.06	0.02	0.08
28.49	0.005795	293.4	0.83	0.05	0.02	0.07

Table E.1 *(continued).*

P **/ MPa**	a^2 **/ cm**^{2}	$\Delta\rho$ **/ kg.m**$^{-3}$	***IFT*** **/ mN.m**$^{-1}$	**Experimental Error / mN.m**$^{-1}$		
				U_1	U_2	$U_c=U_1+U_2$
T **= 442.3 K**						
4.18	0.027188	573.7	7.66	0.09	0.05	0.14
7.18	0.023121	540.9	6.14	0.09	0.05	0.14
11.11	0.018592	494.9	4.52	0.08	0.04	0.12
14.25	0.014825	454.9	3.31	0.07	0.03	0.10
17.43	0.011425	410.9	2.30	0.07	0.02	0.10
20.70	0.007503	360.7	1.33	0.06	0.02	0.08
22.53	0.005729	329.6	0.93	0.05	0.02	0.07
24.63	0.004289	290.2	0.61	0.05	0.01	0.06

Table E.2. *Measured interfacial tension data of the* CO_2 *+ n-decane system. The density difference between equilibrated phases corresponds to correlated data using the PR78 EoS and parameters listed in* ***Table C.1***.

P **/ MPa**	a^2 **/ cm**^{2}	$\Delta\rho$ **/ kg.m**$^{-3}$	***IFT*** **/ mN.m**$^{-1}$	**Experimental error / mN.m**$^{-1}$		
				U_1	U_2	$U_c=U_1+U_2$
T **= 313.5 K**						
3.49	0.040452	669.2	13.29	0.11	0.03	0.14
5.51	0.025601	621.2	7.81	0.10	0.02	0.12
6.71	0.017105	574.1	4.82	0.09	0.02	0.11
6.79	0.015717	569.9	4.40	0.09	0.02	0.11
7.09	0.013273	551.9	3.60	0.09	0.02	0.11
T **= 343.2 K**						
0.99	0.04816	682.4	16.13	0.11	0.17	0.28
3.59	0.03873	640.3	12.17	0.10	0.14	0.24
5.69	0.03007	596.0	8.79	0.10	0.11	0.21
7.02	0.02481	560.6	6.83	0.09	0.10	0.19
8.39	0.01882	514.8	4.76	0.08	0.07	0.15
10.43	0.00991	415.7	2.02	0.07	0.04	0.11
10.84	0.00842	387.9	1.60	0.06	0.04	0.10
11.52	0.00517	331.9	0.84	0.05	0.02	0.07
11.80	0.00403	302.9	0.60	0.05	0.02	0.07
T **= 392.7 K**						
1.21	0.03959	639.3	12.42	0.10	0.04	0.14
4.84	0.03142	584.0	9.01	0.09	0.04	0.13
8.73	0.02190	506.7	5.45	0.08	0.05	0.13
10.81	0.01664	454.2	3.71	0.07	0.04	0.11
12.65	0.01222	398.5	2.39	0.06	0.04	0.10
13.98	0.00938	351.1	1.62	0.06	0.03	0.09
15.47	0.00413	288.1	0.58	0.05	0.02	0.07
T **= 442.5 K**						
3.60	0.02752	564.8	7.63	0.09	0.04	0.13
6.02	0.02342	524.5	6.03	0.09	0.04	0.12
7.86	0.01985	490.2	4.78	0.08	0.03	0.11
10.26	0.01572	439.6	3.39	0.07	0.03	0.10
12.64	0.01166	380.9	2.18	0.06	0.03	0.09
14.44	0.00806	328.7	1.30	0.05	0.02	0.07

Table E.3. *Measured interfacial tension data of the* N_2 *+ n-decane system. The density difference between equilibrated phases corresponds to correlated data using the PR78 EoS and parameters listed in* ***Table C.1***.

P / MPa	**a^2 / cm^2**	**$\Delta\rho$ / kg.m^{-3}**	**IFT / mN.m^{-1}**	**Experimental Error / mN.m^{-1}**		
				U_1	**U_2**	**$U_c=U_1+U_2$**
T = 313.4 K						
1.19	0.061758	712.0	21.58	0.12	0.06	0.18
3.74	0.058648	684.0	19.69	0.11	0.06	0.17
10.54	0.052924	611.7	15.89	0.10	0.08	0.18
14.75	0.050178	569.9	14.04	0.09	0.10	0.19
22.00	0.047366	504.6	11.73	0.08	0.13	0.21
27.98	0.045745	457.1	10.26	0.07	0.15	0.22
34.68	0.043297	410.6	8.72	0.07	0.16	0.23
42.36	0.041875	364.4	7.49	0.06	0.18	0.24
47.33	0.041180	338.1	6.83	0.05	0.19	0.24
51.02	0.040452	320.2	6.36	0.05	0.19	0.24
55.78	0.040055	298.8	5.87	0.05	0.20	0.25
62.17	0.039129	273.0	5.24	0.04	0.21	0.25
T = 343.2 K						
0.71	0.056266	689.3	19.03	0.11	0.04	0.15
3.72	0.053454	659.2	17.29	0.11	0.04	0.15
7.32	0.050145	624.1	15.36	0.10	0.05	0.15
14.50	0.045547	558.0	12.47	0.09	0.07	0.16
21.10	0.042437	502.9	10.47	0.08	0.09	0.17
28.29	0.039294	449.3	8.66	0.07	0.10	0.17
35.01	0.036946	404.9	7.34	0.07	0.11	0.18
41.75	0.034663	365.5	6.22	0.06	0.12	0.18
48.85	0.033274	328.7	5.37	0.05	0.13	0.18
57.07	0.031356	291.4	4.48	0.05	0.13	0.18
64.47	0.029603	261.9	3.81	0.04	0.13	0.17
69.00	0.028445	245.6	3.43	0.04	0.13	0.17
T = 392.6 K						
0.41	0.046374	653.1	14.86	0.11	0.03	0.14
3.80	0.043231	622.6	13.21	0.10	0.03	0.13
7.48	0.041081	590.7	11.91	0.10	0.03	0.13
14.67	0.036582	531.7	9.55	0.09	0.03	0.12
20.90	0.032976	484.7	7.84	0.08	0.03	0.11
28.27	0.028710	434.1	6.12	0.07	0.03	0.10
34.92	0.025899	392.8	4.99	0.06	0.04	0.10
41.99	0.023948	353.0	4.15	0.06	0.04	0.10
49.27	0.020675	316.1	3.21	0.05	0.03	0.08
55.60	0.018956	287.0	2.67	0.05	0.03	0.08
62.59	0.015949	257.5	2.02	0.04	0.03	0.07
64.93	0.015255	248.3	1.86	0.04	0.03	0.07

Table E.3 *(continued).*

P **/ MPa**	***a***^{2} **/ cm**^{2}	***Δρ*** **/ kg.m**$^{-3}$	***IFT*** **/ mN.m**$^{-1}$	**Experimental Error / mN.m**$^{-1}$		
				U_1	U_2	$U_c=U_1+U_2$
			T **= 442.2 K**			
0.90	0.036251	606.3	10.79	0.10	0.01	0.11
4.38	0.033340	576.8	9.44	0.09	0.01	0.10
7.63	0.032050	549.9	8.65	0.09	0.01	0.10
16.35	0.026196	481.3	6.19	0.08	0.01	0.09
21.24	0.023749	445.2	5.19	0.07	0.01	0.08
28.27	0.019947	396.3	3.88	0.06	0.01	0.07
35.48	0.016675	349.2	2.86	0.06	0.01	0.07
45.91	0.011062	285.7	1.55	0.05	0.01	0.06
48.67	0.009874	269.8	1.31	0.04	0.01	0.05
55.67	0.007964	230.4	0.90	0.04	0.01	0.05

Table E.4*. Measured interfacial tension data of MIX-1. The density difference between equilibrated phases corresponds to correlated data using the PPR78 EoS and optimised volume corrections listed in* ***Table C.2****.*

P **/ MPa**	***a***^{2} **/ cm**^{2}	***Δρ*** **/ kg.m**$^{-3}$	***IFT*** **/ mN.m**$^{-1}$	**Experimental Error / mN.m**$^{-1}$		
				U_1	U_2	$U_c=U_1+U_2$
			T **= 393.1 K**			
8.44	0.026858	546.5	7.20	0.09	0.04	0.13
10.12	0.023749	523.0	6.10	0.08	0.04	0.12
13.09	0.019286	478.1	4.53	0.08	0.04	0.12
15.30	0.015982	441.8	3.46	0.07	0.04	0.11
16.99	0.013504	412.1	2.73	0.07	0.04	0.10
19.39	0.010171	365.5	1.82	0.06	0.03	0.09
21.00	0.007964	331.0	1.29	0.05	0.03	0.08
22.88	0.005500	286.1	0.77	0.05	0.02	0.07

Table E.5*. Measured interfacial tension data of MIX-2. The density difference between equilibrated phases corresponds to correlated data using the PPR78 EoS and optimised volume corrections listed in* ***Table C.2****.*

P **/ MPa**	***a***^{2} **/ cm**^{2}	***Δρ*** **/ kg.m**$^{-3}$	***IFT*** **/ mN.m**$^{-1}$	**Experimental Error / mN.m**$^{-1}$		
				U_1	U_2	$U_c=U_1+U_2$
			T **= 393.2 K**			
10.11	0.022328	504.1	5.52	0.08	0.10	0.18
11.23	0.020344	480.6	4.80	0.08	0.10	0.18
12.60	0.016907	449.7	3.73	0.07	0.10	0.17
14.01	0.014660	415.2	2.99	0.07	0.10	0.17
16.03	0.010930	359.9	1.93	0.06	0.09	0.15
18.28	0.006648	288.6	0.94	0.05	0.07	0.11
19.31	0.005106	251.1	0.63	0.04	0.06	0.10
19.56	0.004649	240.9	0.55	0.04	0.05	0.09
19.69	0.004289	235.8	0.50	0.04	0.05	0.09

Table E.6. *Measured interfacial tension data of MIX-3. The density difference between equilibrated phases corresponds to correlated data using the PPR78 EoS and optimised volume corrections listed in* ***Table C.2***.

P **/ MPa**	a^2 **/cm²**	$\Delta\rho$ **/ kg.m⁻³**	***IFT*** **/ mN.m⁻¹**	**Experimental Error / mN.m⁻¹**		
				U_1	U_2	$U_c=U_1+U_2$
			T **= 393.4 K**			
9.34	0.019650	481.5	4.64	0.08	0.07	0.15
9.62	0.019055	474.8	4.44	0.08	0.07	0.14
10.49	0.017039	453.5	3.79	0.07	0.06	0.14
11.35	0.015222	431.4	3.22	0.07	0.06	0.13
12.75	0.012382	392.8	2.39	0.06	0.06	0.12
14.42	0.009248	341.5	1.55	0.06	0.05	0.10
15.22	0.007635	314.3	1.18	0.05	0.04	0.09
16.05	0.006090	283.9	0.85	0.05	0.04	0.08

Table E.7. *Measured interfacial tension data of the CO_2 + H_2O system. The density difference used corresponds to the difference between the values correlated with* **Equation 5.1** *and pure CO_2 obtained from REFPROP* [99]. *L, G and SC stand for liquid, gaseous and supercritical state, respectively.*

T / K	***P*** / MPa	Phase		***Δρ*** / kg.m^{-3}	***IFT*** / mN.m^{-1}	Experimental Error / mN.m^{-1}		
		H_2O	CO_2			U_1	U_2	$U_c = U_1 + U_2$
298.5	0.70	*L*	*G*	989.0	66.95	0.11	0.10	0.21
298.5	1.69	*L*	*G*	971.1	60.56	0.07	0.10	0.17
298.5	3.68	*L*	*G*	924.9	48.70	0.05	0.09	0.14
298.5	5.64	*L*	*G*	847.5	37.74	0.07	0.12	0.19
298.5	6.06	*L*	*G*	817.7	35.06	0.06	0.16	0.22
298.5	6.40	*L*	*G*	779.8	32.97	0.25	0.27	0.52
298.6	6.49*	*L*	*G*	765.4	31.69	0.44	0.71	1.15
298.6	6.49*	*L*	*L*	310.4	30.79	0.17	1.70	1.87
298.4	6.83	*L*	*L*	283.6	31.00	0.14	0.35	0.49
298.5	7.20	*L*	*L*	268.5	30.99	0.10	0.30	0.40
298.5	8.10	*L*	*L*	239.6	31.09	0.06	0.27	0.33
298.6	8.97	*L*	*L*	220.5	30.98	0.08	0.26	0.34
298.6	10.63	*L*	*L*	192.1	30.73	0.08	0.26	0.34
298.6	13.18	*L*	*L*	161.1	30.62	0.08	0.29	0.37
298.6	15.15	*L*	*L*	142.6	30.81	0.10	0.32	0.42
298.6	20.83	*L*	*L*	103.0	29.84	0.08	0.41	0.49
313.3	0.46	*L*	*G*	986.0	68.52	0.23	0.10	0.33
313.3	1.85	*L*	*G*	962.6	59.60	0.22	0.09	0.31
313.3	3.57	*L*	*G*	927.3	50.67	0.32	0.09	0.41
313.3	5.34	*L*	*G*	878.6	42.75	0.13	0.09	0.22
313.3	7.01	*L*	*G*	806.8	36.65	0.24	0.12	0.36
313.2	9.30	*L*	*SC*	459.7	30.62	0.29	0.53	0.82
313.2	10.44	*L*	*SC*	352.0	29.91	0.32	0.26	0.58
313.3	13.92	*L*	*SC*	249.3	29.59	0.20	0.20	0.40
313.3	20.82	*L*	*SC*	166.4	29.20	0.07	0.25	0.32
313.3	25.68	*L*	*SC*	131.8	28.96	0.10	0.31	0.41
313.3	29.11	*L*	*SC*	112.5	29.05	0.10	0.36	0.46
313.2	31.19	*L*	*SC*	101.9	28.88	0.12	0.39	0.51
323.8	0.86	*L*	*G*	974.5	64.79	0.10	0.10	0.20
323.9	2.69	*L*	*G*	943.1	56.44	0.14	0.09	0.23
323.9	5.77	*L*	*G*	870.3	45.26	0.10	0.09	0.19
323.9	9.83	*L*	*SC*	647.4	33.01	0.15	0.23	0.38
323.9	15.54	*L*	*SC*	299.0	30.09	0.19	0.17	0.36
323.9	24.41	*L*	*SC*	183.4	29.08	0.10	0.21	0.32
323.8	37.58	*L*	*SC*	105.7	28.78	0.23	0.33	0.55
323.9	44.82	*L*	*SC*	78.5	28.13	0.18	0.40	0.58
333.0	0.92	*L*	*G*	968.8	62.31	0.06	0.09	0.15
333.0	1.79	*L*	*G*	955.1	58.98	0.08	0.09	0.17
333.0	3.66	*L*	*G*	921.3	52.28	0.07	0.09	0.16
333.0	5.00	*L*	*G*	892.2	47.96	0.04	0.09	0.13
333.0	5.85	*L*	*G*	871.0	45.30	0.06	0.09	0.15
333.0	7.18	*L*	*G*	831.7	41.29	0.11	0.09	0.20
333.0	8.89	*L*	*SC*	764.6	36.76	0.10	0.11	0.21
333.1	10.04	*L*	*SC*	703.3	34.08	0.12	0.14	0.26

* vapour-liquid-liquid point

Table E.7 *(continued)*

T /K	*P* /MPa	Phase		*Δρ* / kg.m^{-3}	*IFT* / mN.m^{-1}	Experimental Error / mN.m^{-1}		
		H_2O	CO_2			U_1	U_2	$U_c = U_1 + U_2$
333.2	11.42	*L*	*SC*	607.6	30.10	0.29	0.17	0.46
333.1	15.01	*L*	*SC*	394.0	29.46	0.19	0.17	0.35
333.2	21.12	*L*	*SC*	261.6	28.13	0.14	0.16	0.30
333.2	24.27	*L*	*SC*	224.6	27.39	0.15	0.18	0.33
333.2	29.58	*L*	*SC*	179.6	27.00	0.14	0.21	0.35
333.2	31.29	*L*	*SC*	167.9	27.25	0.18	0.23	0.41
333.2	39.64	*L*	*SC*	123.0	26.26	0.12	0.29	0.41
333.2	50.31	*L*	*SC*	82.7	26.27	0.11	0.43	0.54
333.2	59.91	*L*	*SC*	55.8	26.16	0.13	0.62	0.75
373.8	0.34	*L*	*G*	952.4	56.79	0.15	0.08	0.23
373.9	1.30	*L*	*G*	939.4	55.02	0.10	0.08	0.18
373.9	3.86	*L*	*G*	901.3	49.03	0.09	0.08	0.17
374.0	5.60	*L*	*G*	871.8	45.62	0.10	0.08	0.18
374.0	7.57	*L*	*SC*	834.1	41.88	0.07	0.08	0.15
374.0	12.09	*L*	*SC*	726.0	34.14	0.11	0.08	0.19
374.0	16.96	*L*	*SC*	580.8	29.00	0.11	0.09	0.20
374.0	25.15	*L*	*SC*	389.6	26.41	0.08	0.10	0.18
373.9	40.03	*L*	*SC*	230.1	24.35	0.12	0.15	0.27
374.0	50.18	*L*	*SC*	172.9	23.64	0.09	0.18	0.27
374.1	62.07	*L*	*SC*	126.7	23.38	0.11	0.25	0.36
374.0	69.12	*L*	*SC*	105.4	23.42	0.06	0.29	0.35
424.4	1.55	*L*	*G*	900.7	46.34	0.07	0.07	0.14
424.4	5.81	*L*	*G*	843.0	40.10	0.09	0.07	0.16
424.4	10.21	*L*	*SC*	776.3	34.60	0.05	0.07	0.12
424.4	16.43	*L*	*SC*	670.0	29.00	0.07	0.06	0.13
424.5	23.83	*L*	*SC*	538.6	25.55	0.08	0.07	0.15
424.6	30.05	*L*	*SC*	450.6	22.82	0.04	0.07	0.11
424.6	39.68	*L*	*SC*	343.3	20.89	0.03	0.08	0.11
424.5	50.11	*L*	*SC*	265.4	19.82	0.15	0.10	0.25
424.6	60.19	*L*	*SC*	211.8	18.83	0.12	0.12	0.24
424.6	69.14	*L*	*SC*	175.8	18.42	0.12	0.14	0.26
469.0	5.90	*L*	*G*	808.0	32.91	0.09	0.06	0.15
469.2	10.08	*L*	*SC*	754.1	28.69	0.10	0.05	0.15
469.1	10.79	*L*	*SC*	744.9	28.49	0.06	0.05	0.11
469.2	14.91	*L*	*SC*	690.1	24.88	0.06	0.05	0.11
469.2	17.70	*L*	*SC*	652.7	23.14	0.05	0.05	0.10
469.2	20.71	*L*	*SC*	612.6	21.82	0.06	0.05	0.11
469.2	29.97	*L*	*SC*	497.1	18.22	0.13	0.05	0.18
469.2	40.06	*L*	*SC*	397.7	15.45	0.09	0.05	0.14
469.2	50.16	*L*	*SC*	318.4	13.84	0.07	0.06	0.13
469.4	59.96	*L*	*SC*	261.0	12.73	0.05	0.07	0.12
469.2	69.09	*L*	*SC*	218.7	12.65	0.10	0.08	0.18

Table E.8. *Measured interfacial tension data of the MIX-4 + H_2O system. The density difference used corresponds to the difference between the values measured in-situ/correlated for the water-rich phase and that of dry MIX-4* [323].

P / MPa	**$\Delta\rho$ / kg.m^{-3}**	**IFT / mN.m^{-1}**	**Experimental Error / mN.m^{-1}**		
			U_1	**U_2**	**$U_c = U_1 + U_2$**
T = 298.2 K					
1.65	971.5	61.29	0.25	0.46	0.71
3.50	932.6	52.02	0.30	0.41	0.71
10.96	263.2	30.21	0.15	0.84	0.99
20.27	151.8	30.17	0.19	1.46	1.65
T = 323.8 K					
1.24	967.1	62.08	0.18	0.47	0.65
2.12	953.0	59.47	0.10	0.46	0.56
2.82	942.0	56.15	0.13	0.44	0.57
3.50	928.0	54.16	0.09	0.43	0.52
7.32	826.4	40.91	0.05	0.36	0.41
21.29	259.5	28.79	0.08	0.81	0.89
36.91	143.9	28.81	0.08	1.47	1.55
T = 373.4 K					
2.11	930.0	53.85	0.20	0.43	0.63
3.57	910.9	51.03	0.25	0.41	0.66
7.32	837.3	42.90	0.12	0.38	0.50
15.86	619.4	29.91	0.10	0.35	0.45
21.29	493.7	28.06	0.10	0.42	0.52
36.91	282.6	25.51	0.06	0.66	0.72
52.88	188.2	25.50	0.05	0.99	1.04
T = 423.7 K					
5.24	853.7	40.93	0.10	0.35	0.45
10.45	781.7	35.28	0.15	0.33	0.48
27.74	525.5	24.79	0.17	0.35	0.52
43.54	334.1	20.73	0.05	0.46	0.51
55.75	255.2	19.43	0.09	0.56	0.65

Table E.9. *Measured interfacial tension data of the MIX-5 + H_2O system. The density difference used corresponds to the difference between the values measured in-situ/correlated for the water-rich phase and that of dry MIX-5* [323].

P / MPa	**$\Delta\rho$ / kg.m^{-3}**	**IFT / mN.m^{-1}**	**Experimental Error / mN.m^{-1}**		
			U_1	**U_2**	**$U_c = U_1 + U_2$**
T = 298.2 K					
2.09	963.8	60.86	0.16	0.46	0.62
3.54	930.8	52.72	0.17	0.42	0.59
20.84	192.7	29.61	0.06	1.13	1.19
T = 323.8 K					
2.57	943.9	58.79	0.10	0.46	0.56
3.70	925.8	55.27	0.12	0.44	0.56
12.28	592.8	32.21	0.15	0.40	0.55
21.05	318.7	30.05	0.10	0.69	0.79
T = 373.4 K					
2.56	926.4	52.27	0.07	0.41	0.48
17.22	615.6	31.59	0.10	0.38	0.48
21.01	532.8	29.74	0.08	0.41	0.49
52.56	209.8	24.60	0.05	0.86	0.91
T = 423.4 K					
2.40	889.6	46.54	0.15	0.38	0.53
3.42	877.0	44.92	0.13	0.38	0.51
17.21	664.8	29.44	0.19	0.33	0.52
21.01	606.7	27.54	0.07	0.33	0.40
52.55	287.9	20.11	0.04	0.51	0.55

Table E.10. *Measured interfacial tension data of the CO_2 + H_2O + NaCl system for a salt molality 0.98 mol.kg^{-1}. The density difference used corresponds to the difference between the values estimated with the model of Duan et al.* [325] *for the CO_2-saturated brine phase and pure CO_2 obtained from REFPROP* [99].

P / MPa	$\Delta\rho$ / kg.m^{-3}	IFT / mN.m^{-1}	Experimental Error / mN.m^{-1}		
			U_1	U_2	$U_c = U_1 + U_2$
		T = 298.6 K			
3.00	980.1	53.39	0.04	0.12	0.16
4.96	918.2	42.37	0.05	0.12	0.17
5.66	882.7	38.43	0.03	0.14	0.17
10.31	236.1	32.98	0.07	0.32	0.39
15.58	177.4	32.35	0.04	0.38	0.42
20.21	145.0	32.33	0.08	0.46	0.54
		T = 333.2 K			
3.91	952.0	52.1	0.04	0.12	0.16
7.40	858.8	41.7	0.04	0.12	0.16
18.84	331.5	31.7	0.06	0.21	0.27
40.94	150.5	29.4	0.14	0.40	0.54
55.07	100.1	29.2	0.09	0.59	0.68
		T = 373.4 K			
7.19	876.9	44.04	0.06	0.11	0.17
12.32	753.1	35.94	0.11	0.11	0.22
20.14	525.2	30.60	0.05	0.13	0.18
40.89	255.9	26.81	0.05	0.21	0.26
69.50	131.6	25.10	0.06	0.38	0.44
		T = 423.3 K			
5.69	882.2	42.3	0.04	0.10	0.14
11.12	798.9	35.6	0.05	0.09	0.14
22.37	600.1	27.3	0.06	0.10	0.16
43.07	346.6	22.2	0.06	0.13	0.19
69.07	204.2	19.9	0.05	0.20	0.25

Table E.11. *Measured interfacial tension data of the $CO_2 + H_2O$ + NaCl system for a salt molality 1.98 mol.kg^{-1}. The density difference used corresponds to the difference between the values estimated with the model of Duan et al.* [325] *for the CO_2-saturated brine phase and pure CO_2 obtained from REFPROP* [99].

***P* / MPa**	***Δρ* / kg.m^{-3}**	***IFT* / mN.m^{-1}**	**Experimental Error / mN.m^{-1}**		
			U_1	U_2	$U_c = U_1 + U_2$
		***T* = 298.6 K**			
2.96	1015.9	54.98	0.04	0.12	0.16
4.12	983.3	48.43	0.03	0.12	0.15
5.69	914.7	39.59	0.03	0.14	0.17
10.25	270.4	34.09	0.06	0.29	0.35
14.82	217.1	33.74	0.07	0.33	0.40
19.90	179.8	33.61	0.07	0.39	0.46
		***T* = 333.2 K**			
4.09	981.9	53.20	0.07	0.12	0.19
7.86	875.2	42.14	0.03	0.12	0.15
18.85	363.0	33.34	0.06	0.21	0.27
41.72	178.6	31.22	0.04	0.36	0.40
54.76	132.1	30.99	0.06	0.47	0.53
		***T* = 373.3 K**			
4.61	959.3	50.69	0.08	0.11	0.19
11.49	809.5	39.01	0.13	0.11	0.24
21.94	515.3	31.76	0.08	0.14	0.22
43.18	273.1	28.31	0.11	0.21	0.32
69.51	162.6	27.16	0.04	0.34	0.38
		***T* = 423.2 K**			
5.65	918.1	44.36	0.07	0.10	0.17
12.17	815.9	36.00	0.09	0.09	0.18
21.88	642.5	29.07	0.05	0.10	0.15
44.35	369.5	23.25	0.09	0.13	0.22
69.00	236.5	21.64	0.05	0.18	0.23

APPENDIX F − Complementary Modelling Results

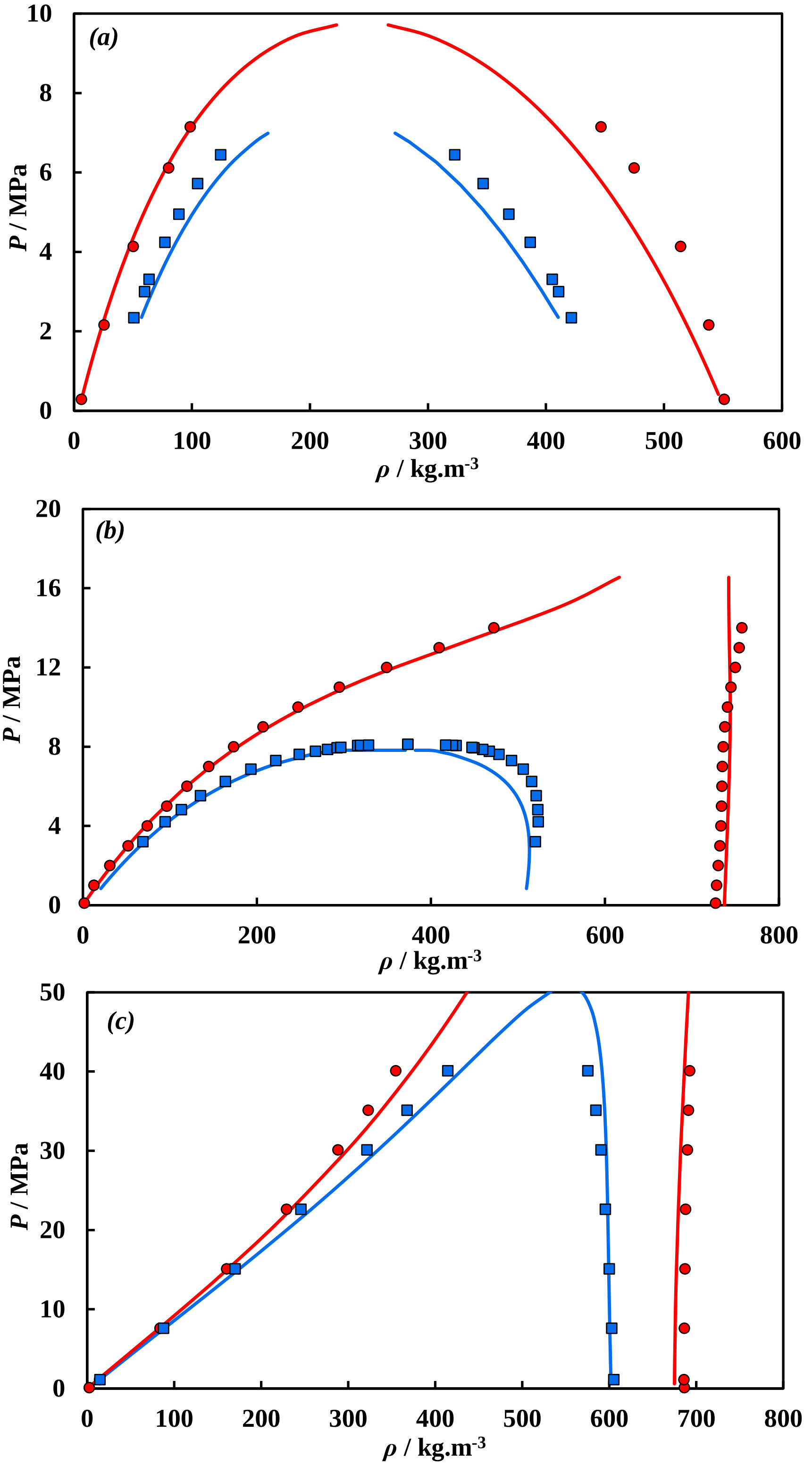

***Figure F.1**. Pressure−density diagrams of **(a)** CH_4 + n-alkane, **(b)** CO_2 + n-alkane and **(c)** N_2 + n-alkane. Symbols in **(a)** represent experimental density data of CH_4 and propane taken from Weinaug and Katz* [41], *T = 258 K (●) and 338 K (■). Symbols in **(b)** represent experimental density data of CO_2 and: n-butane taken from Hsu et al.* [68], *T = 344 K (■) and n-tetradecane taken from Cumicheo et al.* [54], *T = 344 K (●). Symbols in **(c)** represent experimental density data of N_2 and: n-pentane (■) and n-octane (●) from Jianhua et al.* [52], *T = 313 K. Solid lines represent predictions with the VT-PPR78 EoS.*

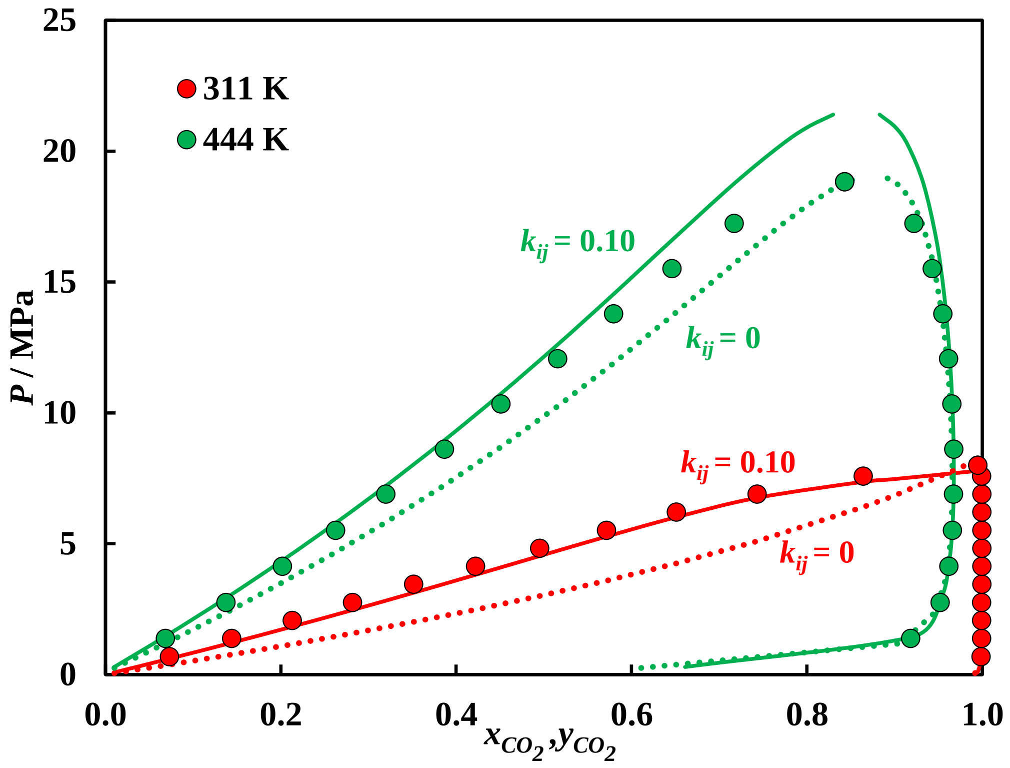

Figure F.2. *Pressure−composition diagram of CO_2 + n-decane. Solid symbols represent experimental solubility data from Reamer and Sage* [45]. *Lines represent CPA EoS predictions i.e. k_{ij} = 0 (dotted) and CPA EoS estimations i.e., $k_{ij} \neq 0$ (solid), at pertinent temperatures.*

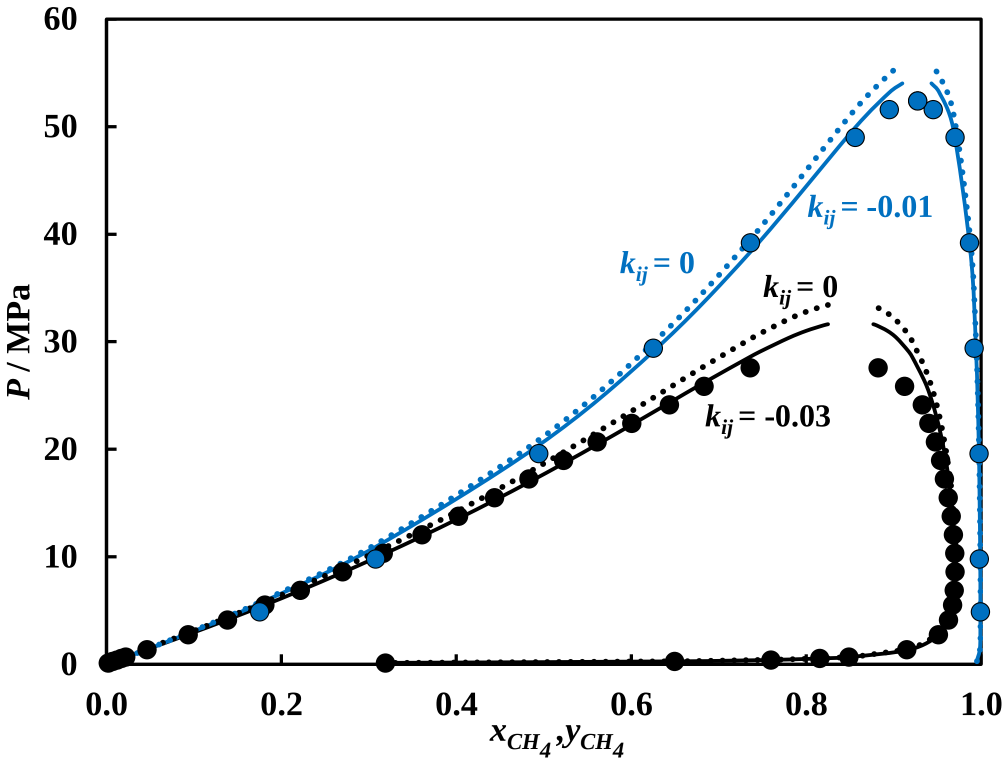

Figure F.3. *Pressure−composition diagram of CH_4 + n-decane (black) and CH_4 + n-hexadecane (blue). Solid symbols represent experimental solubility data at T = 444 K from Reamer et al.* [50] *(black) and from Sultanov et al.* [345] *(blue). Lines represent CPA EoS predictions i.e. k_{ij} = 0 (dotted) and CPA EoS estimations i.e., $k_{ij} \neq 0$ (solid), for pertinent systems.*

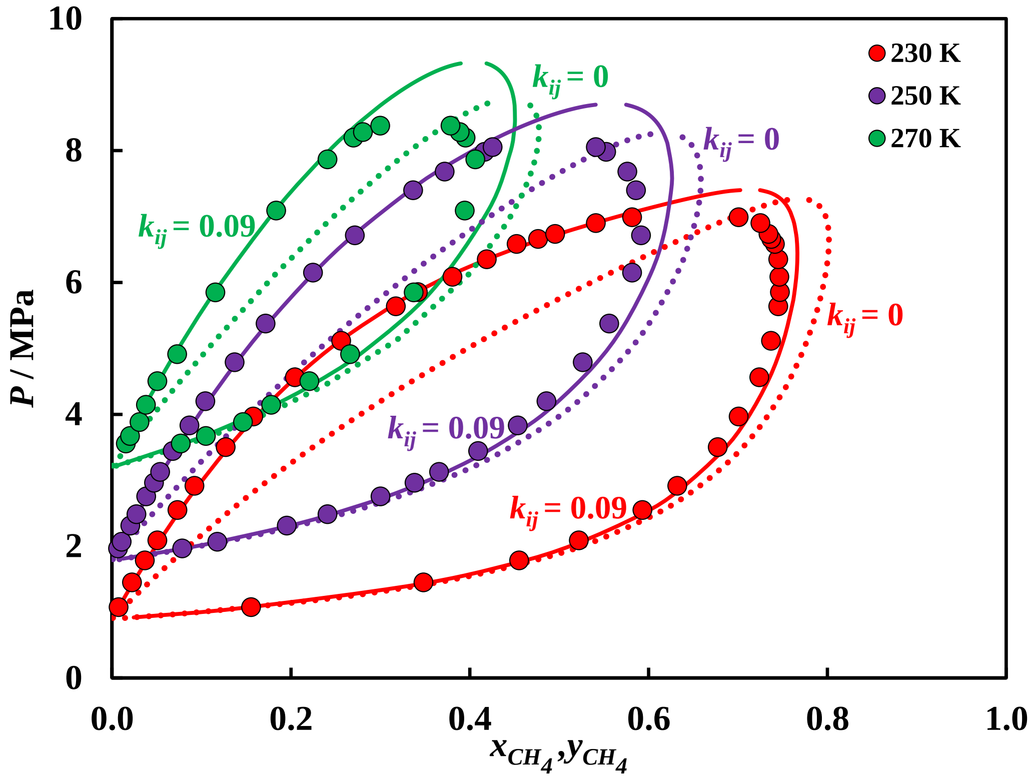

Figure F.4. *Pressure−composition diagram of CH_4 +CO_2. Solid symbols represent experimental solubility data from Wei et al.* [346]. *Lines represent CPA EoS predictions i.e. k_{ij} = 0 (dotted) and CPA EoS estimations i.e., $k_{ij} \neq 0$ (solid), at pertinent temperatures.*

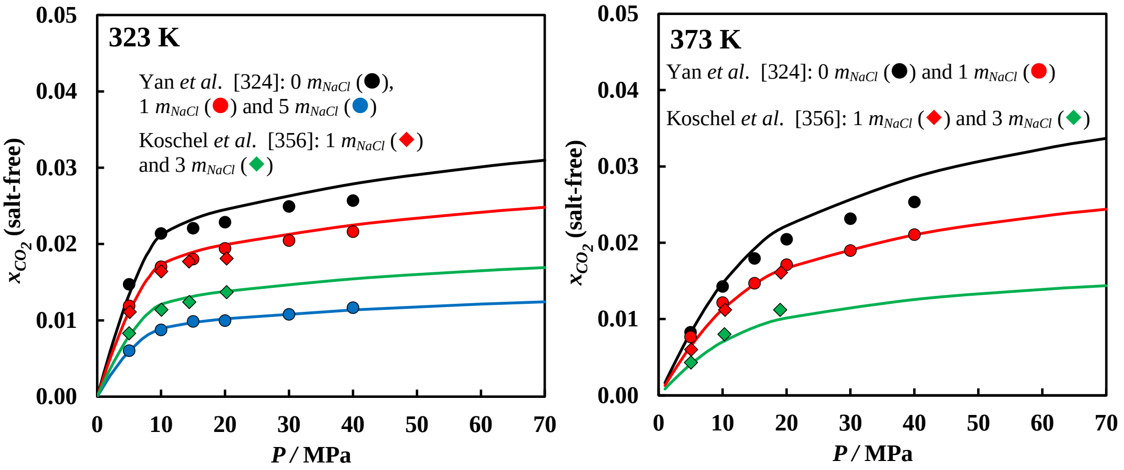

Figure F.5. *CO_2 solubility−composition diagrams of CO_2 + NaCl(aq) mixtures. Lines represent CPA EoS estimates at pertinent conditions.*

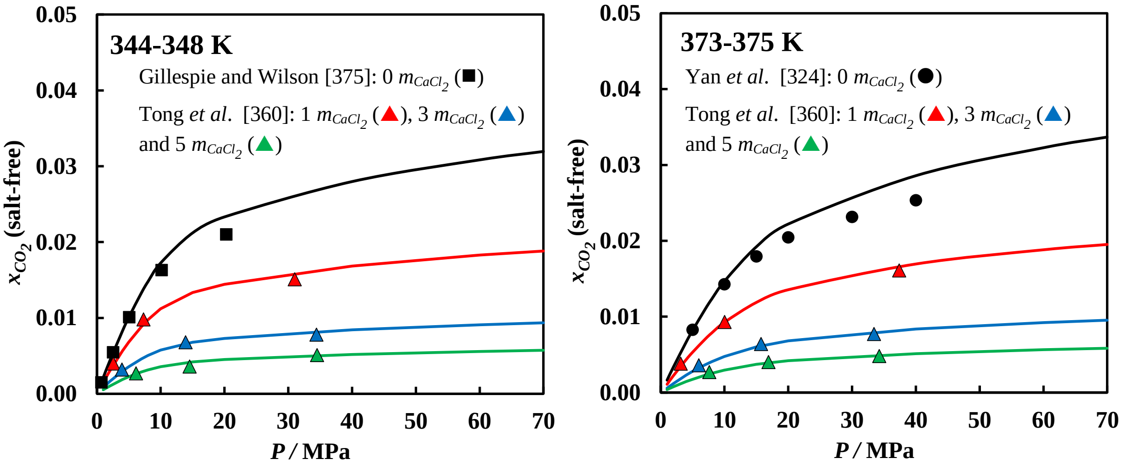

Figure F.6. *CO_2 solubility−composition diagrams of CO_2 + $CaCl_2$(aq) mixtures. Lines represent CPA EoS + Electrolyte model estimates at pertinent conditions.*

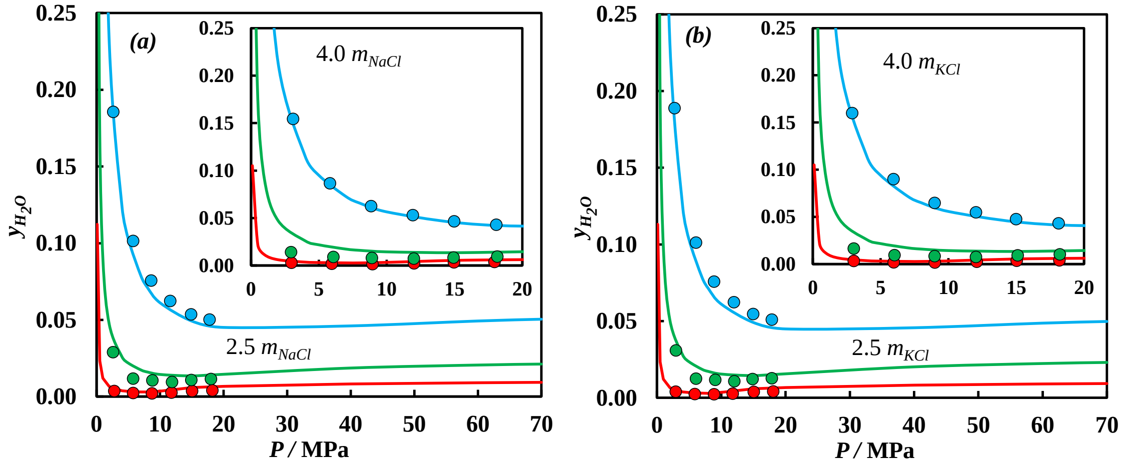

Figure F.7. *Water content−composition diagrams of **(a)** CO_2 + NaCl(aq) and **(b)** CO_2 + KCl(aq) mixtures. Symbols represent experimental data taken from Hou et al. [372]: T = 323 K (🔴), 373 K (🟢) and 423 K (🔵). Lines represent CPA EoS + Electrolyte model predictions at pertinent conditions.*

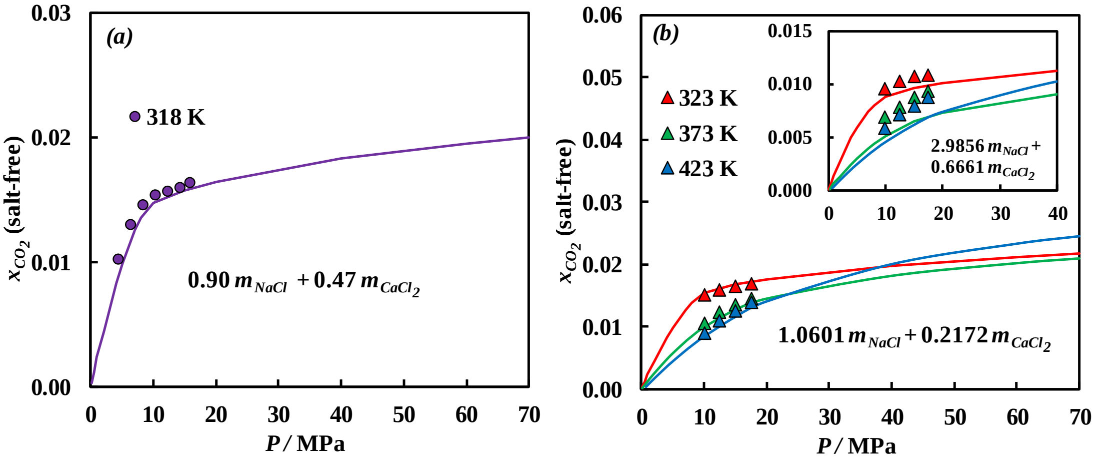

Figure F.8. *CO_2 solubility−composition diagrams of CO_2 + [NaCl + $CaCl_2$](aq) mixtures. Symbols represent experimental data taken from **(a)** Liu et al. [373] and **(b)** Zhao et al.[374]. Lines represent CPA EoS + Electrolyte model predictions at pertinent conditions.*

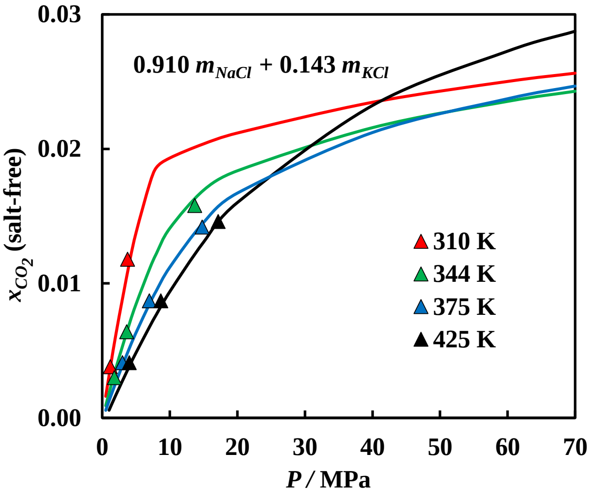

***Figure F.9**. CO_2 solubility−composition diagram of CO_2 + [NaCl + KCl](aq) mixtures. Symbols represent experimental data taken from Tong et al.* [360]. *Lines represent CPA EoS + Electrolyte model predictions at pertinent conditions.*

REFERENCES

[1] S. Pacala, R. Socolow, *Stabilization wedges: solving the climate problem for the next 50 years with current technologies.*, Science. **305**, 968–72 (2004).

[2] S.J. Altman, B. Aminzadeh, M.T. Balhoff, P.C. Bennett, S.L. Bryant, M.B. Cardenas, K. Chaudhary, R.T. Cygan, W. Deng, T. Dewers, D.A. DiCarlo, P. Eichhubl, M.A. Hesse, C. Huh, E.N. Matteo, Y. Mehmani, C.M. Tenney, H. Yoon, *Chemical and hydrodynamic mechanisms for long-term geological carbon storage*, J. Phys. Chem. C. **118**, 15103–15113 (2014).

[3] D.W. Green, G.P. Willhite, *Enhanced oil recovery*, SPE Textbook Series (1998).

[4] J.R. Christensen, E.H. Stenby, A. Skauge, *Review of WAG field experience*, SPE Reserv. Eval. Eng. **4**, 97–106 (2001).

[5] S.H. Talebian, R. Masoudi, I.M. Tan, P.L.J. Zitha, *Foam assisted CO_2-EOR: A review of concept, challenges, and future prospects*, J. Pet. Sci. Eng. **120**, 202–215 (2014).

[6] A.Y. Dandekar, *Petroleum reservoir rock and fluid properties*, CRC Press Taylor & Francis Group (2006).

[7] P. Chiquet, J.-L. Daridon, D. Broseta, S. Thibeau, *CO_2/water interfacial tensions under pressure and temperature conditions of CO_2 geological storage*, Energy Convers. Manag. **48**, 736–744 (2007).

[8] N.K. Adam, *The physics and chemistry of surfaces*, Third ed., Oxford University Press (1941).

[9] H.Y. Erbil, *Surface chemistry of solid and liquid interfaces*, Blackwell Publishing (2006).

[10] J. Pellicer, J.A. Manzanares, S. Mafé, *The physical description of elementary surface phenomena: Thermodynamics versus mechanics*, Am. J. Phys. **63**, 542 (1995).

[11] A.I. Rusanov, V.A. Prokhorov, *Interfacial tensiometry*, Elsevier (1996).

[12] A.W. Neumann, R. David, Y. Zuo, *Applied surface thermodynamics*, Second ed., CRC Press Taylor & Francis Group (2010).

[13] A.W. Adamson, *Physical chemistry of surfaces*, Fifth ed., John Wiley & Sons, Inc. (1990).

[14] K. Holmberg, D.O. Shah, M.J. Schwuger, eds., *Handbook of applied surface and colloid chemistry, Vol 1*, John Wiley & Sons, Ltd (2002).

[15] J. Straub, *The role of surface tension for two-phase heat and mass transfer in the absence of gravity*, Exp. Therm. Fluid Sci. **9**, 253–273 (1994).

[16] J.W. Rose, *Surface tension effects and enhancement of condensation heat transfer*, Chem. Eng. Res. Des. **82**, 419–429 (2004).

[17] A. Abubakar, Y. Al-Wahaibi, T. Al-Wahaibi, A. Al-Hashmi, A. Al-Ajmi, M. Eshrati, *Effect of low interfacial tension on flow patterns, pressure gradients and holdups of medium-viscosity oil/water flow in horizontal pipe*, Exp. Therm. Fluid Sci. **68**, 58–67 (2015).

[18] F.T. Hokmabadi, H. Bahmanyar, M. Amanabadi, J. Safdari, *Dispersed phase*

holdup and slip velocity of phases in a pulsed packed column in conditions with and without mass transfer, Can. J. Chem. Eng. **87**, 855–861 (2009).

[19] W.R. Foster, *A low-tension waterflooding process*, J. Pet. Technol. **25**, 205–210 (1973).

[20] E.J. Lefebvre du Prey, *Factors affecting liquid-liquid relative permeabilities of a consolidated porous medium*, Soc. Pet. Eng. J. **13**, 39–47 (1973).

[21] R. Ehrlich, H.H. Hasiba, P. Raimondi, *Alkaline waterflooding for wettability alteration-evaluating a potential field application*, J. Pet. Technol. **26**, 1335–1343 (1974).

[22] J.C. Melrose, *Role of capillary forces in detennining microscopic displacement efficiency for oil recovery by waterflooding*, J. Can. Pet. Technol. **13**, (1974).

[23] A. Abrams, *The influence of fluid viscosity, interfacial tension, and flow velocity on residual oil saturation left by waterflood*, Soc. Pet. Eng. J. **15**, 437–447 (1975).

[24] S.G. Oh, J.C. Slattery, *Interfacial tension required for significant displacement of residual oil*, Soc. Pet. Eng. J. **19**, 83–96 (1979).

[25] S. Zhang, G.-C. Jiang, L. Wang, H.-T. Guo, X. Tang, D.-G. Bai, *Foam flooding with ultra-low interfacial tension to enhance heavy oil recovery*, J. Dispers. Sci. Technol. **35**, 403–410 (2014).

[26] O.R. Wagner, R.O. Leach, *Effect of interfacial tension on displacement efficiency*, Soc. Pet. Eng. J. **6**, (1966).

[27] A. Firoozabadi, D.L. Katz, H. Soroosh, V.A. Sajjadian, *Surface tension of reservoir crude-oil/gas systems recognizing the asphalt in the heavy fraction*, SPE Reserv. Eng. **3**, 265–272 (1988).

[28] C. Bardon, D.G. Longeron, *Influence of very low interfacial tensions on relative permeability*, Soc. Pet. Eng. J. 391–401 (1980).

[29] M.S. Haniff, J.K. Ali, *Relative permeability and low tension fluid flow in gas condensate systems*, in: Proc. Eur. Pet. Conf., Society of Petroleum Engineers (1990).

[30] J.K. Ali, S. Butler, L. Allen, P. Wardle, *The influence of interfacial tension on liquid mobility in gas condensate systems*, in: Offshore Eur., Society of Petroleum Engineers (1993).

[31] A. Georgiadis, G. Maitland, J.P.M. Trusler, A. Bismarck, *Interfacial tension measurements of the (H_2O + n-Decane + CO_2) ternary system at elevated pressures and temperatures*, J. Chem. Eng. Data. **56**, 4900–4908 (2011).

[32] Z. Li, M. Dong, S. Li, S. Huang, *CO_2 sequestration in depleted oil and gas reservoirs—caprock characterization and storage capacity*, Energy Convers. Manag. **47**, 1372–1382 (2006).

[33] V. Shah, D. Broseta, G. Mouronval, F. Montel, *Water/acid gas interfacial tensions and their impact on acid gas geological storage*, Int. J. Greenh. Gas Control. **2**, 594–604 (2008).

[34] S. Iglauer, C.H. Pentland, A. Busch, *CO_2 wettability of seal and reservoir rocks and the implications for carbon geo-sequestration*, Water Resour. Res. **51**, 729–774 (2015).

[35] E.W. Hough, G.L. Stegemeier, *Correlation of surface and interfacial tension of light hydrocarbons in the critical region*, Soc. Pet. Eng. J. **1**, 259–263 (1961).

[36] S.J.O. Connor, *Hydrocarbon-water interfacial tension values at reservoir conditions: Inconsistencies in the technical literature and the impact on maximum oil and gas column height calculations*, Am. Assoc. Pet. Geol. Bull. **84**, 1537–1541 (2000).

[37] S. Krevor, M.J. Blunt, S.M. Benson, C.H. Pentland, C. Reynolds, A. Al-Menhali, B. Niu, *Capillary trapping for geologic carbon dioxide storage – From pore scale physics to field scale implications*, Int. J. Greenh. Gas Control. **40**, 221–237 (2015).

[38] S. Bachu, D. Bonijoly, J. Bradshaw, R. Burruss, S. Holloway, N.P. Christensen, O.M. Mathiassen, *CO_2 storage capacity estimation: Methodology and gaps*, Int. J. Greenh. Gas Control. **1**, 430–443 (2007).

[39] S. Bachu, *Sequestration of CO_2 in geological media: criteria and approach for site selection in response to climate change*, Energy Convers. Manag. **41**, 953–970 (2000).

[40] D.A. Voormeij, G.J. Simandl, *Geological, ocean, and mineral CO_2 sequestration options: A technical review*, Geosci. Canada. **31**, (2004).

[41] C.F. Weinaug, D.L. Katz, *Surface tensions of methane-propane mixtures*, Ind. Eng. Chem. **35**, 239–246 (1943).

[42] D. Macleod, *On a relation between surface tension and density*, Trans. Faraday Soc. **2**, 2–5 (1923).

[43] S. Sugden, *VI.—The variation of surface tension with temperature and some related functions*, J. Chem. Soc. Trans. 32–41 (1924).

[44] H. Nourozieh, M. Kariznovi, J. Abedi, *Measurements and predictions of density and carbon dioxide solubility in binary mixtures of ethanol and n-decane*, J. Chem. Thermodyn. **58**, 377–384 (2013).

[45] H.H. Reamer, B.H. Sage, *Phase equilibria in hydrocarbon systems. Volumetric and phase behavior of the n-Decane-CO_2 system.*, J. Chem. Eng. Data. **8**, 508–513 (1963).

[46] N. Nagarajan, R.L. Robinson, *Equilibrium phase compositions, phase densities, and interfacial tensions for carbon dioxide + hydrocarbon systems. 2. Carbon dioxide + n-decane*, J. Chem. Eng. Data. **31**, 168–171 (1986).

[47] R.D. Shaver, R.L. Robinson, K.A.M. Gasem, *An automated apparatus for equilibrium phase compositions, densities, and interfacial tensions: data for carbon dioxide + decane*, Fluid Phase Equilib. **179**, 43–66 (2001).

[48] A. Mejía, M. Cartes, H. Segura, E.A. Müller, *Use of equations of state and coarse grained simulations to complement experiments: describing the interfacial properties of carbon dioxide + decane and carbon dioxide + eicosane mixtures*, J. Chem. Eng. Data. **59**, 2928–2941 (2014).

[49] B.H. Sage, H.M. Lavender, W.N. Lacey, *Phase equilibria in hydrocarbon systems methane–decane system*, Ind. Eng. Chem. **32**, 743–747 (1940).

[50] H.H. Reamer, R.H. Olds, B.H. Sage, W.N. Lacey, *Phase equilibria in hydrocarbon systems: methane-decane system*, Ind. Eng. Chem. **34**, 1526–1531 (1942).

[51] R. Amin, T.N. Smith, *Interfacial tension and spreading coefficient under reservoir conditions*, Fluid Phase Equilib. **142**, 231–241 (1998).

[52] T. Jianhua, J. Satherley, D.J. Schiffrin, *Density and interfacial tension of nitrogen-*

hydrocarbon systems at elevated pressures, Chin.J.Chem.Eng. **1**, 223–231 (1993).

[53] A. Georgiadis, F. Llovell, A. Bismarck, F.J. Blas, A. Galindo, G.C. Maitland, J.P.M. Trusler, G. Jackson, *Interfacial tension measurements and modelling of (carbon dioxide+n-alkane) and (carbon dioxide+water) binary mixtures at elevated pressures and temperatures*, J. Supercrit. Fluids. **55**, 743–754 (2010).

[54] C. Cumicheo, M. Cartes, H. Segura, E.A. Müller, A. Mejía, *High-pressure densities and interfacial tensions of binary systems containing carbon dioxide+n-alkanes: (n-Dodecane, n-tridecane, n-tetradecane)*, Fluid Phase Equilib. **380**, 82–92 (2014).

[55] A.S. Danesh, A.Y. Dandekar, A.C. Todd, R. Sarkar, *A modified scaling law and parachor method approach for improved prediction of interfacial tension of gas-condensate systems*, in: SPE Annu. Tech. Conf. Exhib., Society of Petroleum Engineers (1991).

[56] K. Gasem, B. Kenneth, R. Shaver, R. Robert L., *Experimental phase densities and interfacial tensions for a CO_2/synthetic-oil and a CO_2/reservoir-oil system*, SPE Reserv. Eng. **8**, (1993).

[57] R.J.M. Huygens, H. Ronde, J. Hagoort, *Interfacial tension of nitrogen/volatile oil systems*, SPE J. **1**, 125–132 (1996).

[58] V.G. Baidakov, A.M. Kaverin, M.N. Khotienkova, *Surface tension of ethane–methane solutions: 1. Experiment and thermodynamic analysis of the results*, Fluid Phase Equilib. **356**, 90–95 (2013).

[59] B.F. Pennington, E.W. Hough, *Interfacial tension of the methane-normale butane*, Prod. Mon. **July**, 4 (1965).

[60] R. Massoudi, A.D. King, *Effect of pressure on the surface tension of n-hexane. Adsorption of low molecular weight gases on n-hexane at 25 °C.*, J. Phys. Chem. **79**, 1676–1679 (1975).

[61] O.G. Niño-Amezquita, S. Enders, P.T. Jaeger, R. Eggers, *Measurement and prediction of interfacial tension of binary mixtures*, Ind. Eng. Chem. Res. **49**, 592–601 (2010).

[62] H.G. Warren, E.W. Hough, *Interfacial tension of the methane-normal heptane system*, Soc. Pet. Eng. J. **10**, 327–327 (1970).

[63] P.T. Jaeger, M.B. Alotaibi, H.A. Nasr-El-Din, *Influence of compressed carbon dioxide on the capillarity of the gas−crude oil−reservoir water system*, J. Chem. Eng. Data. **55**, 5246–5251 (2010).

[64] P.T. Jaeger, R. Eggers, *Interfacial properties at elevated pressures in reservoir systems containing compressed or supercritical carbon dioxide*, J. Supercrit. Fluids. **66**, 80–85 (2012).

[65] B. Peng, C. Sun, B. Liu, Q. Zhang, J. Chen, W. Li, G. Chen, *Interfacial tension between methane and octane at elevated pressure at five temperatures from (274.2 to 282.2) K*, J. Chem. Eng. Data. **56**, 4623–4626 (2011).

[66] J.R. Deam, R.N. Maddox, *Interfacial tension in hydrocarbon systems*, J. Chem. Eng. Data. **15**, 216–222 (1970).

[67] G. Stegemeier, B. Pennington, E.B. Brauer, E.W. Hough, *Interfacial tension of the methane-normal decane system*, Soc. Pet. Eng. J. **2**, 257–260 (1962).

[68] J.J.C. Hsu, N. Nagarajan, R.L. Robinson, *Equilibrium phase compositions, phase*

densities, and interfacial tensions for carbon dioxide + hydrocarbon systems. 1. Carbon dioxide + n-butane, J. Chem. Eng. Data. **30**, 485–491 (1985).

[69] O.G. Niño Amézquita, S. Enders, P.T. Jaeger, R. Eggers, *Interfacial properties of mixtures containing supercritical gases*, J. Supercrit. Fluids. **55**, 724–734 (2010).

[70] A. Zolghadr, M. Escrochi, S. Ayatollahi, *Temperature and composition effect on CO_2 miscibility by interfacial tension measurement*, J. Chem. Eng. Data. **58**, 1168–1175 (2013).

[71] K.A.M. Gasem, K.B. Dickson, P.B. Dulcamara, N. Nagarajan, R.L. Robinson, *Equilibrium phase compositions, phase densities, and interfacial-tensions for CO_2 + hydrocarbon systems .5. CO_2 + n- tetradecane*, J. Chem. Eng. Data. **34**, 191–195 (1989).

[72] V.G. Baidakov, A.M. Kaverin, M.N. Khotienkova, V.N. Andbaeva, *Surface tension of an ethane–nitrogen solution. 1: Experiment and thermodynamic analysis of the results*, Fluid Phase Equilib. **328**, 13–20 (2012).

[73] G.J. Reno, D.L. Katz, *Surface tension of n-heptane and n-butane containing dissolved nitrogen*, Ind. Eng. Chem. **35**, 1091–1093 (1943).

[74] J.M. Garrido, L. Cifuentes, M. Cartes, H. Segura, A. Mejía, *High-pressure interfacial tensions for nitrogen + ethanol, or hexane or 2-methoxy-2-methylbutane. A comparison between experimental tensiometry and Monte Carlo simulations*, J. Supercrit. Fluids. (2014).

[75] A. Zolghadr, M. Riazi, M. Escrochi, S. Ayatollahi, *Investigating the effects of temperature, pressure, and paraffin groups on the N_2 miscibility in hydrocarbon liquids using the interfacial tension measurement method*, Ind. Eng. Chem. Res. **52**, 9851–9857 (2013).

[76] E.W. Hough, G.J. Heuer, J.W. Walker, *An improved pendant drop, interfacial tension apparatus and data for carbon dioxide and water*, Pet. Trans. AIME. **216**, 469–472 (1959).

[77] R. Massoudi, A.D. King, *Effect of pressure on the surface tension of water. Adsorption of low molecular weight gases on water at 25 °C*, J. Phys. Chem. **78**, 2262–2266 (1974).

[78] C. Jho, D. Nealon, S. Shogbola, A.D. King Jr., *Effect of pressure on the surface tension of water: Adsorption of hydrocarbon gases and carbon dioxide on water at temperatures between 0 and 50°C*, J. Colloid Interface Sci. **65**, 141–154 (1978).

[79] B.-S. Chun, G.T. Wilkinson, *Interfacial tension in high-pressure carbon dioxide mixtures*, Ind. Eng. Chem. Res. **34**, 4371–4377 (1995).

[80] A. Wesch, N. Dahmen, K. Ebert, J. Schön, *Grenzflächenspannungen, Tropfengrößen und Kontaktwinkel im Zweiphasensystem H_2O/CO_2 bei Temperaturen von 298 bis 333 K und Drücken bis 30 MPa*, Chemie Ing. Tech. **69**, 942–946 (1997).

[81] S.R.P. da Rocha, K.L. Harrison, K.P. Johnston, *Effect of surfactants on the interfacial tension and emulsion formation between water and carbon dioxide*, Langmuir. **15**, 419–428 (1999).

[82] A. Hebach, A. Oberhof, N. Dahmen, A. Kögel, H. Ederer, E. Dinjus, *Interfacial tension at elevated pressures - Measurements and correlations in the water + carbon dioxide system*, J. Chem. Eng. Data. **47**, 1540–1546 (2002).

[83] F. Tewes, F. Boury, *Thermodynamic and dynamic interfacial properties of binary*

carbon dioxide−water systems, J. Phys. Chem. B. **108**, 2405–2412 (2004).

[84] J.-Y. Park, J.S. Lim, C.H. Yoon, C.H. Lee, K.P. Park, *Effect of a fluorinated sodium bis(2-ethylhexyl) sulfosuccinate (aerosol-OT, AOT) analogue surfactant on the interfacial tension of* CO_2 *+ water and* CO_2 *+ Ni-plating solution in near- and supercritical* CO_2, J. Chem. Eng. Data. **50**, 299–308 (2005).

[85] D. Yang, P. Tontiwachwuthikul, Y. Gu, *Interfacial interactions between reservoir brine and* CO_2 *at high pressures and elevated temperatures*, Energy & Fuels. **19**, 216–223 (2005).

[86] T. Akutsu, Y. Yamaji, H. Yamaguchi, M. Watanabe, R.L. Smith, H. Inomata, *Interfacial tension between water and high pressure* CO_2 *in the presence of hydrocarbon surfactants*, Fluid Phase Equilib. **257**, 163–168 (2007).

[87] B. Kvamme, T. Kuznetsova, A. Hebach, A. Oberhof, E. Lunde, *Measurements and modelling of interfacial tension for water+carbon dioxide systems at elevated pressures*, Comput. Mater. Sci. **38**, 506–513 (2007).

[88] Y. Sutjiadi-Sia, P. Jaeger, R. Eggers, *Interfacial phenomena of aqueous systems in dense carbon dioxide*, J. Supercrit. Fluids. **46**, 272–279 (2008).

[89] S. Bachu, D.B. Bennion, *Interfacial tension between* CO_2 *, freshwater, and brine in the range of pressure from (2 to 27) MPa, temperature from (20 to 125) °C, and water salinity from (0 to 334 000)* $mg{\cdot}L^{-1}$, J. Chem. Eng. Data. **54**, 765–775 (2009).

[90] C. Chalbaud, M. Robin, J.-M. Lombard, F. Martin, P. Egermann, H. Bertin, *Interfacial tension measurements and wettability evaluation for geological* CO_2 *storage*, Adv. Water Resour. **32**, 98–109 (2009).

[91] A. Georgiadis, G. Maitland, J.P.M. Trusler, A. Bismarck, *Interfacial tension measurements of the* (H_2O + CO_2) *system at elevated pressures and temperatures*, J. Chem. Eng. Data. **55**, 4168–4175 (2010).

[92] P.K. Bikkina, O. Shoham, R. Uppaluri, *Equilibrated interfacial tension data of the* CO_2*-water system at high pressures and moderate temperatures*, J. Chem. Eng. Data. **56**, 3725–3733 (2011).

[93] A. Shariat, R.G. Moore, S.A. Mehta, K.C. Van Fraassen, K.E. Newsham, J.A. Rushing, *Laboratory measurements of* CO_2*-*H_2O *interfacial tension at HP/HT conditions: Implications for* CO_2 *sequestration in deep aquifers*, in: Carbon Manag. Technol. Conf., Carbon Management Technology Conference (2012).

[94] M. Sarmadivaleh, A.Z. Al-Yaseri, S. Iglauer, *Influence of temperature and pressure on quartz–water–*CO_2 *contact angle and* CO_2*–water interfacial tension*, J. Colloid Interface Sci. **441**, 59–64 (2015).

[95] R. Yaginuma, Y. Sato, D. Kodama, *Saturated densities of carbon dioxide+ water mixture at 304.1 K and pressures to 10 MPa*, Nthon Enerugi Galhzislti. **79**, 144–146 (2000).

[96] A. Hebach, A. Oberhof, N. Dahmen, *Density of water + carbon dioxide at elevated pressures: Measurements and correlation*, J. Chem. Eng. Data. **49**, 950–953 (2004).

[97] F. Tabasinejad, Y. Barzin, R.G. Moore, S.A. Mehta, K.C. Van Fraassen, J. Rushing, K.E. Newsham, *Water/*CO_2 *system at high pressure and temperature conditions: Measurement and modeling of density in equilibrium liquid and vapor phases*, in: SPE Eur. Annu. Conf. Exhib., Society of Petroleum Engineers (2010).

[98] E.C. Efika, R. Hoballah, X. Li, E.F. May, M. Nania, Y. Sanchez-Vicente, J.P. Martin Trusler, *Saturated phase densities of (CO_2+H_2O) at temperatures from (293 to 450) K and pressures up to 64 MPa*, J. Chem. Thermodyn. **93**, 347–359 (2016).

[99] E.W. Lemmon, M.O. McLinden, M.L. Huber, *NIST Reference Fluid Thermodynamic and Transport Properties — REFPROP, Version 8.0, NIST, Gaithersburg, MD*, (2007).

[100] G. Wiegand, E.U. Franck, *Interfacial tension between water and non-polar fluids up to 473 K and 2800 bar.*, Berichte der Bunsengesellschaft für Phys. Chemie. **98**, 809–817 (1994).

[101] B.-Y. Cai, J.-T. Yang, T.-M. Guo, *Interfacial tension of hydrocarbon + water/brine systems under high pressure*, J. Chem. Eng. Data. **41**, 493–496 (1996).

[102] G.Y. Zhao, W. Yan, G.J. Chen, X.Q. Guo, *Measurement and calculation of high-pressure interfacial tension of methane+ nitrogen/water system*, Shiyou Daxue Xuebao/Journal Univ. Pet. China. **26**, 75–78+82 (2002).

[103] K. Kashefi, L.M.C. Pereira, A. Chapoy, R. Burgass, B. Tohidi, *Measurement and modelling of interfacial tension in methane/water and methane/brine systems at reservoir conditions*, Fluid Phase Equilib. **409**, 301–311 (2016).

[104] Y. Tian, Y. Xiao, H. Zhu, X. Dong, *Interfacial tensions between water and non-polar fluids at high pressures and high temperatures*, Acta Physico-Chimica Sin. **13**, 89–95 (1997).

[105] Q.Y. Ren, G.J. Chen, W. Yan, T.M. Guo, *Interfacial tension of (CO_2+CH_4) plus water from 298 K to 373 K and pressures up to 30 MPa*, J. Chem. Eng. Data. **45**, 610–612 (2000).

[106] W. Yan, G.-Y. Zhao, G.-J. Chen, T.-M. Guo, *Interfacial tension of (methane + nitrogen) + water and (carbon dioxide + nitrogen) + water systems*, J. Chem. Eng. Data. **46**, 1544–1548 (2001).

[107] J. Ralston, T.W. Healy, *Specific cation effects on water structure at the air-water and air-octadecanol monolayer-water interfaces*, J. Colloid Interface Sci. **42**, 629–644 (1973).

[108] K. Johansson, J.C. Eriksson, *Γ and dγ/dT measurements on aqueous solutions of 1,1-electrolytes*, J. Colloid Interface Sci. **49**, 469–480 (1974).

[109] P.K. Weissenborn, R.J. Pugh, *Surface tension of aqueous solutions of electrolytes: relationship with ion hydration, oxygen solubility, and bubble coalescence*, J. Colloid Interface Sci. **184**, 550–563 (1996).

[110] L.M. Pegram, M.T. Record, *Hofmeister salt effects on surface tension arise from partitioning of anions and cations between bulk water and the air−water interface*, J. Phys. Chem. B. **111**, 5411–5417 (2007).

[111] Y. Levin, A.P. dos Santos, A. Diehl, *Ions at the air-water interface: An end to a hundred-year-old mystery?*, Phys. Rev. Lett. **103**, 257802 (2009).

[112] Y. Marcus, *Effect of ions on the structure of water: structure making and breaking.*, Chem. Rev. **109**, 1346–70 (2009).

[113] C. Duchateau, D. Broseta, *A simple method for determining brine–gas interfacial tensions*, Adv. Water Resour. **42**, 30–36 (2012).

[114] M.J. Hey, D.W. Shield, J.M. Speight, M.C. Will, *Surface tensions of aqueous*

solutions of some 1:1 electrolytes, J. Chem. Soc. Faraday Trans. 1 Phys. Chem. Condens. Phases. **77**, 123 (1981).

[115] X. Li, E. Boek, G.C. Maitland, J.P.M. Trusler, *Interfacial tension of (brines + CO_2): (0.864 NaCl + 0.136 KCl) at yemperatures between (298 and 448) K, pressures between (2 and 50) MPa, and total molalities of (1 to 5) mol·kg* $^{-1}$, J. Chem. Eng. Data. **57**, 1078–1088 (2012).

[116] M.J. Argaud, *Predicting the interfacial tension of brine/gas (or condensates) systems,* in: 3rd Eur. Core Anal. Symp., Society of Core Analysts (1992).

[117] X. Li, D.A. Ross, J.P.M. Trusler, G.C. Maitland, E.S. Boek, *Molecular dynamics simulations of CO_2 and brine interfacial tension at high temperatures and pressures.*, J. Phys. Chem. B. **117**, 5647–52 (2013).

[118] L.M.C. Pereira, A. Chapoy, R. Burgass, M.B. Oliveira, J.A.P. Coutinho, B. Tohidi, *Study of the impact of high temperatures and pressures on the equilibrium densities and interfacial tension of the carbon dioxide/water system*, J. Chem. Thermodyn. **93**, 404–415 (2016).

[119] X. Li, E.S. Boek, G.C. Maitland, J.P.M. Trusler, *Interfacial tension of (brines + CO_2): $CaCl_2$ (aq), $MgCl_2$ (aq), and $NaCl_2SO_4$ (aq) at temperatures between (343 and 423) K, pressures between (2 and 50) MPa, and molalities of (0.5 to 5) mol/kg*, J. Chem. Eng. Data. **57**, 1369–1375 (2012).

[120] A. Badakhshan, P. Bakes, *The influence of temperature and surfactant concentration on interfacial tension of saline water and hydrocarbon systems in relation to enhanced oil recovery by chemical flooding*, Soc. Pet. Eng. (1990).

[121] N. Ikeda, M. Aratono, K. Motomura, *Thermodynamic study on the adsorption of sodium chloride at the water/hexane interface*, J. Colloid Interface Sci. **149**, 208–215 (1992).

[122] J.A. Rushing, K.E. Newsham, K.C. Van Fraassen, S.A. Mehta, G.R. Moore, *Laboratory measurements of gas-water interfacial tension at HP/HT reservoir conditions*, in: CIPC/SPE Gas Technol. Symp. 2008 Jt. Conf., Society of Petroleum Engineers (2008).

[123] H.Y. Jennings, G.H. Newman, *The effect of temperature and pressure on the interfacial tension of water against methane-normal decane mixtures*, Soc. Pet. Eng. J. **11**, 171–175 (1971).

[124] *Reservoir Fluid Studies: 2002-2005 Programme*, Final Report, Heriot-Watt University .

[125] A. Bahramian, A. Danesh, F. Gozalpour, B. Tohidi, A.C. Todd, *Vapour–liquid interfacial tension of water and hydrocarbon mixture at high pressure and high temperature conditions*, Fluid Phase Equilib. **252**, 66–73 (2007).

[126] L.M.C. Pereira, A. Chapoy, B. Tohidi, *Vapor-liquid and liquid-liquid interfacial tension of water and hydrocarbon systems at representative reservoir conditions: Experimental and modelling results,* in: SPE Annu. Tech. Conf. Exhib., Society of Petroleum Engineers (2014).

[127] R. Massoudi, A.D. King, *Effect of pressure on the surface tension of aqueous solutions. Adsorption of hydrocarbon gases, carbon dioxide, and nitrous oxide on aqueous solutions of sodium chloride and tetrabutylammonium bromide at 25 °C.*, J. Phys. Chem. **79**, 1670–1675 (1975).

[128] Y. Liu, M. Mutailipu, L. Jiang, J. Zhao, Y. Song, L. Chen, *Interfacial tension and*

contact angle measurements for the evaluation of CO_2-brine two-phase flow characteristics in porous media, Environ. Prog. Sustain. Energy. **34**, 1756–1762 (2015).

[129] C.A. Aggelopoulos, M. Robin, E. Perfetti, O. Vizika, *CO_2/$CaCl_2$ solution interfacial tensions under CO_2 geological storage conditions: Influence of cation valence on interfacial tension*, Adv. Water Resour. **33**, 691–697 (2010).

[130] C.A. Aggelopoulos, M. Robin, O. Vizika, *Interfacial tension between CO_2 and brine (NaCl+$CaCl_2$) at elevated pressures and temperatures: The additive effect of different salts*, Adv. Water Resour. **34**, 505–511 (2011).

[131] N.E. Dorsey, *Measurement of surface tension*, Sci. Pap. Bur. Stand. **21**, 524–546 (1926).

[132] J. Drelich, C. Fang, C.L. White, *Measurement of interfacial tension in fluid-fluid systems*, Encycl. Surf. Colloid Sci. 3152–3166 (2002).

[133] J.D. Berry, M.J. Neeson, R.R. Dagastine, D.Y.C. Chan, R.F. Tabor, *Measurement of surface and interfacial tension using pendant drop tensiometry*, J. Colloid Interface Sci. **454**, 226–237 (2015).

[134] J.F. Padday, *Surface tension. Part I. The theory of surface tension*, in: E. Matijević (Ed.), Surf. Colloid Surface, Vol . 1, Wiley-Interscience (1969).

[135] U. Henriksson, J.C. Eriksson, *Thermodynamics of capillary rise: Why is the meniscus curved?*, J. Chem. Educ. **81**, 150 (2004).

[136] M.Á. Rodríguez-Valverde, M. Tirado Miranda, *Derivation of Jurin's law revisited*, Eur. J. Phys. **32**, 49–54 (2011).

[137] J.B.T. McCaughan, *Capillarity-a lesson in the epistemology of physics*, Phys. Educ. **22**, 100–106 (1987).

[138] P.C. Hiemenz, R. Rajagopalan, *Principles of colloid and surface chemistry*, Third ed., Marcel Dekker, Inc. (1997).

[139] G.C. Vorlicek, J.W. Warren, G.E. Kilby, *Capillarity revisited - yet again*, Phys. Educ. **23**, 7–8 (1988).

[140] J.B.T. McCaughan, *Capillarity reply*, Phys. Educ. **23**, 205–206 (1988).

[141] E.K. Chapin, *Two contrasting theories of capillary action*, Am. J. Phys. **27**, 617 (1959).

[142] C.W. Extrand, S.I. Moon, *Which controls wetting? Contact line versus interfacial area: Simple experiments on capillary rise*, Langmuir. **28**, 15629–15633 (2012).

[143] L. Rayleigh, *On the theory of the capillary tube*, Proc. R. Soc. A Math. Phys. Eng. Sci. **92**, 184–195 (1916).

[144] G.S. Barozzi, D. Angeli, *A note on capillary rise in tubes*, Energy Procedia. **45**, 548–557 (2014).

[145] S. Sugden, *XCVII.—The determination of surface tension from the maximum pressure in bubbles*, J. Chem. Soc., Trans. **121**, 858–866 (1922).

[146] J. Lane, *Correction terms for calculating surface tension from capillary rise*, J. Colloid Interface Sci. **42**, 145–149 (1973).

[147] S. Ramakrishnan, S. Hartland, *The determination of interfacial tension by differential capillary rise*, J. Chem. Sci. **90**, 215–224 (1981).

[148] H.L. Gielen, O.B. Verbeke, J. Thoen, *The critical behavior of the Sugden*

parameter and the surface tension of simple fluids, J. Chem. Phys. **81**, 6154 (1984).

[149] V.A.M. Soares, B. de J.V.S. Almeida, I.A. McLure, R.A. Higgins, *Surface tension of pure and mixed simple substances at low temperatures*, Fluid Phase Equilib. **32**, 9–16 (1986).

[150] V.A.M. Soares, I.A. McLure, B.S. Almeida, R.A. Higgins, J.C.G. Calado, *Cell for orthobaric surface tension measurements at low temperatures*, Cryogenics (Guildf). **27**, 263–265 (1987).

[151] K.C. Nadler, J.A. Zollweg, W.B. Streett, I.A. McLure, *Surface tension of argon + krypton from 120 to 200 K*, J. Colloid Interface Sci. **122**, 530–536 (1988).

[152] S.B.R. Karri, V.K. Mathur, *Measurement of interfacial tension of immiscible liquids of equal density*, AIChE J. **34**, 155–157 (1988).

[153] B.A. Grigoryev, B. V. Nemzer, D.S. Kurumov, J. V. Sengers, *Surface tension of normal pentane, hexane, heptane, and octane*, Int. J. Thermophys. **13**, 453–464 (1992).

[154] V.G. Baidakov, A.M. Kaverin, M.N. Khotienkova, *Surface tension of ethane–methane solutions: 1. Experiment and thermodynamic analysis of the results*, Fluid Phase Equilib. **356**, 90–95 (2013).

[155] A.M. Worthington, *On pendent drops*, Proc. R. Soc. London. **32**, 362–377 (1881).

[156] F. Bashforth, J.C. Adams, *An attempt to test the theories of capillary action: By comparing the theoretical and measured forms of drops of fluid*, Cambridge University Press (1883).

[157] J.M. Andreas, E.A. Hauser, W.B. Tucker, *Boundary tension by pendant drops*, J. Phys. Chem. **42**, 1001–1019 (1937).

[158] S. Fordham, *On the calculation of surface tension from measurements of pendant drops*, Proc. R. Soc. London. **194**, 1–16 (1948).

[159] D.O. Niederhauser, F.E. Bartell, *A corrected table for the calculation of boundary tensions by the pendant drop method*, API Research Project 27 .

[160] Y. Rotenberg, L. Boruvka, A.W. Neumann, *Determination of surface tension and contact angle from the shapes of axisymmetric fluid interfaces*, J. Colloid Interface Sci. **93**, 169–183 (1983).

[161] P. Cheng, D. Li, L. Boruvka, Y. Rotenberg, A.W. Neumann, *Automation of axisymmetric drop shape analysis for measurements of interfacial tensions and contact angles*, Colloids and Surfaces. **43**, 151–167 (1990).

[162] B. Song, J. Springer, *Determination of interfacial tension from the profile of a pendant drop using computer-aided image processing: 1. Theoretical*, J. Colloid Interface Sci. **184**, 64–76 (1996).

[163] B. Song, J. Springer, *Determination of interfacial tension from the profile of a pendant drop using computer-aided image processing: 2. Experimental*, J. Colloid Interface Sci. **184**, 77–91 (1996).

[164] M. Hoorfar, a W Neumann, *Recent progress in axisymmetric drop shape analysis (ADSA).*, Adv. Colloid Interface Sci. **121**, 25–49 (2006).

[165] J.K. Spelt, Y. Rotenberg, D.R. Absolom, A.W. Neumann, *Sessile-drop contact angle measurements using axisymmetric drop shape analysis*, Colloids and Surfaces. **24**, 127–137 (1987).

[166] O. Río, A. Neumann, *Axisymmetric drop shape analysis: Computational methods for the measurement of interfacial properties from the shape and dimensions of pendant and sessile drops.*, J. Colloid Interface Sci. **196**, 136–147 (1997).

[167] A. Kalantarian, R. David, A.W. Neumann, *Methodology for high accuracy contact angle measurement*, Langmuir. **25**, 14146–14154 (2009).

[168] Y.T.F. Chow, D.K. Eriksen, A. Galindo, A.J. Haslam, G. Jackson, G.C. Maitland, J.P.M. Trusler, *Interfacial tensions of systems comprising water, carbon dioxide and diluent gases at high pressures: Experimental measurements and modelling with SAFT-VR Mie and square-gradient theory*, Fluid Phase Equilib. **407**, 159–176 (2016).

[169] Y.T.F. Chow, G.C. Maitland, J.P.M. Trusler, *Interfacial tensions of the* $(CO_2+N_2+H_2O)$ *system at temperatures of (298 to 448) K and pressures up to 40 MPa*, J. Chem. Thermodyn. **93**, 392–403 (2016).

[170] S.S. Susnar, H.A. Hamza, A.W. Neumann, *Pressure dependence of interfacial tension of hydrocarbon—water systems using axisymmetric drop shape analysis*, Colloids Surfaces A Physicochem. Eng. Asp. **89**, 169–180 (1994).

[171] S.-T. Lee, M. Chien, *A new multicomponent surface tension correlation based on scaling theory*, in: SPE Enhanc. Oil Recover. Symp., Society of Petroleum Engineers (1984).

[172] E.A. Guggenheim, *The principle of corresponding states*, J. Chem. Phys. **13**, 253 (1945).

[173] Y.-X. Zuo, E.H. Stenby, *Corresponding-states and parachor models for the calculation of interfacial tensions*, Can. J. Chem. Eng. **75**, 1130–1137 (1997).

[174] A.J. Queimada, L.I. Rolo, A.I. Caço, I.M. Marrucho, E.H. Stenby, J.A.P. Coutinho, *Prediction of viscosities and surface tensions of fuels using a new corresponding states model*, Fuel. **85**, 874–877 (2006).

[175] L.A. Girifalco, R.J. Good, *A theory for the estimation of surface and interfacial energies. I. Derivation and application to interfacial tension*, J. Phys. Chem. **61**, 904–909 (1957).

[176] P.H. Winterfield, L.E. Scriven, H.T. Davis, *An approximate theory of interfacial tensions of multicomponent systems : Applications to binary liquid-vapour tensions*, AIChE J. **24**, 1010–1014 (1978).

[177] R.P. Sutton, *General engineering, Vol. 1*, in: J.R. Fanchi, L.W. Lake (Eds.), Pet. Eng. Handb., Society of Petroleum Engineers (2006): pp. 257–331.

[178] R.P. Sutton, *An improved model for water-hydrocarbon surface tension at reservoir conditions*, in: SPE Annu. Tech. Conf. Exhib., Society of Petroleum Engineers (2009).

[179] A. Danesh, *PVT and phase behaviour of petroleum reservoir fluids*, Elsevier Publishing (1998).

[180] A. Firoozabadi, H.J. Ramey, *Surface tension of water-hydrocarbon systems at reservoir conditions*, J. Can. Pet. Technol. **27**, (1988).

[181] S. Nordholm, M. Johnson, B. Freasier, *Generalized van der Waals theory. III. The prediction of hard sphere structure*, Aust. J. Chem. **33**, 2139 (1980).

[182] R. Evans, *The nature of the liquid-vapour interface and other topics in the statistical mechanics of non-uniform, classical fluids*, Adv. Phys. **28**, 143–200

(1979).

[183] B.S. Almeida, M.M. Telo da Gama, *Surface tension of simple mixtures: comparison between theory and experiment*, J. Phys. Chem. **93**, 4132–4138 (1989).

[184] V. Bongiorno, H.T. Davis, *Modified Van der Waals theory of fluid interfaces*, Phys. Rev. A. **12**, 2213–2224 (1975).

[185] Y.-X. Zuo, E.H. Stenby, *Calculation of surface tensions of polar mixtures with a simplified gradient theory model*, J. Chem. Eng. Japan. **29**, 159–165 (1996).

[186] Y.-X. Zuo, E.H. Stenby, *A linear gradient theory model for calculating interfacial tensions of mixtures*, J. Colloid Interface Sci. **182**, 126–132 (1996).

[187] J.W. Cahn, J.E. Hilliard, *Free energy of a nonuniform system. I. Interfacial free energy*, J. Chem. Phys. **28**, 258 (1958).

[188] J.S. Rowlinson, *Translation of J. D. van der Waals' The thermodynamik theory of capillarity under the hypothesis of a continuous variation of density*, J. Stat. Phys. **20**, 197–200 (1979).

[189] B.S. Carey, L.E. Scriven, H.T. Davis, *Semiempirical theory of surface tensions of pure normal alkanes and alcohols*, AIChE J. **24**, 1076–1080 (1978).

[190] Y.-X. Zuo, E.H. Stenby, *Calculation of interfacial tensions with gradient theory*, Fluid Phase Equilib. **132**, 139–158 (1997).

[191] C. Miqueu, B. Mendiboure, A. Graciaa, J. Lachaise, *Modelling of the surface tension of pure components with the gradient theory of fluid interfaces: a simple and accurate expression for the influence parameters*, Fluid Phase Equilib. **207**, 225–246 (2003).

[192] C. Miqueu, B. Mendiboure, C. Graciaa, J. Lachaise, *Modelling of the surface tension of binary and ternary mixtures with the gradient theory of fluid interfaces*, Fluid Phase Equilib. **218**, 189–203 (2004).

[193] A. Mejía, I. Polishuk, H. Segura, J. Wisniak, *Estimation of interfacial behavior using the global phase diagram approach I. Carbon dioxide–n-alkanes*, Thermochim. Acta. **411**, 171–176 (2004).

[194] C. Miqueu, B. Mendiboure, A. Graciaa, J. Lachaise, *Modeling of the surface tension of multicomponent mixtures with the gradient theory of fluid interfaces*, Ind. Eng. Chem. Res. **44**, 3321–3329 (2005).

[195] A.J. Queimada, C. Miqueu, I.M. Marrucho, G.M. Kontogeorgis, J.A.P. Coutinho, *Modeling vapor–liquid interfaces with the gradient theory in combination with the CPA equation of state*, Fluid Phase Equilib. **228-229**, 479–485 (2005).

[196] C. Miqueu, B. Mendiboure, A. Graciaa, J. Lachaise, *Petroleum mixtures: An efficient predictive method for surface tension estimations at reservoir conditions*, Fuel. **87**, 612–621 (2008).

[197] E.A. Müller, A. Mejía, *Interfacial properties of selected binary mixtures containing n-alkanes*, Fluid Phase Equilib. **282**, 68–81 (2009).

[198] O. Vilaseca, L.F. Vega, *Direct calculation of interfacial properties of fluids close to the critical region by a molecular-based equation of state*, Fluid Phase Equilib. **306**, 4–14 (2011).

[199] B. Breure, C.J. Peters, *Modeling of the surface tension of pure components and mixtures using the density gradient theory combined with a theoretically derived influence parameter correlation*, Fluid Phase Equilib. **334**, 189–196 (2012).

[200] E. Schäfer, G. Sadowski, S. Enders, *Interfacial tension of binary mixtures exhibiting azeotropic behavior: Measurement and modeling with PCP-SAFT combined with Density Gradient Theory*, Fluid Phase Equilib. **362**, 151–162 (2014).

[201] P.M.W. Cornelisse, M. Wijtkamp, C.J. Peters, J. de Swaan Arons, *Interfacial tensions of fluid mixtures with polar and associating components*, Fluid Phase Equilib. **150-151**, 633–640 (1998).

[202] H. Kahl, S. Enders, *Calculation of surface properties of pure fluids using density gradient theory and SAFT-EOS*, Fluid Phase Equilib. **172**, 27–42 (2000).

[203] D. Fu, *Investigation of surface tensions for pure associating fluids by perturbed-chain statistical associating fluid Theory combined with density-gradient theory*, Ind. Eng. Chem. Res. **46**, 7378–7383 (2007).

[204] M.B. Oliveira, I.M. Marrucho, J.A.P. Coutinho, A.J. Queimada, *Surface tension of chain molecules through a combination of the gradient theory with the CPA EoS*, Fluid Phase Equilib. **267**, 83–91 (2008).

[205] M.B. Oliveira, J.A.P. Coutinho, A.J. Queimada, *Surface tensions of esters from a combination of the gradient theory with the CPA EoS*, Fluid Phase Equilib. **303**, 56–61 (2011).

[206] S.V.D. Freitas, M.B. Oliveira, A.J. Queimada, M.J. Pratas, Á.S. Lima, J.A.P. Coutinho, *Measurement and prediction of biodiesel surface tensions*, Energy & Fuels. **25**, 4811–4817 (2011).

[207] S. Enders, K. Quitzsch, *Calculation of interfacial properties of demixed fluids using density gradient theory*, Langmuir. **14**, 4606–4614 (1998).

[208] C.I. Poser, I.C. Sanchez, *Surface tension theory of pure liquids and polymer melts*, J. Colloid Interface Sci. **69**, 539–548 (1979).

[209] G.T. Dee, B.B. Sauer, *The molecular weight and temperature dependence of polymer surface tension: Comparison of experiment with interface gradient theory*, J. Colloid Interface Sci. **152**, 85–103 (1992).

[210] B.B. Sauer, G.T. Dee, *Studies of polymer, copolymer, and associating liquids by melt surface tension methods and Cahn-Hilliard density-gradient theory*, J. Colloid Interface Sci. **162**, 25–35 (1994).

[211] S. Fisk, *Structure and free energy of the interface between fluid phases in equilibrium near the critical point*, J. Chem. Phys. **50**, 3219 (1969).

[212] A.J.M. Yang, P.D. Fleming III, J.H. Gibbs, *Molecular theory of surface tension*, J. Chem. Phys. **64**, 3732 (1976).

[213] M.K. Gupta, R.L. Robinson Jr., *Application of gradient theory of inhomogeneous fluid to prediction of low interfacial tensions in CO_2/hydrocarbon systems*, SPE Reserv. Eng. 528–530 (1987).

[214] M. Sahimi, B.N. Taylor, *Surface tension of binary liquid–vapor mixtures: A comparison of mean-field and scaling theories*, J. Chem. Phys. **95**, 6749 (1991).

[215] H. Nilssen, A. Fredheim, E. Solbraa, B. Kvamme, *Theoretical prediction of interfacial tensions for hydrocarbon mixtures with gradient theory in combination with Peng-Robinson equation of state*, in: Proc. Offshore Technol. Conf., Society of Petroleum Engineers (2010).

[216] X.-S. Li, J.-M. Liu, D. Fu, *Investigation of interfacial tensions for carbon dioxide*

aqueous solutions by perturbed-chain statistical associating fluid theory combined with density-gradient theory, Ind. Eng. Chem. Res. **47**, 8911–8917 (2008).

[217] T. Lafitte, B. Mendiboure, M.M. Piñeiro, D. Bessières, C. Miqueu, *Interfacial properties of water/CO_2: a comprehensive description through a Gradient Theory-SAFT-VR Mie approach.*, J. Phys. Chem. B. **114**, 11110–6 (2010).

[218] C. Miqueu, J.M. Míguez, M.M. Piñeiro, T. Lafitte, B. Mendiboure, *Simultaneous application of the gradient theory and Monte Carlo molecular simulation for the investigation of methane/water interfacial properties.*, J. Phys. Chem. B. **115**, 9618–25 (2011).

[219] G. Niño-Amézquita, D. van Putten, S. Enders, *Phase equilibrium and interfacial properties of water+CO_2 mixtures*, Fluid Phase Equilib. **332**, 40–47 (2012).

[220] S. Khosharay, M. Abolala, F. Varaminian, *Modeling the surface tension and surface properties of (CO_2 + H_2O) and (H_2S + H_2O) with gradient theory in combination with sPC–SAFT EOS and a new proposed influence parameter*, J. Mol. Liq. **198**, 292–298 (2014).

[221] S. Khosharay, F. Varaminian, *Experimental and modeling investigation on surface tension and surface properties of (CH4 + H2O), (C2H6 + H2O), (CO2 + H2O) and (C3H8 + H2O) from 284.15 K to 312.15 K and pressures up to 60 bar*, Int. J. Refrig. **47**, 26–35 (2014).

[222] O.G. Niño-Amézquita, S. Enders, *Phase equilibrium and interfacial properties of water+methane mixtures*, Fluid Phase Equilib. **407**, 143–151 (2016).

[223] J.M. Míguez, J.M. Garrido, F.J. Blas, H. Segura, A. Mejía, M.M. Piñeiro, *Comprehensive characterization of interfacial behavior for the mixture CO_2 + H_2O + CH_4 : Comparison between atomistic and coarse grained molecular simulation models and density gradient theory*, J. Phys. Chem. C. **118**, 24504–24519 (2014).

[224] L.C. Nielsen, I.C. Bourg, G. Sposito, *Predicting CO_2 –water interfacial tension under pressure and temperature conditions of geologic CO_2 storage*, Geochim. Cosmochim. Acta. **81**, 28–38 (2012).

[225] E.A. Müller, A. Mejía, *Resolving discrepancies in the measurements of the interfacial tension for the CO_2 + H_2 O mixture by computer simulation*, J. Phys. Chem. Lett. **5**, 1267–1271 (2014).

[226] S. Iglauer, M.S. Mathew, F. Bresme, *Molecular dynamics computations of brine-CO_2 interfacial tensions and brine-CO_2 -quartz contact angles and their effects on structural and residual trapping mechanisms in carbon geo-sequestration.*, J. Colloid Interface Sci. **386**, 405–14 (2012).

[227] J. Neyt, A. Wender, V. Lachet, P. Malfreyt, *Modeling the pressure dependence of acid gas + n -alkane interfacial tensions using atomistic monte carlo simulations.*, J. Phys. Chem. C. **116**, 10563–10572 (2012).

[228] O. Lobanova, A. Mejía, G. Jackson, E.A. Müller, *SAFT-γ force field for the simulation of molecular fluids 6: Binary and ternary mixtures comprising water, carbon dioxide, and n-alkanes*, J. Chem. Thermodyn. **93**, 320–336 (2016).

[229] B. Liu, J. Shi, M. Wang, J. Zhang, B. Sun, Y. Shen, X. Sun, *Reduction in interfacial tension of water–oil interface by supercritical CO_2 in enhanced oil recovery processes studied with molecular dynamics simulation*, J. Supercrit. Fluids. **111**, 171–178 (2016).

[230] F. Biscay, A. Ghoufi, V. Lachet, P. Malfreyt, *Monte Carlo calculation of the methane-water interfacial tension at high pressures*, J. Chem. Phys. **131**, 124707 (2009).

[231] R. Sakamaki, A.K. Sum, T. Narumi, R. Ohmura, K. Yasuoka, *Thermodynamic properties of methane/water interface predicted by molecular dynamics simulations.*, J. Chem. Phys. **134**, 144702 (2011).

[232] G. Javanbakht, M. Sedghi, W. Welch, L. Goual, *Molecular Dynamics Simulations of CO2/Water/Quartz Interfacial Properties: Impact of CO2 Dissolution in Water.*, Langmuir. **31**, 5812–9 (2015).

[233] Y. Liu, T. Lafitte, A.Z. Panagiotopoulos, P.G. Debenedetti, *Simulations of vapor-liquid phase equilibrium and interfacial tension in the CO_2-H_2O-NaCl system*, AIChE J. **59**, 3514–3522 (2013).

[234] G. Soave, *Equilibrium constants from a modified Redlich-Kwong equation of state*, Chem. Eng. Sci. **27**, 1197–1203 (1972).

[235] D.B. Robinson, D.-Y. Peng, *The characterization of the heptanes and heavier fractions for the GPA Peng-Robinson programs, Gas Processors Association, Research Report RR-28*, (1978).

[236] W.G. Chapman, K.E. Gubbins, G. Jackson, M. Radosz, *SAFT: Equation-of-state solution model for associating fluids*, Fluid Phase Equilib. **52**, 31–38 (1989).

[237] W.G. Chapman, K.E. Gubbins, G. Jackson, M. Radosz, *New reference equation of state for associating liquids*, Ind. Eng. Chem. Res. **29**, 1709–1721 (1990).

[238] S.H. Huang, M. Radosz, *Equation of state for small, large, polydisperse, and associating molecules*, Ind. Eng. Chem. Res. **29**, 2284–2294 (1990).

[239] G.M. Kontogeorgis, M.L. Michelsen, G.K. Folas, S. Derawi, N. von Solms, E.H. Stenby, *Ten years with the CPA (cubic-plus-association) equation of state. Part 1. Pure compounds and self-associating systems*, Ind. Eng. Chem. Res. **45**, 4855–4868 (2006).

[240] G.M. Kontogeorgis, M.L. Michelsen, G.K. Folas, S. Derawi, N. von Solms, E.H. Stenby, *Ten years with the CPA (cubic-plus-association) equation of state. Part 2. Cross-associating and multicomponent systems*, Ind. Eng. Chem. Res. **45**, 4869–4878 (2006).

[241] J. Ali, *Prediction of parachors of petroleum cuts and pseudocomponents*, Fluid Phase Equilib. **95**, 383–398 (1994).

[242] D. Broseta, Y. Meleán, C. Miqueu, *Parachors of liquid/vapor systems: a set of critical amplitudes*, Fluid Phase Equilib. **233**, 86–95 (2005).

[243] J.R. Fanchi, *Calculation of parachors for compositional simulation: An update*, SPE Reserv. Eng. **5**, 433–436 (1990).

[244] M.J. Fawcett, *Evaluation of correlations and parachors to predict low interfacial tensions in condensate systems*, in: SPE Annu. Tech. Conf. Exhib., Society of Petroleum Engineers (1994).

[245] C. Miqueu, J. Satherley, B. Mendiboure, J. Lachaise, A. Graciaa, *The effect of P/N/A distribution on the parachors of petroleum fractions*, Fluid Phase Equilib. **180**, 327–344 (2001).

[246] J.D. van der Waals, *Thermodynamische Theorie der Kapillarität unter Voraussetzung stetiger Dichteänderung*, Z. Phys. Chem. **13**, 657–725 (1894).

[247] V. Bongiorno, L.E. Scriven, H.T. Davis, *Molecular theory of fluid interfaces*, J. Colloid Interface Sci. **57**, 462–475 (1976).

[248] H.T. Davis, *Statistical mechanics of phases, interfaces and thin films*, Wiley (1995).

[249] B.S. Carey, *The gradient theory of fluid interfaces* (PhD thesis), University of Minnesota, USA (1979).

[250] P.M.W. Cornelisse, *The square gradient theory applied: Simultaneous modelling of interfacial tension and phase behaviour* (PhD thesis), Delft University of Technology, The Netherlands (1997).

[251] B.F. McCoy, H.T. Davis, *Free-energy theory of inhomogeneous fluids*, Phys. Rev. A. **20**, 1201–1207 (1979).

[252] B.S. Carey, L.E. Scriven, H.T. Davis, *Semiempirical theory of surface tension of binary systems*, AIChE J. **26**, 705–711 (1980).

[253] H.T. Davis, L.E. Scriven, *Stress and structure in fluid interfaces*, in: Adv. Chem. Phys., (1982): pp. 357–454.

[254] C. Miqueu, *Modélisation à température et pression élevées de la tension superficielle de composants des fluides pétroliers et de leurs mélanges synthétiques ou réels* (PhD thesis), Université de Pau et des Pays de l'Adour, France (2001).

[255] J.S. Rowlinson, B. Widom, *Molecular theory of capillarity*, Claredon Press: Oxford, U.K. (1982).

[256] H. Lin, Y.-Y. Duan, Q. Min, *Gradient theory modeling of surface tension for pure fluids and binary mixtures*, Fluid Phase Equilib. **254**, 75–90 (2007).

[257] A. Peneloux, E. Rauzy, R. Freze, *A consistent correction for Redlich-Kwong-Soave volumes*, Fluid Phase Equilib. **8**, 7–23 (1982).

[258] S. Khosharay, M.S. Mazraeno, F. Varaminian, *Modeling the surface tension of refrigerant mixtures with linear gradient theory*, Int. J. Refrig. **36**, 2223–2232 (2013).

[259] *DIPPR 801, Themophysical Properties Database*, (1998).

[260] J.M.H.L. Sengers, *Mean-field theories, their weaknesses and strength*, Fluid Phase Equilib. **158-160**, 3–17 (1999).

[261] A. Mejía, *Comportamiento interfacial de mezclas fluidas en equilibrio* (PhD thesis), Universidad de Concepción, Chile (2004).

[262] B.S. Carey, L.E. Scriven, H.T. Davis, *On gradient theories of fluid interfacial stress and structure*, J. Chem. Phys. **69**, 5040 (1978).

[263] M. Sahimi, H.T. Davis, L.E. Scriven, *Thermodynamic modeling of phase and tension behavior of CO_2/hydrocarbon systems*, Soc. Pet. Eng. J. **25**, 235–254 (1985).

[264] M.M. Telo da Gama, R. Evans, *The structure and surface tension of the liquid-vapour interface near the upper critical end point of a binary mixture of Lennard-Jones fluids*, Mol. Phys. **48**, 229–250 (1983).

[265] T. Wadewitz, J. Winkelmann, *Density functional theory: Structure and interfacial properties of binary mixtures*, Berichte der Bunsengesellschaft für Phys. Chemie. **100**, 1825–1832 (1996).

[266] Y.-X. Zuo, E.H. Stenby, *Prediction of interfacial tensions of reservoir crude oil*

and gas condensate systems, SPE J. **3**, 134–145 (1998).

[267] K.A.G. Schmidt, G.K. Folas, B. Kvamme, *Calculation of the interfacial tension of the methane–water system with the linear gradient theory*, Fluid Phase Equilib. **261**, 230–237 (2007).

[268] S. Khosharay, F. Varaminian, *Modeling interfacial tension of (CH_4+N_2)+H_2O and (N_2+CO_2)+H_2O systems using linear gradient theory*, Korean J. Chem. Eng. **30**, 724–732 (2013).

[269] Y.-X. Zuo, E.H. Stenby, *Calculation of interfacial tensions of hydrocarbon-water systems under reservoir conditions*, Situ. **22**, 157–180 (1998).

[270] M.L. Michelsen, J.M. Mollerup, *Thermodynamic models: Fundamentals & Computational aspects*, Second ed., Tie-Line Publications (2007).

[271] J.-N. Jaubert, F. Mutelet, *VLE predictions with the Peng–Robinson equation of state and temperature dependent kij calculated through a group contribution method*, Fluid Phase Equilib. **224**, 285–304 (2004).

[272] J.-N. Jaubert, S. Vitu, F. Mutelet, J.-P. Corriou, *Extension of the PPR78 model (predictive 1978, Peng–Robinson EOS with temperature dependent kij calculated through a group contribution method) to systems containing aromatic compounds*, Fluid Phase Equilib. **237**, 193–211 (2005).

[273] F. Mutelet, S. Vitu, R. Privat, J.-N. Jaubert, *Solubility of CO_2 in branched alkanes in order to extend the PPR78 model (predictive 1978, Peng–Robinson EOS with temperature-dependent kij calculated through a group contribution method) to such systems*, Fluid Phase Equilib. **238**, 157–168 (2005).

[274] J.-N. Jaubert, R. Privat, F. Mutelet, *Predicting the phase equilibria of synthetic petroleum fluids with the PPR78 approach*, AIChE J. **56**, 3225–3235 (2010).

[275] J.-W. Qian, J.-N. Jaubert, R. Privat, *Prediction of the phase behavior of alkene-containing binary systems with the PPR78 model*, Fluid Phase Equilib. **354**, 212–235 (2013).

[276] X. Xu, R. Privat, J.-N. Jaubert, *Addition of the sulfur dioxide group (SO_2), the oxygen Group (O_2), and the nitric oxide Group (NO) to the E-PPR78 Model*, Ind. Eng. Chem. Res. **54**, 9494–9504 (2015).

[277] X. Xu, J.-N. Jaubert, R. Privat, P. Duchet-Suchaux, F. Braña-Mulero, *Predicting binary-interaction parameters of cubic equations of state for petroleum fluids containing pseudo-components*, Ind. Eng. Chem. Res. **54**, 2816–2824 (2015).

[278] J.J. Martin, *Cubic equations of state - Which?*, Ind. Eng. Chem. Fundam. **18**, 81–97 (1979).

[279] A.M. Abudour, S.A. Mohammad, R.L. Robinson, K.A.M. Gasem, *Volume-translated Peng–Robinson equation of state for saturated and single-phase liquid densities*, Fluid Phase Equilib. **335**, 74–87 (2012).

[280] A.M. Abudour, S.A. Mohammad, R.L. Robinson, K.A.M. Gasem, *Volume-translated Peng-Robinson equation of state for liquid densities of diverse binary mixtures*, Fluid Phase Equilib. **349**, 37–55 (2013).

[281] I. V. Yakoumis, G.M. Kontogeorgis, E.C. Voutsas, E.M. Hendriks, D.P. Tassios, *Prediction of phase equilibria in binary aqueous systems containing alkanes, cycloalkanes, and alkenes with the cubic-plus-association equation of state*, Ind. Eng. Chem. Res. **37**, 4175–4182 (1998).

[282] M.B. Oliveira, J.A.P. Coutinho, A.J. Queimada, *Mutual solubilities of hydrocarbons and water with the CPA EoS*, Fluid Phase Equilib. **258**, 58–66 (2007).

[283] G.K. Folas, G.M. Kontogeorgis, M.L. Michelsen, E.H. Stenby, *Application of the cubic-plus-association (CPA) equation of state to complex mixtures with aromatic hydrocarbons*, Ind. Eng. Chem. Res. **45**, 1527–1538 (2006).

[284] G.K. Folas, J. Gabrielsen, M.L. Michelsen, E.H. Stenby, G.M. Kontogeorgis, *Application of the cubic-plus-association (CPA) equation of state to cross-associating systems*, Ind. Eng. Chem. Res. **44**, 3823–3833 (2005).

[285] S.O. Derawi, G.M. Kontogeorgis, M.L. Michelsen, E.H. Stenby, *Extension of the cubic-plus-association equation of state to glycol−water cross-associating systems*, Ind. Eng. Chem. Res. **42**, 1470–1477 (2003).

[286] M.P. Breil, G.M. Kontogeorgis, *Thermodynamics of triethylene glycol and tetraethylene glycol containing systems described by the cubic-plus-association equation of state*, Ind. Eng. Chem. Res. **48**, 5472–5480 (2009).

[287] M.B. Oliveira, M.G. Freire, I.M. Marrucho, G.M. Kontogeorgis, A.J. Queimada, J.A.P. Coutinho, *Modeling the liquid−liquid equilibria of water + fluorocarbons with the cubic-plus-association equation of state*, Ind. Eng. Chem. Res. **46**, 1415–1420 (2007).

[288] I. Tsivintzelis, G.M. Kontogeorgis, M.L. Michelsen, E.H. Stenby, *Modeling phase equilibria for acid gas mixtures using the CPA equation of state. Part II: Binary mixtures with* CO_2, Fluid Phase Equilib. **306**, 38–56 (2011).

[289] H. Haghighi, A. Chapoy, B. Tohidi, *Methane and water phase equilibria in the presence of single and mixed electrolyte solutions using the cubic-plus-association equation of state*, Oil Gas Sci. Technol. **64**, 141–154 (2009).

[290] F. Tabasinejad, R.G. Moore, S.A. Mehta, K.C. Van Fraassen, Y. Barzin, J.A. Rushing, K.E. Newsham, *Water solubility in supercritical methane, nitrogen, and carbon dioxide: measurement and modeling from 422 to 483 K and pressures from 3.6 to 134 MPa*, Ind. Eng. Chem. Res. **50**, 4029–4041 (2011).

[291] P.J. Carvalho, A.R. Ferreira, M.B. Oliveira, M. Besnard, M.I. Cabaço, J.A.P. Coutinho, *High pressure phase behavior of carbon dioxide in carbon disulfide and carbon tetrachloride*, J. Chem. Eng. Data. **56**, 2786–2792 (2011).

[292] M.B. Oliveira, A.J. Queimada, G.M. Kontogeorgis, J.A.P. Coutinho, *Evaluation of the* CO_2 *behavior in binary mixtures with alkanes, alcohols, acids and esters using the Cubic-Plus-Association Equation of State*, J. Supercrit. Fluids. **55**, 876–892 (2011).

[293] G.M. Kontogeorgis, I. V Yakoumis, H. Meijer, E. Hendriks, T. Moorwood, *Multicomponent phase equilibrium calculations for water-methanol-alkane mixtures*, Fluid Phase Equilib. **158-160**, 201–209 (1999).

[294] E.C. Voutsas, G.C. Boulougouris, I.G. Economou, D.P. Tassios, *Water/hydrocarbon phase equilibria using the thermodynamic perturbation theory*, Ind. Eng. Chem. Res. **39**, 797–804 (2000).

[295] J.A. Awan, I. Tsivintzelis, C. Coquelet, G.M. Kontogeorgis, *Phase equilibria of three binary mixtures: Methanethiol + methane, methanethiol + nitrogen, and methanethiol + carbon dioxide*, J. Chem. Eng. Data. **57**, 896–901 (2012).

[296] B.N. Taylor, C.E. Kuyatt, *Guidelines for evaluating and expressing the*

uncertainty of NIST measurement results, National Institute of Standards and Technology (1994).

[297] A. Azarnoosh, J.J. McKetta, *Nitrogen-n-decane system in the two-phase region*, J. Chem. Eng. Data. **8**, 494–496 (1963).

[298] F. Feyzi, M. Seydi, F. Alavi, *Crossover Peng-Robinson equation of state with introduction of a new expression for the crossover function*, Fluid Phase Equilib. **293**, 251–260 (2010).

[299] H. Behnejad, H. Cheshmpak, A. Jamali, *The extended crossover Peng–Robinson equation of state for describing the thermodynamic properties of pure fluids*, J. Stat. Phys. **158**, 372–385 (2015).

[300] D. Fu, Y. Wei, *Investigation of vapor−liquid surface tension for carbon dioxide and hydrocarbon mixtures by perturbed-chain statistical associating fluid theory combined with density-gradient theory*, Ind. Eng. Chem. Res. **47**, 4490–4495 (2008).

[301] *Reservoir Fluid Studies: 1990-1993 Programme*, Final Report, Heriot-Watt University, UK .

[302] A.Y. Dandekar, *Interfacial tension and viscosity of reservoir fluids* (PhD thesis), Heriot Watt University, UK (1994).

[303] M.R. Riazi, *Characterization and properties of petroleum fractions*, American Society for Testing and Materials (2005).

[304] C.H. Whitson, M.R. Brulé, *Phase behavior*, Society of Petroleum Engineering Inc. (2000).

[305] M.R. Riazi, T.E. Daubert, *Characterization parameters for petroleum fractions*, Ind. Eng. Chem. Res. **26**, 755–759 (1987).

[306] W.C. Edmister, *Applied hydrocarbon thermodynamics, Part 4: Compressibility factors and equations of State*, Pet. Refin. **37**, 173–179 (1958).

[307] B.I. Lee, M.G. Kesler, *A generalized thermodynamic correlation based on three-parameter corresponding states*, AIChE J. **21**, 510–527 (1975).

[308] M.G. Kesler, B.I. Lee, *Improve prediction of enthalpy of fractions*, Hydrocarb. Process. **55**, 153–158 (1976).

[309] C.H. Twu, *An internally consistent correlation for predicting the critical properties and molecular weights of petroleum and coal-tar liquids*, Fluid Phase Equilib. **16**, 137–150 (1984).

[310] A. Firoozabadi, A. Khalid, *Analysis and correlation of nitrogen and lean-gas miscibility pressure*, SPE Reserv. Eng. **1**, 575–582 (1986).

[311] H. Doryani, Y. Kazemzadeh, R. Parsaei, M.R. Malayeri, M. Riazi, *Impact of asphaltene and normal paraffins on methane-synthetic oil interfacial tension: An experimental study*, J. Nat. Gas Sci. Eng. **26**, 538–548 (2015).

[312] P.M.W. Cornelisse, C.J. Peters, J.D. Arons, *Application of the Peng-Robinson equation of state to calculate interfacial-tensions and profiles at vapor-liquid interfaces*, Fluid Phase Equilib. **82**, 119–129 (1993).

[313] P.M.W. Cornelisse, C.J. Peters, J. De Swaan Arons, *Simultaneous prediction of phase equilibria, interfacial tension and concentration profiles*, Mol. Phys. **80**, 941–955 (1993).

[314] M.B. King, A. Mubarak, J.D. Kim, T.R. Bott, *The mutual solubilities of water with supercritical and liquid carbon dioxide*, J. Supercrit. Fluids. **5**, 296–302 (1992).

[315] L.W. Diamond, N.N. Akinfiev, *Solubility of CO_2 in water from −1.5 to 100 °C and from 0.1 to 100 MPa: evaluation of literature data and thermodynamic modelling*, Fluid Phase Equilib. **208**, 265–290 (2003).

[316] A. Valtz, A. Chapoy, C. Coquelet, P. Paricaud, D. Richon, *Vapour–liquid equilibria in the carbon dioxide–water system, measurement and modelling from 278.2 to 318.2K*, Fluid Phase Equilib. **226**, 333–344 (2004).

[317] J.M. Míguez, M.C. dos Ramos, M.M. Piñeiro, F.J. Blas, *An examination of the ternary methane + carbon dioxide + water phase diagram using the SAFT-VR approach*, J. Phys. Chem. B. **115**, 9604–9617 (2011).

[318] R.L. Scott, P.H. van Konynenburg, *Static properties of solutions. Van der Waals and related models for hydrocarbon mixtures*, Discuss. Faraday Soc. **49**, 87 (1970).

[319] P.H. V. Konynenburg, R.L. Scott, *Critical lines and phase equilibria in binary van der Waals mixtures*, Philos. Trans. R. Soc. A Math. Phys. Eng. Sci. **298**, 495–540 (1980).

[320] Z. Duan, R. Sun, *An improved model calculating CO_2 solubility in pure water and aqueous NaCl solutions from 273 to 533 K and from 0 to 2000 bar*, Chem. Geol. **193**, 257–271 (2003).

[321] S.-X. Hou, G.C. Maitland, J.P.M. Trusler, *Measurement and modeling of the phase behavior of the (carbon dioxide+water) mixture at temperatures from 298.15K to 448.15K*, J. Supercrit. Fluids. **73**, 87–96 (2013).

[322] A. Chapoy, M. Nazeri, M. Kapateh, R. Burgass, C. Coquelet, B. Tohidi, *Effect of impurities on thermophysical properties and phase behaviour of a CO_2-rich system in CCS*, Int. J. Greenh. Gas Control. **19**, 92–100 (2013).

[323] M.N. Ghojogh, *Impact of impurities on thermo-physical properties of CO_2-rich systems: Experimental and modelling* (PhD thesis), Heriot-Watt University, UK (2015).

[324] W. Yan, S. Huang, E.H. Stenby, *Measurement and modeling of CO_2 solubility in NaCl brine and CO_2–saturated NaCl brine density*, Int. J. Greenh. Gas Control. **5**, 1460–1477 (2011).

[325] Z. Duan, J. Hu, D. Li, S. Mao, *Densities of the CO_2 –H_2O and CO_2 –H_2O–NaCl systems up to 647 K and 100 MPa*, Energy & Fuels. **22**, 1666–1674 (2008).

[326] Z. Duan, N. Møller, J.H. Weare, *An equation of state for the CH_4-CO_2-H_2O system: I. Pure systems from 0 to 1000°C and 0 to 8000 bar*, Geochim. Cosmochim. Acta. **56**, 2605–2617 (1992).

[327] Z. Duan, R. Sun, C. Zhu, I.-M. Chou, *An improved model for the calculation of CO_2 solubility in aqueous solutions containing Na^+, K^+, Ca^{2+}, Mg^{2+}, Cl^-, and SO_4^{2-}*, Mar. Chem. **98**, 131–139 (2006).

[328] J.C. Peiper, K.S. Pitzer, *Thermodynamics of aqueous carbonate solutions including mixtures of sodium carbonate, bicarbonate, and chloride*, J. Chem. Thermodyn. **14**, 613–638 (1982).

[329] S. Mao, Z. Duan, *A thermodynamic model for calculating nitrogen solubility, gas phase composition and density of the N_2–H_2O–NaCl system*, Fluid Phase Equilib. **248**, 103–114 (2006).

[330] G. Bergin, *Prévision de la solubilité des hydrocarbures dans l'eau en fonction de la température et de la pression* (PhD thesis), Université Blaise Pascal-Clermont-Ferrand, France (2002).

[331] *IUPAC-NIST Solubility data series. 81. Hydrocarbons with water and seawater—Revised and updated. Part 4. C_6H_{14} hydrocarbons with water*, J. Phys. Chem. Ref. Data. **34**, 709 (2005).

[332] *IUPAC-NIST Solubility data series. 81. Hydrocarbons with water and seawater—Revised and updated. Part 11. C_{13}–C_{36} hydrocarbons with water*, J. Phys. Chem. Ref. Data. **35**, 687 (2006).

[333] *IUPAC-NIST Solubility data series. 81. Hydrocarbons with water and seawater—Revised and updated. Part 9. C_{10} hydrocarbons with water*, J. Phys. Chem. Ref. Data. **35**, 93 (2006).

[334] A. Mączyński, *Recommended liquid–liquid equilibrium data. Part 1. Binary alkane–water Systems*, J. Phys. Chem. Ref. Data. **33**, 549 (2004).

[335] M. Medeiros, *Mutual solubilities of water and hydrocarbons from the Cubic plus Association equation of state: A new mixing rule for the correlation of observed minimum hydrocarbon solubilities*, Fluid Phase Equilib. **368**, 5–13 (2014).

[336] N. Spycher, K. Pruess, J. Ennis-King, *CO_2-H_2O mixtures in the geological sequestration of CO_2. I. Assessment and calculation of mutual solubilities from 12 to 100°C and up to 600 bar*, Geochim. Cosmochim. Acta. **67**, 3015–3031 (2003).

[337] S. Takenouchi, G.C. Kennedy, *The binary system H_2O-CO_2 at high temperatures and pressures*, Am. J. Sci. **262**, 1055–1074 (1964).

[338] A. Chapoy, A.H. Mohammadi, D. Richon, B. Tohidi, *Gas solubility measurement and modeling for methane–water and methane–ethane–n-butane–water systems at low temperature conditions*, Fluid Phase Equilib. **220**, 111–119 (2004).

[339] O.L. Culberson, H. A.B., J.J.J. McKetta, *Phase equilibria in hydrocarbon-water systems*, Pet. Trans. AIME. **189**, 1–6 (1950).

[340] R.G. Sultanov, V.G. Skripka, A.Y. Namiot, *Rastvormost Metana V Vode Pri Novysjennykh Temperaturakh I Davlenijakh*, Gaz. Prom. 6–7 (1971).

[341] M. Rigby, J.M. Prausnitz, *Solubility of water in compressed nitrogen, argon, and methane*, J. Phys. Chem. **72**, 330–334 (1968).

[342] R. Wiebe, V.L. Gaddy, C. Heinss, *Solubility of nitrogen in water in at 25oC from 25 to 1000 atmospheres*, Ind. Eng. Chem. **24**, 927–927 (1932).

[343] T.D. O'Sullivan, N.O. Smith, *Solubility and partial molar volume of nitrogen and methane in water and in aqueous sodium chloride from 50 to 125°C and 100 to 600 atm*, J. Phys. Chem. **74**, 1460–1466 (1970).

[344] T.S. Khasanshin, V.S. Samuilov, A.P. Shchemelev, *Determination of the thermodynamic properties of liquid n-hexadecane from the measurements of the velocity of sound*, J. Eng. Phys. Thermophys. **82**, 149–156 (2009).

[345] R.G. Sultanov, V.G. Skripka, A.Y. Namoit, *No Title*, Gazov. Delo. **10**, (1972).

[346] M.S.-W. Wei, T.S. Brown, A.J. Kidnay, E.D. Sloan, *Vapor + liquid equilibria for the ternary system methane + ethane + carbon dioxide at 230 K and its constituent binaries at temperatures from 207 to 270 K*, J. Chem. Eng. Data. **40**, 726–731 (1995).

[347] S.Z.S. Al Ghafri, E. Forte, G.C. Maitland, J.J. Rodriguez-Henríquez, J.P.M.

Trusler, *Experimental and modeling study of the phase behavior of (methane + CO_2 + water) mixtures.*, J. Phys. Chem. B. **118**, 14461–78 (2014).

[348] E. Forte, A. Galindo, J.P.M. Trusler, *Experimental and molecular modeling study of the three-phase behavior of (n-decane + carbon dioxide + water) at reservoir conditions*, 14591–14609 (2011).

[349] Z. Duan, S. Mao, *A thermodynamic model for calculating methane solubility, density and gas phase composition of methane-bearing aqueous fluids from 273 to 523 K and from 1 to 2000 bar*, Geochim. Cosmochim. Acta. **70**, 3369–3386 (2006).

[350] K.Y. Song, R. Kobayashi, *The water content of a carbon dioxide-rich gas mixture containing 5.31 mol% methane along the three-phase and supercritical conditions*, J. Chem. Eng. Data. **35**, 320–322 (1990).

[351] K. Aasberg-Petersen, E. Stenby, A. Fredenslund, *Prediction of high-pressure gas solubilities in aqueous mixtures of electrolytes*, Ind. Eng. Chem. Res. **30**, 2180–2185 (1991).

[352] H. Haghighi, *Phase equilibria modelling of petroleum reservoir fluids containing water, hydrate inhibitors and electrolyte solutions* (PhD thesis), Heriot-Watt University, UK (2009).

[353] V.S. Patwardhan, A. Kumar, *A unified approach for prediction of thermodynamic properties of aqueous mixed-electrolyte solutions. Part I: Vapor pressure and heat of vaporization*, AIChE J. **32**, 1419–1428 (1986).

[354] B. Tohidi, *Gas hydrate equilibria in the presence of electrolyte solutions* (PhD thesis), Heriot-Watt University, UK (1995).

[355] S. Takenouchi, G.C. Kennedy, *The solubility of carbon Dioxide in NaCl solutions at high temperatures and pressures*, Am. J. Sci. **263**, 445–454 (1965).

[356] D. Koschel, J.-Y. Coxam, L. Rodier, V. Majer, *Enthalpy and solubility data of CO_2 in water and NaCl(aq) at conditions of interest for geological sequestration*, Fluid Phase Equilib. **247**, 107–120 (2006).

[357] P.J. Carvalho, L.M.C. Pereira, N.P.F. Gonçalves, A.J. Queimada, J.A.P. Coutinho, *Carbon dioxide solubility in aqueous solutions of NaCl: Measurements and modeling with electrolyte equations of state*, Fluid Phase Equilib. **388**, 100–106 (2015).

[358] Á. Pérez-Salado Kamps, E. Meyer, B. Rumpf, G. Maurer, *Solubility of CO_2 in Aqueous Solutions of KCl and in Aqueous Solutions of K_2CO_3*, J. Chem. Eng. Data. **52**, 817–832 (2007).

[359] H. Zhao, R.M. Dilmore, S.N. Lvov, *Experimental studies and modeling of CO_2 solubility in high temperature aqueous $CaCl_2$, $MgCl_2$, Na_2SO_4, and KCl solutions*, AIChE J. **61**, 2286–2297 (2015).

[360] D. Tong, J.P.M. Trusler, D. Vega-Maza, *Solubility of CO_2 in aqueous solutions of $CaCl_2$ or $MgCl_2$ and in a synthetic formation brine at temperatures up to 423 K and pressures up to 40 MPa*, J. Chem. Eng. Data. **58**, 2116–2124 (2013).

[361] C.J. Radke, *Gibbs adsorption equation for planar fluid-fluid interfaces: Invariant formalism.*, Adv. Colloid Interface Sci. **222**, 600–14 (2015).

[362] L.A. Turkevich, J.A. Mann, *Pressure dependence of the interfacial tension between fluid phases. 1. Formalism and application to simple fluids*, Langmuir. **6**, 445–456 (1990).

[363] E. Bertrand, H. Dobbs, D. Broseta, J. Indekeu, D. Bonn, J. Meunier, *First-order and critical wetting of alkanes on water*, Phys. Rev. Lett. **85**, 1282–5 (2000).

[364] D.R. Babu, V. Hornof, G. Neale, *Effects of temperature and time on interfacial tension behavior between heavy oils and alkaline solutions*, Can. J. Chem. Eng. **62**, 156–159 (1984).

[365] A.A.S. Al-Rossies, B.D. Al-Anazi, A.M. Paiaman, *Effect of pH-values on the contact angle and interfacial tension*, Nafta. **61**, 181–186 (2010).

[366] P.M. Larsen, B. Maribo-Mogensen, G.M. Kontogeorgis, *A collocation method for surface tension calculations with the density gradient theory*, Fluid Phase Equilib. **408**, 170–179 (2015).

[367] J. Kou, S. Sun, *An adaptive finite element method for simulating surface tension with the gradient theory of fluid interfaces*, J. Comput. Appl. Math. **255**, 593–604 (2014).

[368] J. Kou, S. Sun, X. Wang, *Efficient numerical methods for simulating surface tension of multi-component mixtures with the gradient theory of fluid interfaces*, Comput. Methods Appl. Mech. Eng. **292**, 92–106 (2015).

[369] J. Kou, S. Sun, *Numerical methods for a multicomponent two-phase interface model with geometric mean influence parameters*, SIAM J. Sci. Comput. **37**, B543–B569 (2015).

[370] X.-H. Xu, Y.-Y. Duan, *Crossover CPA equation of state for associating fluids*, Fluid Phase Equilib. **290**, 148–152 (2010).

[371] X.-H. Xu, Y.-Y. Duan, Z. Yang, *Prediction of the critical properties of binary alkanol+alkane mixtures using a crossover CPA equation of state*, Fluid Phase Equilib. **309**, 168–173 (2011).

[372] S.-X. Hou, G.C. Maitland, J.P.M. Trusler, *Phase equilibria of* (CO_2+H_2O+NaCl) *and* (CO_2+H_2O+KCl)*: Measurements and modeling*, J. Supercrit. Fluids. **78**, 78–88 (2013).

[373] Y. Liu, M. Hou, G. Yang, B. Han, *Solubility of* CO_2 *in aqueous solutions of NaCl, KCl,* $CaCl_2$ *and their mixed salts at different temperatures and pressures*, J. Supercrit. Fluids. **56**, 125–129 (2011).

[374] H. Zhao, R. Dilmore, D.E. Allen, S.W. Hedges, Y. Soong, S.N. Lvov, *Measurement and modeling of* CO_2 *solubility in natural and synthetic formation brines for* CO_2 *sequestration*, Environ. Sci. Technol. **49**, 1972–80 (2015).

[375] P.C. Gillespie, G.M. Wilson, *Vapor-liquid and liquid-liquid equilibria: water-methane, water-carbon dioxide, water-hydrogen sulfide, water-n-pentane, water-methane-n-pentane. Gas Processors Assocaition. Tulsa. Research Report RR 48*, (1982).